ABSTRACT

Title of dissertation: PRIMARY CONTROL OF A MACH SCALE SWASHPLATELESS ROTOR USING BRUSHLESS DC MOTOR ACTUATED TRAILING EDGE FLAPS

Anand Saxena, Doctor of Philosophy, 2015

Dissertation directed by: Professor Inderjit Chopra
Department of Aerospace Engineering

The focus of this research was to demonstrate a four blade rotor trim in forward flight using integrated trailing edge flaps instead of using a swashplate controls. A compact brushless DC motor was evaluated as an on-blade actuator, with the possibility of achieving large trailing edge flap amplitudes. A control strategy to actuate the trailing edge flap at desired frequency and amplitude was developed and large trailing edge flap amplitudes from the motor (instead of rotational motion) were obtained. Once the actuator was tested on the bench-top, a lightweight mechanism was designed to incorporate the motor in the blade and actuate the trailing edge flaps. A six feet diameter, four bladed composite rotor with motor-flap system integrated into the NACA 0012 airfoil section was fabricated. Systematic testing was carried out for a range of load conditions, first in the vacuum chamber followed by hover tests. Large trailing edge flap deflections were observed during the hover testing, and a peak to peak trailing edge flap amplitude of 18 degree was achieved at 2000 rotor RPM with hover tip Mach number of 0.628. A closed loop controller

was designed to demonstrate trailing edge flap mean position and the peak to peak amplitude control. Further, a soft pitch link was designed and fabricated, to replace the stiff pitch link and thereby reduce the torsional stiffness of the blade to 2/rev. This soft pitch link allowed for blade root pitch motion in response to the trailing edge flap inputs. Blade pitch response due to both steady as well as sinusoidal flap deflections were demonstrated. Finally, tests were performed in Glenn L. Martin wind tunnel using a model rotor rig to assess the performance of motor-flap system in forward flight. A swashplateless trim using brushless DC motor actuated trailing edge flaps was achieved for a rotor operating at 1200 RPM and an advance ratio of 0.28. Also, preliminary exploration was carried out to test the scalability of the motor driven trailing edge flap concept. In conclusion, the concept of using brushless DC motors as on-blade actuators, actuating trailing edge flaps has the potential to replace the current mechanically complex swashplate with a hydraulic-free swashplateless system and thereby reduce overall weight and hub drag.

PRIMARY CONTROL OF A MACH SCALE SWASHPLATELESS ROTOR USING BRUSHLESS DC MOTOR ACTUATED TRAILING EDGE FLAPS

by

Anand Saxena

Dissertation submitted to the Faculty of the Graduate School of the
University of Maryland, College Park in partial fulfillment
of the requirements for the degree of
Doctor of Philosophy
2015

Advisory Committee:
Dr. Inderjit Chopra, Chair & Advisor
Dr. Norman Wereley
Dr. James Baeder
Dr. Sung Lee
Dr. Amr Baz, Dean's Representative

In fond memory of my Grandfather

Kailash Narayan Saxena

Thank you for holding my hands, walking me to and from the school

each and every day, rain or shine.

You are greatly missed.

Acknowledgments

I would like to thank Dr. Inderjit Chopra for giving me the opportunity to work on such an interesting research project. The journey though tumultuous, has been very rewarding and it would not have been possible without the support, patience and guidance of Dr. Chopra.

I would also like to thank members of the committee, Dr. Norman Wereley, Dr. James Baeder, Dr. Sung Lee and Dr. Amr Baz, for reviewing my research as well as their guidance and support through the doctoral program. I would also like to acknowledge Dr. Michael Coplan for being an initial member on the committee and thank him for his continued interest in my research.

I am grateful to Peter Copp and Vikram Hrishikeshavan for helping me get started in the rotorcraft lab. Over the course of my PhD, a strong friendship has developed and discussing various ideas with them and seeking their advice has been very beneficial to me. I am also grateful to Abhishek for making my transition from India to USA smooth and fun filled. Although senior by a few years, he has always treated me as a friend. I wish all of them unabated success and great health.

I would like to specially acknowledge Dr. V.T. Nagaraj for his technical help, counsel and support. Interactions with Dr. Moble Benedict, Dr. Anubhav Datta and Dr. Jayant Sirohi have been rewarding as well. Their inputs in my research and guidance is greatly appreciated.

I had a wonderful experience being a teaching assistant for Dr. Robert Korkegi. He was the first professor at Maryland with whom I interacted at length. His

modesty and determination deeply touched me. I would like to specially acknowledge Dr. S.C. Sharma, my undergraduate professor and mentor for his continued encouragement and belief in me.

During my multiple entires at the Glenn L. Martin Wind Tunnel, Dr. Jewel Barlow, Hareen, Ahmed, Alex and the rest of the staff have been very accommodating and helpful. Watching Dr. Winkelmann work on the wind tunnels at the high bay engineering lab has been a constant source of motivation. He was easy to engage in discussion whenever I needed any fabrication or machining advice.

All my colleagues at the rotorcraft center have been a source of encouragement over the years. I would like specially mention Kumar, Ananth, Ben, Graham, Joe, Andrew, and Aaron for their assistance and discussions on various topics.

I am grateful to undergraduates: Attin Mitra, Colin Adamson, Deon Tran, Lyndon Baltazar, Luke Smith, Michelle Cady, Patrick Dunleavy, Peter Oas, and Wiam Attar for their assistance. Kevin Baeder helped us in the lab as well. I wish them all a bright future.

Interaction with research interns from France: Marc, Yoann, David, and France has been enriching as well. I have formed a friendship with Marc and I wish them all *bonne chance!*

This journey would not have been possible without the loving support of my friends: Sachit, Suba, Soma, Michael, Sachin, Mayank, Siddharth, and Harinder.

Finally, all that I am today and ever will be, is a testament of efforts and foresight of my father, Ajai Kumar Saxena and my mother, Aneeta Saxena. Their unconditional love and support and that of my grandparents and my brother, Ashish

Saxena is my biggest asset in any undertaking. The love and support from my girlfriend, Marti Gray was instrumental in finishing the project. At times when the going was really tough, she stood with me and helped me stay on track. I cannot imagine a life journey without her.

This project was partly funded by National Rotorcraft Technology Center.

Table of Contents

List of Tables

List of Figures

List of Abbreviations

AC	Alternating Current
ACSR	Active Control of Structural Response
ACU	Actuator Control Unit
AECS	Analogue EC Controller Sensorless
AFDD	(US Army) Aero Flight Dynamics Directorate
AGRC	Alfred Gessow Rotorcraft Center
ARES	Aeroelastic Rotor Experimental Setup
BVI	Blade Vortex Interaction
CAD	Computer Aided Drawing
CAMRAD	Comprehensive Analytical Model of Rotor Aerodynamics and Dynamics
CATIA	Computer Aided Three-dimensional Interactive Application
CFD	Computational Fluid Dynamics
CNC	Computer Numerical Control
CSD	Computational Structural Dynamics
DC	Direct Current
DoF	Degree of Freedom
EC	Electronic Commutation
EMA	Electro Magnetic Actuator
EMF	Electro Motive Force
EMI	Electro Magnetic Interference
FEA	Finite Element Analysis
FEM	Finite Element Method
FFT	Fast Fourier Transform
GLMWT	Glenn L. Martin Wind Tunnel
HART	Higher harmonic control Aeroacoustics Rotor Test
HHC	Higher Harmonic Control
IBC	Individual Blade Control
JAXA	Japan Aerospace eXploration Agency
JMRTS	JAXA Multi-purpose Rotor Test Stand

LabVIEW	Laboratory Virtual Instrument Engineering Workbench
LRTA	Large Rotor Test Apparatus
LVDT	Linear Variable Displacement Transducer
MAV	Micro Aerial Vehicle
MDART	McDonnell-Douglas Advance Rotor Technology
MOS-FET	Metal Oxide Semiconductor Field Effect Transistor
NACA	National Advisory Committee for Aeronautics
NASA	National Aeronautics and Space Administration
NFAC	National Full-scale Aerodynamics Complex
ONERA	Office National d'Etudes et de Recherches Aerospatiale
PAM	Pneumatic Artificial Muscle
PCR	Pitch Control Rod
PID	Proportional Integral Derivative
PZT	Lead (Pb) Zirconate Titanate
RCAS	Rotorcraft Comprehensive Analysis System
RMDAS	Rotor Mounted Data Acquisition System
RPM	Rotations Per Minute
SMART	Smart Materials Actuated Rotor Technology
SPL	Soft Pitch Link
TDT	Transonic Dynamics Tunnel
TEF	Trailing Edge Flap
TT	Tension - Torsion
UAV	Unmanned Aerial Vehicle
UMARC	University of Maryland Advanced Rotorcraft Code
UMD	University of Maryland
USB	Universal Serial Bus
UTD	Universal Tracking Device
UTRC	United Technology Research Center
VG	Viscosity Grade
VI	Virtual Instrument

UNITS:

A	Ampere
C	Celsius
F	Fahrenheit
HP	Horse Power
Hz	Hertz
N	Newton
V	Volt
W	Watt

dB	decibel
ft	feet
gpm	gallons per minute
in	inch
in Hg	inches of Mercury
kg	kilogram
kts	knots
lb	pounds
lbf	pound-force
m	meter
mph	miles per hour
m/s	meter per second
oz	ounce
psi	pounds per square inch
rad/s	radians per second

Chapter 1: **Introduction**

The ability to hover in-position, operate efficiently at low speeds, and take-off and land in constricted areas makes the helicopter a unique and versatile air vehicle. The rotor is the defining feature of the helicopter as it provides both the propulsive as well as the lift force for the vehicle. Helicopter control has been conventionally performed by the hydraulic actuated swashplate mechanism, which then controls the aerodynamic forces on the rotor. Over the years, the swashplate mechanism has proved highly reliable, in spite of its mechanical complexity and high maintenance costs. In addition, numerous exposed linkages, bearings, push rods and hinges contribute significantly both to the helicopter structural weight as well as parasite drag.

These limitations have motivated research into alternate ways of providing helicopter control. Eliminating the swashplate could possibly lead to reduced weight and drag resulting in improved mission performance. To address these limitations and to achieve a successful alternative to the swashplate, it is important to systematically understand the role of swashplate and outline the evolution of the current control system.

With this in mind, the following sections are laid out to first discuss various

rotor primary control mechanisms. Once the rotor primary control mechanism is understood, it may be logical to lay emphasis on reducing the helicopter vibrations, noise and improving its performance. To this end, passive and active approaches in both non-rotating frame as well as rotating frame are briefly discussed. Further, it will be shown that using trailing edge flaps as an active primary rotor control is the most attractive option and various previous research activities using trailing edge flaps are discussed. Finally, the objective and the scope of the current research is detailed.

1.1 Background

Cierva Autogyro C-4 [1], built in 1923 is the first successful rotary wing aircraft. Autogyros were primarily motivated by the need to safely operate at low speeds. It has a set of unpowered and uncontrolled blades that are free to rotate (auto-rotate) as the vehicle moves forward. It has all the typical control surfaces of a fixed wing airplane. The autogyro rotor blades are free to flap about the hinge at the center of rotation. The flapping motion compensates for angle of attack asymmetry. Thus, the rotor system is essentially a system in resonance with its rotational speed as the fundamental frequency.

Acknowledging the potential of such a vehicle, efforts were made to add a control system to use the rotor for controlling the flight path. This would allow to reduce aircraft drag by eliminating the fixed wing control surfaces. Such a system was implemented by Cierva in 1933 by directly tilting the rotor plane (*hanging stick*

mechanism). Leishman [2] presented a technical review outlining the early evolution of the autogyro and eventual convergence to helicopters.

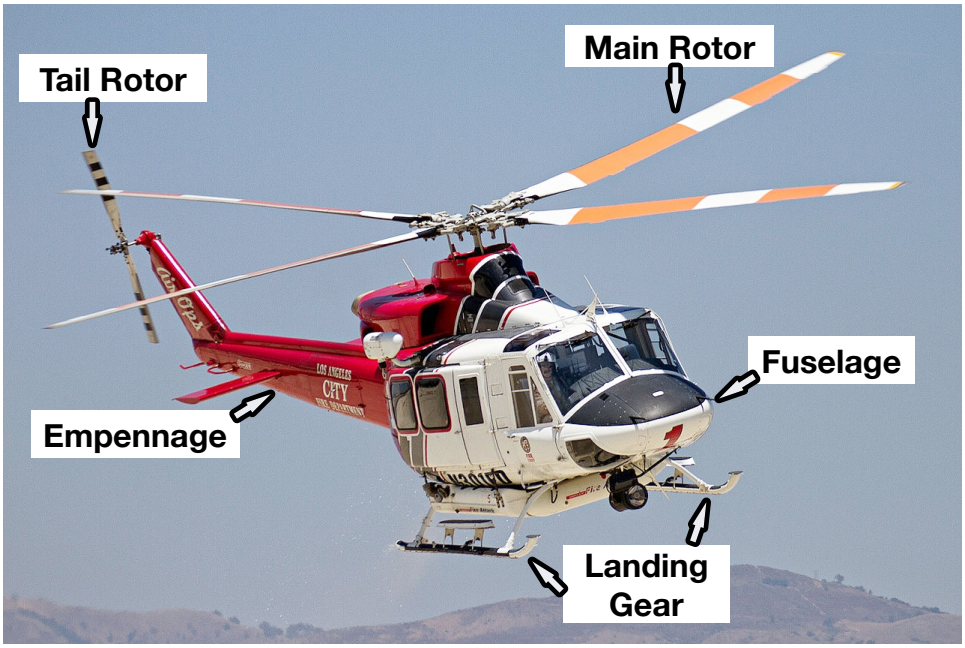

Figure 1.1: Parts of a typical helicopter (Bell 412) [3].

Figure 1.1 shows a typical helicopter; it consists of a main rotor, a counter torque device usually tail rotor and an empennage with horizontal and vertical tail for stability augmentation. It is worth mentioning that helicopter configurations like co-axial, tandem and intermeshing rotors negate the need for a tail rotor as counter torque device. Many contemporary helicopter rotors have four aerodynamically shaped slender blades and the loads generated on these blades are controlled by commanding the relative incidence (pitch) of these blades to the airflow. It provides both the propulsive as well as the control forces for the helicopter.

In forward flight, the rotor operates in an asymmetric flow field due to difference in relative airspeed on two sides of the rotor disk, advancing side (into the flow) and retreating side (out of the flow). Figure 1.2 presents the complex airflow over

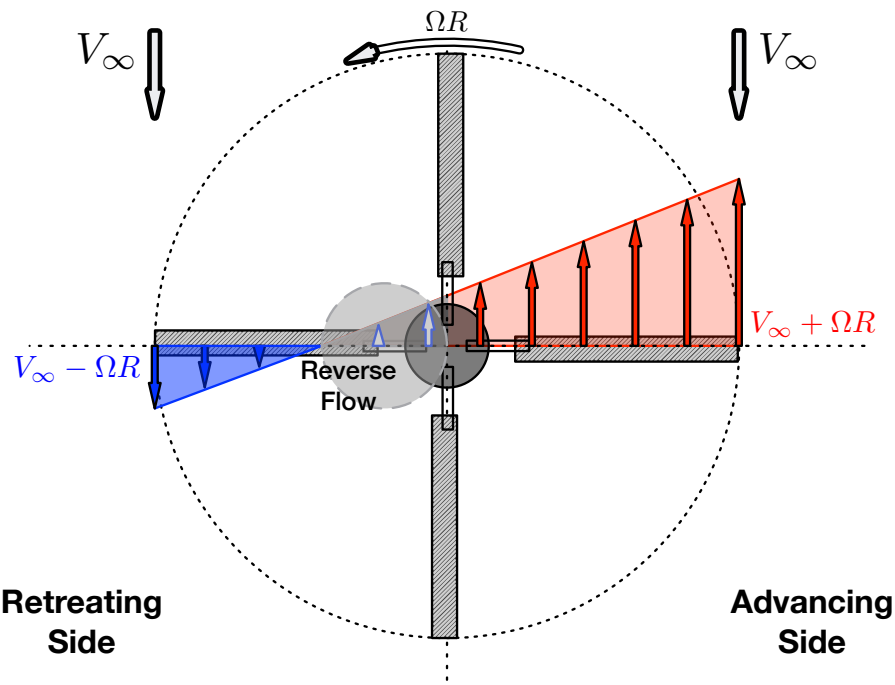

Figure 1.2: Top view of airflow over a rotor disc in forward flight.

the rotor disc. Thus, in addition to a fixed change in blade pitch (collective pitch), a time varying pitch input (cyclic pitch) is also required to negotiate these flow field variations. Primary control mechanisms would have to provide the required pitch input for rotor control in hover as well as in forward flight.

Aeroelastic coupling due to slender flexible blades operating in unsteady aerodynamic environment makes them particularly susceptible to vibrations. On the advancing side, the larger relative airspeed near the tips can lead to locally transonic flow and associated sharp rise in drag. On the retreating side, the regions of reverse flow constantly grow as the forward flight speed increases. In addition, the front and the back portions of the rotor disk experience large radial flow components. Essentially, the advancing side is increasingly becoming less efficient in producing lift (rise in drag) and there is also an increasing region of reversed flow and blade

stall on the retreating side. This manifests in rise in the rotor power requirement, and thereby limiting the maximum forward flight speed. Thus, efforts were made to address helicopter vibration, and enhance its performance.

Table 1.1: Rotor phenomenon and associated load harmonics for a four bladed rotor.

Objective	Load harmonics in rotating frame (/rev)
Rotor trim	1
Power reduction	2
Vibration reduction	3, 4, 5
Noise reduction	2, 3

As mentioned previously, the rotor system with zero flap hinge is a system in resonance with its rotational speed as the fundamental frequency. This frequency is non-dimensionally referred to as *1/rev*. This representation helps in comparing aeromechanics of various rotor systems with different rotational speeds. Thus, the harmonic rotor hub loads are generally presented as an integral multiple of the rotational speed. For a tracked rotor (structurally, inertially and aerodynamics identical blades), hub loads are transferred to the fixed frame as integral multiples of number of rotor blades, referred to as blade passage frequency. Table 1.1 identifies prominent load harmonics in the rotating frame associated with various rotor aeromechanics phenomenon. Significant efforts with specific objectives have been made to passively or actively target these harmonics, and these are discussed next.

1.2 Rotor Primary Control

In helicopter flight, the rotor generates the vertical lift force to support the vehicle weight and the horizontal propulsion force for the vehicle. Controlling the rotor forces to achieve desired flight path is fundamental to the operation of the helicopter and is appropriately termed as primary control.

In theory, primary control of the rotor is achieved by controlling both the magnitude as well as the direction of the thrust from the rotor. The rotor thrust is an integrated effect of lift generated on individual rotor blades, which in turn depends on blade pitch angle distribution. Rotor thrust is defined as the resultant force normal to the plane formed by the tip of the rotating blades termed as tip path plane. In essence, changing the blade pitch uniformly over the entire rotor revolution controls the magnitude of the rotor thrust and is termed as collective pitch control. While changing the blade pitch cyclically over the rotor revolution controls the direction of rotor thrust and is termed as cyclic pitch control. A complete mathematical discussion of primary control is included in Refs. [4, 5].

A mechanism to realize primary control was one of the toughest design challenges faced by the early helicopter pioneers. Hafner [6], in the late 1920s proposed and developed a swashplate mechanism that would change the pitch of the blade at the location where blades are connected to the hub. On the other hand, Pescara [7] favored use of control surfaces embedded in the rotor blade to produce the control loads needed for primary control. In the following sections, some of the prominent primary control methods are detailed, and their relative merits are discussed.

1.2.1 Swashplate Control

Swashplate is the most prevalent rotor control system in production helicopters. Operation of the swashplate can be understood with the help of schematic shown in Fig. 1.3. The swashplate consists of two main parts: a non-rotating (lower) swashplate and a rotating (upper) swashplate. The lower swashplate doesn't rotate and is connected to the pitch servos. Both plates are mounted on a bearing to allow change in orientation and pitch scissors allow to orient the plate.

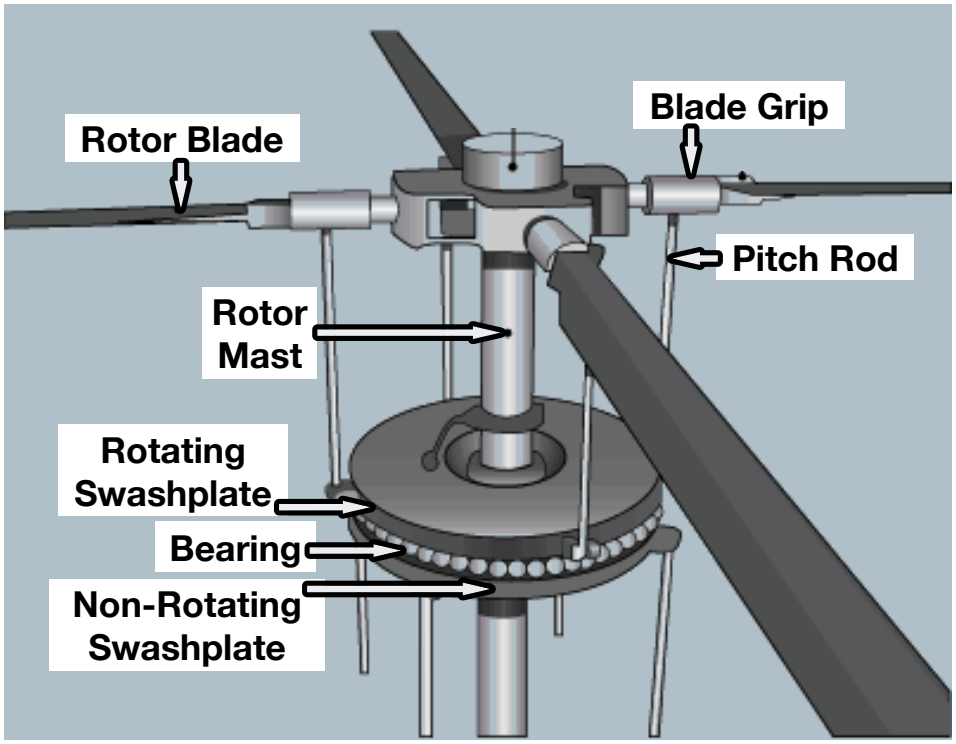

Figure 1.3: Schematic of a typical helicopter swashplate [8].

To control the collective pitch of the rotor blades, the entire swashplate is moved up or down along the rotor shaft without changing the planer orientation of the plate. Thus, the entire swashplate is moved along the rotor mast by a collective pitch actuator. To control the blade cyclic pitch, the planer orientation of the plate

is changed. Three pitch actuators distributed azimuthally provide the lateral and longitudinal tilt of the plate. The rotor blades grips are connected to the swashplate via pitch control rods or pitch links, which transfer the swashplate motion to blade root pitch input. The inputs from the pilot controls the pitch actuators in the fixed frame, which in turn orient the swashplate assembly to achieve the desired pilot controls.

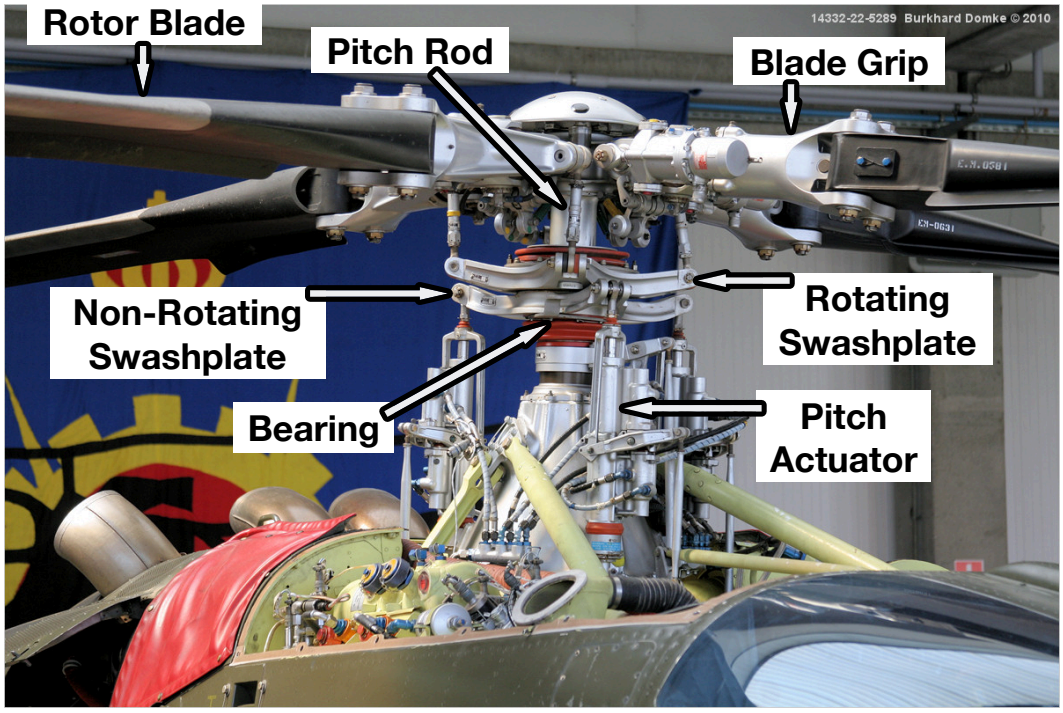

Figure 1.4: Swashplate assembly in Agusta A109 helicopter [9].

Figure 1.4 shows the swashplate assembly in Agusta A109 (1590 kg [3500 lb]) helicopter. The swashplates, pitch rods and pitch actuators are clearly visible. In most cases, hydraulic or hydro-electric actuators are used as pitch actuators that are sufficiently capable of providing the large control forces required to pitch the entire rotor blades. Generally, the pitch actuators and the lower pitch rods are

covered by fairing to streamline the flow around the rotor hub, in an effort to reduce the hub drag. Figures 1.5 and 1.6 show close-up view of swashplate assembly respectively on Sikorsky CH 53G (20865kg [46000 lb]) and MBB Bo 105 (2600 kg [5700 lb]) helicopters, with hub fairings installed. In spite of these efforts, by some estimates [5, 10], the swashplate assembly contributes about half of the total hub drag and about 35% of the helicopter parasite drag.

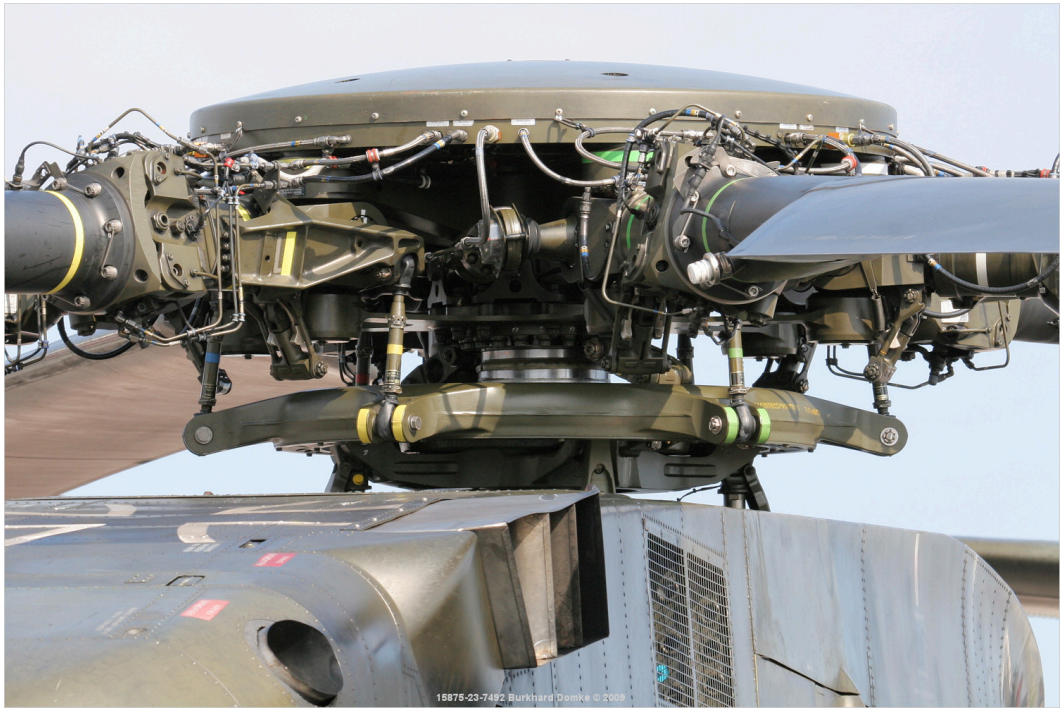

Figure 1.5: Close-up view of CH 53G fully-articulated rotor system [11].

It is important to note that although swashplate has remained relatively unaltered, the rotor design and fabrication technology has rapidly evolved. In general, out-of-plane (flap), in-plane (lag) and feathering (pitch) are the most important rigid degree of freedom for the rotor blade. Initially, mechanical hinges provided for all the degrees of freedom (fully articulated rotor system: Fig. 1.5). The rotor blades

Figure 1.6: Close-up view of Bo 105 hingeless rotor system [12].

were usually of metal construction. With the advances in composite manufacturing, rotor blades are now designed and fabricated using composites with tailored stiffness, thereby incorporating flap and lag degrees of freedom with flexible components near the blade root. No mechanical hinges are used for flap and lag, however feathering bearing is still utilized for pitch degree of freedom (hingeless rotor system: Fig. 1.6). Finally, elastomers were utilized to replace the feathering bearings in the hingeless design and most modern rotors are trending towards bearingless configuration (Fig. 1.4). A more detailed discussion about various rotor systems is in Refs. [13–16].

1.2.2 Westland Spider Control

As an alternative to using the swashplate for rotor controls, a *spider* system was developed and used by Westland company particularly in Lynx helicopters. It consists of a rotating ball joint to transfer the motion between stationary and rotating frames. Figure 1.7 shows a schematic of the Westland *spider* system.

The hub design is similar to a hingeless design with flexible elements made of titanium providing the required softness for flap and lag motion. A feathering bearing assembly permits the blade pitch motion. The pitch rods are connected to the blade root at one end and to the spider arms on the other end. The spider arm for each of the four blades are connected to the control spindle that runs through the rotor shaft. The control spindle can be moved up or down to change the blade collective pitch or can be moved side to side to change the blade cyclic pitches.

Figure 1.8 shows a close-up view of the Westland WG-13 Lynx (5125 kg [11300 lb]) hub. A summary of design and development of Westland Sea Lynx is presented in [17], 1/5th-scaled rotor testing details are in [18] and flight test description with performance analysis is in [19]. Significant reduction in maintenance time and service part count on the hub was recorded, however these benefit were attributed more to the hingeless rotor design rather than spider-linkage control system. Though this control system doesn't use a swashplate it has similar drawbacks like exposed linkages and the associated drag and weight penalty. Nevertheless, it is a noteworthy and unique rotor primary control system.

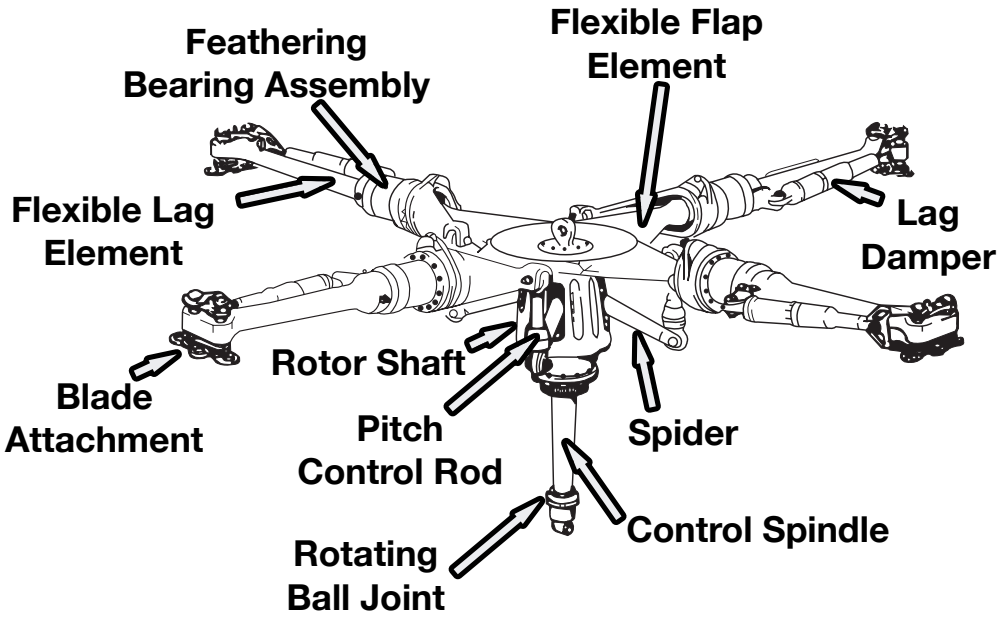

Figure 1.7: Schematic of a Westland *spider* control system [20].

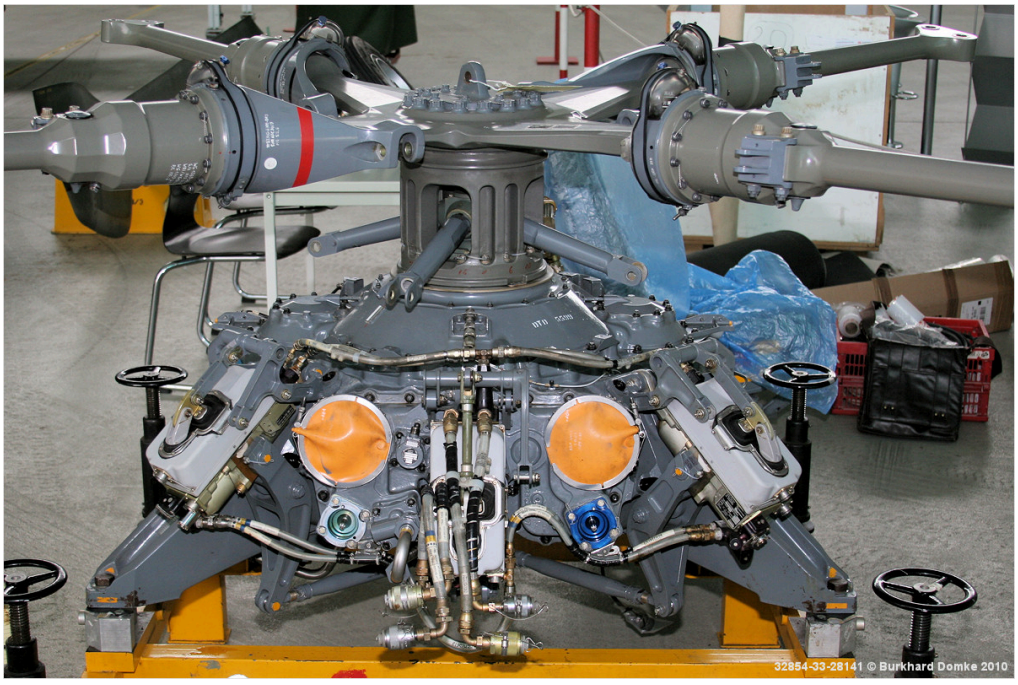

Figure 1.8: Close-up view of Westland WG-13 Lynx hub [21].

1.2.3 Kaman Servo-Flap Control

The concept of using trailing edge flaps for helicopter primary control was proposed early in the development of the helicopter [7,22]. However relative difficulty in installing and operating control surfaces on a rotating blade under significant centrifugal loads posed a challenge to practical realization of the concept. Today, Kaman [23, 24] is the only helicopter manufacturer that uses servo-flaps for primary control in a production helicopter.

It is important to distinguish between plain flap and servo flap. A servo flap is a separate airfoil shaped auxiliary body situated aft of the trailing edge of the main rotor blade. In contrast, a plain flap is part of the main rotor blade, the support structure and actuation mechanism are integrated within the profile of the rotor body. For this reason, it is also referred to as integrated flap. Figure 1.9 shows a pictorial comparison of the servo and integrated flaps. Irrespective of the type, these flaps are placed in the outboard section (usually trailing edge flap mid-span around 75% rotor radius) of the blade, to take advantage of the higher local dynamic pressure.

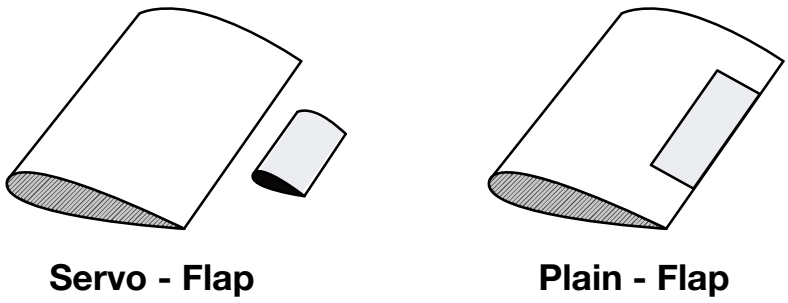

Figure 1.9: Servo and plain flaps

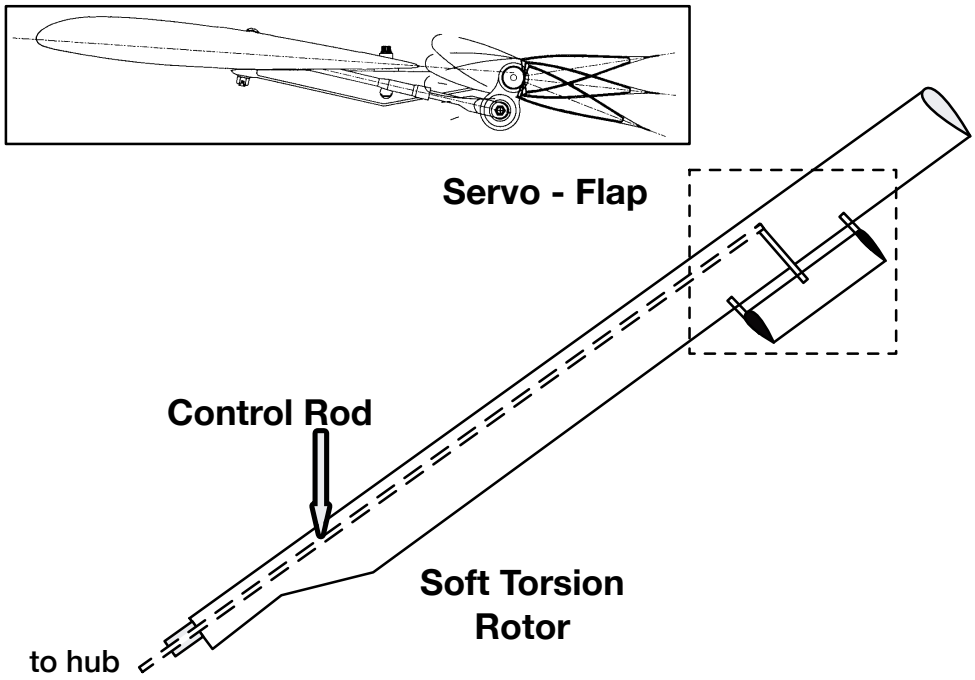

Figure 1.10: Schematic of Kaman SH 2F rotor blade with servo flap.

Figure 1.10 shows the schematic of the Kaman SH 2F (3190 kg [7040 lb]) rotor blade with servo flaps. A swashplate like mechanism at the rotor hub is connected to the flap via control rod that is passed through a hollow cavity in the rotor blade. The pitch inputs from the pilot move the servo flap and the torsionally soft rotor blade pitches in response. This softness in pitch is often accommodated by using stiffness tailored tension-torsion straps at the blade retention grip. Wei *et al.* has presented several studies [25–34] detailing systematic design and development process of servo-flap rotors at Kaman Aerospace. Figure 1.11 shows the servo-flap in a production K-MAX (2300 kg [5100 lb]) helicopter. The servo flaps provide larger moment arm compared to plain flaps, thus lowering the required flap deflection and control moment for primary control. This also reduces the complexity in the rotor hub, as

seen in Fig. 1.12, reducing the part count and associated hub drag. However, due to additional body aft of the blade and linkages exposed in a high dynamic pressure flow, there is significant aerodynamic drag from the servo flaps.

Figure 1.11: Servo - flap on a Kaman K-MAX rotor [35].

To assess the benefit of the integrated flap over the original servo-flap design, two one-third scaled integrated and servo-flap sections were tested in a wind tunnel [36]. The new design integrated the servo-flap in the main blade section and compared it to the original servo-flap section. It was observed that the lift to drag ratio of the new configuration was as much as 13 times the original configuration for some test cases. It is to be kept in mind that the chord of the integrated servo-flap section was equal to the sum total of the original blade and servo-flap combined, essentially making it a wide chord blade.

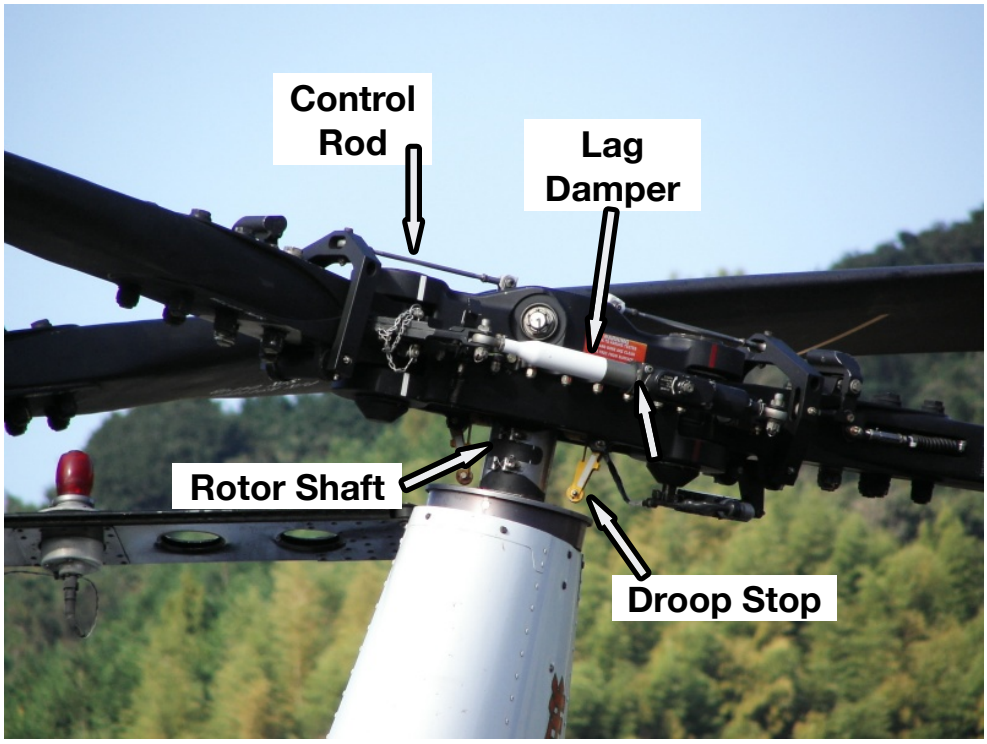

Figure 1.12: Close-up view of K-MAX rotor hub [35].

Prouty [37] presented a summary of the various helicopter control systems.

1.3 Helicopter Vibrations and Performance

As mentioned before, the interaction of elastic rotor with unsteady and non-uniform aerodynamic environment is the prime cause of the rotor vibrations [38, 39]. The rotor in addition to having a steady and one per revolution loads, also encounters multiple harmonics loads. These rotor vibrations then transfer to the fuselage and passenger cabin through the rotor shaft and hub mounting. For a tracked rotor, only harmonics that are integral multiples of the number of main rotor blades are observed in the fixed frame, the rotor system can be thought of as a filter for all the other harmonics. This has been observed in several wind tunnel

and flight tests data over the years as well [40–43].

Sustained efforts [44] have been underway to understand and predict rotor steady and vibratory loads using comprehensive analyses. University of Maryland Advanced Rotorcraft Code (UMARC) [45] and Comprehensive Analytical Model of Rotorcraft Aerodynamics and Dynamics-II (CAMRAD-II) [46] are examples of such analyses. The accuracy of prediction, though has improved over the years, it is still not up to the acceptable accuracy for a wide range of flight conditions [47–49]. This can be attributed to difficulty in precise modeling of the complex aerodynamics and structural deformations. Recently it has been observed that coupling the Computational Fluid Dynamics (CFD) analysis with Computational Structural Dynamics (CSD) can better capture the aeroelastic nature of the rotor vibrations problem [50–54].

Helicopter vibration levels, if left unchecked, can significantly reduce the life of the components of the vehicle. In addition, these vibrations cause pilot and passenger discomfort and an increase in maintenance efforts and costs. Most production helicopters have some vibration attenuation device installed to address these concerns. Some of these concepts are described next.

1.3.1 Pre-Flight Measures

Because main rotor is the primary source of vibrations, it is pertinent that any dissimilarity between individual blades is minimized. Dissimilarity in inertial, structural and aerodynamic characteristics of individual blades leads to differences

between the motions of the blade and this shows up as large 1/rev rotor loads. After composite blade manufacturing process, each rotor blade undergoes strict similarity checks before they are selected to be installed on the vehicle. Blade mass balance in chordwise and spanwise direction, mass distribution and stiffness properties are some of the key parameters that are matched. These measures are generally referred to as rotor track and balance. References [55,56] present analytical modeling of rotor track and balance.

In practice, rotor tracking exercise is an effort to ensure that all blade tips trace the same trajectory, in other words, undergo identical tip path tracks. The blade tips trajectory are illuminated by optical means and are recorded. Tracking adjustments are made by adjusting pitch links as well as by adjusting trim tabs located at the trailing edge of the outboard section of the rotor blade. Rotor track procedure is discussed in detail in Section 2.6.

It was also observed in some cases that a perfectly tracked rotor could experience high levels of vibrations. This lead to development of advanced tuning systems, wherein several accelerometers were installed at key locations on fuselage and empennage. Computer codes guide the rotor smoothing exercise and several research studies have tried to optimize this process [57–59]. The rotor tuning includes reduction of the rotor out-of-track as well as the fuselage vibrations. This is also referred to as rotor smoothing.

In recent years, efforts have been made to reduce the time spent in manually adjusting track and automate the rotor smoothing process. Low bandwidth adjustments using either an active trim tab [60] or an active pitch link [61] have been

tested though not yet implemented in a production helicopter.

Traditionally rotor in-plane mass imbalance is generally corrected by bolt-on masses on the rotor hub arms. Automating mass balance has been tried by mounting small motor driven masses on a semicircular track beneath the rotorhead [61].

1.3.2 Passive Measures

In-flight vibration reduction using passive approaches specifically target 3, 4 and 5/rev vibratory loads in the rotating frame. These may be classified into categories based on their applications [62]:

(a) Fixed frame devices: *Cabin suppressors* increase apparent fuselage impedance or control the location of node of important modes. These are mounted on selected fuselage locations reducing local vibrations and improving pilot and passenger comfort. These suppressors are usually passive spring-mass system tuned to the blade passage frequency (N_b/rev, where N_b is number of blades). *Isolators* are also installed between fuselage and main rotor/transmission to isolate main rotor vibrations from fuselage. These fixed frame devices incur large weight penalty and have poor off-design performance (away from tuned frequency).

(b) Rotating frame devices: *Pendulum absorbers* are mounted on the rotor hub, which are tuned to cancel dominant source of 4/rev hub loads. They can be installed to absorb out-of-plane (pendulums) and in-plane (bifilar) vibrations. *Attenuators* are installed on the rotor blade to minimize vibratory loads in the

rotating frame. The goal is to reduce the blade root vibratory loads. These devices tend to be heavy and cause significant drag penalty when installed on the blade.

Figure 1.13 shows a few of the passive vibration absorbers used in production helicopters.

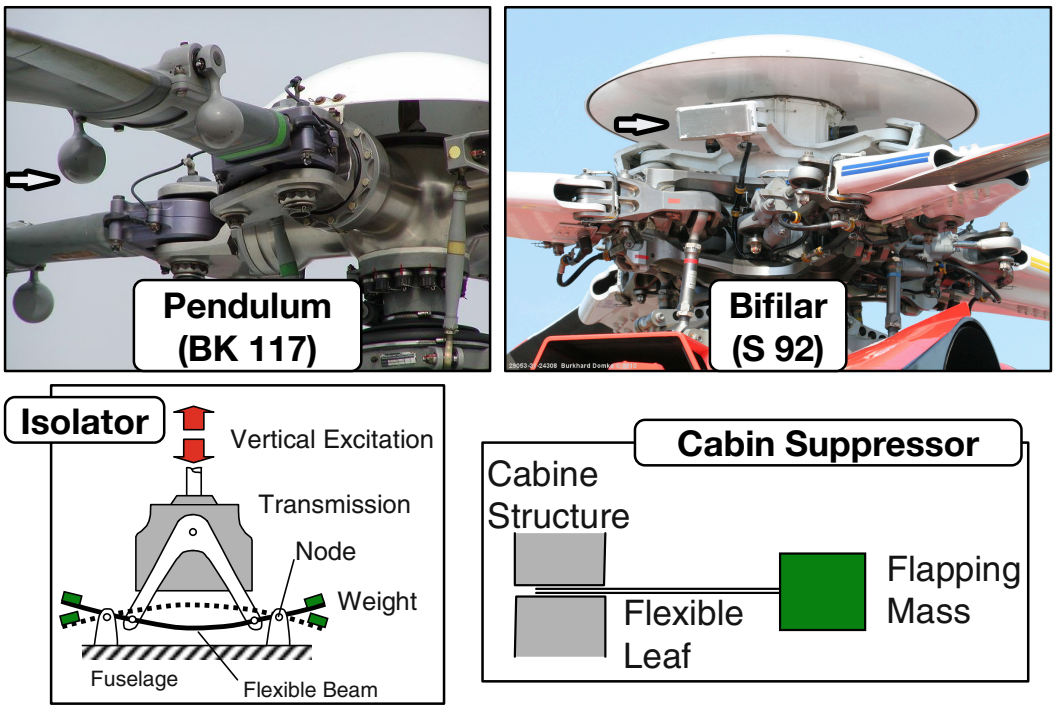

Figure 1.13: Vibration absorbers - passive measures [63–65].

Several researchers have also explored potential benefits of composite tailored couplings for vibration reduction. Recently, Bao *et al.* [66–68] conducted coupled aeroelastic comprehensive analysis as well as fabricated a set of five high quality UH-60A type Mach scale rotors with segmented flap-bending/torsion couplings. Wind tunnel test of these Mach scale blades on an articulated rotor hub demonstrated that with proper design optimization, composite blade flap-bending/torsion coupling could reduce vibratory hub loads.

1.3.3 Active Measures

The passive vibration control devices add significant weight penalty to the helicopter and generally have a poor off-design performance from the tuned frequency. Active vibration control concepts could be adjusted based on the flight conditions allowing better effectiveness at various operational fight conditions.

1.3.3.1 Active Control of Structural Response

Active Control of Structural Response (ACSR) refers to vibration cancellation in the fuselage load paths (in fixed frame) using force actuators to counteract the structural response based on the flight conditions and minimize local vibration. These are an extension of cabin suppressors and isolators with an aim of improving their effectiveness over the operational envelope of the helicopter. References [69–74] detail development and testing of various methods used to control the structural response leading to vibration reduction.

1.3.3.2 Higher Harmonic Control

All the vibration control devices that either passively or actively target structural response only suppress vibration at few locations. They don't impact the source of vibration, which is the aeroelastic interaction of rotor blades with airflow. To directly influence the source of rotor vibrations, Higher Harmonic Control (HHC) was proposed [75, 76]. For HHC, actuators are incorporated below the swashplate in the non-rotating frame. In addition to the 1/rev cyclic inputs by the swashplate,

higher harmonic inputs are superimposed on the pitch input. These were usually hydraulic actuators and had to be sized not only for primary control but as well as HHC. Several analytical [77–79] as well as experimental [80–83] studies have examined the potential of HHC. The effects of HHC on rotor vibrations and noise were also extensively explored in wind tunnel tests of a geometrically and dynamically scaled Bo 105 rotor. These constituted the two part Higher Harmonic Control Aeroacoustic Rotor Test (HART I & II) program [84–87]. HHC was shown effective in reducing vibration as well as noise, however often not simultaneously. If the control inputs were aimed at vibration reduction, noise was adversely affected and vice-versa. Generally, low actuation amplitudes were required, though large control loads were observed.

HHC suffered from several limitations that made their practical implementation difficult. The control force needed to actuate the complete rotor system was large leading to heavy hydraulic actuators. Although these actuators would not be exposed to centrifugal loads, they were to be designed for both low frequency primary control as well as high frequency HHC, leading to increased wear and tear of primary control system. For a four bladed rotor, higher harmonic control inputs to the swashplate in the fixed frame is 4/rev which in turn results in 3, 4, and 5/rev pitch inputs to the blade in the rotating frame. Thus, 2/rev control input as needed for performance enhancement was not available using HHC for a four bladed rotor and as a result, no significant performance enhancements were noticed. Kessler [65] presented a comprehensive survey of the various HHC systems.

Recently, concept of using multiple swashplates to increase the number of

control degrees of freedom has been tested. Although feasible, multiple swashplates further increase the design complexity, hub drag and weight penalty [88].

1.3.3.3 Individual Blade Control

To address the bandwidth limitation of HHC, it was proposed to move the control to the rotating frame via Individual Blade Control (IBC) [89,90]. This would separate the primary control system from IBC, reduce the control force required from the actuators thus bringing down system weight [89]. Compared to HHC, IBC systems have actuators in the rotating frame; this necessitates hydraulic or electrical slip rings to operate these actuators.

Over the years, several potential concepts have been explored. These include blade camber control [91, 92], blade twist control [93–99], active tips [100, 101], blade root pitch control [102–110], active servo flaps [24, 25, 111–116], active micro-flaps [117] and active integrated trailing edge flaps. Kessler *et al.* [118,119] presented a detailed review of the various IBC systems.

For a four bladed rotor system, IBC allows introducing all harmonics (2 - 5/rev) and other non integral multiple frequencies in the rotating to directly counter vibration and noise at its source. In addition to 3, 4 & 5/rev control for vibration alleviation, harmonics such as 1/rev to counter loads due to rotor dissymmetry [120, 121], 2/rev for performance enhancement [122, 123] and stall delay [124, 125] and mixture of 2/rev and 3/rev for noise reduction [126, 127] could be implemented. Often simultaneous vibration reduction and noise alleviation could be achieved using

IBC [118, 119].

Friedmann *et al.* [128,129] assessed various approaches for helicopter vibration reduction and concluded that actively controlled flaps were most effective IBC system with practical deflection angles. They could achieve similar vibration reduction as achieved by HHC at an order of magnitude less actuation power requirement.

1.4 Vibration Control using IBC Active Flaps

The advent of smart materials with high bandwidth and compact size, IBC actuators could be incorporated in the rotor blades. These actuators then drive discrete control surfaces like trailing edge flap placed in high dynamic pressure locations of the blade. Chopra [130, 131] presented a review of the smart materials, Giurgiutiu [132] assessed the suitability of smart materials for rotorcraft applications. Sirohi *et al.* [133] analyzed the fundamental behavior of individual piezoceramic plates operating under simulated centrifugal loads. Based on the strain effects, two types of piezo based actuators have been developed namely, Piezostack (d_{33}) and Piezobender (d_{31}).

To minimize the drag and weight penalty associated with servo flaps, piezo actuator driven integrated flaps were considered. Figure 1.14 presents the nomenclature used for an integrated flap in a rotor blade. A trailing edge flap location (mid-span as %R), flap length (as %R) and flap chord (as %c) are most critical flap parameters. In addition, flap overhang and gap between flap element and main blade body in chordwise and spanwise direction are also important to consider.

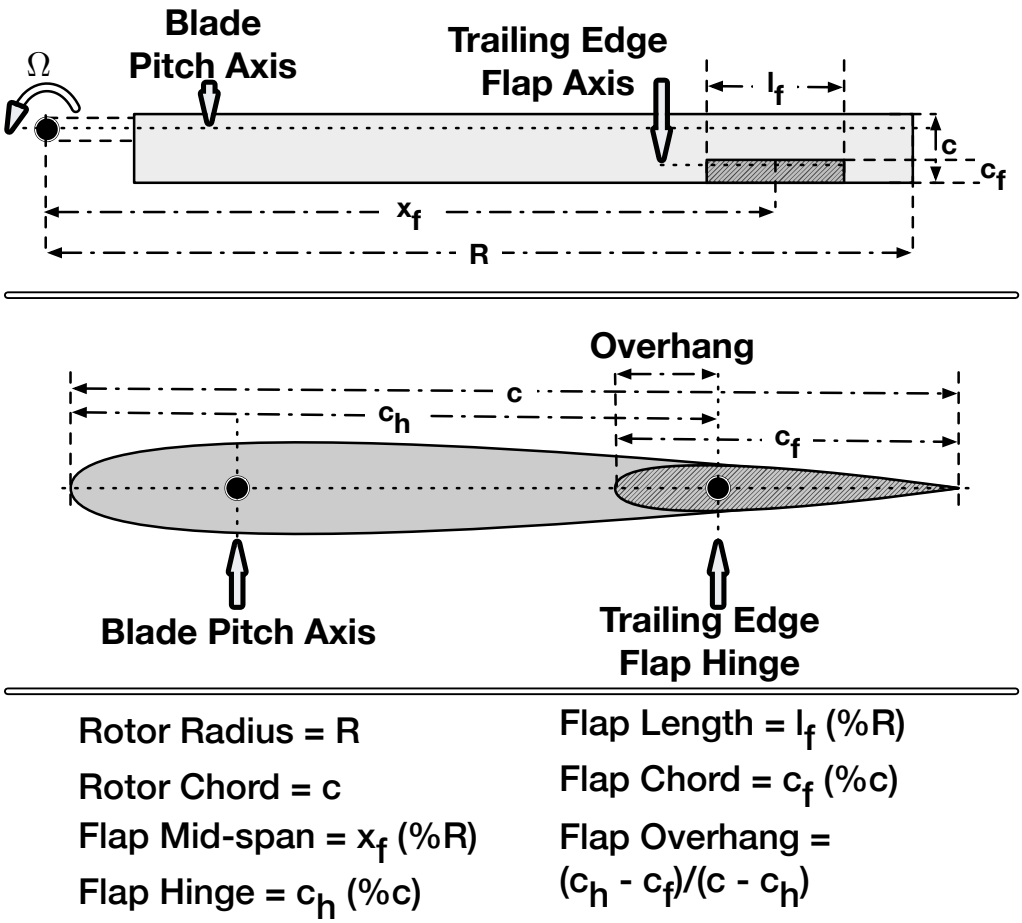

Figure 1.14: Nomenclature for trailing edge flap rotor.

Several experimental studies have explored vibration reduction using piezo actuated flaps, culminating in successful wind tunnel demonstration of SMART rotor [134] and flight test demonstration of BK 117 helicopter [74]. Table 1.2 summaries some of these experiments. Important parameters of MD 900 SMART rotor and BK 117 rotor are listed in Table 1.3. Results from SMART rotor tests conclusively show reductions in blade-vortex interaction (BVI) and in-plane noise as well as vibratory hub loads. Noise reductions up to 6dB, as well as vibratory hub load reductions of about 80% were measured. However, flap deflections at 1/rev were limited from primary control perspective.

Table 1.2: Vibration control using active flaps.

Study	Actuator	Model
Lee *et al.* [135, 136]	Piezostack, L-L mech	2-D section, open jet 150 ft/s
Prechtl *et al.* [137]	Piezostack, X-frame	1/6 CH 47-D Mach scale, hover
Spangler *et al.* [138]	Piezobender, PZT-5A	bench-top
Fulton *et al.* [139–142]	Bimorph, 2 PZT-5A	3.75 ft dia, Froude-scale, hover
Koratkar *et al.* [143–146]	Piezobender, PZT-5H	5-ft dia, Mach scale, μ 0.3
Roget *et al.* [147]	Piezobender, PZT-5H	5-ft dia, Mach scale, μ 0.25
Straub *et al.* [134, 148–152]	Piezostack, 2 X-frame	MD 900 full scale, μ 0.375
Konstanzer *et al.* [74]	Piezostack	BK 117 flight test, μ 0.257

Table 1.3: Important parameters for MD 900 and BK 117 active rotors.

Parameter	MD 900 rotor	BK 117 rotor
Rotor radius (R)	5.2 m [17 ft]	5.5 m [18 ft]
Rotor chord (c)	0.25 m [10 in]	0.32 m [12.6 in]
Max. wind speed	80 m/s [155 kts]	57 m/s [110 kts]
Rotor speed (RPM)	392	383
Number of blades	5	4
Flap midspan (%R)	83	75
Flap length (%R)	18	10.9
Flap chord (%c)	25	15.6
Tor. freq. (/rev)	5.8	3.5

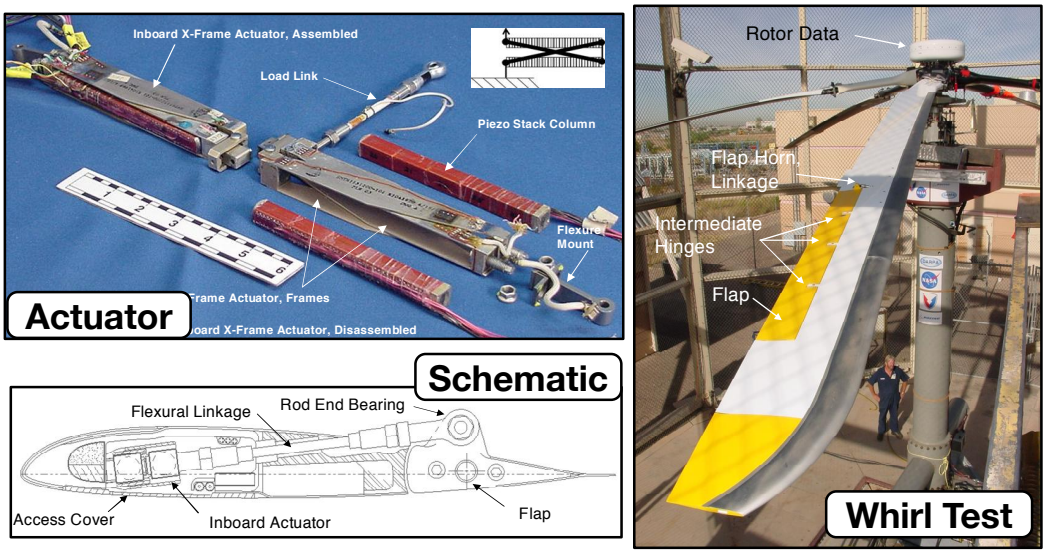

Figure 1.15: MD 900 SMART rotor with active flaps.

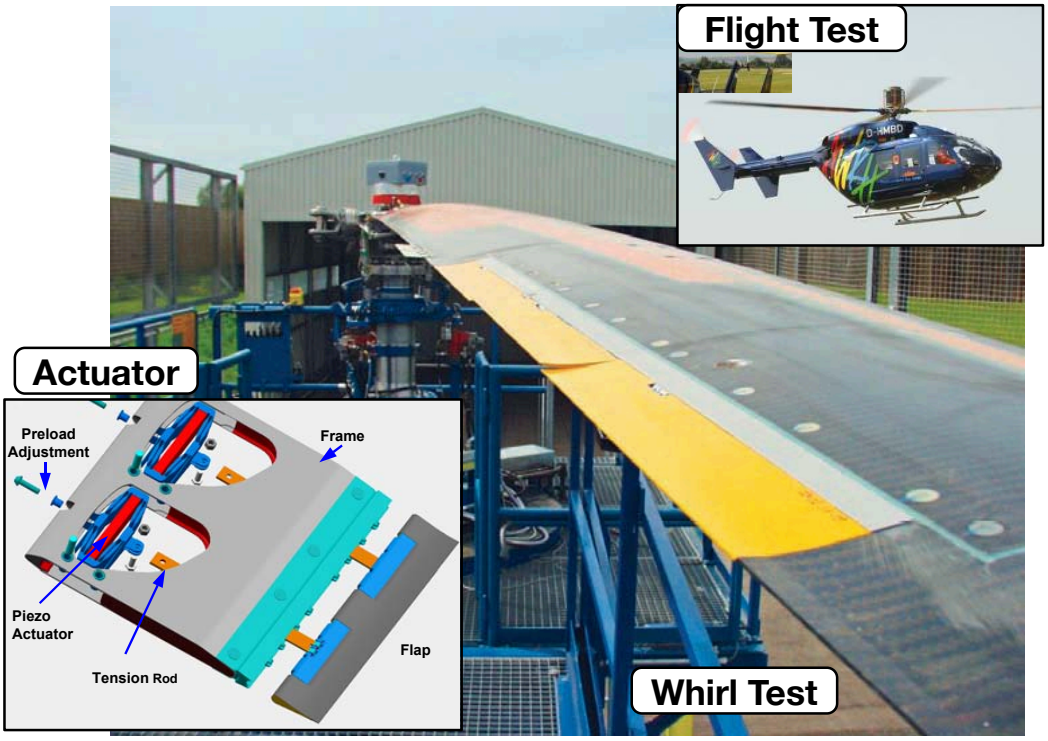

Figure 1.16: Flight testing of BK 117 with active flaps.

1.5 Swashplateless Rotor Primary Control

Based on the understanding that any substantial success in rotor smoothing and quieting can only be achieved by active control in rotating frame, the focus shifts to using on-blade control surfaces to achieve primary control as well. Further, successful vibration reduction demonstrations by Boeing (MD-900 rotor in NFAC [134]) and Eurocopter (BK-117 in flight tests [74]) using trailing edge flaps as on-blade control surfaces. This provided renewed impetus to assess if rotor primary control, in addition to vibration reduction, could be achieved using trailing edge flaps. Analytical studies examining capabilities and challenges arising from using these flaps for rotor primary control are reviewed next.

1.5.1 Analytical Studies

Ormiston [153] initiated a feasibility study of flaps (referred to as elevons in his study) for primary control using a simple aeroelastic analysis. The blades were assumed to be rigid and quasi-steady thin airfoil two dimensional theory with uniform rotor inflow was used. The study found that primary control of the rotor (rotor trim) could be achieved using trailing edge flaps, provided the torsion frequency of the blade is significantly reduced from about 5/rev for conventional rotor to about 2/rev for swashplateless rotor. This was modeled in the analysis by treating the blade as torsionally rigid, with a soft pitch link at the root. The pitching moment created by the trailing edge flap would result in blade pitch response at the root, which in turn twists the blade. Also, flap (elevon) reversal was observed when the

lift contribution from the flap was greater than the opposing lift from the induced blade twist. Thus, using moment flap with low blade torsional frequency was recommended to maximize blade pitch response and operate beyond flap reversal speed. Finally, in order to operate the airfoil sections with flap with minimum actuation force, blade indexing was recommended. Blade indexing refers to setting the blades at a high pre-collective pitch angles prior to operating the rotor. As the rotor spins up, the blade pitching moment would bring the rotor pitch to the desired pitch angle. This would greatly reduce the steady trailing edge flap deflections required for trim.

Shen *et al.* [154–160] carried out a series of numerical studies to investigate use of trailing edge flaps for swashplateless rotors using comprehensive analysis code, UMARC. The aerodynamic model was based on thin airfoil theory with unsteady model for flap lift and drag. A multi-cyclic controller was implemented for actuating trailing edge flap for simultaneous primary control as well as vibration reduction. Also, eigenvalue analysis was used to study active rotor stability. The analysis was validated by comparing the baseline conventional rotor results with results from CAMRAD-II and wind tunnel data [154, 155].

The studies were carried out for various weight class helicopters such as an ultralight ASI 496 (512 kg [1130 lb]) teetering rotor helicopter, bearingless MD 900 (1361 kg [3000 lb]) rotor and a typical utility UH-60A (8610 kg [19000 lb]) helicopter. Blade index angle and torsional frequency were found to be primary design parameters for swashplateless rotors. For the ultralight helicopter, optimal flap system design consists of an 18%R plain flap with 25%c flap chord located at

82%R. The blade torsional frequency was kept same as the baseline swashplate rotor at 2.2/rev. Both flap collective and cyclic deflections were calculated to be below 4 degrees to trim the rotor in the complete range of flight speeds [156].

For the McDonnell-Douglas Advance Rotor Technology (MDART) rotor, a multi-cyclic controller was used. It was shown that the trailing edge flap could simultaneously trim swashplateless rotor and achieve 99% reduction in baseline rotor vibration at an advance ratio of 0.25. A steady flap angle of 5 degree with half peak to peak cyclic flap angles of less than 6 degree were required. An optimal blade index angle of 18 degree was also needed. When the rotor was trimmed, first using swashplate for baseline case and then using trailing edge flaps, similar collective and cyclic blade pitch angles were observed. In both cases, the torsional frequency was maintained at 2.1/rev [157].

Next, parametric studies of flap configuration examined flap overhang, chord, flap length, spanwise location and blade index angle in order to minimize flap control angle and hinge moment at high speed rotor flight. This parametric study showed that blade index angle, flap length and torsional frequency mostly influence the required flap deflection whereas optimizing flap overhang was critical in reducing the flap hinge moment requirement. Overall, these parameters were important for design of swashplateless rotor irrespective of the weight class or rotor type [159].

Another important observation from the analytical studies was that actuator dynamics can not be neglected. Inclusion of actuator dynamics results in larger flap control angles as well as more power for various flap spanwise placements [158].

Finally, analysis of UH-60 rotor demonstrated the capability of performing

both primary flight control and active vibration control functions using trailing-edge flaps. At a high advance ratio of 0.32, the 4/rev vertical force and roll and pitch moments at hub were successfully eliminated (by 90%), and the 4/rev in-plane hub forces are reduced by more than 40%. The half peak-to-peak value of the trailing-edge flap deflection for primary flight control is 7.1 degree, and an additional 4.7 degree is required for active vibration control [160]. The observed trends were similar for all the rotor types considered, with highest flap deflection requirements for trim was calculated for UH-60A.

Falls *et al.* [161–165] extended the comprehensive code to include better wake model and lift-drag calculations for flapped airfoils. In addition to using free wake for rotor, additional wake trailers were added to the ends of the trailing edge flap element. The aerodynamic model included either using a quasi-steady thin airfoil theory or an unsteady lifting line model with airfoil table lookup. The table lookup was based on wind tunnel test data and CFD allowing accurate calculation of rotor power. The baseline rotor performance predictions from the UMARC analysis were validated against flight test data [166, 167]. Similar to previous analyses, for the swashplateless rotor configuration, the rotor blade was left unaltered and torsional frequency was modeled using as a soft pitch link at the root. For most cases, the torsional frequency was kept at 2/rev and the rotor was trimmed up to an advance ratio of 0.3.

It was shown that blade index angle was strongly dependent on blade torsional stiffness, softer the blade in torsion, higher is the pitch response and higher blade index angle is desired to keep steady flap deflections low. In addition, higher the rotor

operating thrust, higher is the blade index angle required. It is worth mentioning that the blade index angle was optimized based on the extreme operating condition of high rotor thrust and high advance ratio, and for all other flight conditions, it was left unaltered. Based on an extensive parametric study, the optimum trailing edge flap geometry was shown to be with 15%c chord, 0.33% flap chord overhang, 39%R length, centered at 75%R span. A blade index angle of 20 degree was found to minimize the flap deflections and hinge moments at a high advance ratio of 0.368. Mean flap deflections of -3 to -9 degrees and half peak to peak deflections of 4 to 11 degree were found sufficient to trim the rotor over the entire flight envelope (steady flight up to advance ratio of 0.368) [164].

From performance perspective, the swashplateless rotor was found to consume less power than baseline rotor in hover and at low flight speeds. This could be due to redistribution of blade airloads in presence of the trailing edge flap deflections. At advance ratios above 0.25, the swashplateless configuration consumed more power. The analysis did not account for any reduction in the flat plate area for helicopter drag calculations in case of a swashplateless configuration, which could alter the comparison at high advance ratios. In addition to analyzing the integrated flap configuration, trailing edge flap with servotabs were also studied. It was found that that tab actuated flaps could also trim the rotor with smaller tab deflections and hinge moments. However, the performance falls sharply as the actuation frequency is increased implying that they may not have the required bandwidth to perform vibration control applications [165].

Coupled CFD-CSD analysis done by Jose *et al.* [168–171] focussed primarily

on understanding the aerodynamics of the integrated flap rotors. Based on the two dimensional airfoil studies, it was shown that the use of the effective angle of attack concept could be used for modeling lift and drag of flapped airfoil sections. Also, in un-stalled conditions, flap overhang has a relatively small effect on lift and pitching moment. Based on three dimensional CFD simulations, it was concluded that the gaps between the trailing edge flap and the rotor blade main body adversely affect the rotor performance. These gaps also reduce the effectiveness of the trailing edge flap in trimming the rotor. Quantitatively the effect of spanwise gaps was found to be lower compared to chordwise gaps.

Survivability is a key consideration when designing a flightworthy vehicle. To this objective, Ganguli *et al.* [172] studied the possibility of trimming a swashplateless rotor with one or more damaged blades. The analysis was carried out on a Bo 105 (2600 kg [5700 lb]) rotor using UMARC and the on-blade actuator on the damaged blade was assumed to be non functional by suppressing the collective and cyclic pitch on the damaged blade. It was shown that the remaining blades with trailing edge flaps could allow for trimming the rotor but required higher trailing flap deflections. This translates to greater survivability of swashplateless helicopters. However, increased root flap motion of the damaged blade and increased 1/rev and 2/rev loads due to reconfigured hub pose significant increase in rotor loads and vibrations and it became progressively difficult to trim damaged rotor as the advance ratio increased.

In another study, Ganguli *et al.* [173] explored the possibility of reconfiguring the fuselage cg to reduce the cyclic flap deflections required. It was shown that

optimizing cg location and proper choice of blade indexing could reduce the peak to peak flap deflection requirements by as much as 50%. In addition, for smaller scale vehicles (UAVs and MAVs), active control of cg position could also be employed to completely eliminate cyclic pitch requirements for a large range of flight conditions.

Before summarizing these analytical studies, a couple of pertinent observations are necessary. For the future analytical studies, the effect of change in blade moment of inertia due to presence of integrated flaps and associated mechanisms needs to be included. Presence of on-blade components significantly increases the blade weight and alters the mass distribution. Since this inertia is an important factor in blade torsional stiffness calculations, it might be beneficial to include this change in the analysis. Second, a dedicated study is needed to explore the effect of variable blade index angle. At present the index angle is set based on one flight condition, thus operating sub optimally at all the other conditions. An understanding of the penalty due to a fixed blade index angle is desired. Lastly, further analysis is required into understanding swashplateless rotors with soft in torsion elastic blades. Though the swashplateless feasibility has been established by modeling reduced torsional stiffness using a soft pitch link, production units would necessitate removing linkages and mounting on the hub. The reduced torsional stiffness would then have to be structurally included in the design of the composite rotor blades, changing the dynamics of the system. An understanding of effects of such an alteration would be critically important.

1.5.2 Summary of Analytical Studies

From the various parametric and optimization studies it appears that an integrated trailing edge flap could successfully trim a swashplateless rotor provided a few key design criterion are kept in mind.

(a) The torsional stiffness of the rotor has to be reduced to around 2/rev from 4 - 5/rev of conventional rotor to obtain sufficient blade pitch response as needed for trim.

(b) Blade indexing is critical in lowering the steady flap deflection requirements and ensuring that the flapped airfoil sections operate in low drag regions. Improper blade index angle may result in large rotor power as well as actuation power penalty.

(c) Optimizing flap geometry and spanwise location is essential for minimizing the actuation requirements.

(d) Minimizing gaps between the flap and main body is desired as they adversely affect trailing edge flap effectiveness.

(e) Keeping the rotor blade unaltered and introducing soft pitch links seems to be most straightforward way of lowering the rotor torsional stiffness.

In summary, based on UH-60A type swashplateless rotor analysis, a 15%c flap chord, 40%R flap length, located with flap midspan at 75%R is an optimum

flap geometry. Also, index angles in excess of 15 degree would be required and minimizing gaps is highly desired.

1.5.3 Sikorsky Active Flap Demonstration Rotor

Active rotor research using trailing edge flaps at Sikorsky were made with goals to demonstrate technologies that could reduce vibration by at least 20%, acoustic detection by at least 6 dB, and increase maximum blade loading by at least 16% on a full-scale rotor system. In addition, demonstration of primary control capability was also desired.

Most of the prior effort focussed on optimizing the piezoelectric based actuators for driving trailing edge flaps. Due to their excellent bandwidth, piezo-based actuators have proven to be successful for HHC devices. However, at lower frequencies which correspond to 1/rev for primary control, large amplitudes are required. Typically amplification mechanisms used traded force for displacement and thus there has been no successful demonstration of primary control using piezo-driven trailing edge flaps thus far.

With this background, efforts were focussed on assessing use of electro-magnetic actuators. In 2005, high authority actuator development begun as a joint effort between United Technology Research Center (UTRC), Sikorsky Aircraft Corporation and Hamilton, Sundstrand and Calverham. Focus was on developing actuator capable of delivering high amplitudes at 0 to 2/rev frequencies and perform higher harmonic input at frequencies up to 5/rev.

Systematic actuator design and testing resulted in development of high power Electro-Magnetic Actuator (EMA). These EMAs consist of a planetary roller-screw and a permanent magnet brushless motor. A Linear Variable Displacement Transducer (LVDT) is used for position feedback [174,175]. Figure 1.17 shows a schematic of the actuator and an assembled unit. The design process also optimized EMAs to minimize weight, maximize dynamic performance, maximize endurance under high centrifugal loading (up to 750g) and actuator thermal management. Bench top and vacuum chamber testing under simulated loads was carried out and the actuator was operated at a range of frequencies. Actuator response, power, current and temperature were recorded. Endurance testing was also carried out.

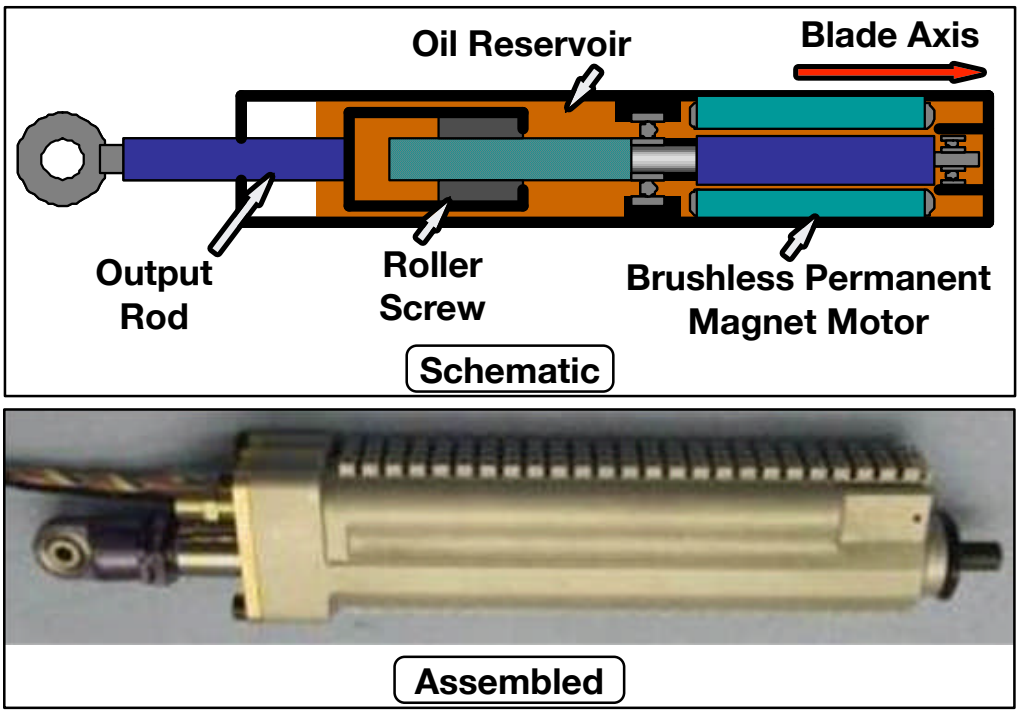

Figure 1.17: Electro - magnetic actuator used in Sikorsky Active Rotor System [176].

Once a satisfactory actuator was developed, efforts were made to ensure re-

peatable performance and reduce any variability from one unit to another. Although the actuator was sized based on load requirements of a UH-60 rotor (16.36 m [53.67 ft]), the whirl and wind tunnel testing was tested on a smaller diameter S-434 rotor (8.53 m [28 ft]). The trailing edge flap on each blade was centered at 72%R with dimensions of 24%c flap-chord and 12%R flap-length. Figure 1.18 shows the actuator installed in the rotor blade, close to the quarter chord. The trailing edge flap was driven by the EMA using a bell-crank mechanism with a travel range of ±15 degree. Pre-existing S-434 blades were modified to accommodate the on-blade actuator and the flap mechanism. Additional leading edge weights were added to ensure proper chordwise cg positioning from stability perspective. The blades were also instrumented with surface strain gages and calibrated for blade loads measurement. Finite element structural analysis was conducted to ensure structural integrity of the modified blade. In addition, Rotorcraft Comprehensive Analysis System (RCAS) [177] was used to predict active rotor stability.

The first hover tests were conducted from June - Sep 2009 followed by additional tests from Apr - Jun 2010. The rotor was spun at 475 RPM using a 3000 HP drive system at Sikorsky Engineering Main Rotor Whirl Stand. The Actuator Control Units (ACUs) used to control the actuators were mounted on the rotor hub and connected to on-blade actuators via power slip rings. A protective dome was used to house the ACUs on the rotor hub. The torsional stiffness was reduced by using a secondary pitch cuff developed by Sikorsky, UTRC, and Eagle Applied Technologies.

The cuff system (Fig. 1.19) was tailored to provide ±10 degree of pitch range

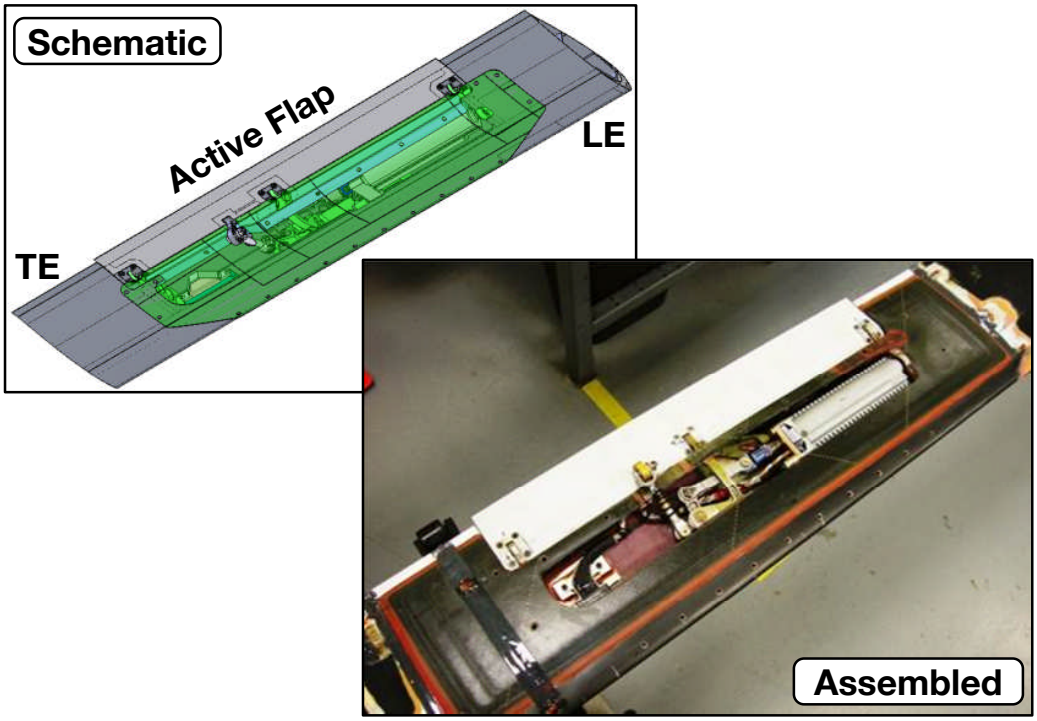

Figure 1.18: Actuator - flap mechanism installed in S-434 blade [176].

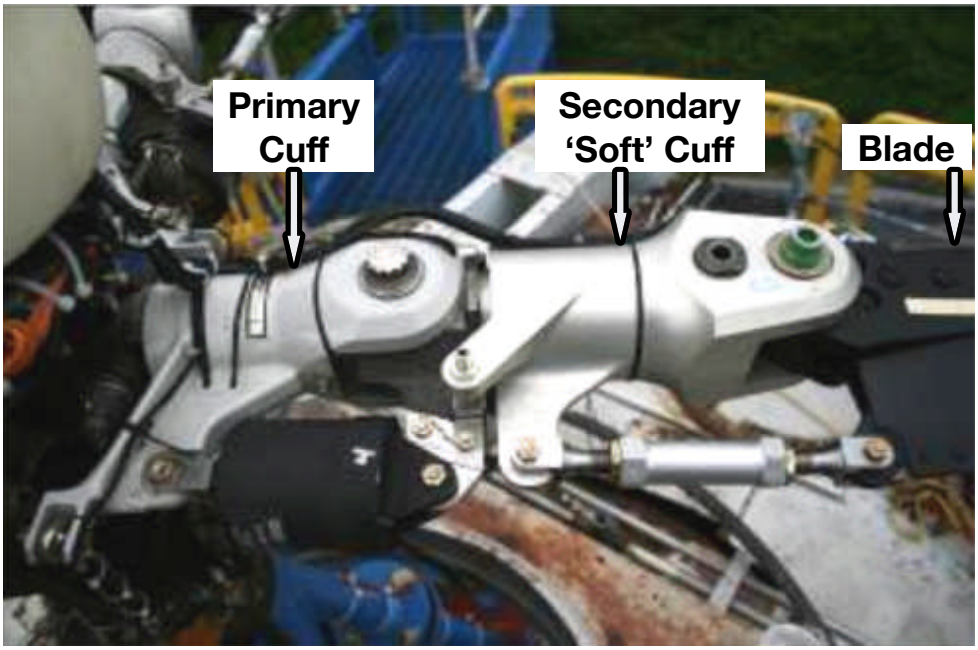

Figure 1.19: Secondary cuff mounted between primary cuff and blade root [176].

and low frictional damping. It was installed between blade root and primary blade cuff resulting in an increase of rotor radius. The rotor speed was appropriately

reduced to maintain tip speed. The objectives of the whirl tests were to verify actuator performance and flap effectiveness under rotating environment at various frequencies and operating loads. In addition, the dynamic stability of the active rotor and closed loop actuator control system were tested as well.

The hover tests successfully demonstrated active flaps performing steady motion, collective, cyclic, and individual mode to simulate system failures. The maximum amplitude for steady and 1/rev motion was ± 10 degree, and the maximum flap frequency was limited to 5/rev. The secondary cuff system with active flap actuated at 2/rev frequency, showed a pitch response ratio of 0.8 degree per every degree of trailing edge flap amplitude and was deemed satisfactory per design requirements. Frequency chirps were also used for active rotor system identification purposes.

Following the hover tests, wind tunnel tests were conducted in the 40 x 80 feet test section at NASA Full Scale Aerodynamics facility (NFAC). Preliminary hover runs with the aim of checking the installation and operation were carried out in Nov-Dec 2010 followed by forward flight runs in Jan-Feb 2011. The active rotor system was tested at various wind speeds up to a maximum of 150 knots. Acoustic, stability and control effectiveness measurements were made in the tunnel. It was found that 2/rev excitation had strong influence on 4/rev edgewise blade loads and flap actuation phase was critical in minimizing these loads. Also, a large component of 4/rev fixed frame vibration was the 3/rev vibratory force on the rotor blade. This 3/rev component was targeted by actuating flaps at that frequency and the closed-loop controller was able to achieve a 75% reduction in 4/rev vertical vibrations in the fixed frame [176]. Significant noise reduction was also achieved [178].

Although excellent flap performance was demonstrated at higher harmonics, primary control, i.e., rotor trim using these active flaps were not demonstrated in forward flight. This was due to stability concern when the secondary cuff was introduced and the trailing edge flaps were excited at 1/rev frequency. Nevertheless, it was concluded that electromagnetic actuators seemed capable of delivering the authority needed for primary and secondary flight control. References [176,178,179] detail the design, pretest setup and results from whirl tests and the wind tunnel tests.

1.5.4 Pneumatic Artificial Muscle driven Flap

Trailing edge flap actuation using pneumatic based actuator was explored by Woods *et al.* [180–183]. A Pneumatic Artificial Muscle (PAM) is composed of an elastomeric bladder enclosed in a helically braided sleeve clamped by end fittings. PAM is a unidirectional actuator which means that it can only contract when inflated by pressurized air. For this reason, a pair of PAMs were used for actuating trailing edge flap as shown in Fig. 1.20.

These PAMs were sized for a full scale rotor application. To test these actuators, an experimental setup was designed (Fig. 1.21). A pair of PAMs (referred to as PAM cartridge) was installed at the root of the blade. A bell crank mechanism converts the motion from the actuator into push-pull motion. These linkages run through the length of the rotor blade and a second bell crank mechanism converts the spanwise motion into chordwise motion providing the necessary hinge moment

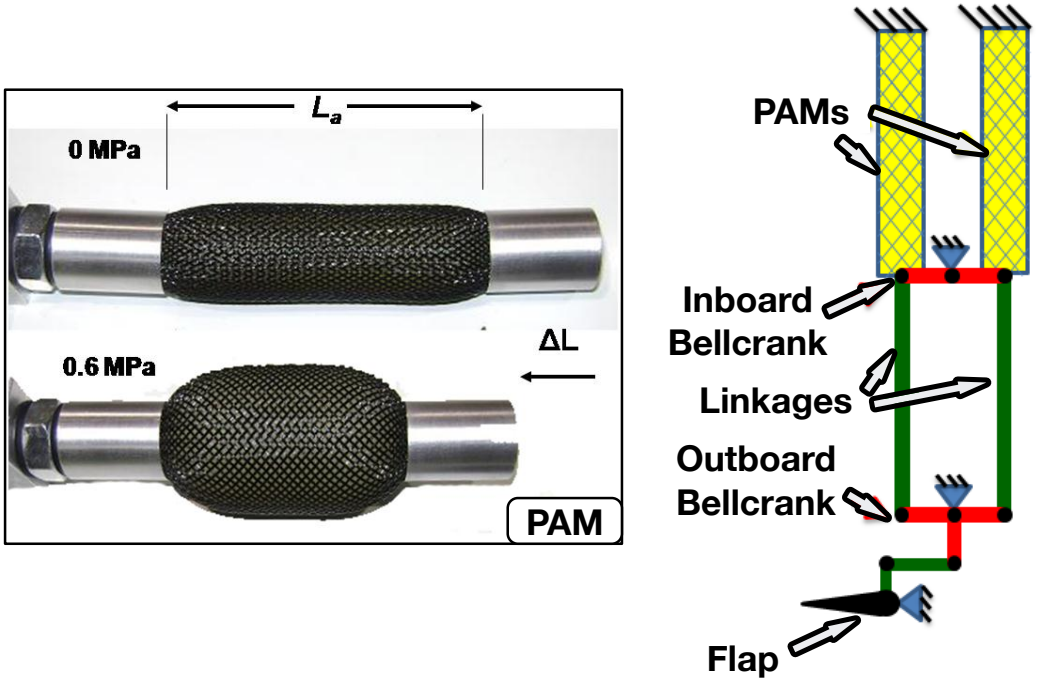

Figure 1.20: Pneumatic Artificial Muscle actuator for trailing edge flap [181].

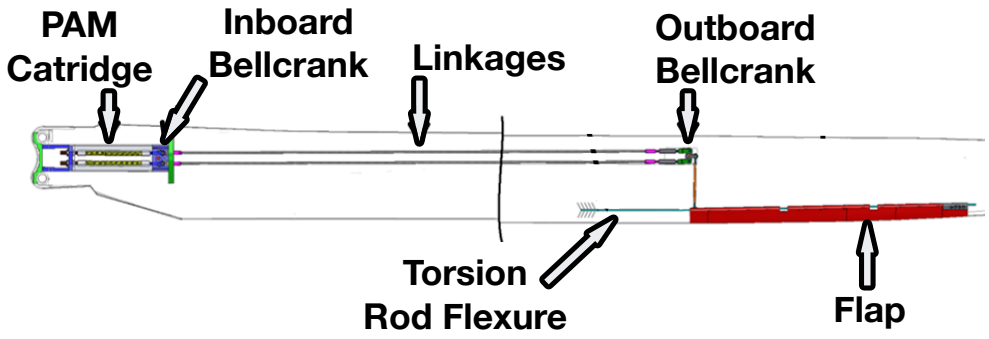

Figure 1.21: Schematic of PAM actuation system in a Bell 407 rotor blade [181].

to actuate the flap. The trailing edge flap was sized to have 16%R flap length, 15%c flap chord centered at 83%R span location.

This non-rotating model was assembled by modifying outboard section of a Bell 407 blade and tested in the Glenn L. Martin wind tunnel (Fig. 1.22). It was tested at number of wind speeds up to a maximum Mach number of 0.3. At 30%

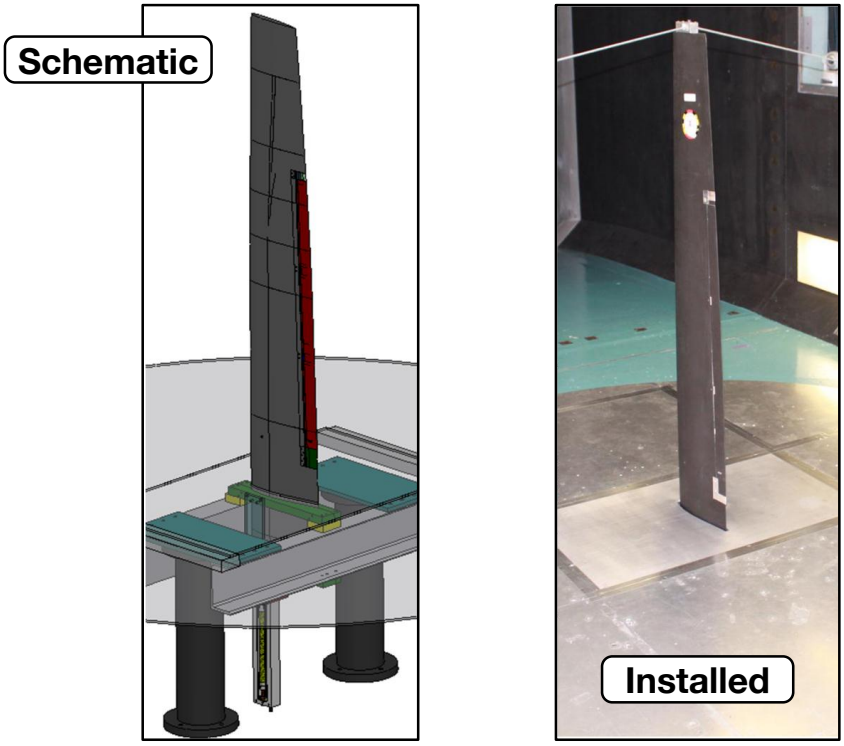

Figure 1.22: Outboard section of Bell 407 rotor blade with PAM actuated trailing edge flap [181].

of full-scale loading, system provided about 19 degree of half peak to peak flap deflection at 1/rev (7 Hz). In addition, half peak to peak flap amplitude of 17 degree at higher frequency of 5/rev shows excellent bandwidth capability of these actuators [180]. These wind tunnel tests examined PAM actuated flaps under limited aerodynamic loading and no centrifugal loads. A torsion rod flexure simulated the hinge moment loading on the trailing edge flap.

A separate experiment was carried out where the PAMs were tested under centrifugal load only in a vacuum chamber. The centrifugal load on the flap was matched to what it would experience at nominal RPM on the Bell 407 full-scale blade. The actuators with the bell crank mechanism were mounted on a rotating

beam and a flexure was used to simulate torsional load at flap hinge. The rotating beam was mass balanced using counter weights. The PAMs were supplied pressured air using a pneumatic slip ring. At 80% of the full scale load, half peak to peak trailing edge flap deflection of 17 degree at 1/rev and 8 degree at 5/rev were recorded [181].

The centrifugal load does seem to lower the actuator performance at higher frequencies. However, large flap deflections at 1/rev frequency using PAMs seems sufficient for primary control. An inner loop feedback controller was also developed that commanded the flap to track the complex waveforms. Satisfactory controller performance was also demonstrated [182, 183].

1.5.5 Piezobender Driven Active Flap for Primary Control

Copp *et al* [184–186] optimized a piezobender for actuating a trailing edge flap on a Mach scale rotor with the aim of achieving primary control. As will be discussed in Section 1.6.1, Mach scaling requires matching the rotor tip speed with the representative full scale rotor. This significantly increases the centrifugal load on the on-blade components. The geometric scaling down reduces the internal volume available in the blade. All these factors add integration and structural challenges to Mach scale active rotor testing.

As discussed previously, all the full-scale smart rotors used piezostacks. Piezostacks utilize d_{33} strain effect and thus have large block force. However, the output stroke is quite low. Amplification mechanisms like X-frame were utilized to provide twenty

times stroke magnification. These mechanisms tend to be rather bulky. The support arms have to be designed to ensure stiff boundary conditions else the mechanism efficiency would be adversely affected. In addition, it was recorded that the amplitude needed at 1/rev frequency for rotor primary control was limited using piezostack actuators. Limited stroke at primary control frequency, and the competing requirements of the weight of the stroke amplification mechanism and limited internal volume of the Mach scale rotor blades, make these piezostack actuators impractical for sub-scale rotor application [185].

To achieve higher output stroke without needing significant lever amplifications, piezobender actuators were developed. These consist of layers of piezoceramic sheets that were bonded together to achieve larger output strokes. The sheets above and below the neutral axis were energized respectively with opposite fields to induce bending strains. This resulted in a net bending moment, causing motion of the tip of the cantilevered actuator. The positive-negative field was oscillated at desired frequency to achieve flap deflection at required frequency at the actuator tip. Since the piezobender used d_{31} strain effect, their energy density was less than quarter of the piezostack actuators.

Figure 1.23 presents an optimized piezobender and a rod-cusp mechanism was used to achieve flap deflection from actuator tip translation motion. A finite element model of the piezobender using Euler - Bernoulli beam formulation with induced strain was used to optimize the piezobender. The constraints on design were placed by the geometric considerations of the available space as well as individual piezoceramic sheets. The design variables included bender length, number of layers

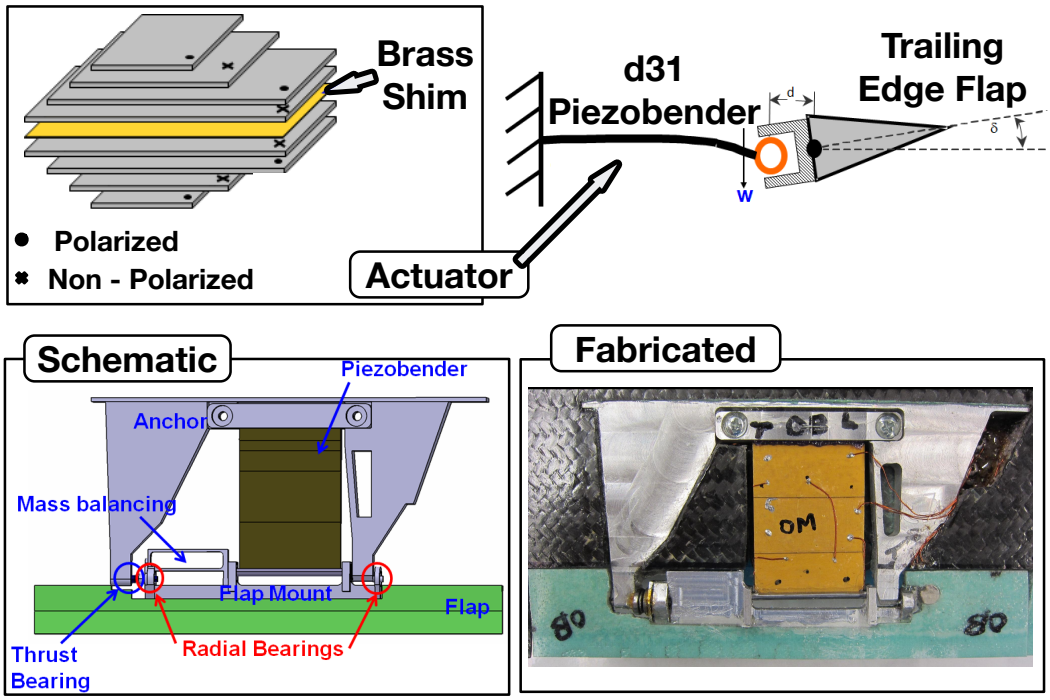

Figure 1.23: Piezobender driven active flap for primary control [186].

and taper. A survey of the available piezoceramic materials available was also conducted and comparisons were made based on the strain energy capacity. The optimized piezobender configuration consisted of eight layers of PZT-5k4 sheets, each layer being 10 mil (0.25 mm) thick. These are arranged in a tapered fashion, and the total weight of the optimized actuator came out to be 18 g. Reference [186] details the optimization considerations, choice of material, fabrication process of the bender and effect of temperature, high actuation fields and actuation field bias on the piezobender output.

Next, significant efforts were made to design a flap mechanism that would be incorporated in the scaled rotor blade. The final mechanism is shown in Fig. 1.23 and Table 1.4 presents comparison between vibration and primary control active flap

Table 1.4: Comparison of vibration and primary control flap configurations [186].

Parameter	Roget [147]	Copp [186]
Configuration	Hingeless	Articulated
Rotor diameter (R)	1.52 m [5.00 ft]	1.66 m [5.46 ft]
Rotor chord (c)	0.076 m [3.00 in]	0.080 m [3.15 in]
Rotor speed (RPM)	1800 [30 Hz]	2400 [40 Hz]
Tip Mach Number	0.42	0.61
Flap midspan (%R)	75	82
Flap length (%R)	8	14
Flap chord (%c)	20	15
Tor. Freq. (/rev)	> 4	1.53

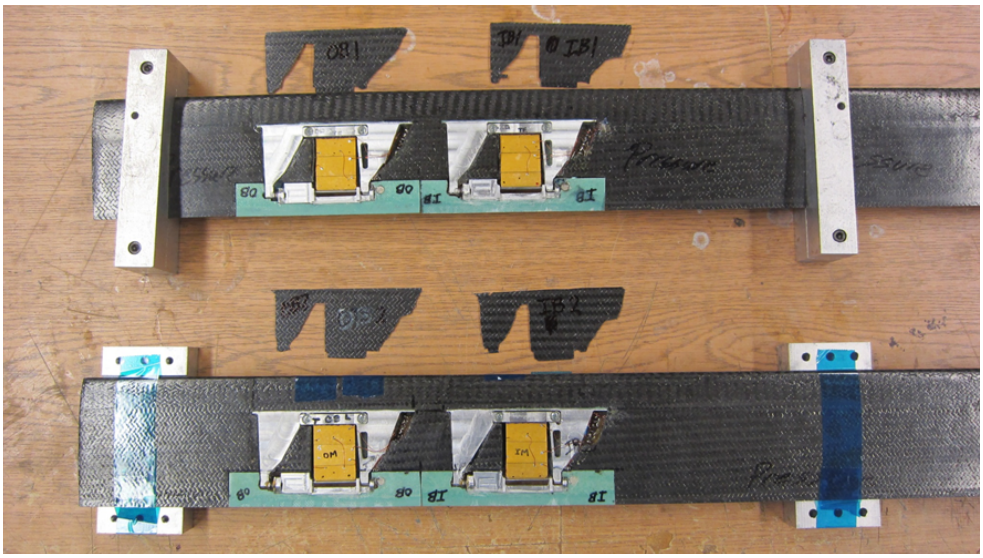

Figure 1.24: Active rotor with inboard and outboard flap assemblies [186].

configuration. It is clear from the table that, compared to vibration control, larger flap and lower torsional stiffness are required for primary control. In addition, two such piezobender-flap mechanism were installed, the inboard flap centered at 75% and outboard at 82% span locations (Fig. 1.24). This piezobender-flap mechanism was incorporated in a composite Mach scale blade and a two bladed rotor was systematically tested on the bench top, followed by vacuum chamber testing and finally hover testing.

On the bench-top, a maximum half peak to peak flap deflection of 15 degree was achieved with the piezobender driven at -90V/+270V excitation field. When the rotor was spun at 900 RPM on the hover tower, the flap amplitude at 15 Hz (1/rev) fell to 12.7 degree half peak to peak deflection. At higher rotor speeds, the fall in flap deflection was even steeper. This could have been due to loads on the mechanism or inability of the piezobender actuator to meet the required hinge moments to produce flap deflections. In either case, the hover testing was limited to a maximum rotor speed of 900 RPM. Closed loop flap deflection control was also implemented using a proportional feedback controller.

Finally, the torsional stiffness of the rotor was reduced by replacing the stiff pitch link with a soft pitch link. The stiffness was tuned to reduce the torsional frequency at 900 RPM to 1.53/rev. Up to 1 degree half peak to peak blade root pitch with both the trailing edge flaps operating at maximum deflections was demonstrated. Oscillations in hub loads in response to flap deflections were also recorded, and trailing edge flap effectiveness was also assessed. Due to limited control authority, no wind tunnel investigations were carried out.

1.6 Model Scale Rotor Testing

Rotor testing is a critical phase in rotorcraft design, development and certification. The operational requirements of a rotorcraft to perform increasingly complex and demanding mission profiles has led the design to the edge of operational capability of these vehicles. The performance and operational benefits that were once achieved with blade geometry tailoring and airfoil design are no longer sufficient by themselves. Instead a fundamentally different approach is required to meet the design objectives. Swashplateless rotor control using active trailing edge flaps is one of such approaches.

Model scale rotor tests are desirable to verify the candidate design before committing large amount of resources to full scale design and testing. Model scale tests are cost effective and allow easier and swifter parameter changes for design and optimization studies. However, to achieve representative measurements from the model scale tests, geometric and dynamic scaling laws have to be carefully applied to ensure representative results from these model tests. These are called scaling parameters and are discussed next.

1.6.1 Rotor Scaling Parameters

Generally, there are three types of scaled rotor models: rigid models, Froude scale models and Mach scale models. Rigid models simulate only the aerodynamic profile of the full scale blade and are used to study the basic aerodynamic characteristics under ideal conditions. These models incorporate geometric details and are

less expensive to fabricate than dynamically scaled models. Froude scale models simulate the blade static deflection and are used for aero-mechanical stability testing of rotors. Scaled structural and inertial characteristics are simulated in Froude scale models. Mach scale models are designed to match the tip Mach number of full scale rotors. These models simulate compressibility effects in addition to scaled structural and inertial characteristics and are used to study rotor vibratory response, loads, and basic performance. References [187–191] discuss in detail these similarity parameters.

Small scale rotor models are unable to simultaneously satisfy multiple scaling parameters (such as Mach number, Froude number and Reynolds number) in air. A comparison of some of the parameters is presented in Table 1.5. It is also seen that the model Reynolds number is lower than that of the full scale rotor by the geometric scale factor, in order to match the Mach number.

Table 1.5: Scaling parameters of small scale rotor.

Ratio of model to full scale	Mach scale	Froude scale
Length parameter	S	S
Rotor radius	S	S
Rotor speed	1/S	$1/S^{\frac{1}{2}}$
Mach number	1	$S^{\frac{1}{2}}$
Froude number	1/S	1
Reynolds number	S	$S^{\frac{2}{3}}$

1.6.2 Scaling Parameters Considerations

Generally, it is not possible to meet all the scaling requirements and some hierarchy in similarity parameters is practiced based on the requirements. The model-scale test rotors can be broadly classified as:

(a) Research Models: These models are aero-elastically matched and are not based on a specific rotor but are broadly representative of a full-scale design. These models are used for gaining insight into novel or unusual design configurations, generating data for benchmarking various codes or testing implementation of high risk advanced technologies. The important scaling requirement is to ensure similar aerodynamic environment by matching the tip Mach number, and if possible matching the Reynolds number. It is often not possible to simultaneously match Mach number and Reynolds number, unless the density of test medium can be controlled. For example, the use of Freon gas in NASA Transonic Dynamics Tunnel allows to match both tip Mach and Froude numbers. In all other test facilities, matching Mach number takes precedence over Froude number.

Structurally it is important to ensure representative blade stiffness and elasticity properties. Model blades must have similar bending stiffness and torsion stiffness. When designing the blades, it is essential to ensure structural frequencies are well separated to avoid any unintended resonance conditions. Inertially, blade mass moment of inertia and Lock number must be similar to

full-scale blade to ensure similar blade flap response.

Finally, the scaling constraints on geometry are less restrictive, the blades must be of similar aspect ratio. Blade airfoils need not be as sophisticated as actual rotor blades and features such as twist, taper and sweep are generally omitted for simplicity in design and fabrication.

(b) Simulation Model: These models have a stringent requirement to be as close to the candidate full-scale rotor as possible. This includes precisely modeling geometric features like airfoil shape, twist, taper and sweep. In order to accurately predict the full-scale performance, tip Mach number must be matched. Reynolds number matching is also essential to accurately account for profile power measurements, especially for complex planform rotors with taper and rotors in forward flight. Correct aeroelastic response can only be achieved by matching the torsional stiffness and mode shapes. Coupling effects require matching flap and chord elastic characteristics and to capture coupling of higher blade flap and torsional motions. These prediction models are highly specific to a unique full-scale rotor and are generally used to study a design change or to understand any peculiar phenomenon observed in flight testing. Though, these can be used for research, generally the complex nature of these blades and a number of coupled aero-structural responses limits their use to very specific cases. Data generated by these models can be used as test case for validation of advanced codes, only after basic validation has been obtained using research models.

For the current research, the emphasis is to test an on-blade actuator and thus a research model rotor blade is suitable. It provides for simple geometry aiding in repeatable fabrication. Constraints are placed on the scaling dimensions of the rotor based on the test hardware available especially the Glenn L. Martin wind tunnel. The wind tunnel test section is 7.75 ft wide and 11 ft high. To avoid wall interference, the model rotor diameter must not exceed 55% of the test section width. This limits the rotor radius to about 6 ft. Also, the articulated rotor hub has a hinge offset of 2.125 in and the maximum RPM the hub can spin up to is 2400. Table 1.6 shows the comparison of properties for scaled research rotor and UH-60A rotor blade. The non-dimensional parameters are expressed mathematically in Eqs. 1.1.

$$\begin{aligned} Rotor\ Solidity, \quad \sigma &= \frac{N_b c}{\pi R} \\ Lock\ Number, \quad \gamma &= \frac{\rho a c R^4}{I_b} \\ Reynolds\ Number, \ Re &= \frac{\rho V c}{\mu} \\ Froude\ Number, \ Fr &= \frac{V^2}{gR} \end{aligned} \tag{1.1}$$

where N_b is the number of blades, c is the blade chord, R is the rotor radius, ρ is the air density, μ is the dynamic viscosity of air, I_b is the blade mass moment of inertia, V is the rotor tip speed, and g is the acceleration due to gravity.

Table 1.6: Comparison of basic parameters of UH-60A and scaled research rotors.

Parameter		UH-60A Rotor	Research rotor
Hover tip Mach number	M_{tip}	0.65	
Hover tip speed	V	221 m/s [725 ft/s]	
Number of blades	N_b	4	
Nominal RPM	Ω	258	2400
Blade chord	c	0.53 m [20.76 in]	0.08 m [3.15 in]
Rotor diameter	D	16.36 m [53.67 ft]	1.68 m [5.5 ft]
Aspect ratio	AR	15.5	10.5
Rotor solidity	σ	0.0826	0.1197
Lock number	γ	8.12	5.12
Reynolds number ($\times 10^6$)	Re	7.75	1.17
Froude number	Fr	608	5927
Twist (deg.)	θ_{tw}	-16	zero
Hinge offset	e/R	4.7 %	6.3 %
First flap frequency (/rev)	ν_β	1.035	1.046
Blade airfoil		SC 1095/(R8)	NACA 0012

1.7 Selection of On-Blade Actuator

A suitable actuator is central to a successful implementation of swashplateless rotor control. It is to be kept in mind that in a Mach scale rotor, the centrifugal loading cannot be simulated, and as a result, the actuation authority requirement for primary control far exceeds the actuation requirement in a full-scale system. To maximize the control effectiveness, the active trailing edge flaps have to operate in the outboard span location of the blade. This necessitates the on-blade actuators to perform in a challenging operating environment. A suitable actuation system must have following characteristics:

(a) It must be of lightweight construction. Any additional structural weight takes away from the payload capability of the helicopter. A heavier on-blade actuator would necessitate bulkier support structure, driving the weight of the blades up, thus increasing the overall weight the vehicle.

(b) It must be of compact form factor. The space in the rotor blade is limited. A compact and self-contained actuator would make it easier to accommodate it in the blade profile.

(c) It must be capable of operating under high g-loads. The flaps are located on relatively outboard section of the blade. Any actuator placed at such radial locations would be under tremendous centrifugal loads. The on-blade actuator must operate satisfactorily under such high load environment.

(d) It must have a large output stroke. From primary control perspective, larger

flap amplitudes are required to trim the helicopter.

(e) It must have a low power requirement. A high efficiency, low input power requirement actuator would be suited for on blade application.

(f) It must have a wide operation bandwidth, and therefore the trailing edge flap could accomplish multiple roles of primary flight control, performance improvement, and vibration and acoustic noise reduction. This imposes a diverse frequency operation envelope for the actuator.

(g) It must be easy to operate and incorporate in linear control systems.

Thus, an ideal on-blade actuator for trailing edge flap control must be lightweight, compact, linear, energy efficient, sturdy, provides large flap amplitudes and has wide operational bandwidth. Over the years, multi-layer piezoelectric sheet benders have been extensively employed both at model scale as well as full scale rotors as on-blade actuators. They have proven effective for rotor active vibration control. However, a limited stroke from these piezo actuated trailing edge flaps has been a major impediment in achieving rotor primary control. Pneumatic actuators have demonstrated large deflections and a wide operational bandwidth when designed for full-scale applications. However, they are not easy to scale down and as such no small scale PAM actuators exist. Electric motors have matured over the years and with the use of high density ferroelectric materials, their energy density has increased as well. Sikorsky active flap demonstration rotor uses an electromechanical actuator as well. Thus, in this study a compact brushless dc motor would be evaluated as a potential on-blade actuator capable of achieving swashplateless rotor primary control.

1.8 Objective and Scope of Current Research

This dissertation focusses on demonstrating a Mach scale swashplateless rotor control by using a trailing edge flap. All the previous research at Mach scale performed at University of Maryland has utilized piezo-based actuators for active flaps. They have been successful at vibration reduction, but their limited authority at primary control has been a major limitation. It has been clearly realized that a different actuator needs to be utilized if primary control using these flaps is desired.

To this end, compact brushless DC motors are assessed as on-blade actuators for driving the trailing edge flaps. They are systematically tested on the bench top with simulated loading and then gradually under centrifugal loads. A control strategy is devised to actuate the flaps at desired amplitudes and frequency and demonstrate complete control of the actuator. Large output flap deflections at 40 Hz actuation frequency are demonstrated on the bench top under simulated torsional loading. Then, a mechanism is designed and fabricated to actuate the trailing edge flaps using compact DC motors. The design challenges due to large centrifugal load and restricted blade volume are important considerations, and several iterations are made to refine the structural design and fabrication process. A Mach scale composite rotor with four blades is also fabricated and special emphasis is laid on ensuring proper spanwise and chordwise weight balance.

The assembled active rotor is tested in hover at various rotor speeds. In addition to existing loads and torque measurements, the hover stand is extensively instrumented to record blade root flap, and pitch angles. The active blades are

first tested with stiff pitch links and actuator performance is analyzed at a range of operational frequencies. A closed loop control of flap amplitude is implemented. Then, the torsional frequency is gradually lowered by replacing the stiff pitch link with a custom designed soft pitch link. The torsion frequency is tuned to be 2/rev and the blade pitch response to trailing edge flap inputs is demonstrated. The trailing edge flap frequency and phase is synced to the rotor shaft azimuth and all the four active blades are actuated to control the blade tip path plane.

Finally, forward flight testing in Glenn L. Martin wind tunnel is carried out. In the first phase, the motor-flap performance is evaluated keeping the rotor stiff in torsion. The rotor is operated at a number of RPM and wind speed combinations and flaps performance operating at 1/rev frequency is recorded. In the second phase, the torsion stiffness is reduced to around 2/rev and wind tunnel trim is attempted. At 1200 RPM, wind speed up to 50 mph and 2 degree blade collective, wind tunnel trim of the Mach scale rotor using motor actuated trailing edge flaps is successfully demonstrated.

1.9 Dissertation Outline

Chapter 1 introduces the concept of rotor primary control and explores the possibility of achieving it without using a swashplate. It also outlines, in rough chronological order, the path leading to active flaps on a rotor blade, first as a better alternative to HHC for vibration control and then with a greater objective of primary control. Analytical work exploring swashplateless rotor feasibility and requirements is also discussed in detail. Finally, Mach scale testing of the rotor is introduced and pertinent design challenges are discussed.

Chapter 2 details the rotor test facility at the University of Maryland. A detailed description is provided, and an expansive discussion on various component is included. Rotor fabrication, track, trim and measurements related to testing are presented as well. Vacuum chamber test facility and Glenn L. Martin wind tunnel are also described. A few state-of-the-art rotor test facilities around the world are also briefly included.

Chapter 3 introduces brushless DC motor and controller technology, its operational principles followed by bench top testing of the selected motor under simulated torsional load. The actuator control strategy is described and the effect of temperature on the actuator is also studied. A comparison on brushless dc motor and piezobender in terms of relative power density is also included.

Chapter 4 details the design and fabrication of the motor-flap system, the evolution of the design and FEM analysis of the mechanism. Comparison of the system output waveform with four-bar analytical expectation is also included.

Chapter 5 includes motor-only and motor-flap system testing under centrifugal loads in vacuum chamber.

Chapter 6 presents the fabrication of composite rotor blade, assembling the flap mechanism in the blade and structural testing of the active blade. It is followed by careful description of component-wise weight breakdown and cg balancing of the blades.

Chapter 7 details hover testing first with stiff pitch link and then soft pitch link. The design and calibration of the soft pitch link is also included here. Blade pitch response to trailing edge flap inputs at various rotor speeds is demonstrated and implementation of a closed loop controller of flap amplitude is also described.

Chapter 8 details wind tunnel testing of the active rotor blade. The motor-flap performance evaluated with rotor stiff in torsion and operating at a number of RPM and wind speed combinations is presented. Next, the torsion stiffness is reduced to around 2/rev and wind tunnel trim is discussed. At 1200 RPM, wind speed up to 50 mph and 2 degree blade collective, wind tunnel trim of the Mach scale rotor using motor actuated trailing edge flaps is successfully demonstrated.

Chapter 9 presents summary of the research effort and lists a number of conclusions from the current work. A few recommendations for the future research are also included.

Technical drawings are included at the end followed by bibliography.

Chapter 2: **University of Maryland Rotor Test Facilities**

The rotor test facilities at the University of Maryland include a hover tower for scaled rotor hover testing, a 10-ft diameter vacuum chamber for testing under centrifugal loads only, and Glenn L. Martin low speed wind tunnel for rotor forward flight testing. First the hover test stand, rotor drive system, rotor hub, control and instrumentation are extensively discussed. Rotor blade design and fabrication considerations are also included. Next, the vacuum chamber and the wind tunnel are detailed. Finally, a select state-of-the-art rotor test facilities around the world are briefly presented.

2.1 Hover Test Stand

The main application of the hover test stand is to examine the aeromechanics of the rotor in hover. In addition, it enables testing structural and functional integrity of the rotor as well as embedded components such as actuators, strain gages, accelerometers, etc in a rotating environment. It also serves as a test bench for evaluating various hub instrumentations, rotor control and data acquisition systems, as a precursor to forward flight testing in the wind tunnel.

The hover test stand at Alfred Gessow Rotorcraft Center is one of the rotor

test facilities in the country. It is mounted on a tall column such that the rotor plane is separated by about two rotor diameters from both the ground as well as the ceiling (Fig. 2.1). This is to ensure unobstructed inflow conditions and out-of-ground effect operation in hover. The column is installed roughly in the center of a nylon netting curtained space to keep personnel out while rotor is in operation. In addition, one feet above and below the rotor plane is bounded using torpedo grade braided steel wires netting (Fig. 2.2). The hydraulic unit is kept outside the test parameter and is controlled remotely from the adjacent control room. The rotor rig is operated by a hydraulic system, which allows for operating the rotor at various rotational speeds and torque requirements.

Figure 2.3 shows the rotor hover test rig. The rotor rig features an adaptable hub which can be used to test either an articulated or bearing-less rotor system. The hub is instrumented to monitor the blade flap, lag and torsion motions, control pitch inputs, the rotor azimuth position, and rotor speed (RPM). In addition, the drive shaft is instrumented using strain gages to measure rotor torque, and a six degree of freedom balance is mounted in fixed frame to measure rotor hub loads. It is a very versatile test facility and has been in use since 1985 when its key components were donated by Boeing-Philadelphia Company and subsequently refurbished in-house.

In the following sections the hydraulic system which runs and controls rotor system is discussed. Then the hub system is detailed followed by various instrumentation both in rotating and non-rotating frames.

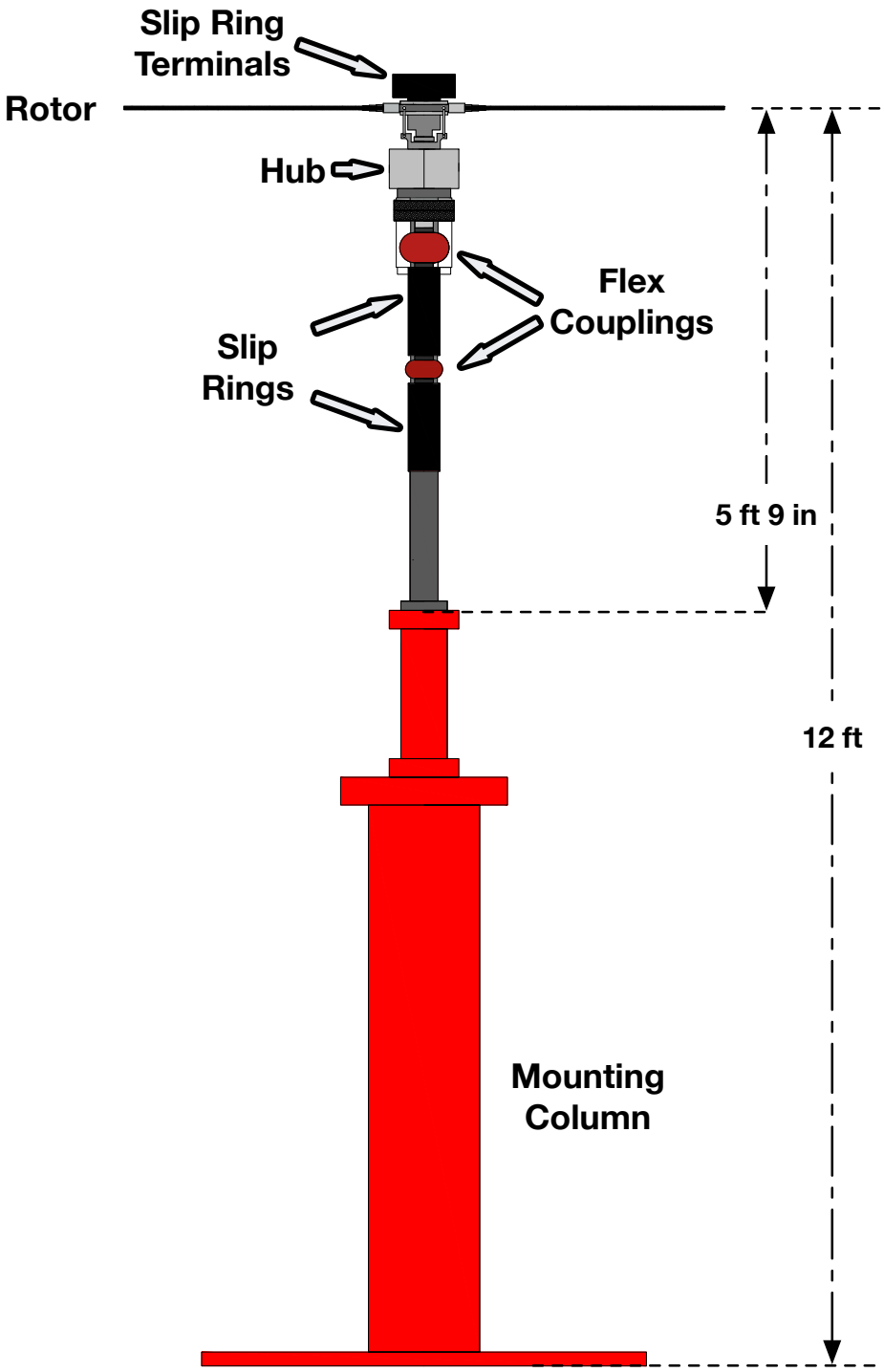

Figure 2.1: Front view of hover test stand at University of Maryland.

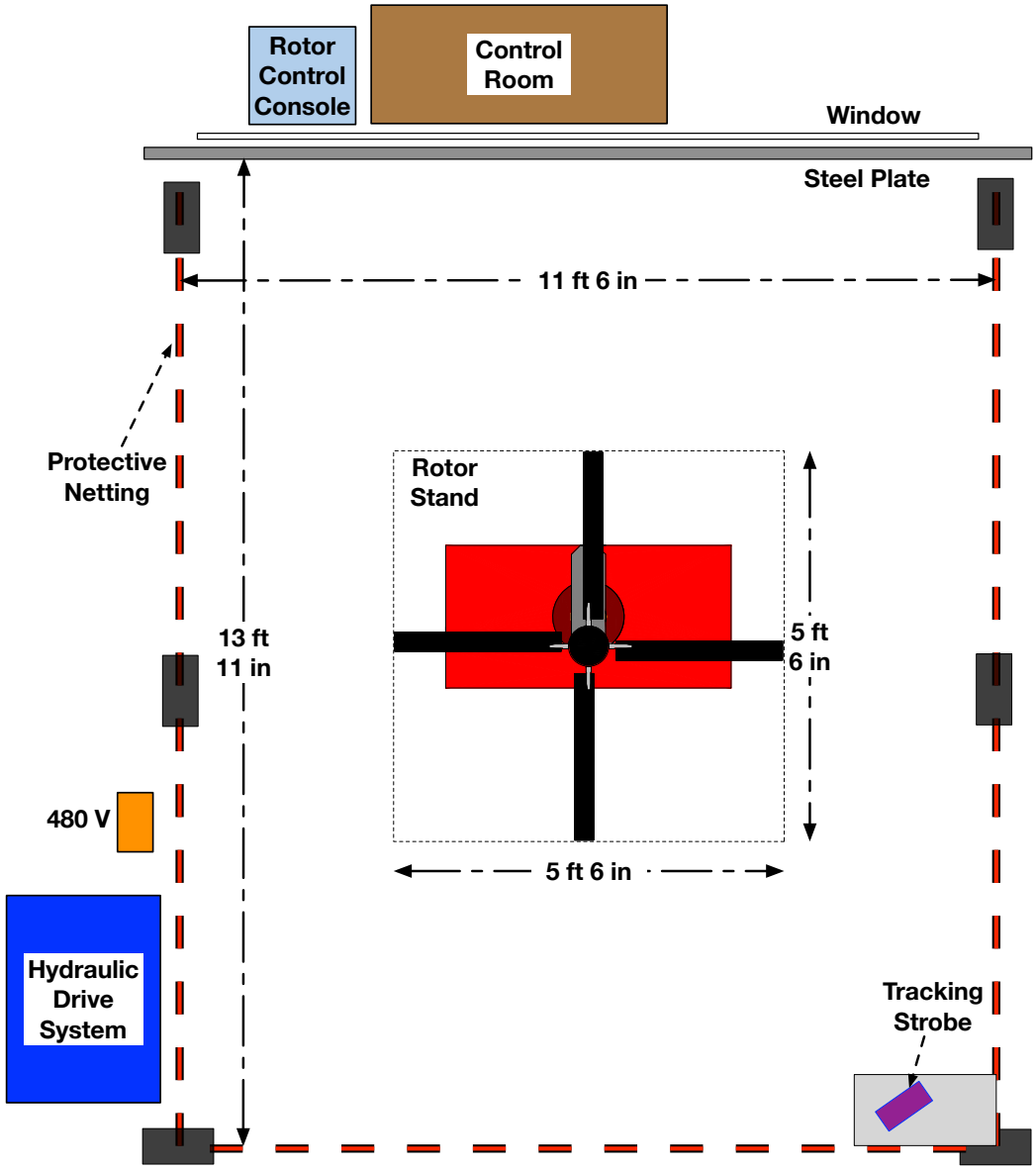

Figure 2.2: Layout of hover test stand at University of Maryland.

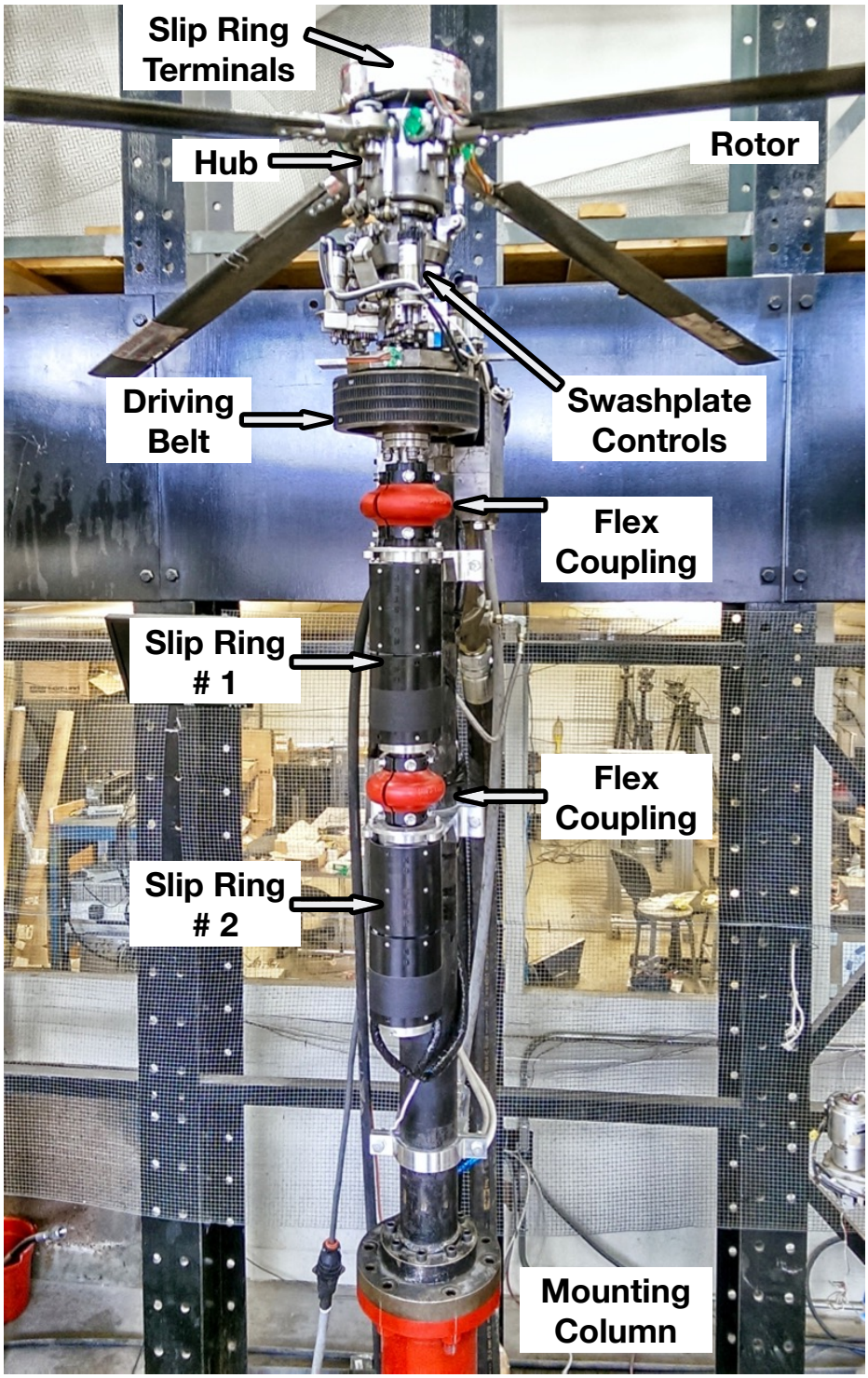

Figure 2.3: Hover test stand at University of Maryland.

2.2 Rotor Drive System

The rotor can be operated either by an electric motor or a hydraulic motor. In principle, both are equally capable of providing the required drive capabilities, however the choice of the prime mover depends on a number of factors like maximum required power, torque, range of operational rotor RPM, ease of maintenance, ease of use and control, reliability and portability of the unit, among other factors.

2.2.1 Choice of Drive System: Hydraulic vs Electric

The rotor drive system is required to operate the rotor at desired rotor speed (RPM) and provide the necessary torque required to support the rotor loads at the operating flight conditions. An electric drive system would typically consist of an electric motor operated by a motor controller. The motor is usually a high speed, high voltage three phase AC induction motor. The motor controller is essentially a solid-state power electronics conversion system termed as variable frequency drive. It is used to control AC motor speed and torque by varying input AC frequency and voltage. Generally these AC motors are high speed drivers and a gear-down transmission is required to meet the RPM requirements at the rotor drive shaft. Also, some water or oil based cooling around the motor may also be required to prevent heating damage from extended motor operation.

A hydraulic system would be composed of a pump circulating a suitable fluid from a reservoir to a motor. To operate a hydraulic unit, the energy to drive the pump to supply the hydraulic fluid has to be provided either by an electric motor or

a gasoline engine. In a test facility, invariably an electric motor is used to drive the hydraulic pump. In addition, some electrically controlled valves would be required to control the speed and torque at the rotor drive shaft. Generally a cooling system may be required to maintain the fluid within the required temperature limits.

In broad terms, the electric motor directly converts electric power into rotational torque whereas hydraulic motor converts hydrostatic energy into rotational torque, the fluid energy being generated by an electric motor. Thus, the hydraulic system has an additional energy conversion step that adds some additional losses to the system.

Challenges associated with electric drives include operating at high voltage AC transmission and design of water based cooling for the motor as any water leakages could present serious operational hazards. These motors tend to be heavy, and are high speed drives requiring a high gear-down transmission adding weight and limiting portability of the system. However, the AC motor and control technology is very mature and no excessive maintenance is required. In contrast, the hydraulic motors are compact and reliable, with easy serviceability. The hydraulic pump driven by an electric motor can be located away from the test section supplying fluid to the motor via hydraulic lines. A compact hydraulic motor driving the rotor shaft minimizes the blockage in the test section. Another advantage is that the oil cooling system can run in a separate circuit and thus is uncoupled from the hydraulic system. However, in general a hydraulic system needs regular maintenance compared to an electric system and special attention has to be given to the filtration of the hydraulic fluid and general cleanliness of the operational environment. High

pressure, high temperature hydraulic oil lines can also add additional safety and operational concerns.

Another important consideration for choosing appropriate drive system for the rotor test stand is the proximity of the motor to the slip rings or data acquisition systems. The slip rings help in communicating with the actuators, sensors and instrumentation in the rotating frame and are essential to the rotor testing and data acquisition. The objective is to minimize the Electro Magnetic Interference (EMI) thus, enhancing the signal-to-noise ratio.

The rotor test facility at NASA TDT uses an electric motor to drive the rotor. For their test setup, the data acquisition unit is located on the top of the rotor hub whereas the electric motor rests in the fuselage nacelle. This separation ensures a low level of interference between data acquisition lines and the electric motor. At University of Maryland the data slip rings are in close proximity with the motor. Due to smaller scale and compact design, any electric motor would induce a substantial EMI, leading to noisy data. The presence of slip ring based data acquisition also adds about 50-ft of cable between the transducers on the blade (or hub) and the Analog-to-Digital (A/D) conversion at the Data Acquisition System in the control room. Every effort needs to be made to ensure as low a noise profile as possible to obtain a high signal-to-noise ratio. This was the main reason, for choosing a hydraulic motor to drive the rotor at the test facility.

The hydraulic drive system that operates the rotor test stand at UMD is detailed next.

2.2.2 Hydraulic Motor

A fixed displacement axial piston hydraulic motor (Rexroth AA2FM32/61W) [192] is used to power the rotor at the University of Maryland. The motor produces torque as a result of pressure differential between the input and output hydraulic lines. Consider the components of the motor shown in Fig. 2.4.

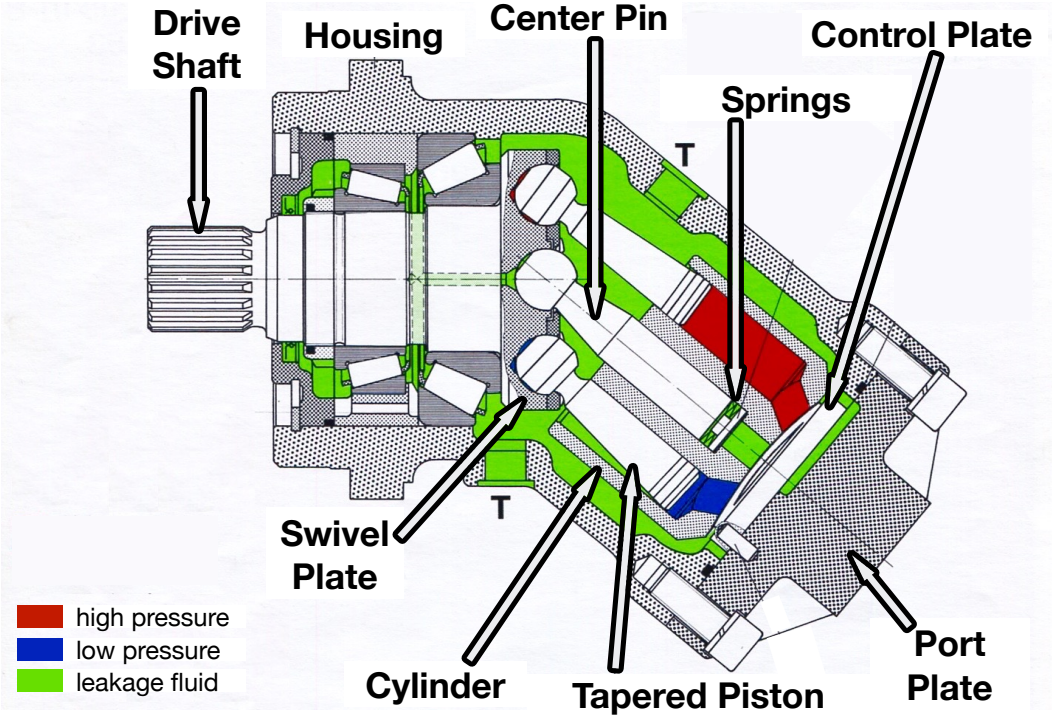

Figure 2.4: Fixed displacement hydraulic motor.

The drive shaft is supported on radial bearings and is attached to a cylindrical plate referred to as a swivel plate or swashplate (not to be confused with rotor swashplate, henceforth hydraulic motor/pump swashplate is referred to as swivel plate). The swivel plate is connected to a number of tapered pistons, aligned axially to the motor and distributed azimuthally on the swashplate. Usually odd number of pistons (seven or nine) are used. In addition, a central pin aligns the swivel plate

to the cylinder and takes any radial load on the cylinder. The hydraulic ports are installed on the control plate which has two kidney-shaped slots to distribute the hydraulic fluid selectively to the piston-cylinders. At any given instance, three to three and half cylinder bores are open to the pressure side and remaining are open to the outlet side (low pressure or exhaust port). The oil pressure is forced into the cylinder bores and the resulting piston motions produce rotation of the swivel plate. In this motor, the swivel plate inclination is fixed, thus limiting the displacement of the pistons to preset geometric constraints (fixed displacement). The main body of the motor is inclined at 40 degree to minimize the axial load on the swivel plate. The radial load develops a torque on the splined drive shaft which is connected to the rotor shaft via a belt-pulley transmission. The space between the cylinder and housing is constantly supplied by a leakage fluid, which ensures a thin film between the moving surfaces.

For a fixed displacement motor design, the volume per revolution is fixed. In this case, the output speed at the drive shaft depends on the flow rate of the fluid supplied to the motor. The torque output depends only on the pressure differential between the high pressure input port and the low pressure return port. A distinct advantage of this motor is a simple construction and high mechanical efficiency. The motor can operate at various speeds and torque levels for an extended period of time.

The two main requirements for the rotor test rig are to control the rotor speed (RPM) and meet the necessary torque requirements. The torque requirement is meet by the hydraulic pump which supplies the oil at pressure to the motor and the

rotor speed is controlled by flow control valve which dictates the flow rate to the motor. Each of these components are discussed next.

2.2.3 Hydraulic Pump

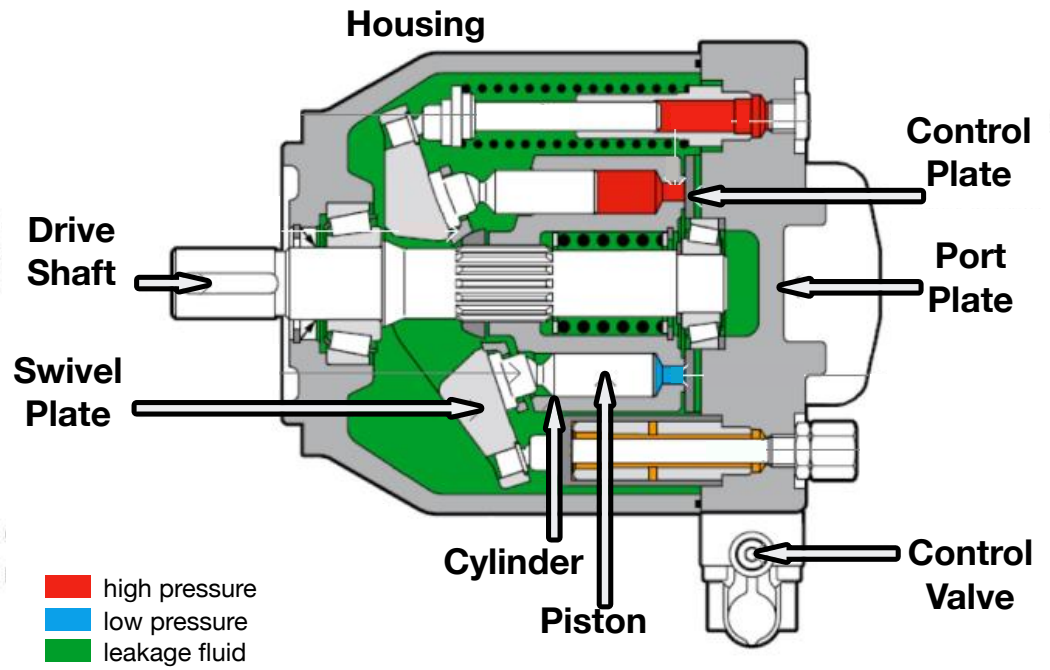

Figure 2.5: Variable displacement hydraulic pump.

A variable displacement pump (Rexroth AA10VSO100DR/31R) [193] is used to supply the hydraulic fluid at pressure to the motor. The construction of a typical hydraulic pump is shown in Fig. 2.5. The operating principles are very similar to the motor described in the section 2.2.2, except the mechanical motion of the pump shaft is used to force the fluid at pressure to the motor. In contrast to the fixed displacement design, here a hydraulic feedback circuit can change the swivel plate inclination (or swivel) angle based on the load requirement. Changing the swivel

angle changes the piston stroke, thus allowing variable displacement.

Refer to the Fig. 2.6, a pressure compensated variable displacement pump supplies near constant flow rate at all load pressure below the compensator or peak pressure. As the load increases the pressure compensator unit senses the change and appropriately adjusts the swivel to meet the required load at near constant flow rate. If the load pressure builds above peak pressure, the pump will de-stroke to level needed to maintain peak pressure setting. A relief valve set at a safety pressure above the peak pressure is also installed to relieve any sudden increase in pressure above and beyond the peak pressure. This gives enough time for the swivel plate to adjust and bleed fluid to reduce dangerous pressure buildup.

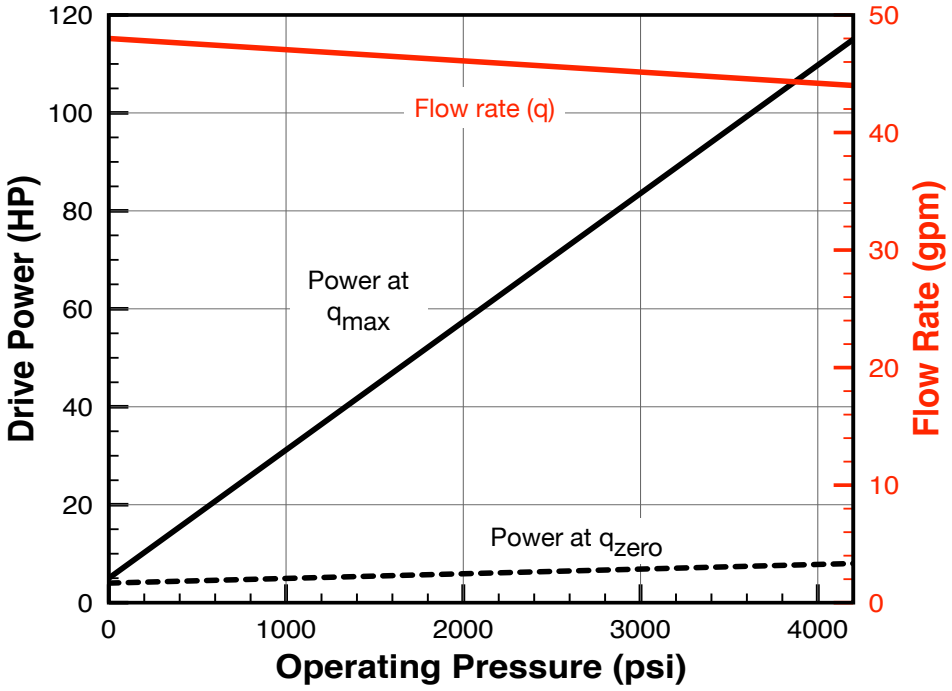

Figure 2.6: Hydraulic pump characteristics at operating speed.

In the current setup, the hydraulic pump is driven by a constant speed electric

motor. The compensator is set at a peak pressure of 4000 psi and the relief valve is set at 4200 psi. When operating in loads such that the pressure at the pump is less than the peak pressure, the pump operates near constant flow rate (about 50 gallons per minute). Once the pressure exceeds 4000 psi, the flow rate sharply reduces to maintain pump operation at peak pressure albeit with significantly lower flow rate. The relief valve set at 4200 psi is a safety feature to allow for time for the compensator to adjust the swashplate swivel in case of a sudden uptake in the load pressure. This way, a variable displacement pump allows to operate the rotor at various torque loads at any given rotor speed. However to control the flow rate, an additional flow control valve is required and is discussed next.

Nominally, the current system is rated at about 50 gallon per minute peak flow rate and about 100 HP at the pump shaft. The power available at the rotor drive shaft is significantly lower to account for additional losses such as pumping the fluid from reservoir to the motor situated at height above the ground level, pressure losses in fittings and other inefficiencies. Also, the electric motor that drives the hydraulic pump is rated at 75 HP. Technically, the hydraulic motor is rated for in excess of 100 HP, but being run by an electric motor rated at 75 HP and thus in practice the peak power available at the rotor shaft will not exceed 60 HP.

2.2.4 Flow Control Valve

The flow control valve [194] allows to remotely modulate the amount of fluid sent to the hydraulic motor, thereby controlling the rotor speed. It is installed at

the outlet of the hydraulic pump. As stated in section 2.2.3, the pump delivers near constant flow rate as long as pressure doesn't exceed the peak setting. The flow control valve allows to control what fraction of the output from the pump goes to the hydraulic motor running the rotor system and rest is bypass to the reservoir. To achieve this goal, the valve unit performs dual functions of setting the flow rate at desired level remotely and at a given flow rate, ensure delivery is unaffected by the variation in the pressure at inlet and/or outlet.

The design is based on the principle that for a short orifice of a given area, a flow rate can be maintained as long as the pressure differential across it is maintained. Thus, some means of sensing a change in upstream and downstream pressure is needed and then compensated to maintain same pressure drop across inlet and outlet, thereby ensuring desired flow rate.

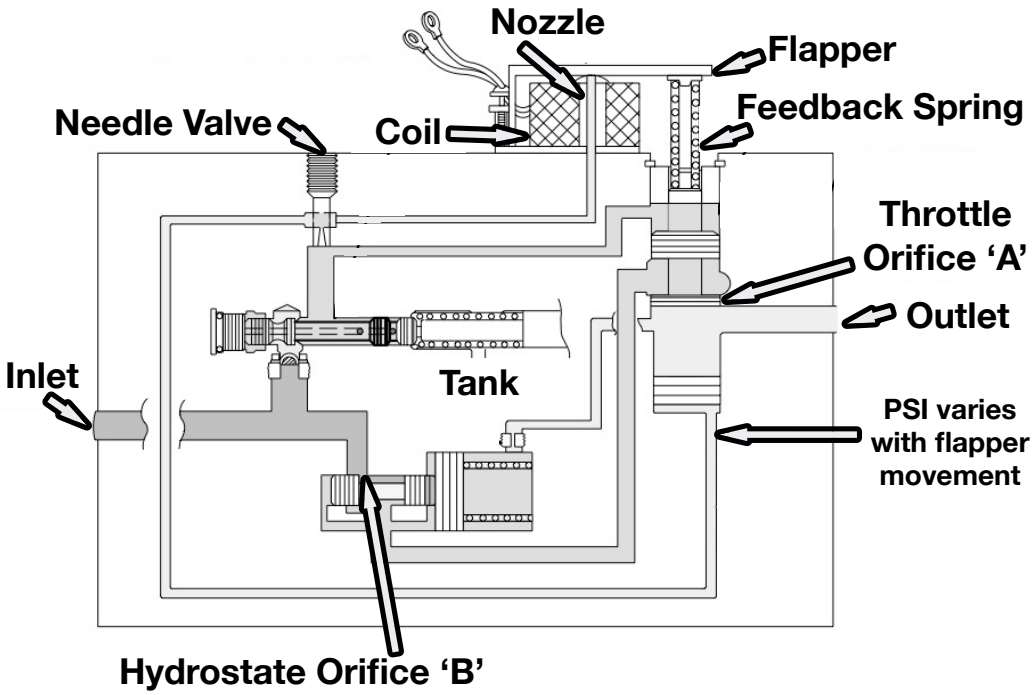

Figure 2.7: Flow control valve operation diagram.

Consider the Fig. 2.7, the flapper - nozzle assembly is an electrically controlled unit. It consists of a square piece referred to as flapper, set in close proximity to the nozzle, which senses the pressure at the outlet. The opening of the nozzle can be adjusted by applying current to the coil, which creates a magnetic field attracting the flapper and partially chocking the nozzle. This leads to pressure buildup under the throttle spool resulting in the spool pushing up. The spool is connected to the flapper via a feedback spring. In response to spool moving up, the spring pushes the flapper away from the nozzle relieving the pressure. Once the forces on either side of the throttle spool are at equilibrium, the flapper will stay to maintain the throttle setting. This sets the flow rate at the outlet, deciding how much flow goes to the motor and remaining goes to the reservoir.

Once the flow rate is set, a compensator circuit is introduced. This ensures that the pressure drop between the inlet and the outlet is kept same, In case the load changes, the control hydro-stat controls the orifice to maintain the pressure drop. This way the flow control valve maintains the desired oil flow rate and the rotor can operate at a desired rotational speed.

2.2.5 Hydraulic Oil

Choice of hydraulic fluid has a direct impact on the efficiency and service life of the equipment. Since the viscosity of the oil changes with operating temperature, a suitable viscosity grade oil is required. The viscous behavior of the oil changes from the cold start to continuous operation at hotter temperatures. There are some

limits that need to be observed to ensure efficient and safe operation of the system, Typically the recommended fluid is a mineral oil, though other fluids could also be used.

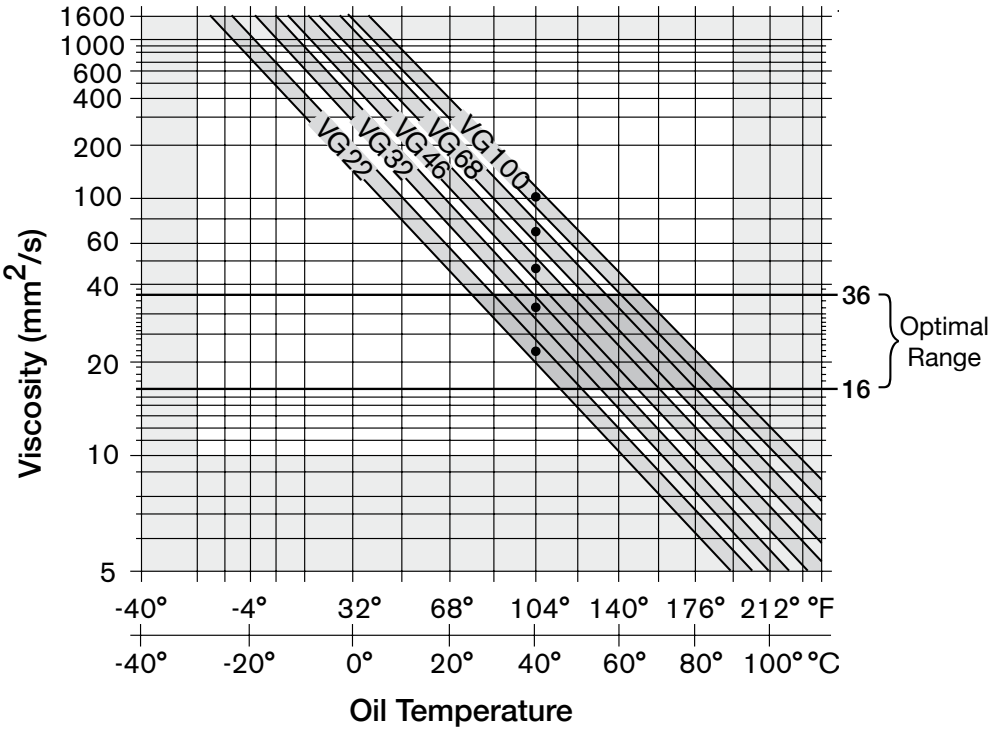

Figure 2.8: Viscosity - temperature characteristics of hydraulic oil.

It is recommended that oil steady state temperature must not exceed 90 degree Celsius under any load condition and the oil viscosity at peak temperature must not fall below 16 mm^2/s (Fig. 2.8) [192]. Depending on the application, a number of viscosity grade oils are commercially available to choose from. For current application, Mobil DTE-24 oil is used, It is a 32 grade oil which means the oil temperature is to be constantly monitored to not let it rise above 55 degree Celsius. Above this temperature, the oil viscosity for this particular grade oil falls below the lower limit. This grade is suitable in colder test environments. During hotter climates,

DTE-26 [195] is recommended as the system runs at higher temperature in general and can be operated up to an oil temperature of 75 degree Celsius. In general, a higher viscosity oil is preferable as all the hydraulic components depend on a thin layer of oil to lubricate the moving parts and a higher viscosity oil offers a greater temperature operation range.

2.2.6 Oil Filtration System

Clean fluid is essential for functioning of the hydraulic system. Majority of operational problems and failures in the system are due to contamination of the fluid. There are four primary sources of fluid contamination [196]:

(a) Contaminated New Oil: Although utmost care is taken in refining and packaging oil, fluid travels in various lines and hoses picking up silica dirt and other items. Prominent contagions are metal shavings, rubber particles, sand, rust from containers, and other atmospheric dirts.

(b) Built-in Contamination: Any new or re-built hydraulic unit has contaminants like burrs, chips, flash, dirt, dust, fiber, sand, moisture, sealant, weld spatter, paint among other things. A high viscosity, high turbulence pressure fluid flush is recommended, even before the unit is installed. Further, a no or low load initial run with full filtration system in-loop is recommended as well.

(c) Ingressed Contamination: Immediate surroundings have large effect on the kind of contaminants. The most common points of ingress are reservoir ports, seals, mating joints, system access ports and panels, or during maintenance

and transport of mobile units. Lint free rags and absorbent material in socks mist be used to clean and maintain the equipment. Also, care must be taken to keep the operational environment clean and dust free.

(d) Generated Contamination: In general operation all components generate a small amount of particles, due to nominal wear and tear. The contamination are produced due to abrasive wear between moving surfaces, adhesive wear due to loss of oil film leading to metal on metal contact, fatigue wear, erosion wear, cavitation wear due to constrained inlets, aeration wear due to air bubbles in the unit and corrosive wear. The best way to prevent a buildup of contamination is to start with a fully flushed clean system and keep the system fluid clean.

An inadequate filtration would lead to system damage or degradation. The damage can range from intermittent, unpredictable performance to degraded performance creeping onto catastrophic failure. A gradual buildup of erosion or wear can cause increased leakages, loss of efficiency and eventually catastrophic failure. Typically the hydraulic systems have very tight tolerances up to 5 micron for high pressure systems and up to 20 micron for low pressure system. These clearances dictate the size of filter elements required to clean the fluid. Surfaces within the components are designed to operate with a thin layer of oil, whose thickness changes with temperature and viscosity. Presence of contaminants can bridge these clearances and cause excessive wear, producing more particles. An excessive build up in the pump and the motor can lead to seizure of the unit as well. The contaminants

can also block the orifices and control nozzles in the flow control valves leading to intermittent and eventually complete failure of the flow control.

Moog A31255 High Pressure Filter

Vickers 941107 Low Pressure Filter

Figure 2.9: Oil filter installed in the hydraulic circuit.

In the current application (Fig. 2.9), a high pressure 25 micron size filter (Moog A31255, 3000 psi filter) is used with fiber glass filter elements at the inlet to the flow control valve. Also a low pressure 10 micron cellulose filter element (Vickers 941107, 150 psi, spin on filter) is installed on the return line before the fluid enters the reservoir.

2.2.7 Oil Cooling System

Water-type oil cooler (Fig. 2.10) [197] is used for the current system. It has a fixed tube bundle construction with an internal multiple fin arrangement. Hydraulic

fluid circulates through the cooler and around copper tubes containing the water. The water carries the heat away from the hydraulic fluid and can be regulated thermostatically to maintain a desired temperature. In addition, a large air circulator is also used to cool the oil in the reservoir.

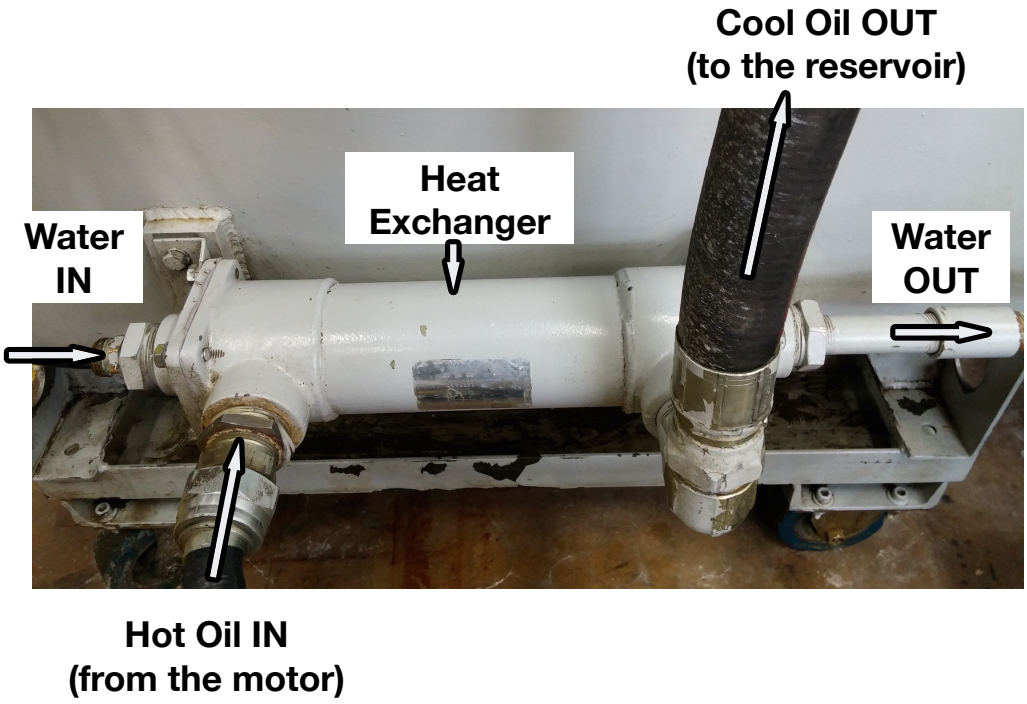

Figure 2.10: Water based heat exchanger for oil cooling.

2.2.8 Direction Control Valve with Relief Valve

The solenoid operated directional control valves [198,199] are used for directing and stopping flow at any point in a hydraulic system. Pressure relief valves mount between the pump and valve system to protect against overloads. These units allow for safe startup of the hydraulic system at low pressure.

2.2.9 Hydraulic Hoses

The hoses need to be MIL-DTL-8795G compliant, must be able to operate at a nominal pressure of 3000 psi and have burst pressure of at-least twice that pressure. They are rated for the required flow rate, operating pressure and temperature.

2.2.10 Electric Motor

The hydraulic pump is run by Baldor manufactured CM4316T motor [200], rated at 75 HP at 1775 RPM. It is a constant speed, three phase squirrel cage type AC induction motor. The induction motor has two main parts, a stator and a rotor sitting inside the stator with a few millimeter air gap (Fig. 2.11). The stator is made by stacking thin-slotted highly permeable steel laminations inside a steel or cast iron frame. Winding passes through slots of the stator. The rotor is shaped like a squirrel cage, horizontal bars shorted by end rings.The bars of a squirrel cage are inclined or skewed to the axis of rotation. This is to prevent torque fluctuation. To aid such electromagnetic induction, insulated iron core lamina are packed inside the rotor.

When a three phase AC current passes through the stator windings, it produces a rotating magnetic field which induces EMF in the rotor. This EMF produce a current through the rotor and this current carrying conductor in magnetic field experiences force, producing torque. That's why the name induction motor is used, electricity is induced in rotor by magnetic induction rather than direct electric connection.

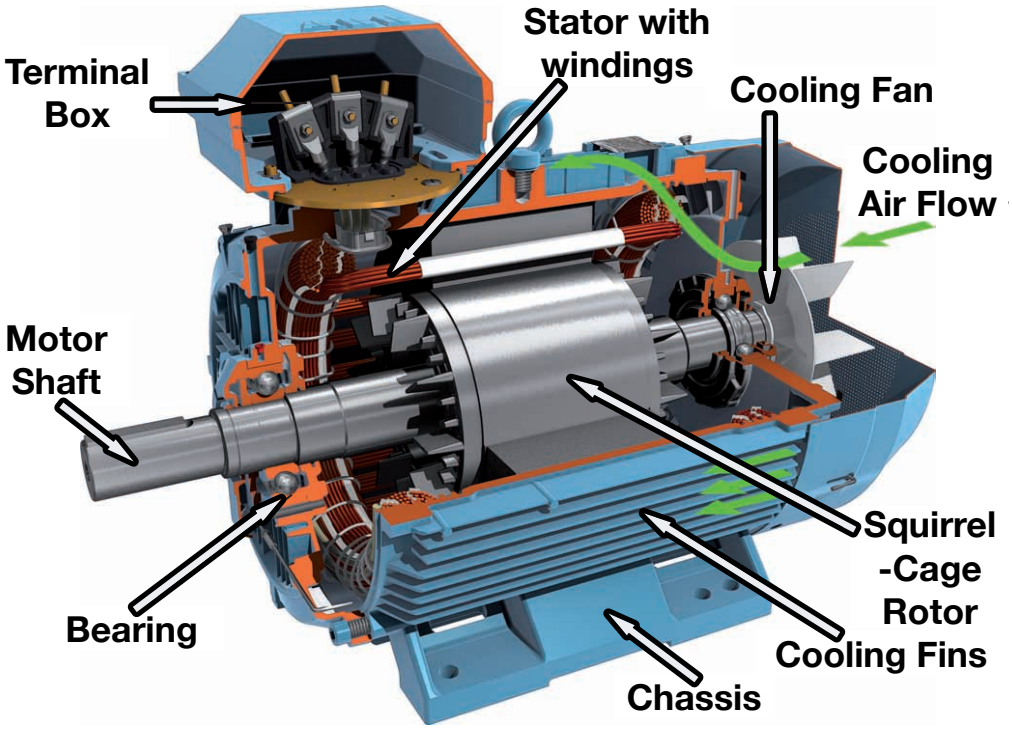

Figure 2.11: AC Induction squirrel-cage motor - cutaway.

The rotor will never be able to catch up with the speed of the magnetic field. It rotates at a specific speed which is slightly less than AC frequency. Various losses associated with these motors are friction loss, copper loss, eddy current and hysteresis loss. Such energy loss during the motor operation is dissipated as heat, so a fan at the other end helps in cooling down the motor. The rotational mechanical power obtained from the rotor is transferred through a power shaft to the hydraulic pump, which provides hydraulic oil to motor at pressure, meeting rotor torque requirements.

2.2.11 Electric Power Panel

The electric power panel houses AC motor starter. It is intended to start and accelerate motors to normal speed, to ensure continuous operation of motors, to switch off the supply from the motor and to provide means for the protection of motors and associated circuits against operating overloads.

It also houses the soft-starter circuit for the motor (Fig. 2.12). The soft starter temporarily reduces the load and torque in the power train and electrical current surge of the motor during start-up. This reduces the mechanical stress on the motor and shaft, as well as the electrodynamic stresses on the attached power cables and electrical distribution network, extending the lifespan of the system.

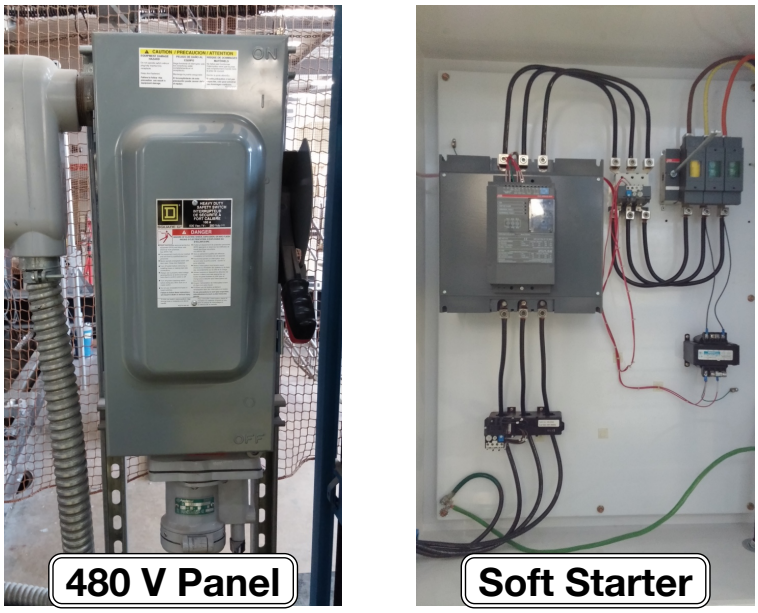

Figure 2.12: Electric power panel and soft starter for hydraulic system.

The complete rotor drive system components and their operation is summarized in the Fig. 2.13.

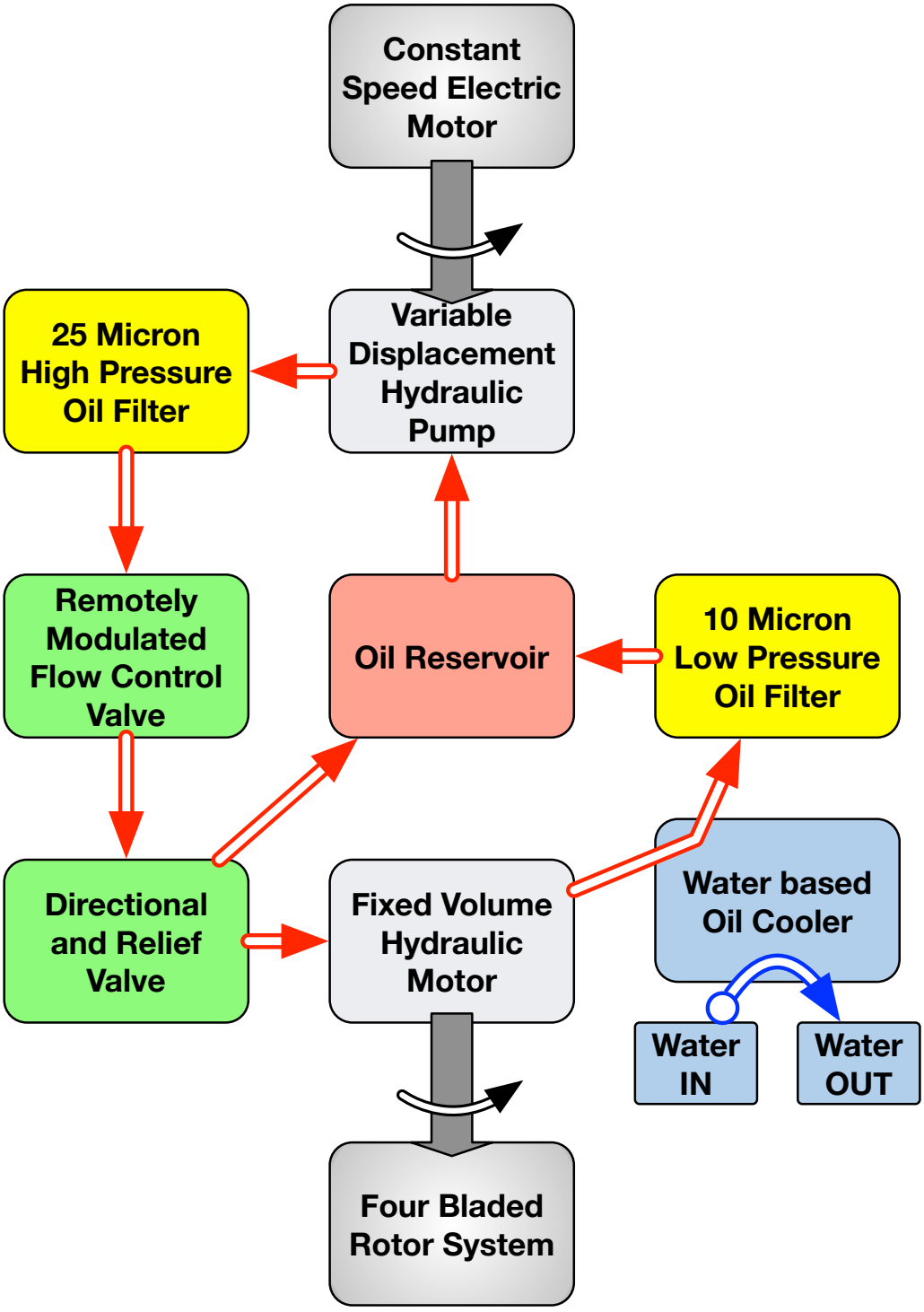

Figure 2.13: Hydraulic system layout.

2.3 Rotor Hub

The rotor test stand at the Alfred Gessow Rotor Center can provide support platform for Mach-scale testing of both bearingless hub and articulated hub with either two or four blades. For the current research, a four bladed articulated rotor hub was used (Fig. 2.14). A 2:1 reduction belt and pulley arrangement is incorporated to transfer torque from the hydraulic motor spindle to the main rotor shaft.

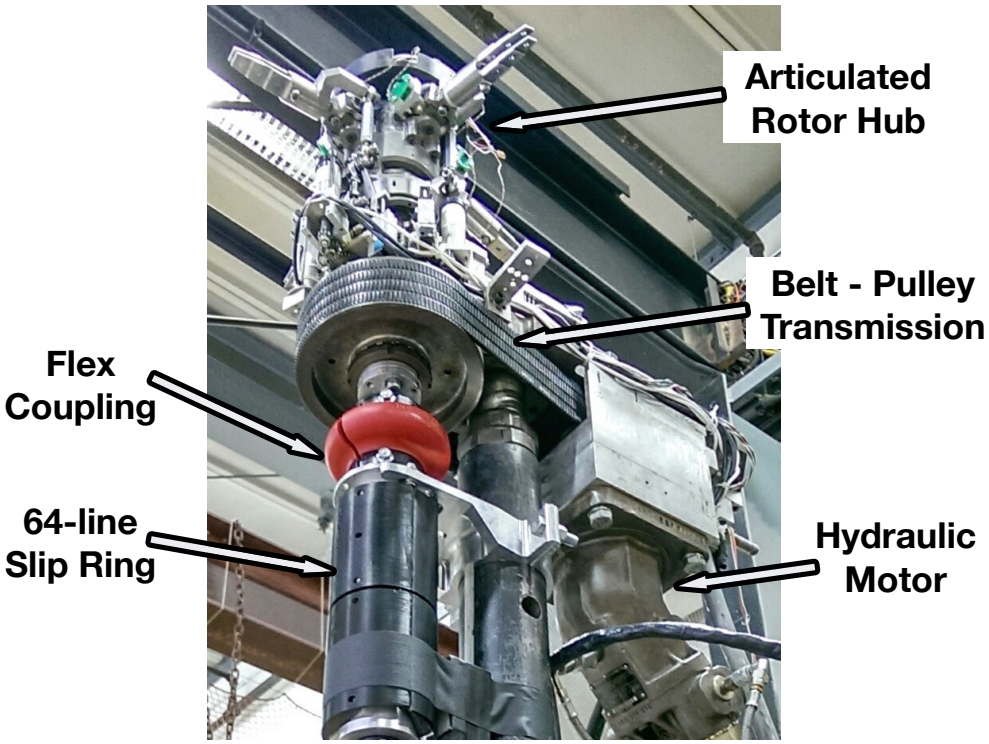

Figure 2.14: Rotor test stand at University of Maryland.

The rotor hub supports four articulated blade grips held between a set of plates. The swashplate is connected to pitch horns on the blade grips by pitch links. The rotor drive shaft has a through bore to accommodate slip ring wires. Figures 2.15 and 2.16 shows two different views of the assembled articulated hub. Figures 2.17, 2.18, and 2.19 show some of sub-assemblies of the rotor hub.

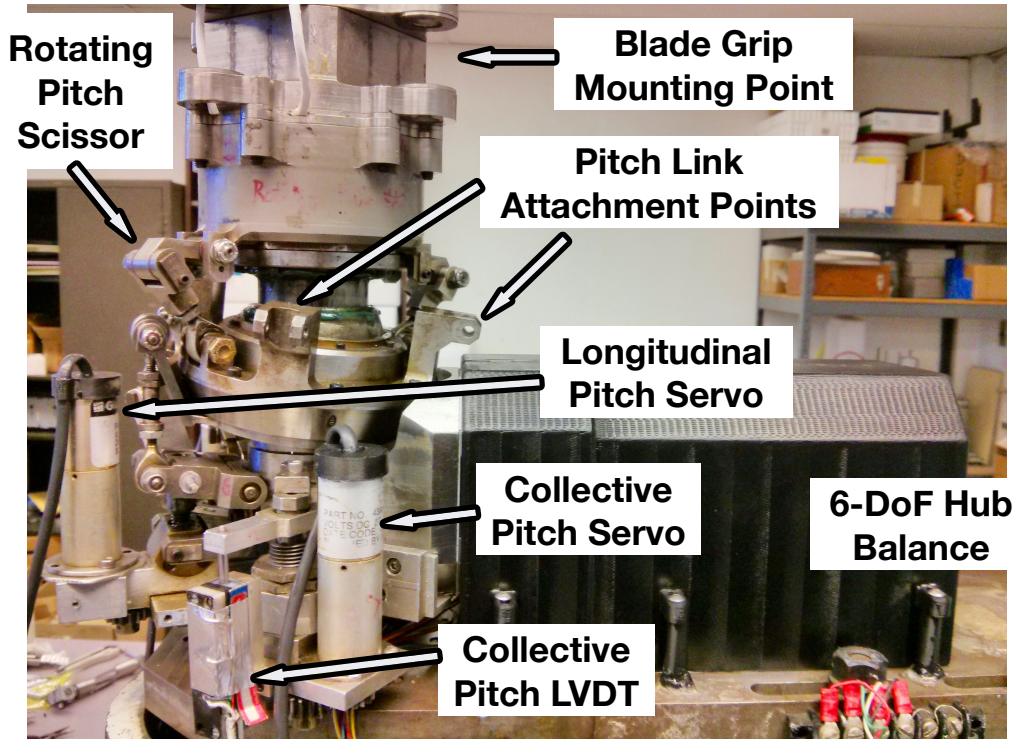

Figure 2.15: Rotor hub assembly - side view.

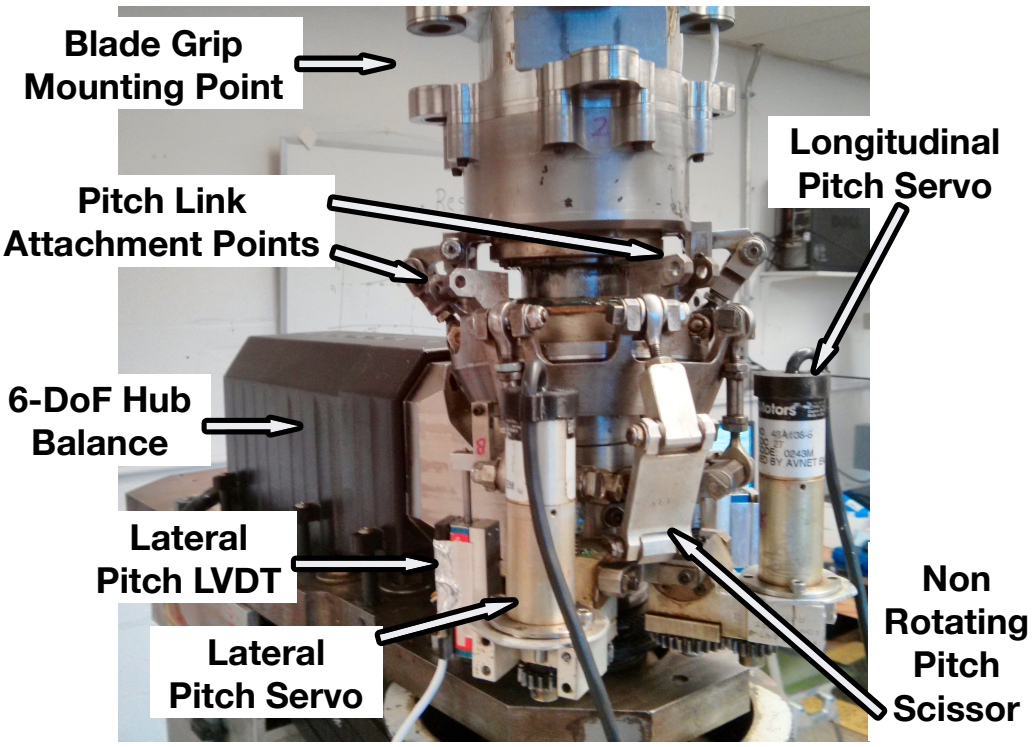

Figure 2.16: Rotor hub assembly - isometric view.

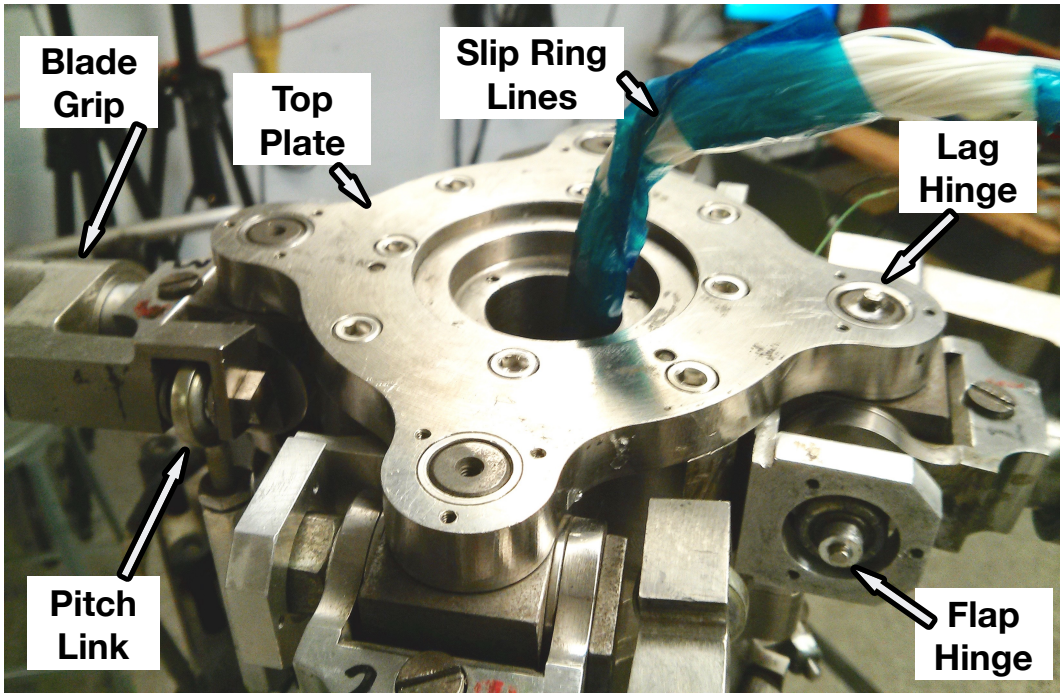

Figure 2.17: Top retaining plate on the hub.

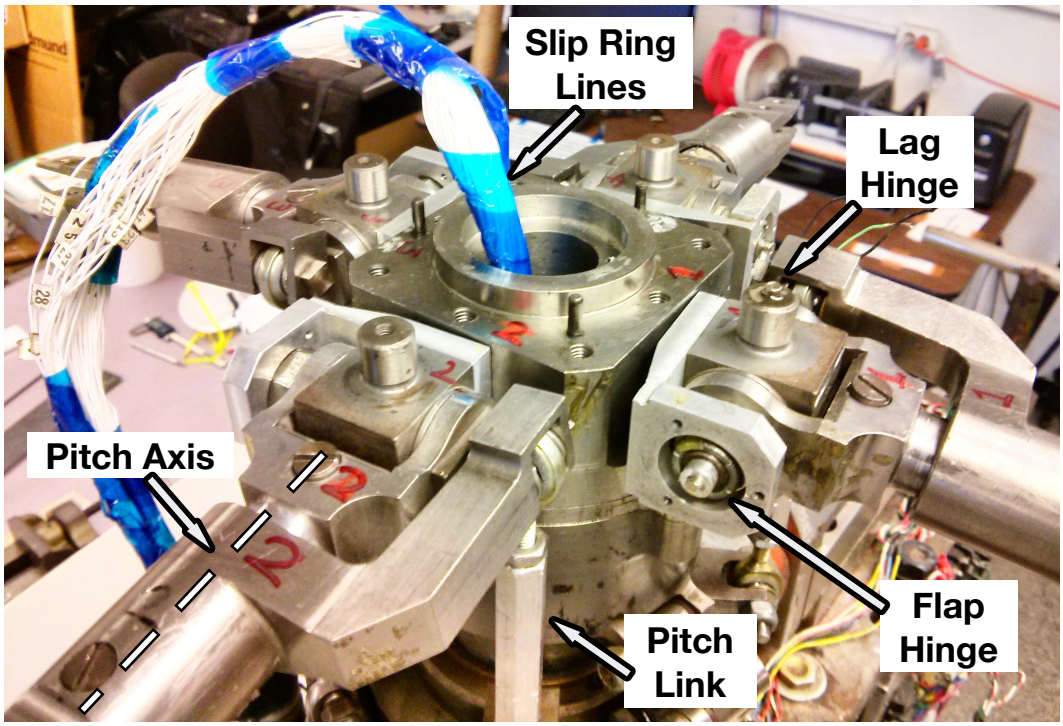

Figure 2.18: Various degree of freedom of an articulated hub.

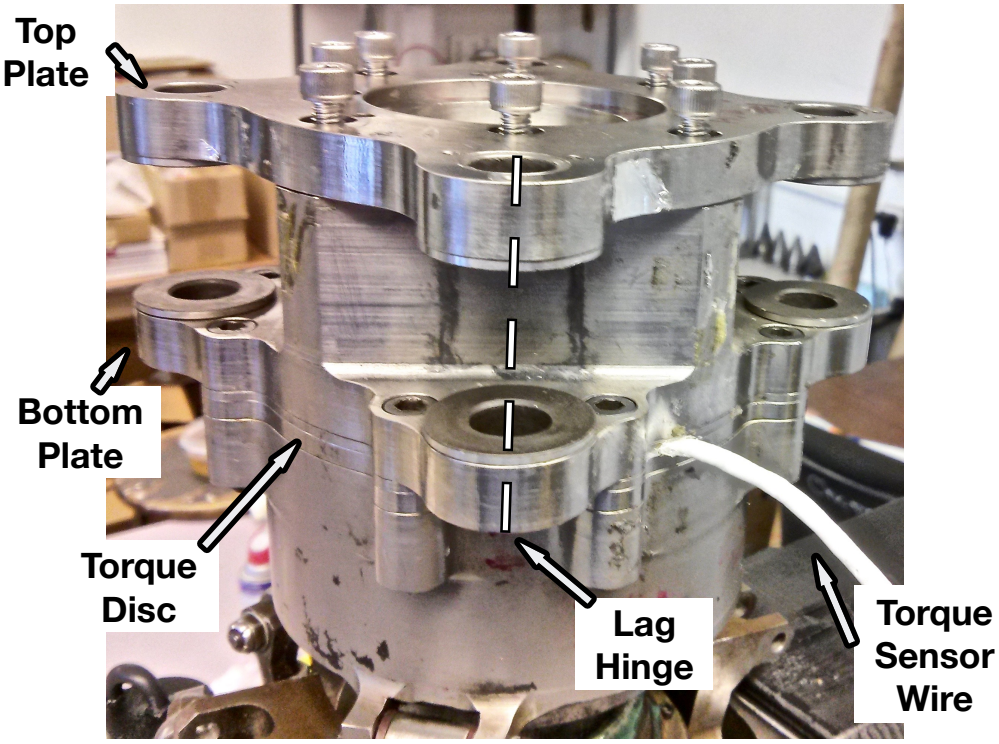

Figure 2.19: Rotor hub with blade grips.

The rotor hub is mounted on a six component strain gage based balance and is driven by the hydraulic motor via a belt-pulley arrangement. The details of the hub mounting are shown in Figs. 2.20 and 2.21.

Major components of the articulated rotor hub are explained next.

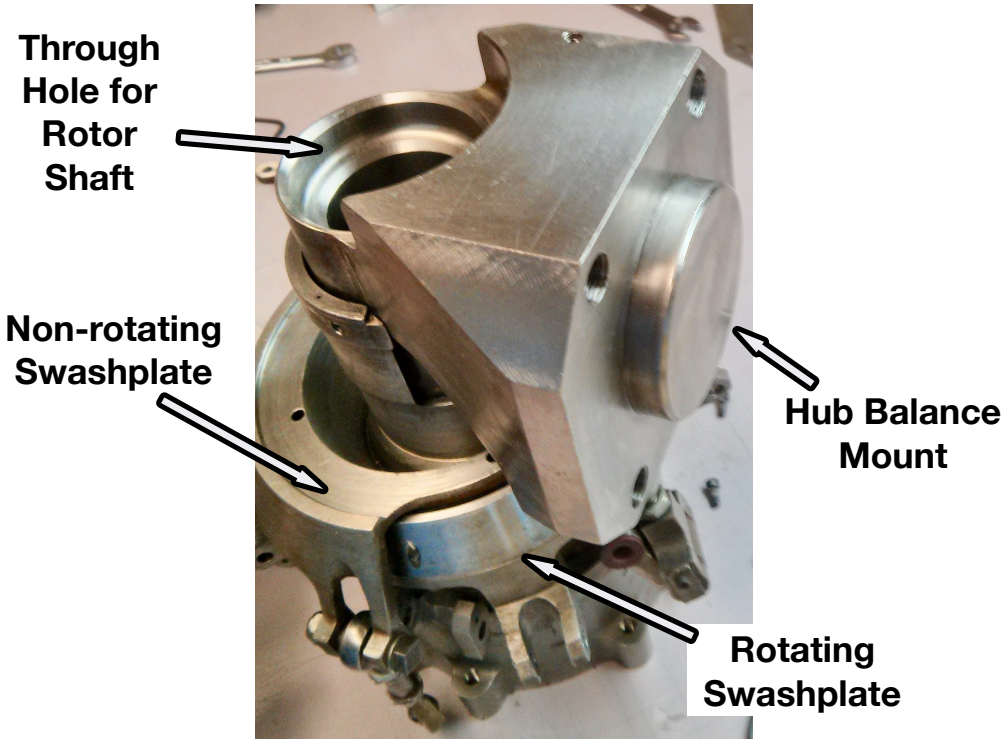

Figure 2.20: Rotor hub (upside down view).

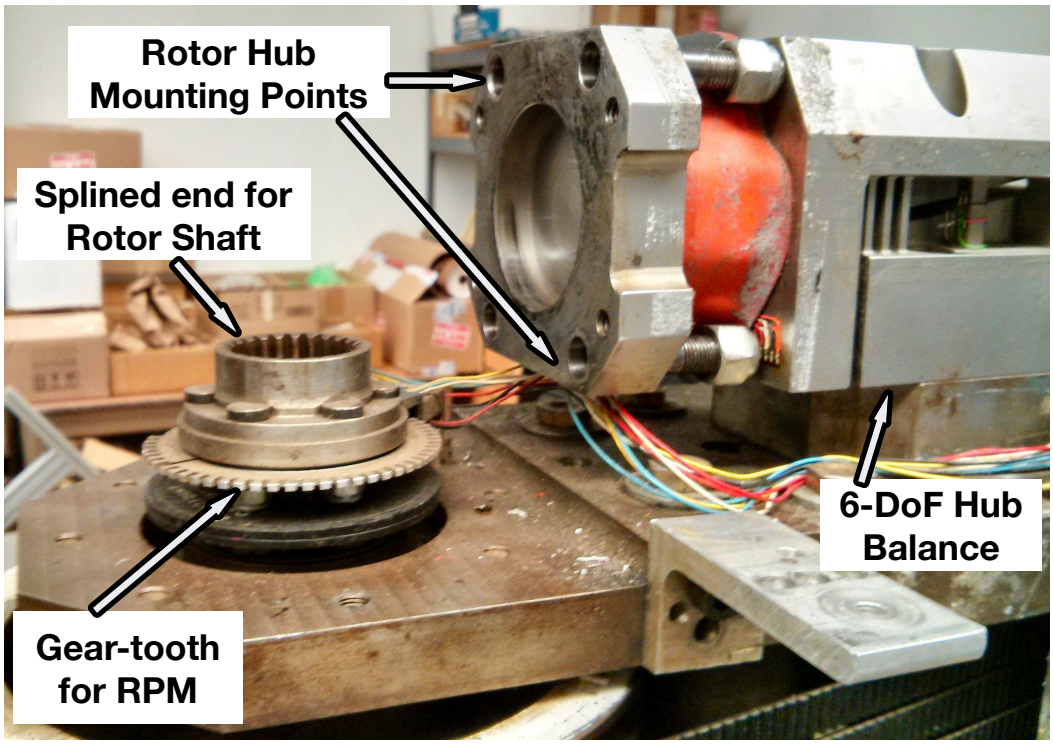

Figure 2.21: Hub mounting location.

2.3.1 Swashplate Assembly

The swashplate allows to control the blade pitch thus controlling the rotor thrust as well as rotor disc orientation in pitch and roll.

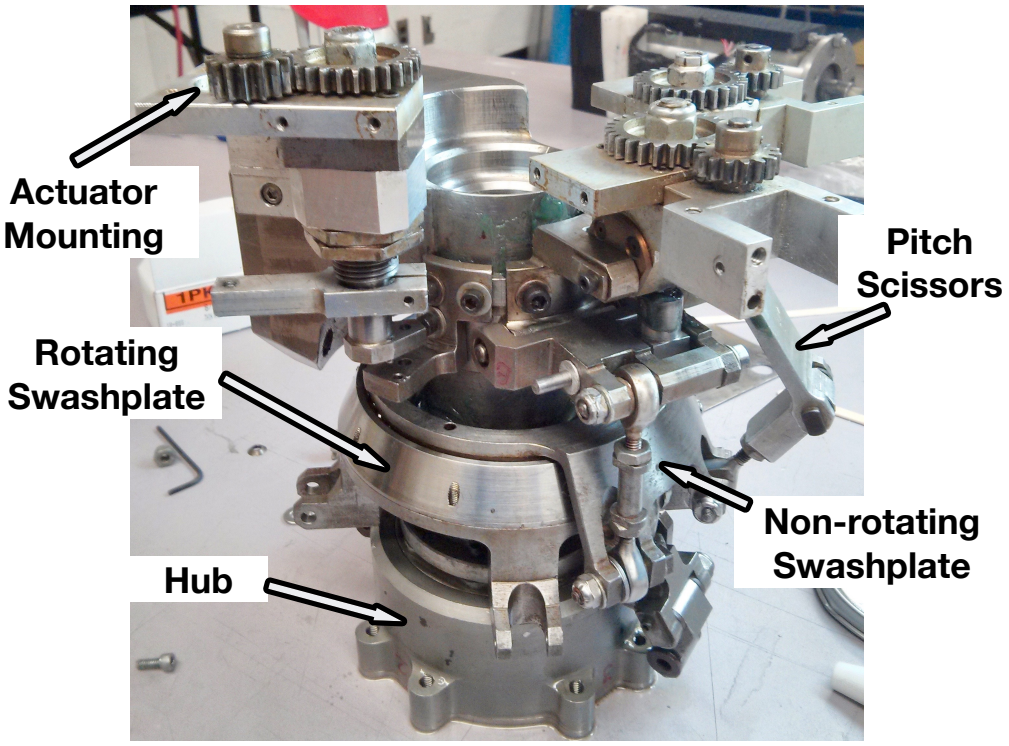

Figure 2.22: Rotor swashplate assembly.

The swashplate consists of two main parts: a non-rotating (lower) swashplate and a rotating (upper) swashplate (Fig. 2.22). The lower swashplate doesn't rotate and is connected to the pitch servos. It is mounted on a spherical bearing to allow change in orientation and pitch scissors allow to orient the plate.

To control the collective pitch of the rotor blades, the entire swashplate is moved up or down along its axis without changing the planer orientation of the plate. Thus, the entire swashplate is moved along the main shaft by a collective pitch actuator. To control the blade cyclic pitch, the planer orientation of the plate

is changed. Two pitch actuators separated by 90 degree azimuthally provide the lateral and longitudinal tilt of the plate.

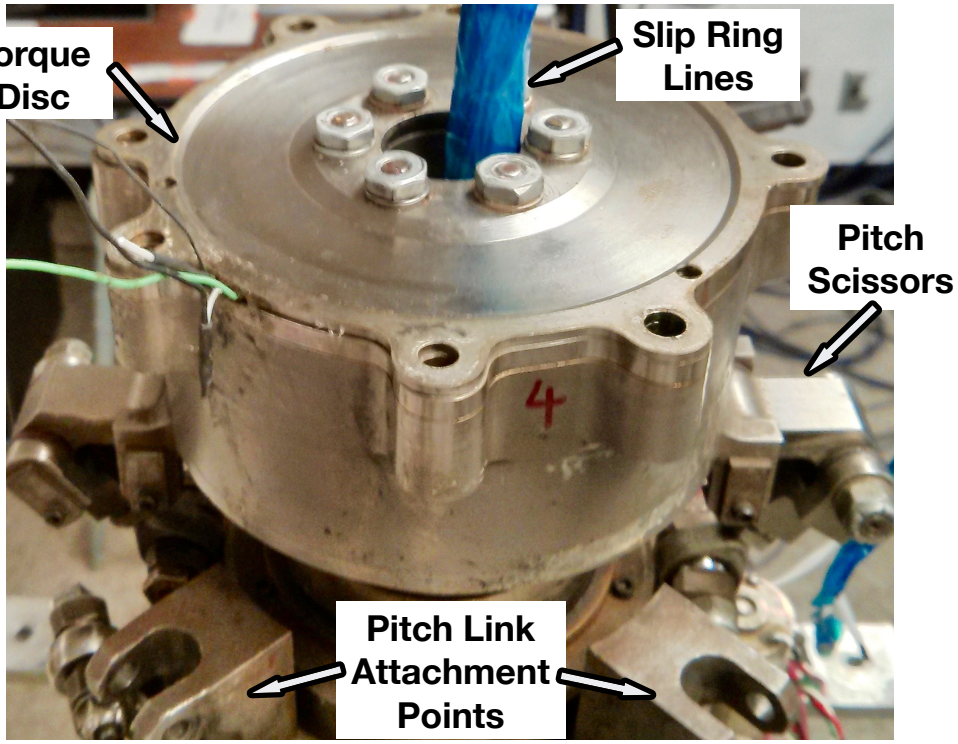

Figure 2.23: Rotor drive shaft installed in the hub.

Ball bearings between the upper and lower swashplate allows the upper plate to spin freely on top of the lower plate. The pitch inputs to the lower swashplate are then transferred to the upper swashplate and thus, both swashplate orient as one unit. The upper swashplate connects to the rotor shaft via a torque disc, which may be instrumented for torque measurement (Fig. 2.23). As the rotor shaft is driven, it also turns the upper swashplate and the rotor blade system. This system includes blade grips, which connect the blades to a hub. The rotating swashplate is connected to the pitch horns using the pitch links, which transfers the swashplate motion to the rotor blade pitch.

2.3.2 Swashplate Actuators

There are generally three fixed frame actuators, one each for collective, lateral and longitudinal pitch inputs. Since the bandwidth requirement for primary rotor control is relatively low, the choice of actuators can include using either an electric or a hydraulic actuator. Although, hydraulic actuators provide high torque, they can be bulky in size and are generally used for full-scale rotors. For the actuation power required at model scale rotor testing, invariably electric motors with high gear ratios are used. These motors are DC electric motors with a large gear ratio to reduce the output speed and augment the torque.

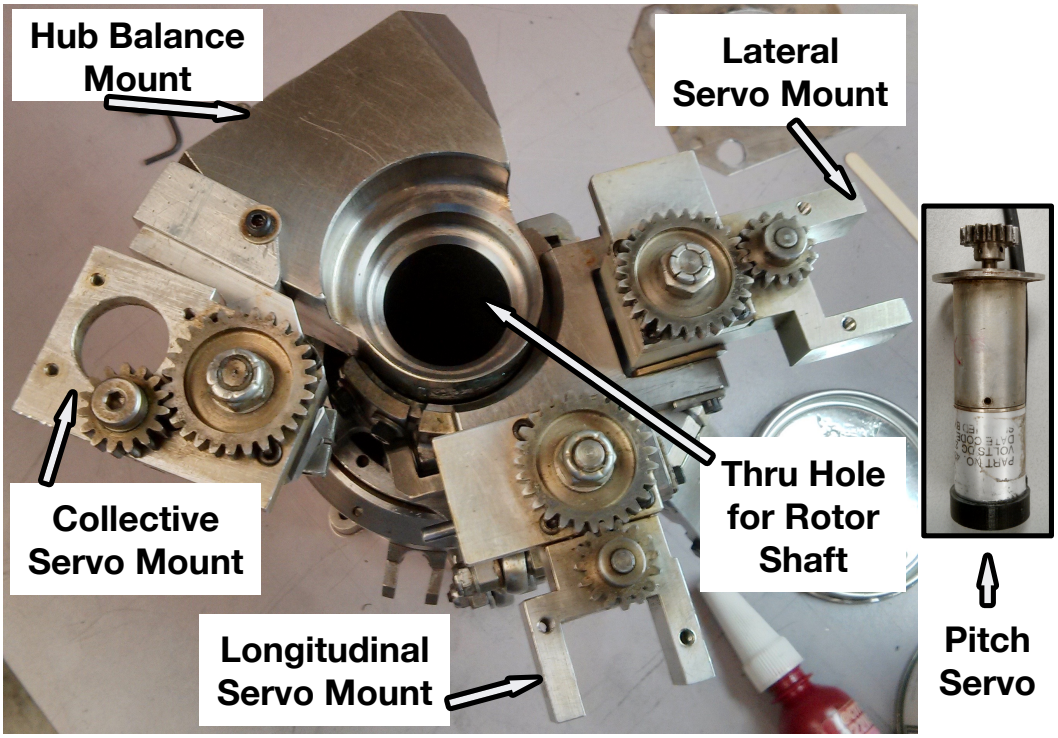

Figure 2.24: Swashplate actuators mountings.

Figure 2.24 shows the actuator mounting locations for the model scale rotor hub used at UMD. Globe motors manufactured (Model: 43A108-5) [201] high torque,

low bandwidth DC servomotors are used as actuators. These servos operate at 27 V DC, can provide a maximum output torque of 0.5 Nm (70 oz.-in.) and are controlled by the pitch controllers in the rotor control console (Sec. 2.5).

The swashplate actuators change the orientation of the rotor disc, by controlling blade flap response. For articulated rotor hub with small hinge offset, the phase delay between the pitch input and blade flap response in hover is about 90 degree. So, a pitch input given at zero rotor azimuth would cause the blade to flap around 90 degree azimuth. The collective servo actuates the swashplate vertically up and down, about the rotor shaft. The longitudinal servo is mounted at 180 degree azimuth location and it tilts the rotor hub back and front, controlling the longitudinal blade flap response. The lateral servo is mounted at 90 degree azimuth and tilts the hub side to side, controlling the lateral blade flap response.

2.3.3 Rotor Drive Shaft

The rotor drive shaft transfers the torque from the belt transmission to rotor. At the driven end, it has a splined geometry that allows to mate with the transmission pulley. This design allows to transfer torque at the same time allow unrestricted vertical motion of the shaft. The drive shaft is connected to the top of hub via a torque disc. It is a thin membrane shear plate that is instrumented for torque measurement. The shaft has through bore to pass the slip rings wires to the top of rotor hub.

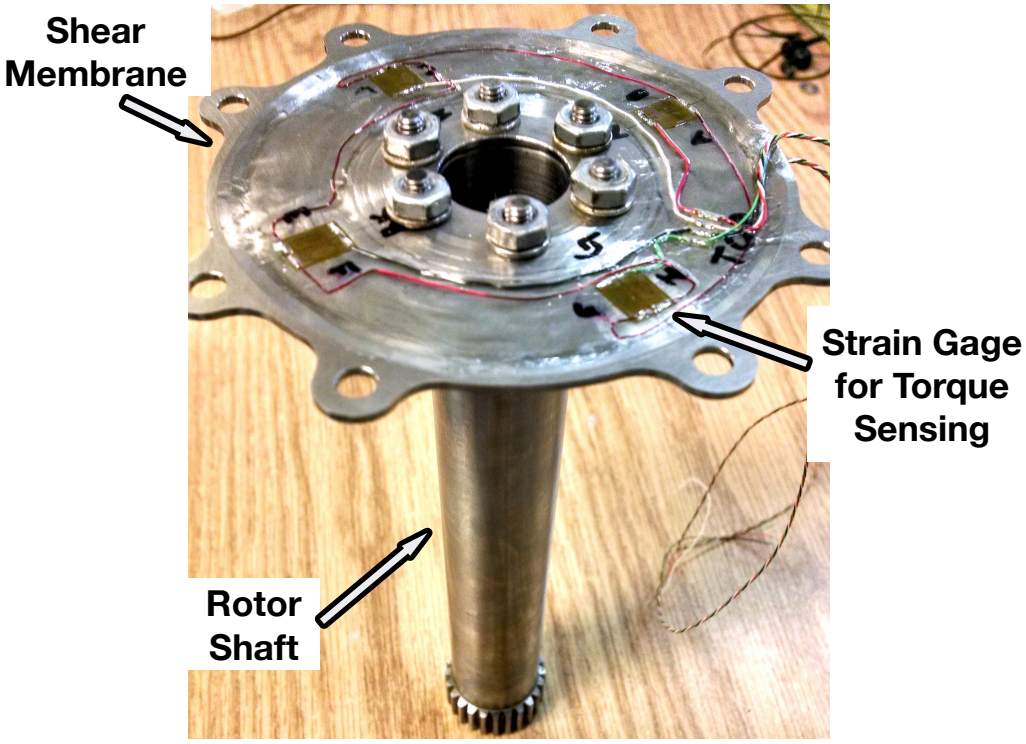

Figure 2.25: Rotor drive shaft.

2.3.4 Blade Grip Assembly

The articulated rotor blade grip holds the rotor blade and allows for flap, lag and torsion degrees of freedom at blade root. The various components of the blade grip are shown in Fig. 2.26.

The end block is held between the top and bottom retaining plates. The inner tube is connected to the outer tube via a tension-torsion strap which takes all the centrifugal loads on the blade while allowing smooth torsion motion. Set of radial bearings keep the two tubes aligned, negating any flat-wise bending in the tension-torsion strap and reduce any friction in the torsion motion. This blade grip ensures co-incident flap and lag hinges. Also, the pitch link attachment point of the pitch horn is coincident with flap hinge as well. Thus, there are no kinematic couplings

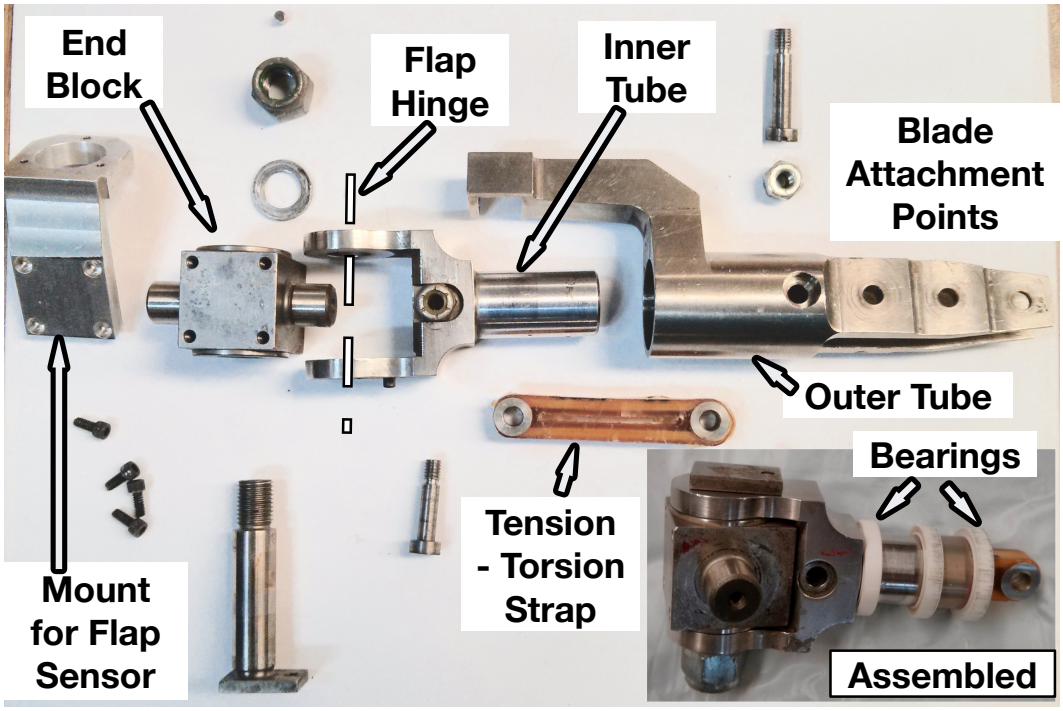

Figure 2.26: Components of an articulated rotor blade grip.

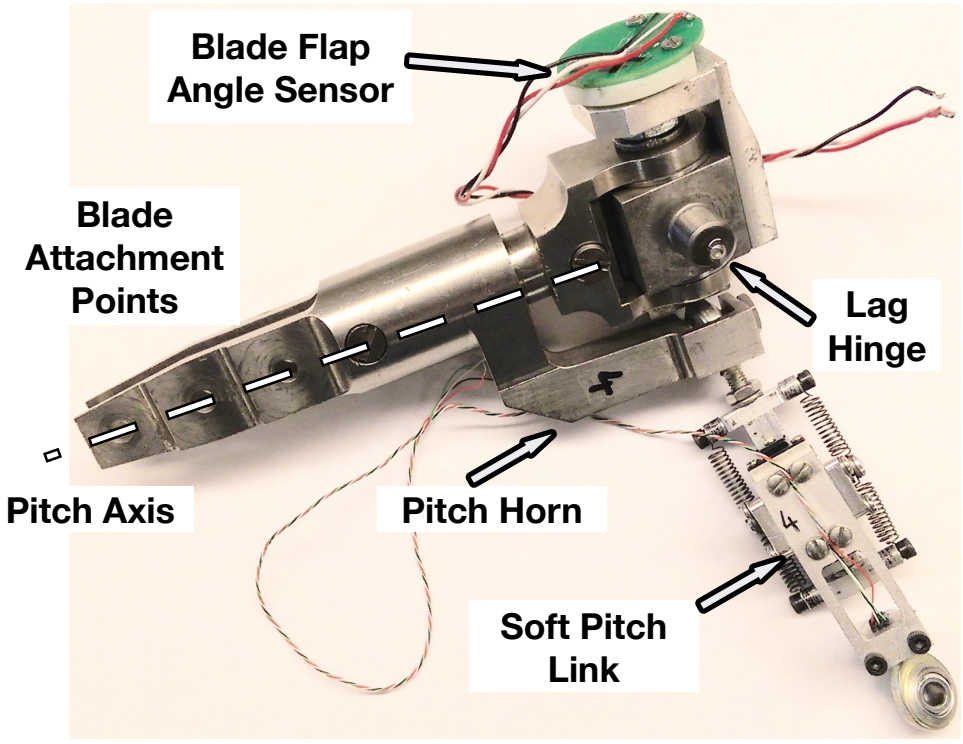

Figure 2.27: Assembled view of the blade grip.

in this hub design.

Figure 2.27 shows assembled blade grip with a Hall sensor mounted for flap angle measurement and a soft pitch link. Conventionally, a stiff pitch link as shown in Fig. 2.18 is used to connect the swashplate to the pitch horn.

2.3.5 Tension - Torsion Strap

The rotor system is designed with the use of a tension-torsion straps for blades retention. This strap needs to withstand tensile load due to centrifugal force and twisting due to blade pitch inputs. This requires that the tension-torsion strap must have a high ultimate tensile strength and a low torsion stiffness. Moreover, the component must not undergo plastic deformation under dynamic loading, and the tensile yield strength limits the maximum load on this component. This is one of the primary centrifugal load carrying structural component of the hub and thus limits the maximum blade weight that can be tested on the stand.

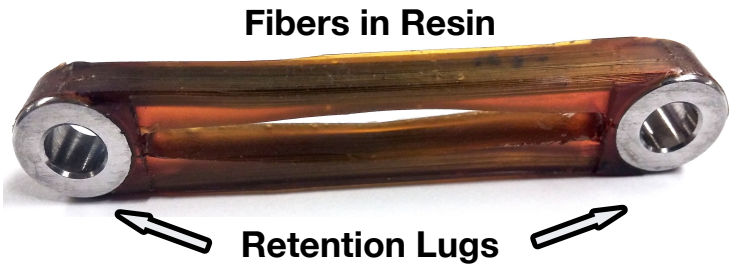

Figure 2.28: Tension - torsion strap.

The design of the tension-torsion (TT) strap is made up of two grooved bushings separated by a specific distance, winded with a stainless steel fiber and wrap with resin (Fig. 2.28).The resin protects the fiber and helps in uniformly distributing

the loads on the strap. The slot in the middle of the component allows a better twist motion when the strap receives a torsion load. These straps were designed to handle a maximum tensile load of 6672 N (1500 lbf) without plastic deformation, and to allow a 20 degree twist around their axis.

However, with the need for testing active rotor blades for primary rotor control and/or rotor vibration reduction, the blade weight has gone up. The presence of on-blade actuators and supporting structure can as much as double the blade weight, severely limiting the top rotational speed that these active blades could be operated. Consider the loads comparison presented in Table 2.1. The blade weight is assumed to double for an active blade compared to the original blades. Since most active components are located on the outboard radial location (to take advantage of higher dynamic pressure), the span-wise c.g. of the blade will also shift from 50% to 55% location. It can be seen that to operate the active rotor at the peak rotor speed (2400 RPM), there is a significant increase in the load on the tension-torsion strap. As such the current strap is not rated for higher loads. To account for these elevated load requirements, new straps were manufactured in house and tested under tensile load to certify for higher centrifugal loads.

2.3.5.1 Fabrication of Tension - Torsion Strap

The two main components of the tension-torsion strap are the fibers and the enclosing resin. The resin has two goals. The first one is to shield the fibers and prevent damage from air, dust, humidity and friction. The second goal is to make the

Table 2.1: Comparison of centrifugal load on tension-torsion strap.

Blade Parameter	Original Blade		Active Blades	
Mass, m	0.2 kg	0.44 lb	0.4 kg	0.88 lb
Radius, R	1.83 m	3.0 ft		
C.G. (%R)	0.5		0.55	
C.G., x	0.92 m	1.50 ft	1.02 m	1.65 ft
RPM, Ω	2400	251 rad/s		
Load, $mx\Omega^2$	5776 N	1300 lbf	12700 N	2855 lbf

strap stiffer for a compression load and to avoid flat-wise deformation. In addition, the resin has to be sufficiently flexible to allow the twist of the strap and sufficiently strong to resist damages.

The characteristic of the resin used in the original strap were given by Bendix company. This resin was a mix between a urethane elastomer named Adiprene L100 and a delayed- action diamine curative named Caytur 31 DA. After a number of iterations, the mix mass proportion was chosen to be 80% Adiprene L100 and 20% Caytur 31 DA. The mixing temperature was 65C and the cure temperature fixed at 120C during 2 hours.

Several fibers were also tested to find a stronger alternative than the stainless steel wires used in original strap. After testing several straps with three kinds of fibers (stainless steel, Spectra and Kevlar) and different numbers of winding turns, the chosen configuration was Kevlar fibers with 120 winding turns. The details of

resin preparation, fiber winding and curing are in Ref. [202]. Figure 2.29 shows the new strap manufactured using this process.

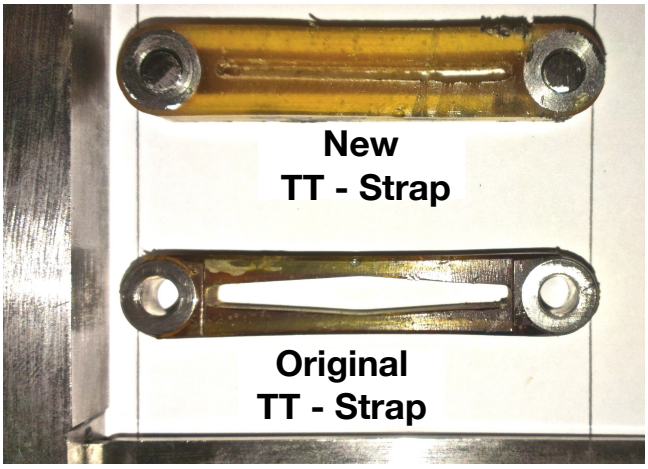

Figure 2.29: New tension - torsion strap.

2.3.5.2 Tensile Testing of Tension-Torsion Strap

Once the strap is fabricated to required geometric dimensions, tensile testing is performed to test the load bearing capabilities of the new tension-torsion strap. The behavior of the strap configuration has to be tested in the worst operating conditions, which is centrifugal loads while operating at a high twist angle. Therefore the tension tests were done on a MTS machine (Fig. 2.30) with a 20 degree pre-twist angle. The test showed a peak tensile load of around 14234 N (3200 lbf) and no plastic deformation. Moreover the repeatability was good as showed in the graph (Fig. 2.31) representing tension test on three samples . Dynamic loading testing was also carried out, with the samples loaded from zero to 6672 N (1500 lbf) tensile load in 30 seconds and then relaxed to zero load in 5 seconds. Three samples were tested with 20 degree pre-twist angle using this load profile. They operated satisfactorily

for in excess of 2000 load cycles.

A complete discussion of design, optimization and analysis of composite tension-torsion strap is included in Ref. [203].

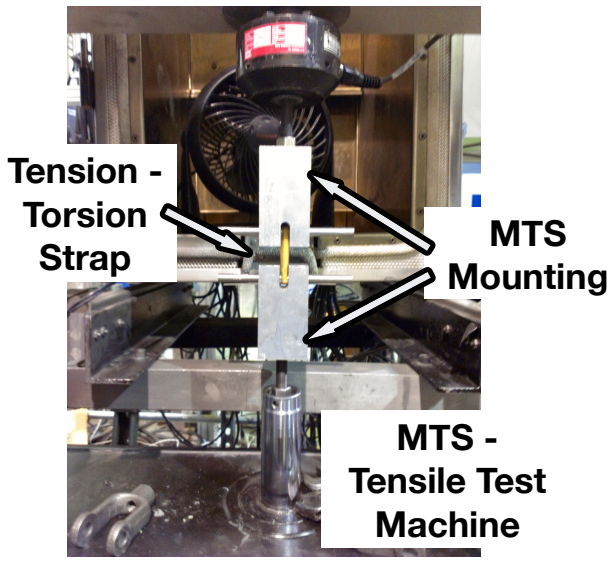

Figure 2.30: New tension - torsion strap being tested on MTS machine.

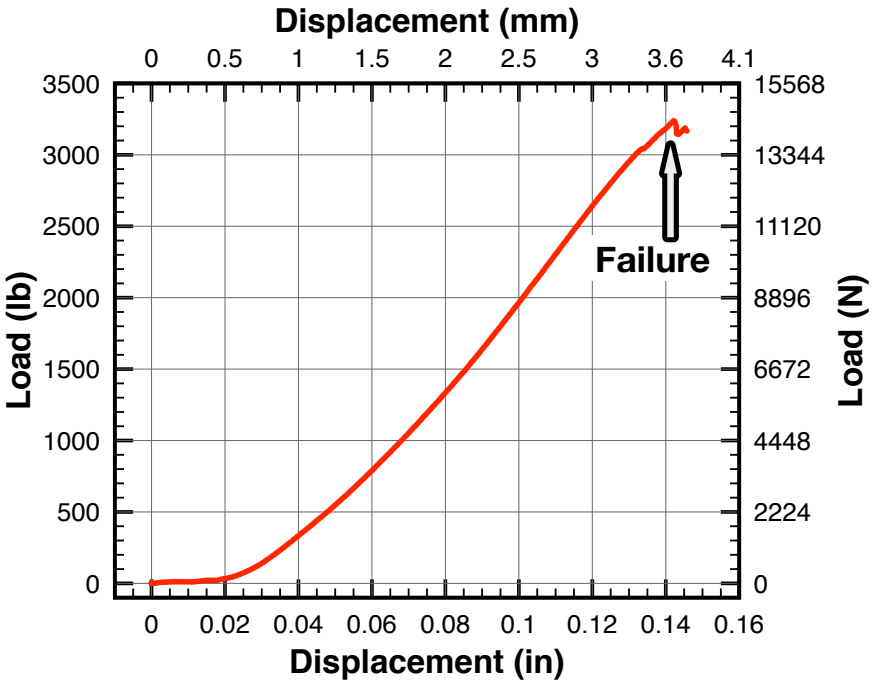

Figure 2.31: Tensile strength of new tension - torsion strap.

2.4 Rotor Test Stand Instrumentation

Various sensors are installed on the blades, hub and rotor shaft to monitor and record parameters during testing. Rotor speed, pitch setting and blade root motion are some of the prominent parameters to be recorded and are discussed next.

2.4.1 Rotor Speed Measurement

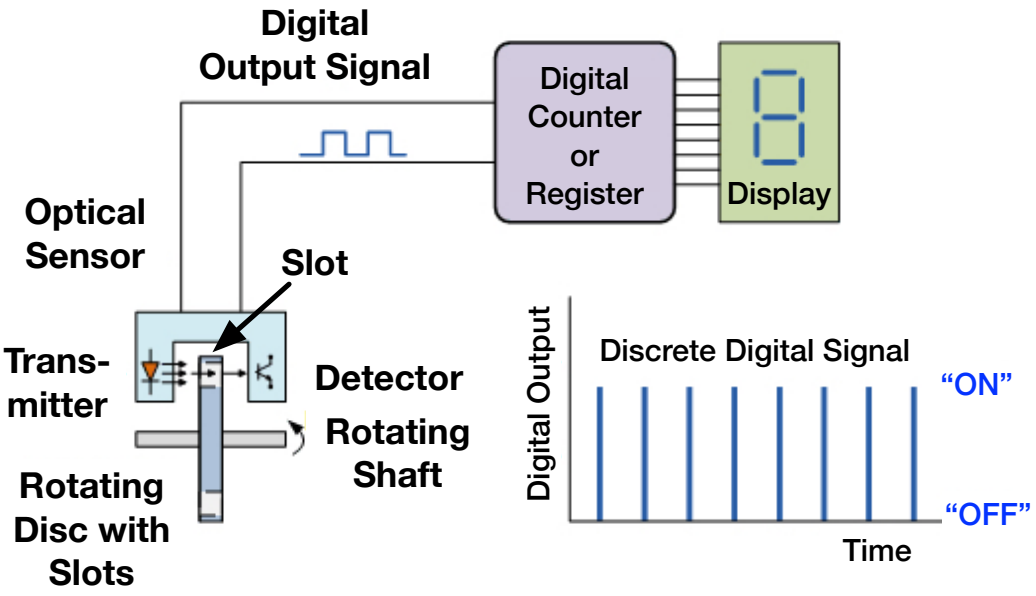

Figure 2.32: Optical sensor for RPM measurement.

Rotor speed measurement is one of the key parameter to be measured and monitored during rotor operation. A photodiode opto-isolator with a 60-tooth gear tooth wheel is used to measure the rotor speed. The optical sensor is a slotted design with light emitting diode on the top arm and a light receiver on the bottom. The photo-diode converts the input voltage into an infrared light and the photon

receiver in the bottom generates electric current on detecting the light (Fig. 2.32). A gear-tooth as shown in Fig. 2.33, is operating in the slot, leading to a switching output signal from the sensor, signaling ON when the gap is unobstructed and OFF when obstructed. A counter is used at the rotor control console to convert the switching signal into rotor RPM measurement. In addition to 60 shallow teeth (6 degree azimuth resolution), a single deep tooth is used to mark the zero azimuth position on the rotor, which is the reference blade (blade one) aligned with fuselage tail.

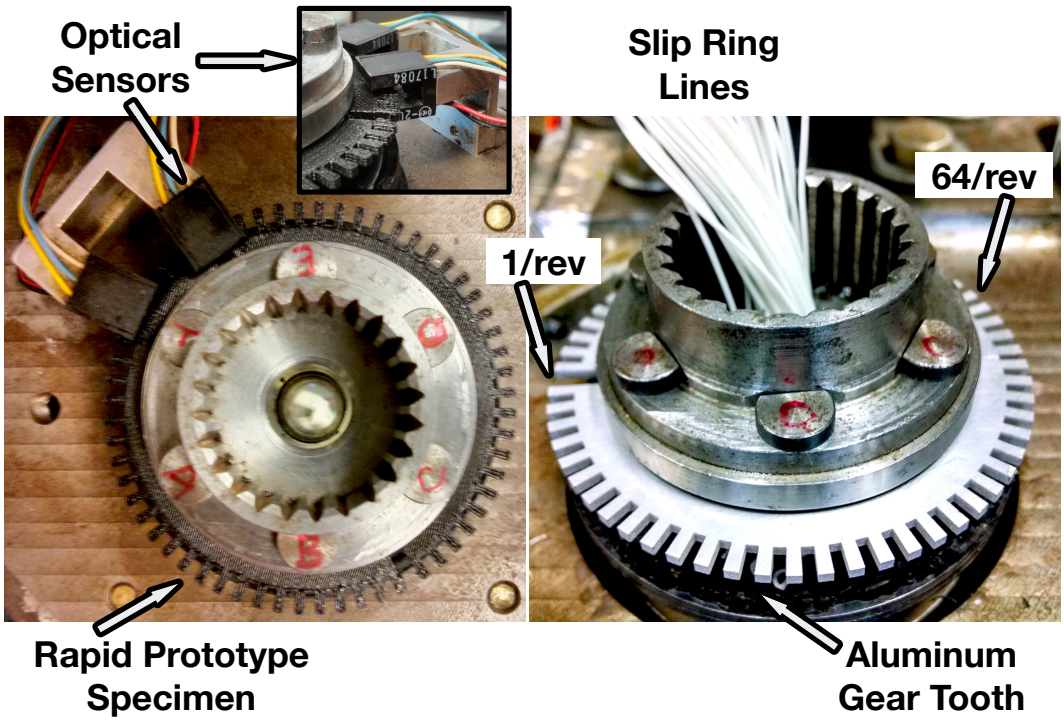

Figure 2.33: RPM measurement gear tooth.

2.4.2 Rotor Shaft Encoder

A Hall-effect based rotary position sensor is used to precisely measure the rotor azimuth. Melexis MLX90316 [204] is a non-contact rotary position integrated chip sensor capable of decoding the absolute rotary (angular) position from 0 to 360 degree. It has a 12-bit accuracy and produces a ratio-metric analog output corresponding to angular position of a diametrical polarized magnet. A ramp signal is produced and rotor azimuth location can be precisely recorded (Fig. 2.34). Table 2.2 shows the calibration co-efficients for the shaft encoder.

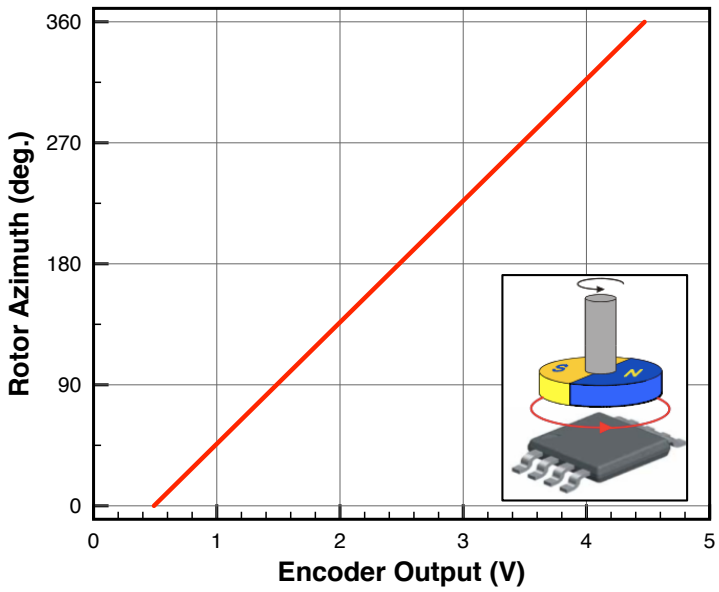

Figure 2.34: Hall-effect based rotary sensor used as a shaft encoder.

Table 2.2: Calibration co-efficients for rotor shaft encoder.

Azimuth (deg.)	Slope	Intercept	R^2 value
Shaft Encoder	90.393	-44.311	1

2.4.3 Blade Root Motion Measurement

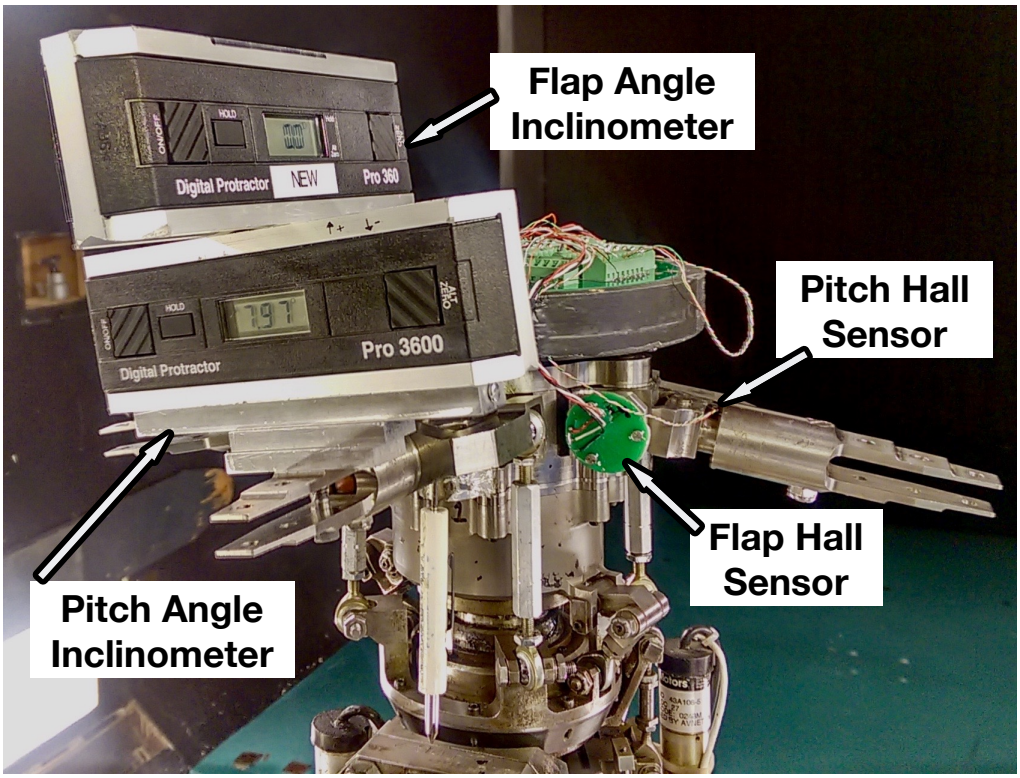

Figure 2.35: Setup for blade root flap and pitch calibration.

Table 2.3: Calibration co-efficients for blade root flap angle.

Flap Angle (deg.)	Slope	Intercept	R^2 value
Blade 1	-93.882	320.870	1.000
Blade 2	-91.488	240.977	0.999
Blade 3	-88.029	268.282	0.999
Blade 4	-93.164	323.275	1.000

Blade root motion measurement is critical to monitor blade root deflections on an articulated hub as well to measure trim of the rotor. The flap and lag hinges

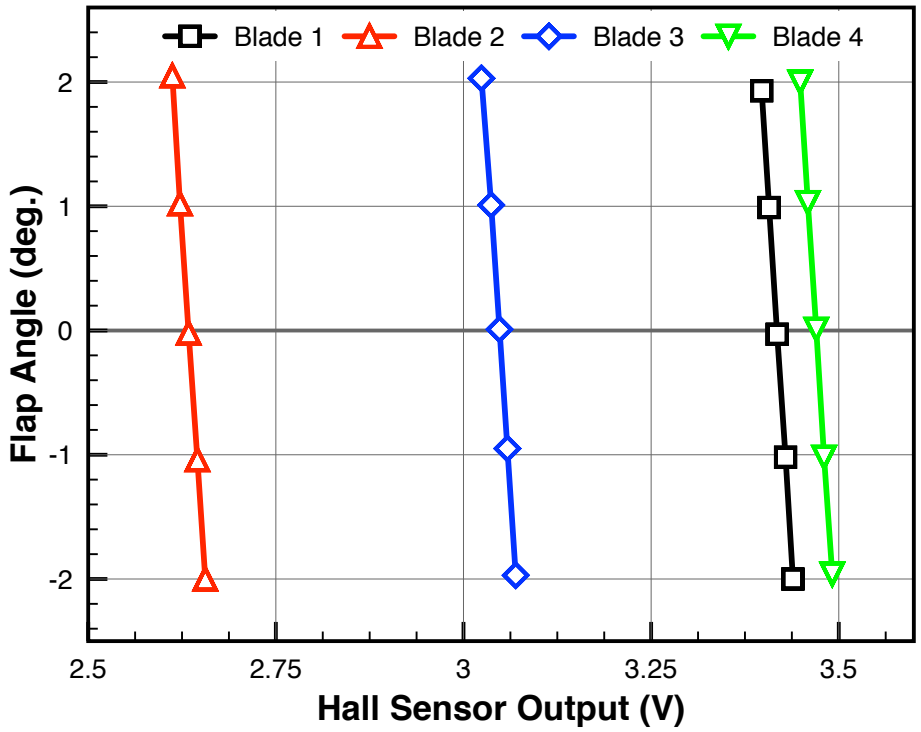

Figure 2.36: Blade root flap calibration.

on each of the four blades are instrumented with a rotary position sensor. These are the same sensors as used for shaft encoder and are described in the section 2.4.2. The blade root flap is calibrated by fixing the blade pitch to be zero and measuring blade flap for a range of flap positions. A gravity based inclinometer is used to directly measure the root flap angle. Figure 2.35 shows the setup for calibration using two orthogonal inclinometers. If there is any shaft tilt, it has to be included appropriately as well. Flap up is considered as positive flap direction. The total flap travel ranges from -10 deg. to +14 deg. but only a subset of the calibration is shown in Fig. 2.36. Each blade flap sensor is calibrated at zero blade pitch, zero blade lag and at zero azimuth location. Table 2.3 presents the calibration co-efficients for each blade root flap angle.

In addition to these sensors rotary potentiometers could also be used. The flap angle would then be calibrated against a voltage drop which changes with flap angle. However these sensors present friction due to physical contact and thus non-contact Hall-effect sensors are preferred.

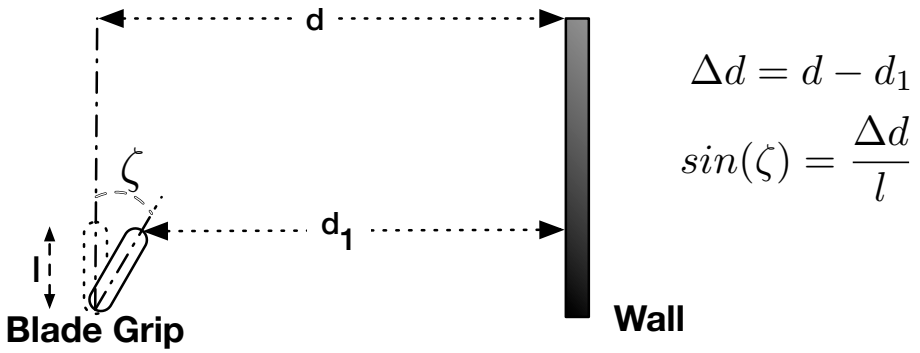

Figure 2.37: Setup for blade root lag calibration.

Blade root lag is an in-plane motion and calibration is more involved as no gravity sensor can be used. For calibrating the lag sensor, a vertical wall at a known distance is used as reference. The blade grip is moved from zero lag position to lead-most and then the lag-most position. The distance of the tip of the blade grip form the reference wall is noted. Using the geometrical relationship shown in Fig. 2.37, the lag angle is calculated. It is then plotted again the hall sensor voltage (Fig. 2.38) and calibration co-efficents are found using least-square linear fit. These co-efficients are in Table 2.4.

In addition, each of the blade attachments are instrumented using linear hall effect sensors (Allegro A1324LAU-T) [205] to measure the individual blade pitch as well. Blade pitch sensor is calibrated at zero lag and zero flap angle, using a gravity

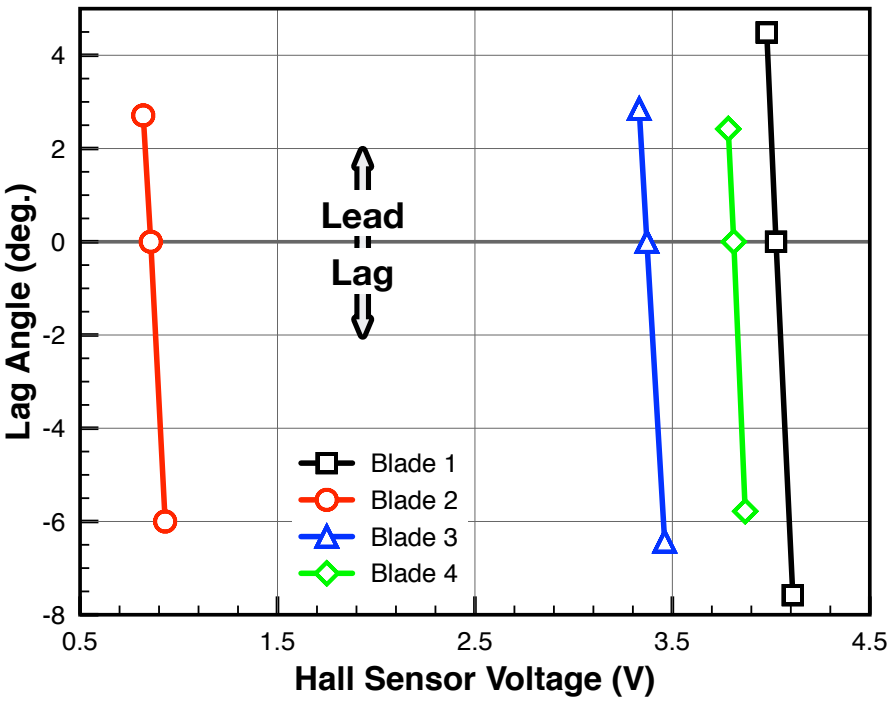

Figure 2.38: Blade root lag angle calibration.

Table 2.4: Calibration co-efficients for blade root lag angle.

Lag Angle (deg.)	Slope	Intercept	R^2 value
Blade 1	-91.16	367.06	1.00
Blade 2	-78.93	67.55	1.00
Blade 3	-71.84	242.20	1.00
Blade 4	-96.06	365.93	1.00

based inclinometer. The calibration setup is shown in Fig. 2.35 The total range of the pitch motion is from -10 degree to 20 degree but only a subset of the calibration is presented in Fig. 2.39. Since the pitch motion is rotational, the output from the linear hall sensor is not linear. A second order least square fit is used (Ax^2+Bx+C)

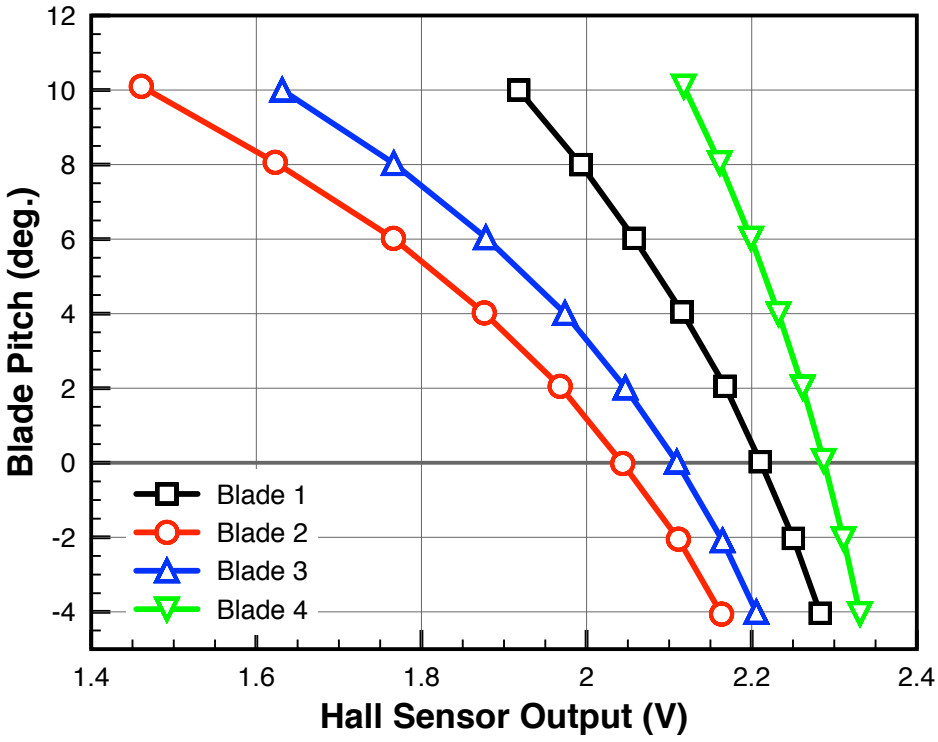

Figure 2.39: Blade root pitch angle calibration.

Table 2.5: Calibration co-efficients for blade root pitch angle.

Pitch Angle (deg.)	A	B	C	R^2 value
Blade 1	-49.031	168.341	-132.626	0.999
Blade 2	-18.071	46.007	-18.727	0.998
Blade 3	-27.497	81.896	-50.592	0.998
Blade 4	-132.540	542.421	-506.160	1.000

and Table 2.5 contains the calibration co-efficients for each blade root pitch motion.

2.4.4 Rotor Pitch Measurement

In addition to individual blade pitch sensors, pitch sensors are also mounted in the non-rotating frame. Each of the swashplate actuators are complimented with a Linear Variable Differential Transformer (LVDT). The LVDT consists of three solenoidal coils, the center primary coil is sandwiched between two secondary coils (Fig. 2.40). A ferromagnetic cylinder is axially located in the coils. The excited primary coil induces voltage on the secondary coils depending on the location of the ferromagnetic rod.

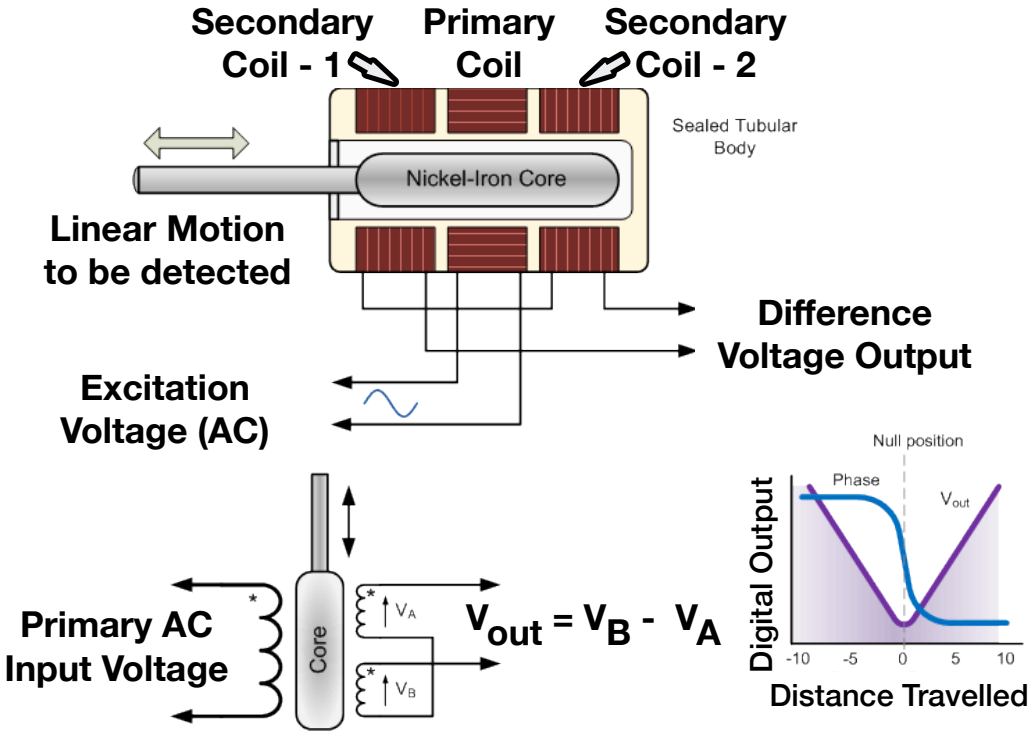

Figure 2.40: Operating principle of LVDT.

Even if the power is switched off, on restarting it, the LVDT shows the same measurement, and no positional information is lost. The rotation of the ferromagnetic cylinder doesn't change the output from the sensors either. In addition, their

operation does not require an electrical contact between the moving part and the coil assembly, but instead relies on electromagnetic coupling. Thus, these sensors are robust, absolute position and frictionless linear motion potentiometer. They have low hysteresis and excellent repeatability, making them suitable for current application.

Linear potentiometers could also be used instead of LVDT, however lower friction and excellent repeatability from LVDTs makes them a superior sensor compared to linear potentiometers.

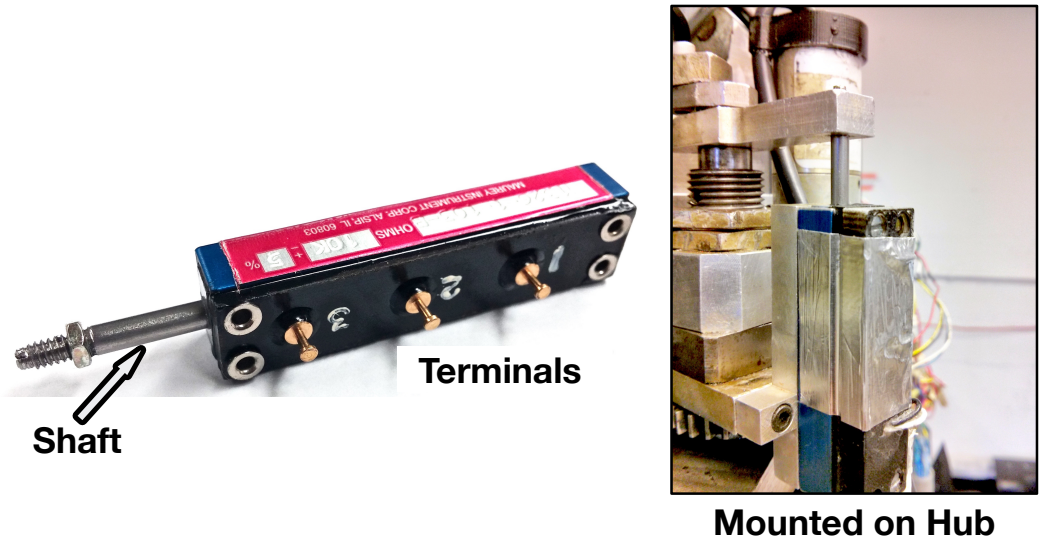

Figure 2.41: Maurey Instruments LVDT used as pitch sensor.

Maurey Instruments M1326-1-103 B [206] units with about an inch of travel and a resistance 10,000 ohms with threaded shaft are used in the hub (Fig. 2.41). These LVDTs are robust, absolute position and frictionless linear motion potentiometer. The motion from the servomotors actuators is calibrated for collective and cyclic pitch of the reference blade, usually blade one. The remaining blades are adjusted to have the same pitch as reference blade at zero azimuth location. Fig-

ure 2.42 shows the LVDT voltage output for various rotor pitch angles. Table 2.6 shows the calibration co-efficients for swashplate pitch angles.

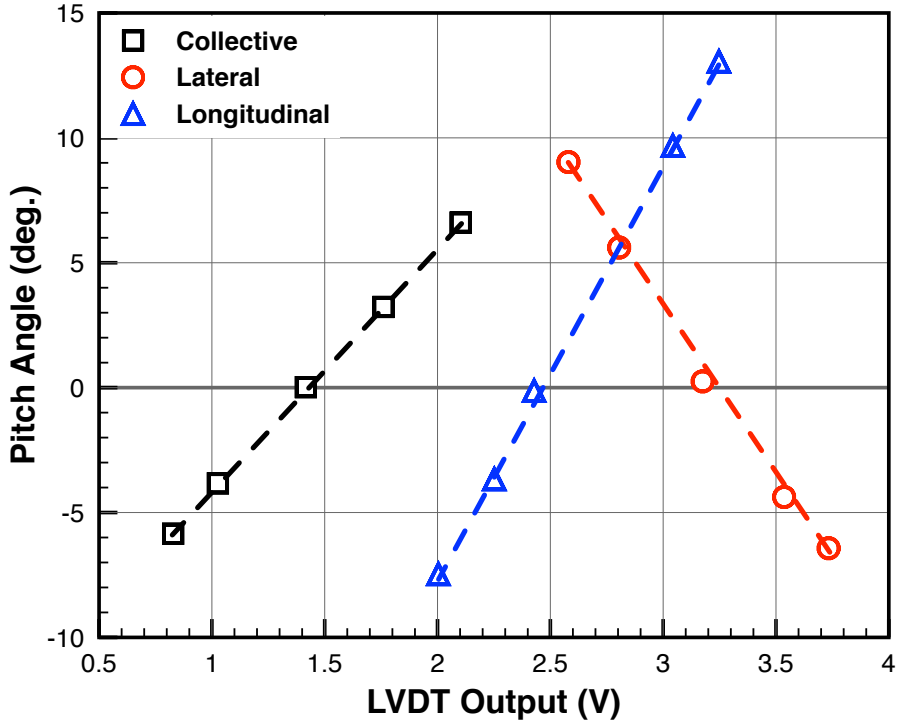

Figure 2.42: Swashplate pitch calibration.

Table 2.6: Calibration co-efficients for rotor swashplate pitch.

Pitch (deg.)	Slope	Intercept	R^2 value
Collective	9.706	-13.767	0.999
Longitudinal	16.541	-40.627	0.999
Lateral	-13.468	-43.385	0.996

2.4.5 Rotor Torque Measurement

Rotor torque is measured by sensing the strain caused in a shear membrane held between the rotor hub and the drive shaft (Fig. 2.25). The torque disc shown in Fig. 2.43 highlights the thin shear membrane in the cut section view and the full-bridge strain gage network installed on it.

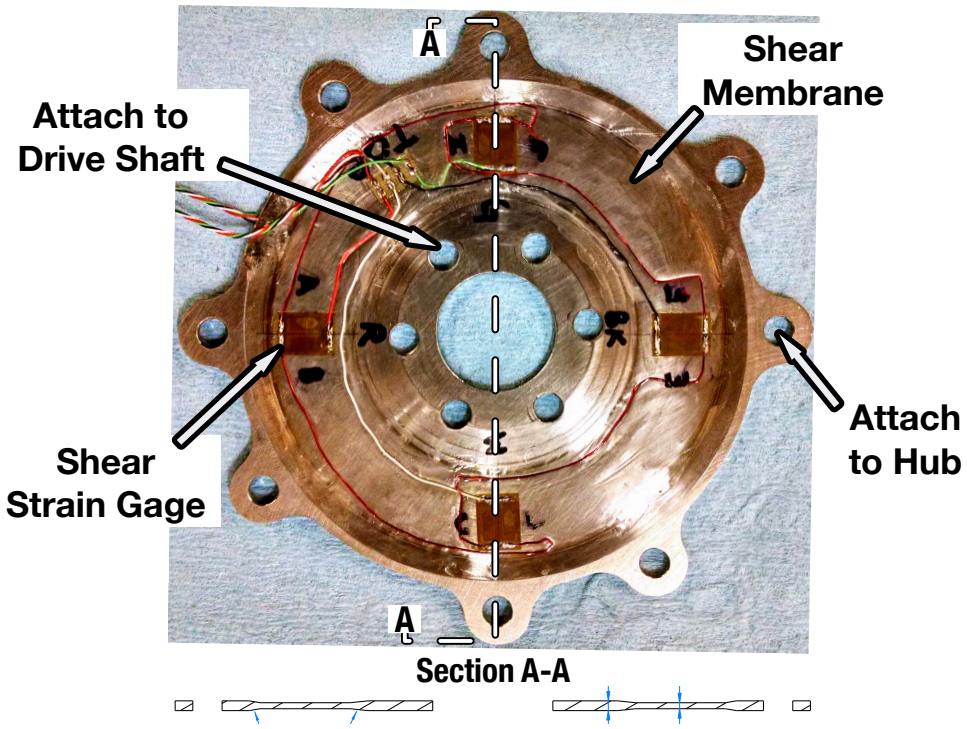

Figure 2.43: Torque disc instrumented with strain gages.

Initially only the bottom surface was instrumented. However, it was noticed that the strain-gage network was sensitive to out-of-plane deformations. Torque measurements were being recorded not only in response to torque but also warping in the disc plane, even in absence of any torque loading. To remedy this error, a new torque disc was machined with tight tolerances. Both the top and bottom surface of the shear membrane were instrumented with identical full-bridge strain

gage network to neutralize the warping effect. This was tested on the bench top by applying torque using a pulley-weight arrangement as shown in Fig. 2.44.

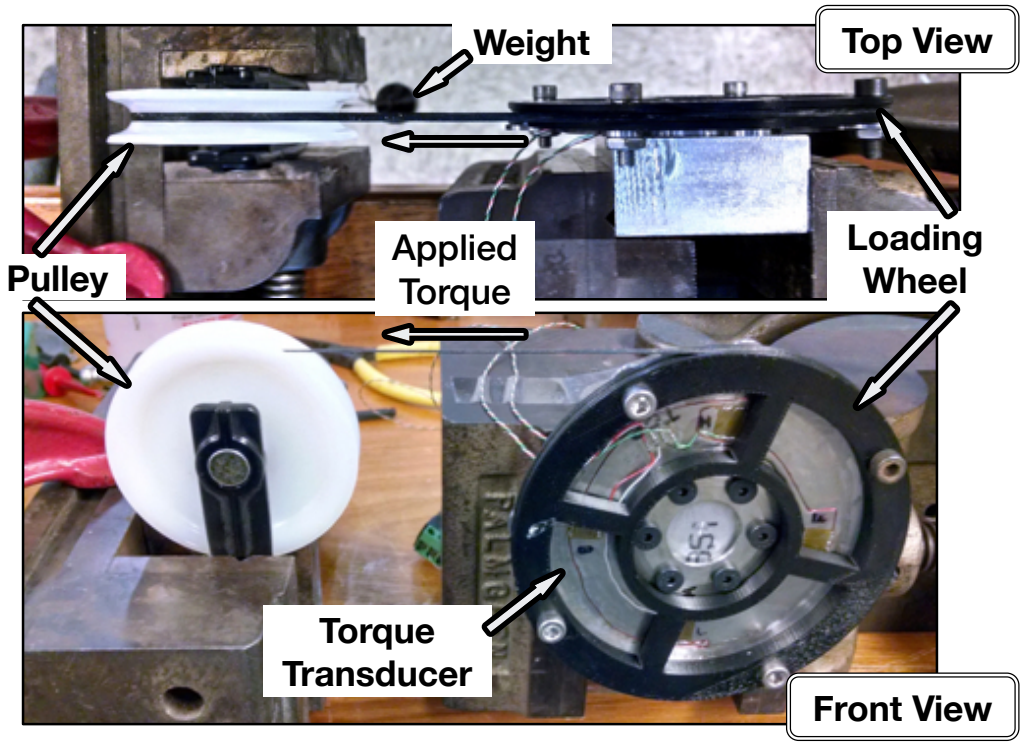

Figure 2.44: Torque transducer calibration bench-top setup.

A linear calibration was observed on the bench top (Fig. 2.45). On the bench top, no effect of out-of-plane deformations were noticed on the torque measurement with the new torque disc. Further, the torque disc was installed in the hub, and calibrated to a much larger torque loading. Again, a linear calibration was obtained (Fig. 2.46) and the torque transducer performance was comparable to that on bench-top (Table 2.7).

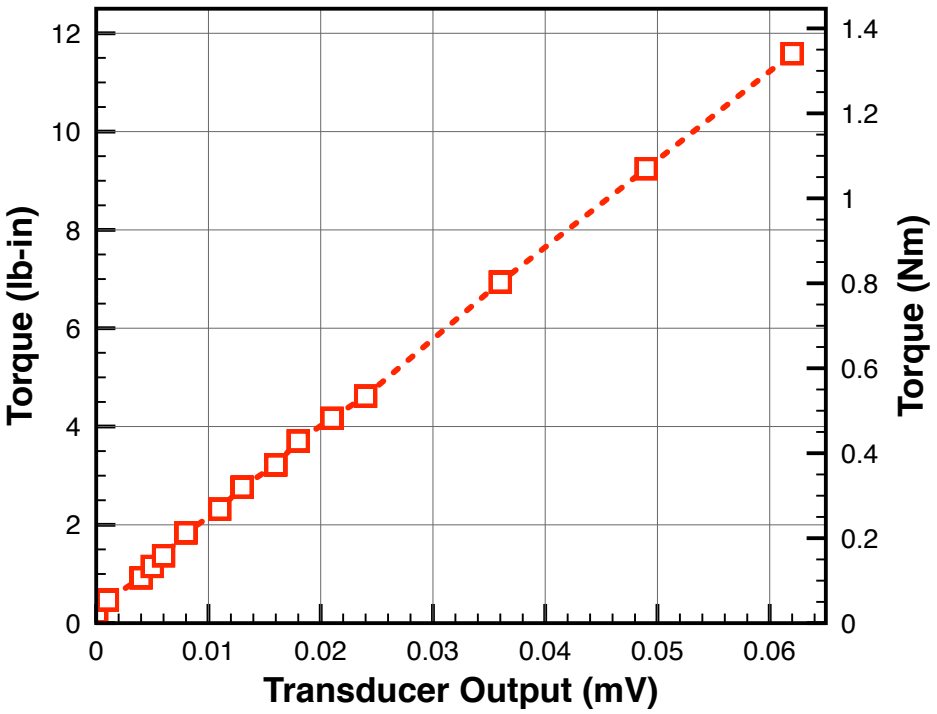

Figure 2.45: Torque transducer calibration on bench-top.

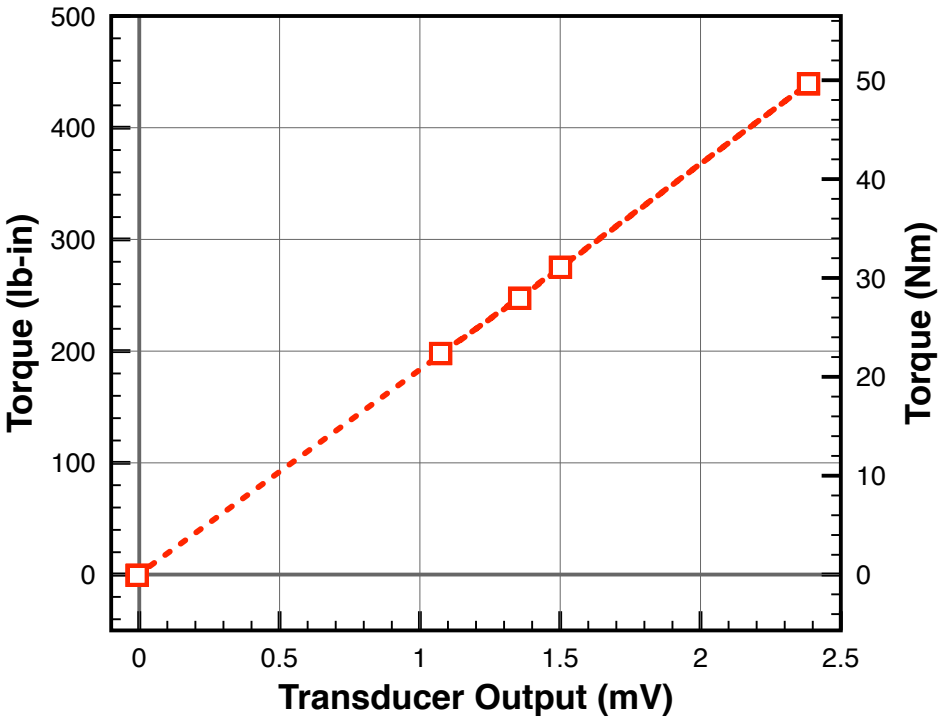

Figure 2.46: Torque transducer calibration installed on rotor hub.

Table 2.7: Calibration co-efficients for rotor torque transducer.

Torque (lb-in)	Slope	Intercept	R^2 value
Bench-top	191714	0	0.995
Rotor hub	183717	0	0.999

Further the effect of bending load on the torque disc was evaluated. The disc was loaded as shown in Fig. 2.47. Theoretically, no torque measurement is expected, however, there was a small but non-negligible effect of this loading and torque measurements were recorded (Fig. 2.48).

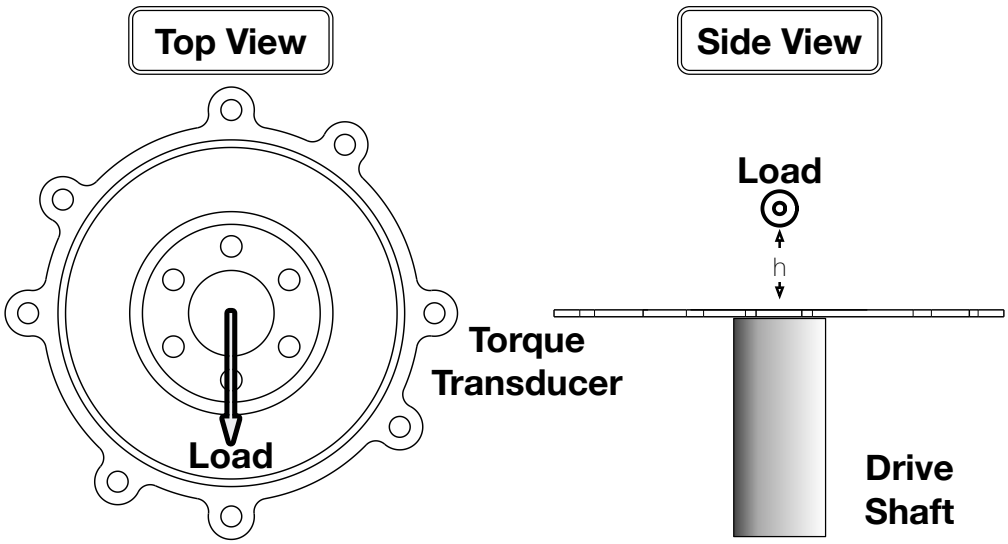

Figure 2.47: Torque transducer under side and bending load, no torque applied.

This discrepancy may not be as prominent at high torque rotor conditions, but would be critical when low torque measurements are desired, for instance when testing a slowed rotor. This error could be due to misalignment in the rotor drive shaft due to a structural damage. Multiple efforts were made to accurately access

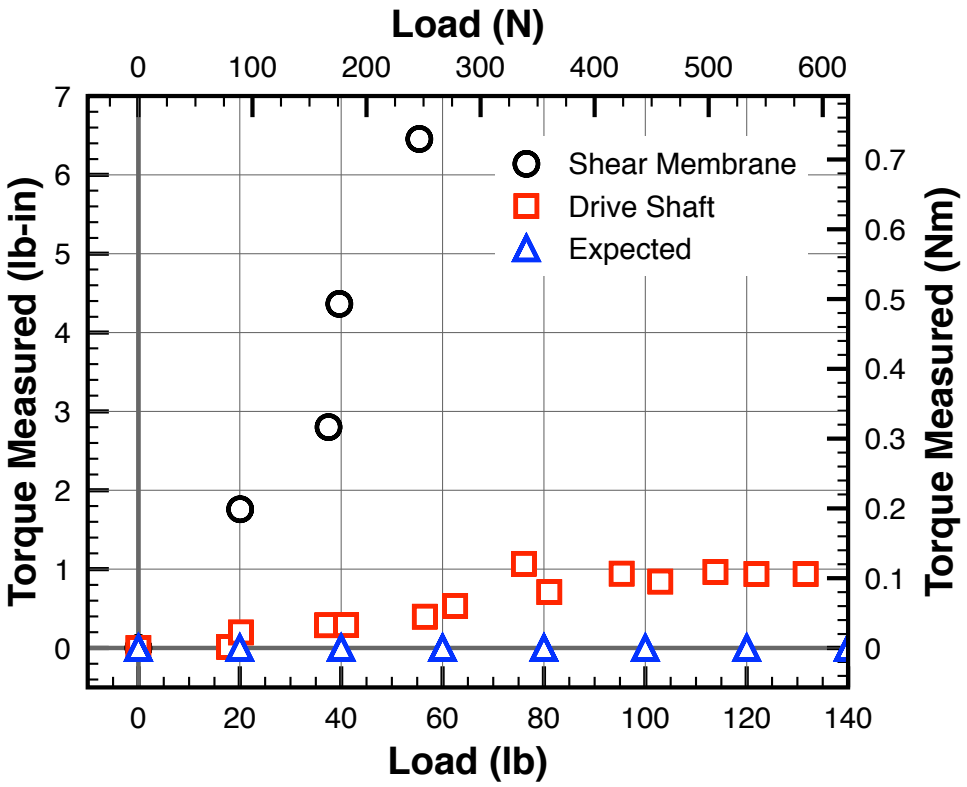

Figure 2.48: Torque measured due to side and bending load, no torque applied.

the cause and it was concluded that a complete re-fabrication of drive shaft would be needed. To mitigate this error, the drive shaft itself was instrumented with torsion gage as well. It was found to be significantly more immune to non-torque loading (Fig. 2.48). Figure 2.49 presents the torque measured with a full-bridge strain gage installed on the rotor drive shaft. Table 2.8 compares the sensitivity of the two torque transducers. Instrumented rotor shaft was used as primary torque transducer for the current research.

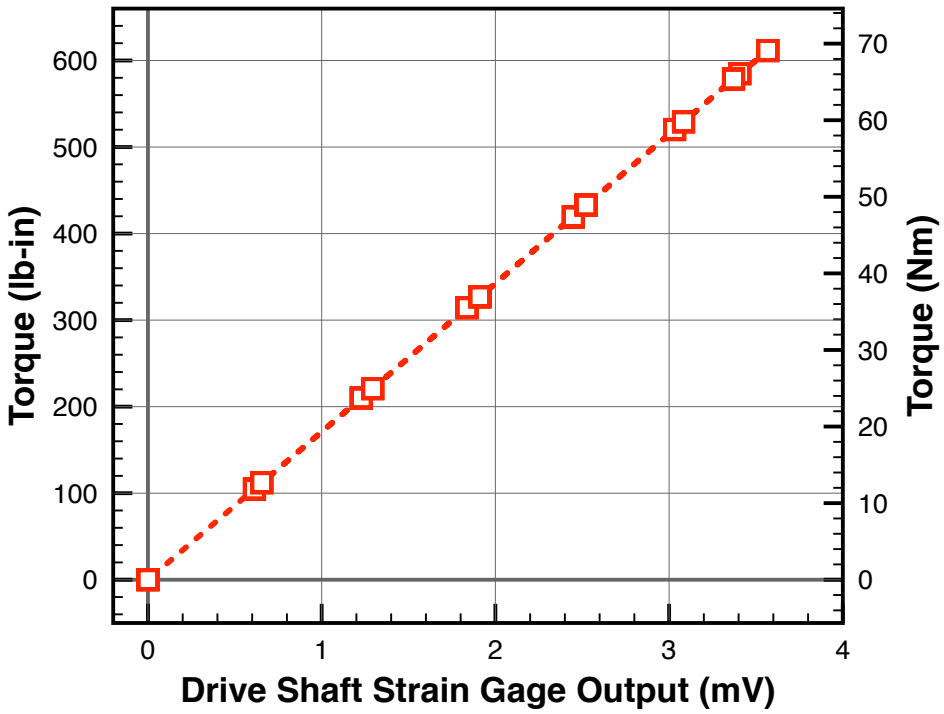

Figure 2.49: Torque calibration from strain gage installed on rotor drive shaft.

Table 2.8: Calibration co-efficients for instrumented rotor drive shaft.

Torque (lb-in)	Slope	Intercept	R^2 value
Shear Membrane	183717	0	0.999
Drive Shaft	171478	0	0.999

2.4.6 Fixed Frame Hub Balance

A six component strain gage based fixed frame balance (Fig. 2.50) is used to measure hub forces and moments. The balance consists of precisely machined flexures which were gaged and calibrated to measure forces and moments in all three directions. One end of the balance was fixed to the rotor stand, while the rotor hub was mounted on the other end. This was to ensure all the rotor hub loads passed through the balance. A calibration matrix relates the six output voltage signals to the measured forces and moments. The calibration process for the hub balance is discussed next.

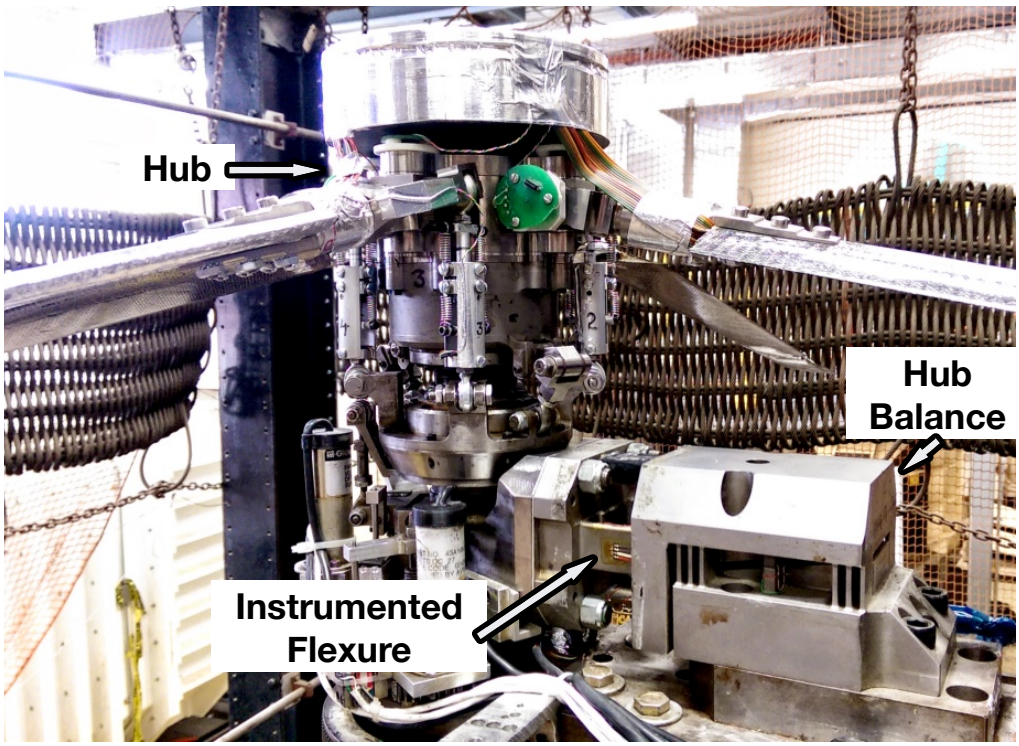

Figure 2.50: Rotor hub balance.

2.4.6.1 Steady loads calibration

For static calibration, a loading rig (Fig. 2.51) was constructed out of 80-20 frames. It allowed to apply loads in all axes. A load cell was placed in-line between the pulley and load application point, to precisely measure the applied load. The calibration was performed with rotor hub center as the origin. The loading fixture along with pulley arrangement allowed application of various loads and moments. However, due to offset of the application point from the hub center, pure loads were difficult to apply. Generally, force application in a planer direction was also accompanied with moments.

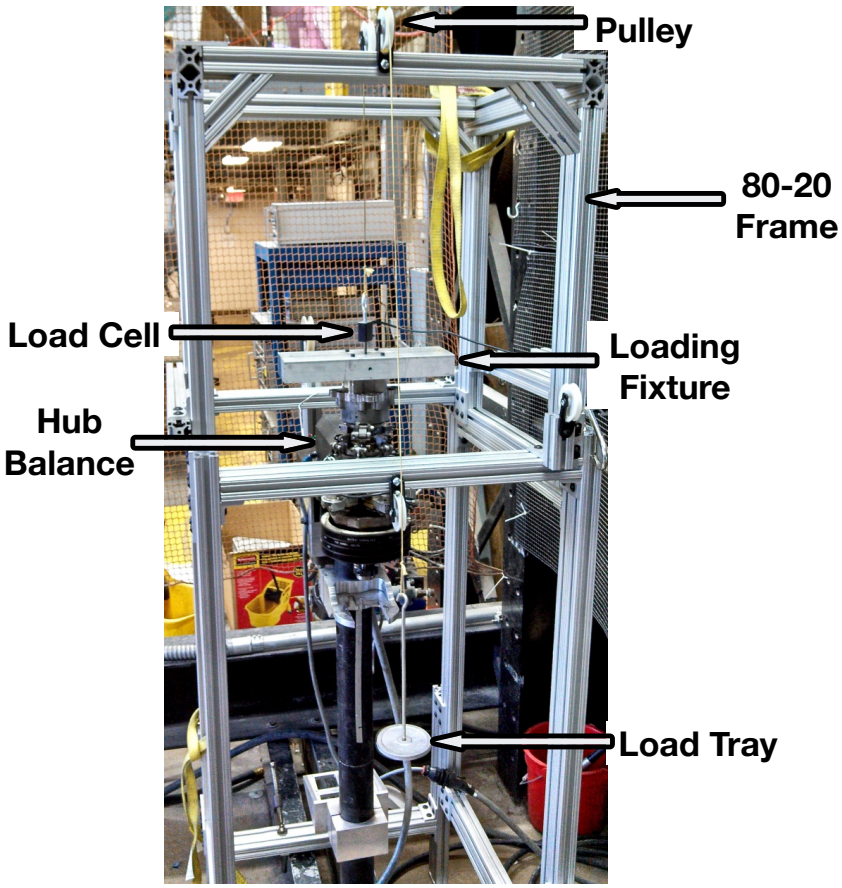

Figure 2.51: Setup for rotor hub balance calibration.

The output voltage from all the six components along with applied loads and moments were recorded for various loading configurations. Since the fixed frame yaw moment only accounts for drive system friction and not rotor loads, it was not applied. However, the voltage output was recorded due to coupled nature of the calibration matrix. A least square solution was found considering all the loading configurations and a calibration matrix was obtained. Table 2.9 contains the calibration matrix for steady hub loads.

Table 2.9: Calibration matrix for steady hub loads.

	F_x	F_y	F_y	M_x	M_y	M_z
F_x	94937	5629	-3112	-19236	-563393	0
F_y	104320	479853	780361	-6383880	-7433310	0
F_z	-435	15154	416635	-84959	-1733376	0
M_x	14158	51235	69982	915913	-751575	0
M_y	-18060	-19	54250	-97290	1408120	0
M_z	86342	735405	616114	-7550196	-5919961	0

2.4.6.2 Dynamic loads calibration

A dynamic calibration was essential to account for structural dynamics such that these effects could be removed from hub balance measurements. This would allow precise measurement of rotor vibratory loads, removing any contamination from structural spectral response. The same rig as used for static calibration was used, however vibratory loads of known amplitude and frequency were required to be applied instead of steady loads. A shaker (B&K model LDS V408) with an in-line load cell (Transducer Techniques model MDB-75) was used for applying vibratory loads. To capture a large frequency range, the data was acquired at a very high sampling rate (5 kHz).

Once the shaker and load cell were setup for load application, a frequency sweep load input was performed. Based on the static calibration, the output from the hub balance was converted to loads. These loads could then be compared to the known applied loads as recorded by the in-line load cell. This data was then converted to frequency domain representation so that amplitude and phase at discrete frequencies could be compared and corrections calculated. This was represented as transfer functions, thus providing correction to vibratory loads specific to applied loads and frequency.

2.4.7 Miscellaneous

A three component accelerometer is mounted in the fixed frame under the rotor hub to monitor test stand vibrations. Since the rotor is mounted on top of a tall

column, the accelerometer helps in monitoring and avoiding any support structural resonance.

In addition, a thermocouple is installed on the hydraulic oil line to monitor fluid temperature and keep it within the specified range. Exceeding the temperature limits can cause the hydraulic motor to fail, leading in loss of rotor torque and possible damage to the hub and the blades.

As a planned upgrade, the hydraulic lines to the motor will be fitted with flow rate and fluid pressure sensors to provide an additional source of measurement of rotor torque. The calculation would be based on the input power to the hydraulic motor and then would be compared to the torque measured by instrumented rotor shaft.

2.5 Rotor Control Console

The rotor speed and swashplate actuators are controlled from the console in the control room. It is shown in Fig. 2.52.

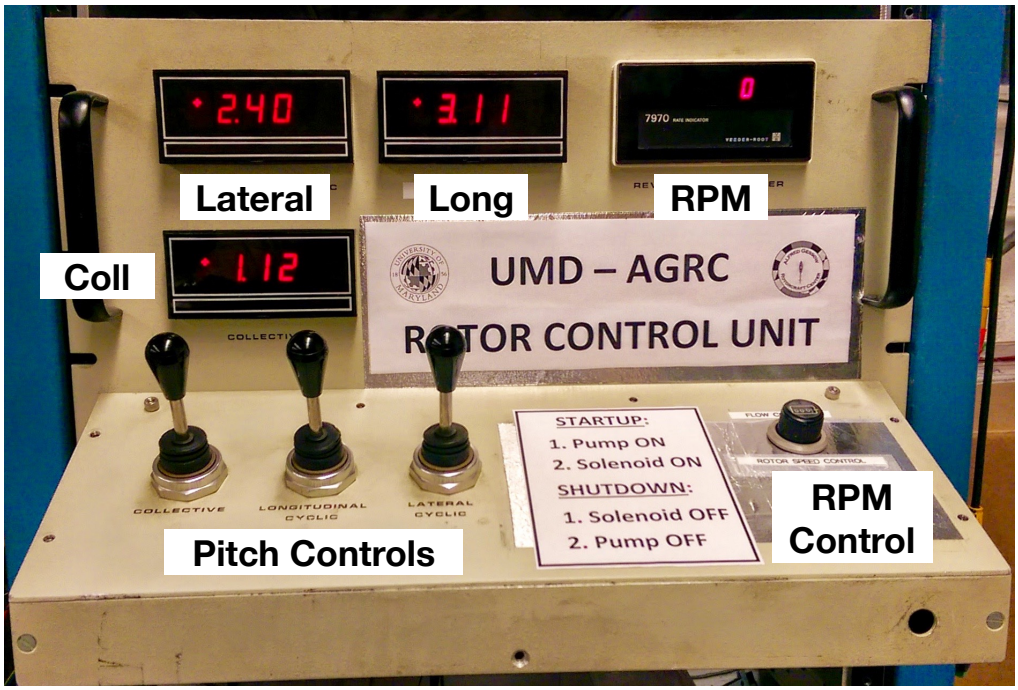

Figure 2.52: Rotor control console.

The pitch servomotors in the swashplate are supplied by a constant 27 Volt DC input. The servos move the swashplate by a lead screw arrangement. The pitch can be altered by controlling ON duration and direction of rotation of the dc servomotors. These servomotors are controlled by joystick on the rotor control console. Moving the stick up increases and moving it down decreases the blade pitch. Pitch adjustments as fine as quarter of a degree can be made using these control joysticks.

The rotor rpm is adjusted by a control dial on the rotor control console. The

control dial adjusts the current input to the flow control valve, which then controls the amount of fluid supplied to the hydraulic motor, thus changing the rotor speed. Once the dial is set at a flow rate, the flow control valve maintains the desired rotor rpm.

2.6 Rotor Tracking Procedure

Rotor tracking is an important pre-flight operation. It can be understood as the process of determining the positions of the tips of the rotating blade relative to each other, and of determining the corrections necessary to hold these positions within certain tolerances. The blades should all track one another as closely as possible. The purpose of blade tracking is to bring the tips of all blades into the same tip path throughout their entire cycle of rotation. Figure 2.53 shows a schematic representation of rotor blade tracking.

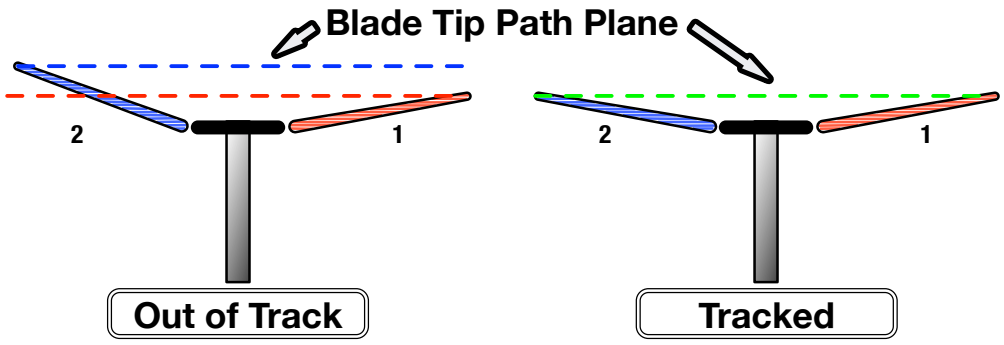

Figure 2.53: Schematic of rotor blade tracking.

Although initially the objective of rotor tracking was identified as maintaining the blade tips within certain tolerance, the larger objective is to reduce the vibrations associated with the unequal lift on out of track rotor blades. Usually accelerometers

mounted at key locations on the rotorcraft are also monitored while the rotor tracking process is underway. This process is sometimes also termed as helicopter rotor smoothing. It is accomplished in a sequence of four separate steps:ground tracking, hover verification, forward flight tracking,and auto rotation rpm adjustment. In addition to main rotor blades tracking, tail rotor blades are tracked as well. The procedure for tracking is discussed next.

Over the years various methods of blade tracking have been experimented with. The most primitive method was to mark the tips of the blades with different color paint and have the rotor tips rub against a flag on a pole to show the relative positions of the rotor blades. With advances in technology, an electro-optical method is current industry standard for tracking [207]. This system uses a highly concentrated light beam flashing in sequence with the rotation of the main rotor blades so that a fixed target at the blade tips will appear to be stopped. Each blade is identified by an elongated retro-reflective number taped or attached to the underside of the blade in a uniform location. When viewed at an angle from inside the helicopter, the taped numbers will appear normal. Figure 2.54 shows a schematic of pre-flight tracking setup using an elctro-optical system. Figure 2.55 shows the typical hardware used for rotor tracking by this method.

The hardware includes a optical source and receiver referred to as Universal Tracing Device (UTD). It is usually mounted on the nose of the fuselage (Fig. 2.56) roughly at an angle of 75 degree, focussed at outboard location of rotor blade. It may be used with a glare reduction unit. In addition a data acquisition system is also used to record the rotor azimuth location and sync the universal tracking

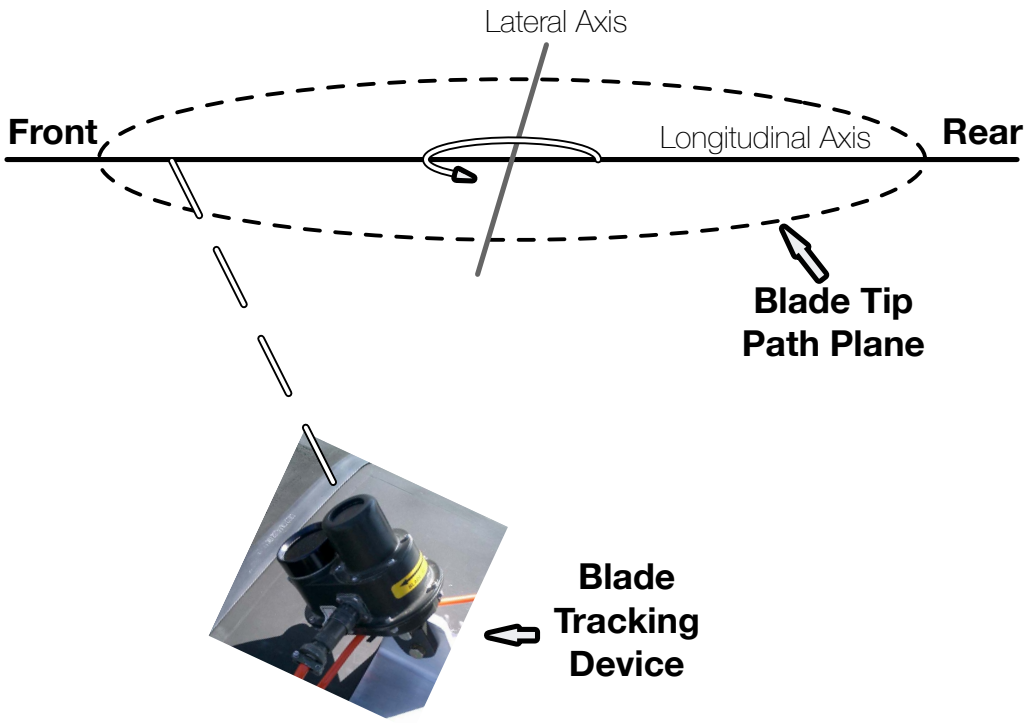

Figure 2.54: Pre-flight rotor tracking setup.

device with rotor speed. A control and display unit aids in visualizing the rotor blades location.

There are two ways to adjust the tracking of the rotor blade. Conventionally trim tabs (Fig. 2.57) located at the trailing edge of the rotor blades on outboard locations are adjusted to change the blade camber and achieve rotor track. Recently, adjustable pitch links are also used to change the angle of attack of the blade by adjusting the length of the pitch link. Figure 2.58 shows adjustable pitch link on a UH-60 rotor hub. While pitch link adjustments change the angle of attack of the entire blade, trim tab adjustments only affects the camber of the blade over the length of the trim tab. In addition, pitch link adjustment offers a much finer control of blade tracking compared to trim tabs.

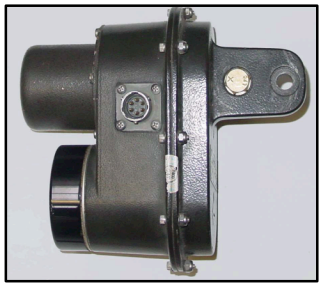

Universal Tracking Device

Glare Reduction Unit

Data Acquisition System

Control and Display Unit

Figure 2.55: Typical hardware used for helicopter rotor tracking application.

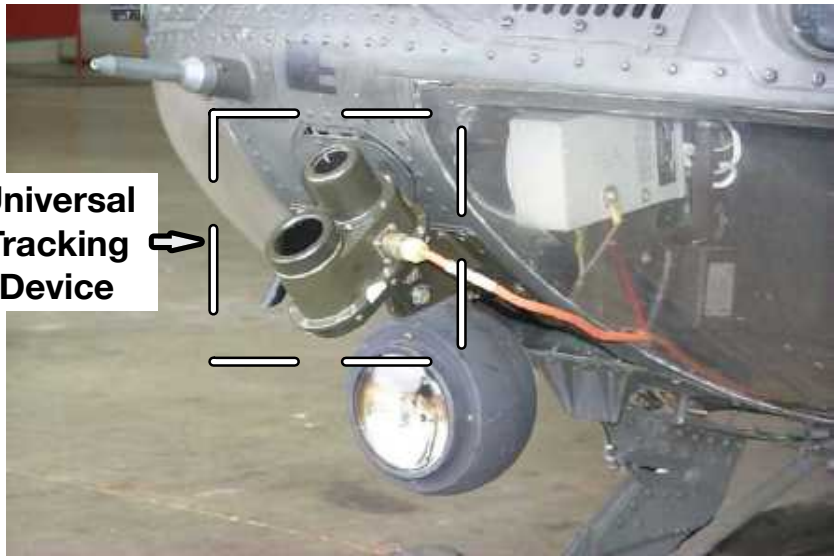

Figure 2.56: Universal Tracking Device mounted on rotor fuselage nose.

The tracking process is a time consuming, manual and on-ground process. Rotor tracking can degrade in flight due to various conditions such as blade icing, abrasion due to sand or damage due to debris. This loss of track and rotor balance

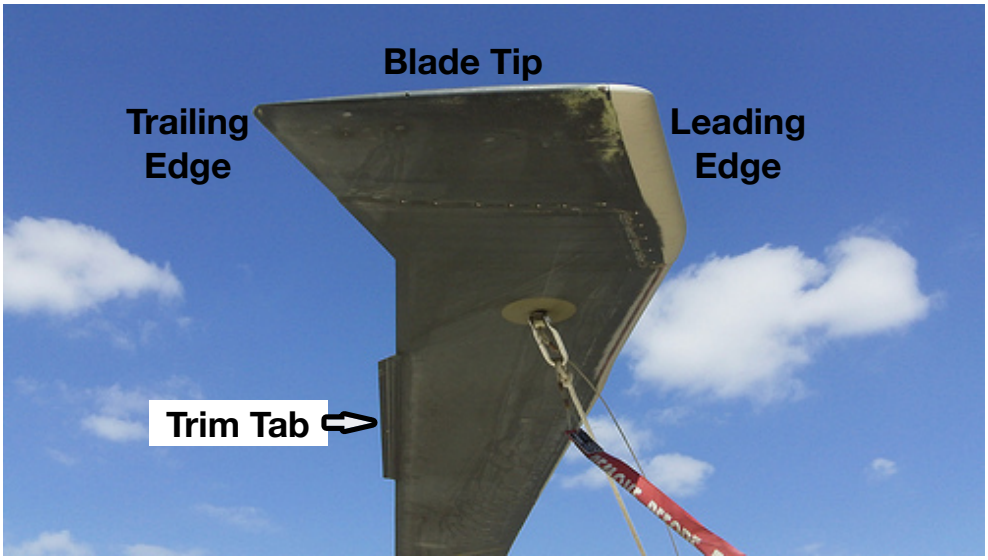

Figure 2.57: Trim tab on UH-60 rotor blades.

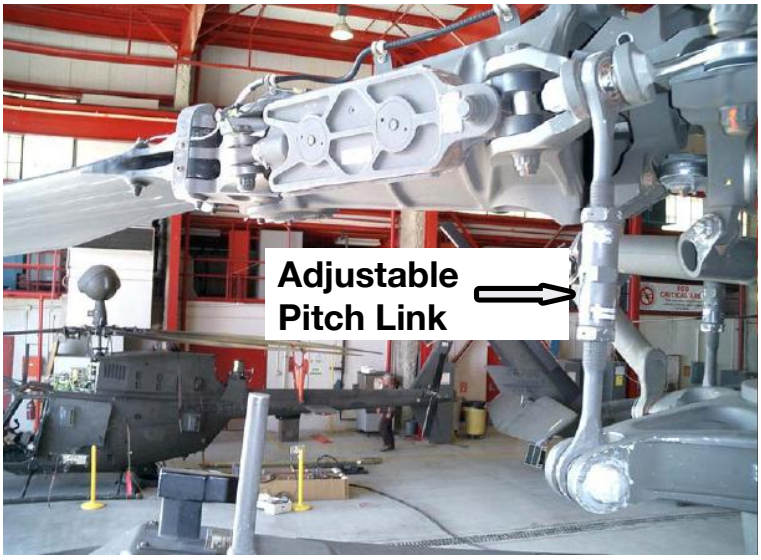

Figure 2.58: Pitch Control Rod (PCR) on a UH-60 rotor hub.

has negative effect of the helicopter handling, flight comfort and structural loads on the rotor blade and hub.

For model scale rotors, a trim tab is not included. Instead the blade root pitch is adjusted to counter blade-to-blade differences. Reflective adhesive tapes at the blade tips (Fig. 2.59) are used and illuminated by a high intensity strobe. Fig-

Figure 2.59: Reflective tapes on blade tips.

ure 2.60 shows the schematic of tracking setup for model scale rotors at UMD. The strobe frequency is synced with rotor speed, and set at four times the rotor RPM. This creates a visual impression that all the blade tips are frozen at same azimuth location. In addition, the phase is also synced with rotor azimuth to illuminate the blades between 180 and 270 degree rotor azimuth.

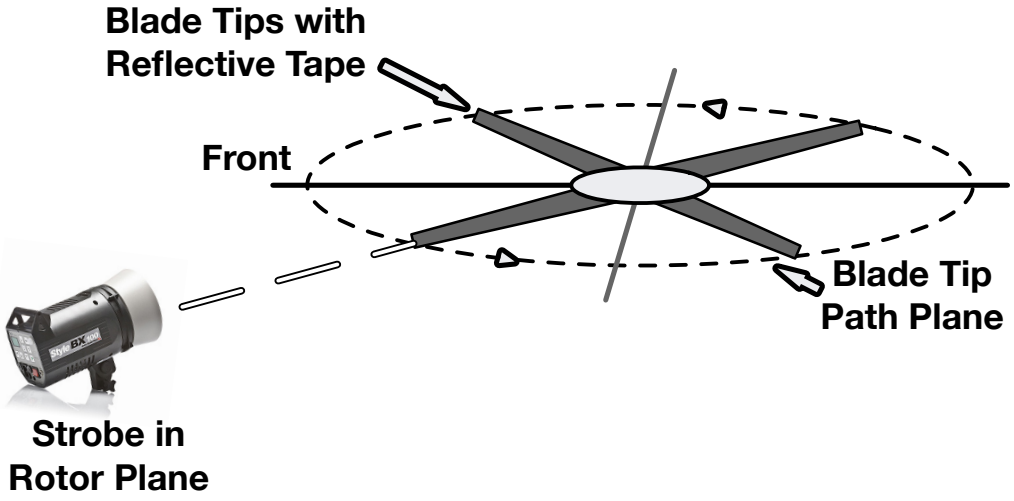

Figure 2.60: Rotor blade tracking setup for Mach scale rotor testing.

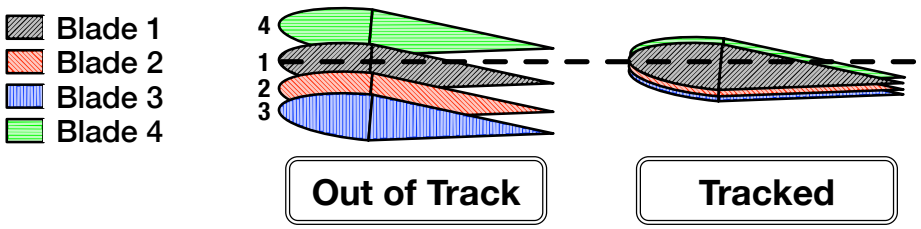

Figure 2.61: Schematic of rotor blade tracking.

As seen in Fig. 2.61, blade one is treated as the reference blade. In an untracked rotor, the remaining blades can be above or below the reference blade plane. To trim the blades, the corresponding blade root pitch is appropriately adjusted to increase or decrease the blade lift. The blade pitch adjustment is made by precisely changing the length of the pitch link. This adjustment moves the blade tip to bring it in line with the reference blade. Tracking is an iterative process with small adjustments being made in each attempt. The rotor is considered tracked with all the blade tips are in a plane within half blade thickness.

2.7 Rotor Trim Procedure

In general, trimming an helicopter means maintaining equilibrium in space. The steady forces and moments generated by the rotor should be equal and opposite to those generated by the other parts of the helicopter, e.g. the tail rotor, the fuselage, the horizontal stabilizer etc. The steady forces and moments generated by the rotor should remain the same from one rotor revolution to another. A trimmed flight can be achieved under any steady flight condition.

For most hover tower and wind tunnel experiments, isolated rotors are tested.

For an isolated rotor trim, the three rotor control angles are determined based on three specified trim targets. One of these targets is rotor thrust. For moment trim, target rotor pitch and roll moments are zero, Alternatively, in addition to the specified thrust target, zero first harmonic flapping is imposed. Generally, wind tunnel trim is used widely for articulated rotors and zero moment trim for hingeless rotor systems. Isolated rotor trim is used in wind-tunnels to achieve specific flight conditions in a controlled environment. The procedure to achieve wind tunnel trim is explained next.

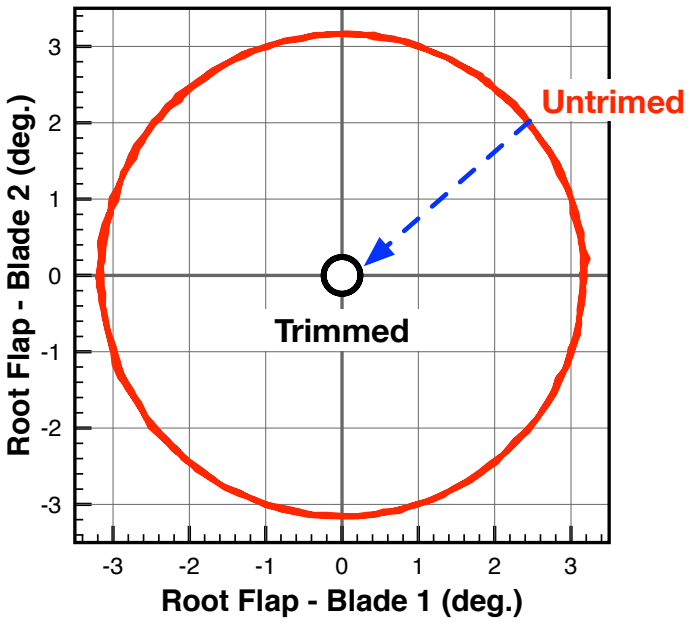

Figure 2.62: Lissajous figure for wind tunnel trim.

For swashplate rotors, the trim is achieved by adjusting the cyclic blade pitch inputs to the rotor. A popular means of visualizing trim is by use of Lissajous figures. The time history of blade flap data from two orthogonal blades is plotted against each other. Usually only the first harmonic is plotted, the resultant figure

being a circle (Fig. 2.62). Visually trim target is to shrink the size of the circle and trim is said to be achieved when the lateral and longitudinal pitches are so adjusted to reduce blade cyclic flapping below a threshold value (a tenth of a degree).

A more mathematical approach to achieve wind tunnel trim is by calculating lateral and longitudinal blade flap in real time. Consider only the first harmonic of the blade root flap motion, the harmonic variation of blade flap with rotor azimuth can be described as:

$$\beta(\psi) = \beta_0 + \beta_{1c}\ cos(\psi) + \beta_{1s}\ sin(\psi) \tag{2.1}$$

where β_0 is conning angle, β_{1c} is lateral flap angle and β_{1s} is longitudinal flap angle.

The blade flap time history (Fig. 2.63 (a)) and shaft encoder data (Fig. 2.63 (b)) is used to resolve the flap motion in terms of rotor azimuth (Fig. 2.63 (c)). In each data acquisition cycle, a number of rotor revolutions were captured. These multiple revolution data was then averaged to generated a phase resolved blade flap motion (Fig. 2.64). The blade flap angle at 0, 90, 180 and 270 degree azimuth are extracted and β_0, β_{1c} and β_{1s} for one blade are calculated as per Eqs. 2.2.

$$\begin{aligned}
\beta_1 &= \beta(0) &&= \beta_0 + \beta_{1c};\\
\beta_2 &= \beta(90) &&= \beta_0 + \beta_{1s};\\
\beta_3 &= \beta(180) &&= \beta_0 - \beta_{1c};\\
\beta_4 &= \beta(270) &&= \beta_0 - \beta_{1s};\\
\beta_0 &= \frac{1}{4}\left[\beta_1 + \beta_2 + \beta_3 + \beta_4\right];\\
\beta_{1c} &= \frac{1}{2}\left[\beta_1 - \beta_3\right];\\
\beta_{1s} &= \frac{1}{2}\left[\beta_2 - \beta_4\right];
\end{aligned} \tag{2.2}$$

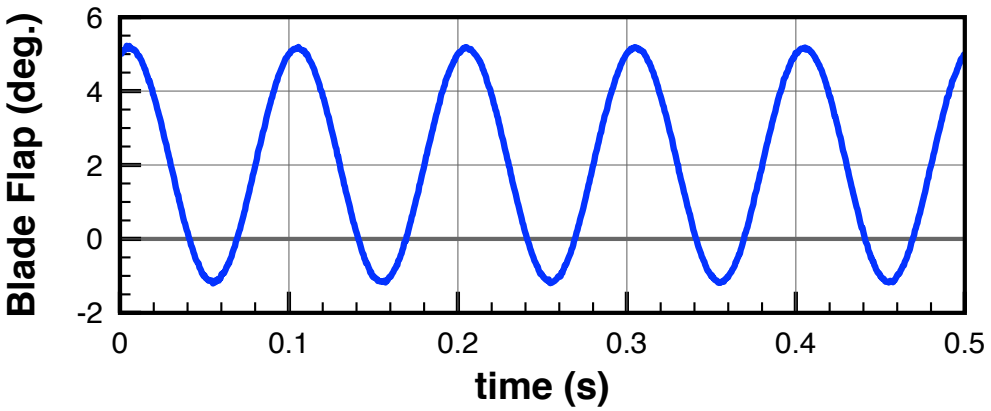

(a) Time history of root flap for blade 1.

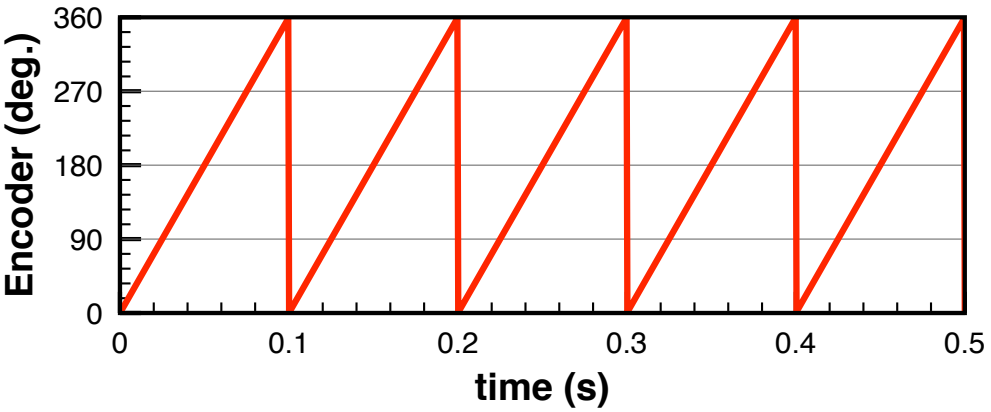

(b) Time history of rotor shaft encoder.

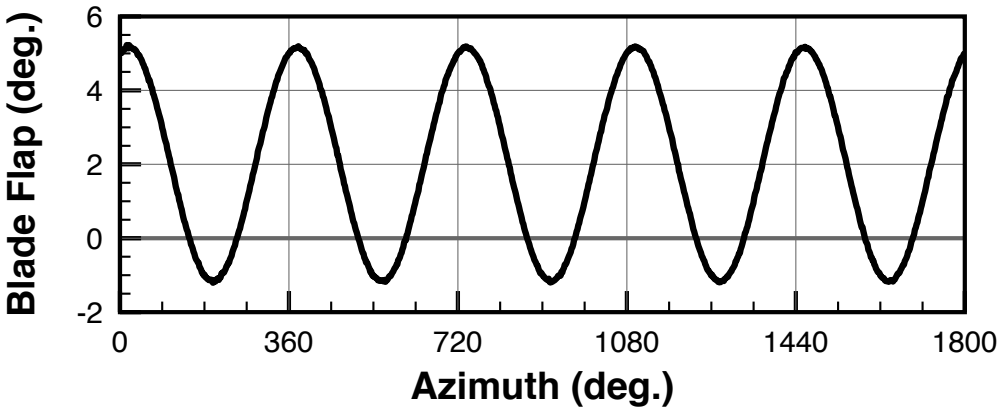

(c) Blade 1 flap motion resolved in multiple rotor revolutions.

Figure 2.63: Resolving time data into rotor azimuth.

From all the four blades, averaged flap angles are calculated (Eqs. 2.3).

$$\beta_0{}^{(rotor)} = \frac{1}{4}\left[\beta_0{}^{(1)} + \beta_0{}^{(2)} + \beta_0{}^{(3)} + \beta_0{}^{(4)}\right];$$
$$\beta_{1c}{}^{(rotor)} = \frac{1}{4}\left[\beta_{1c}{}^{(1)} + \beta_{1c}{}^{(2)} + \beta_{1c}{}^{(3)} + \beta_{1c}{}^{(4)}\right];$$
$$\beta_{1s}{}^{(rotor)} = \frac{1}{4}\left[\beta_{1s}{}^{(1)} + \beta_{1s}{}^{(2)} + \beta_{1s}{}^{(3)} + \beta_{1s}{}^{(4)}\right]; \tag{2.3}$$

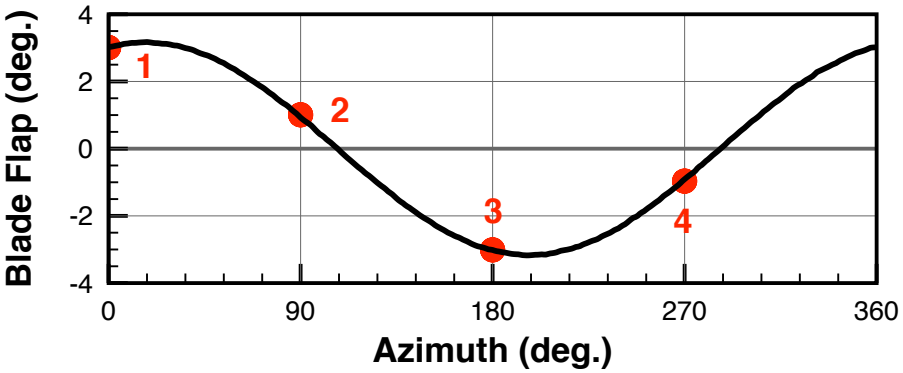

Figure 2.64: Cyclic blade flapping angles for blade 1.

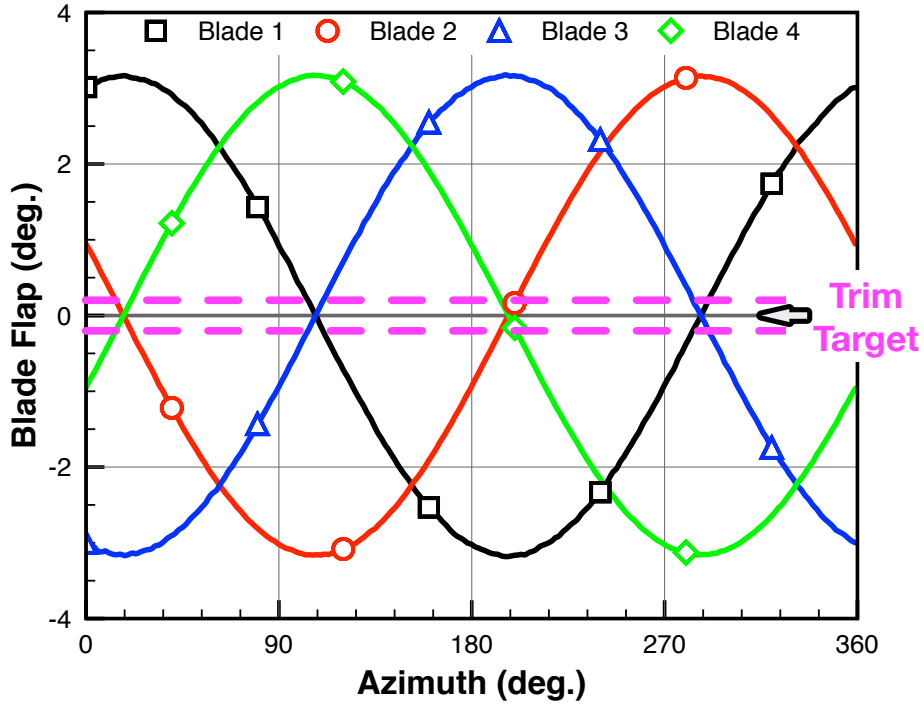

Figure 2.65: Cyclic blade flapping for all blades.

The mean flap angle is removed from the data and cyclic pitch inputs are then chosen to reduce cyclic flap angles (Fig. 2.65). The iterative process is carried out until lateral and longitudinal flapping is negotiated to be below a tolerance value (a tenth of a degree). For an articulated rotor with small hinge offsets, the blade flap response lags pitch input by about quarter rotor revolution. To accommodate this phase delay, cyclic pitch servos are installed 90 degree offset from rotor axes.

Generally, only considering the first harmonic in flapping is sufficient for trimming rotor up to a moderate advance ratio. However for slowed rotors with operating advance ratios of one and above, there could be significant higher harmonic components in the blade motion. In such operating conditions, only one per rev control input (using swashplate) to target one per rev blade root flapping might not be sufficient and higher harmonic control inputs could be necessary for even trimming the rotor.

2.8 Data Acquisition System

Data acquisition is the process of acquiring signals that measure physical phenomena and converting the analog information into digital data for storage and further analysis. Physical parameters like flap, lag, pitch angles and rotor loads are first converted into electrical signals using sensors and transducers. Section 2.4 details various instrumentation on the hover test stand. The analog data from the rotating frame is transfer to control room using slip rings. The control room houses the data acquisition hardware. This hardware conditions the raw data to improve signal to noise ratio. Finally, the system carries out an Analog-to-Digital conversion. A data acquisition software is used to control the hardware as well as process the data for review and storage.

2.8.1 Slip rings

Data transfer between the rotating frame and the fixed frame is done via a slip-ring. Typically, it consists of a stationary graphite or metal contact (brush) which rubs on the outside diameter of a rotating metal ring. As the metal ring turns, the electrical current or signal is conducted through the stationary brush to the metal ring making the connection. Additional ring/brush assemblies are stacked along the rotating axis for multiple lines. The choice of material for the brushes and rings is dependent on the rated rotational speed as well as the maximum voltage-current transmitted through the unit. The life of the unit is specified as number of linear miles of operation at the rated speed. Radial bearings are used to ensure

rotor alignment and mimnimize friction. Figure 2.66 shows various components of a typical slip ring.

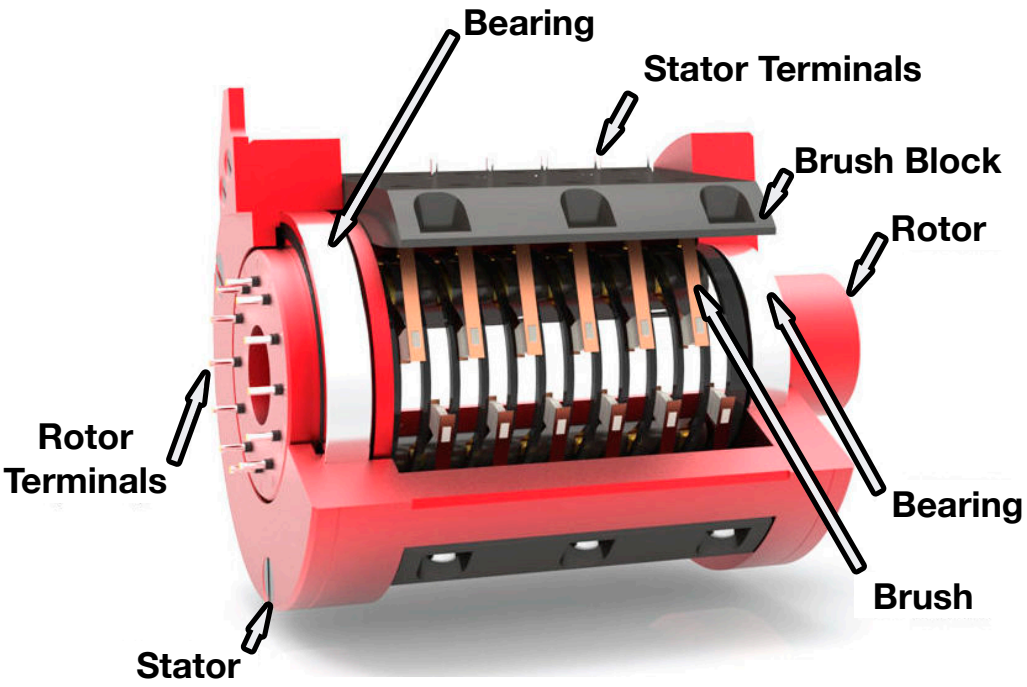

Figure 2.66: Components of a typical slip ring.

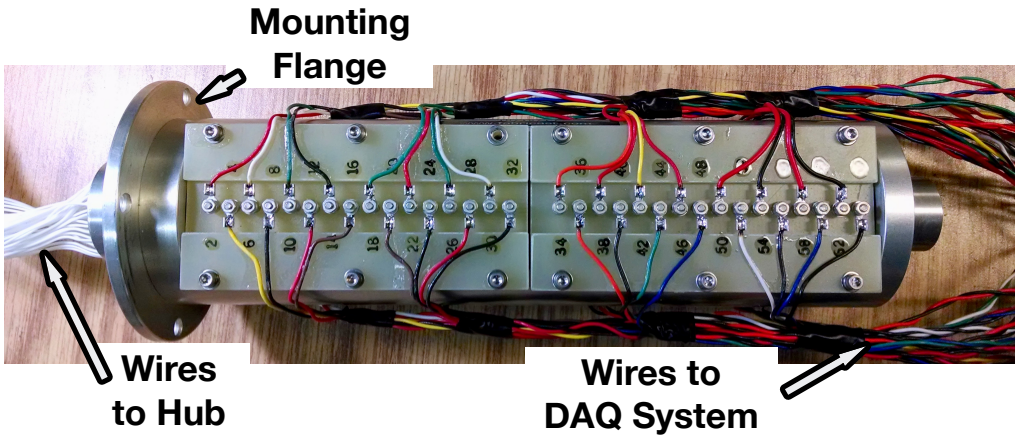

Figure 2.67: Fabricast manufactured 64-line slip ring.

For the test setup at UMD, Fabricast manufactured unit (Fig. 2.67) was custom designed to accommodate in the test setup. Each unit is capable of 64-wires,

two such units are currently in use. They are rated at 5 A and 1 A continuous current respectively with 0.01 ohm line resistance for stain gage type application.

In addition, a 16 channel power slip ring is also available. This could be installed for applications where high electrical power inputs are required to on-bade actuators, such as for powering piezo-bender actuators. It is rated for 0.5 A continuous current at 250 VAC excitation voltage.

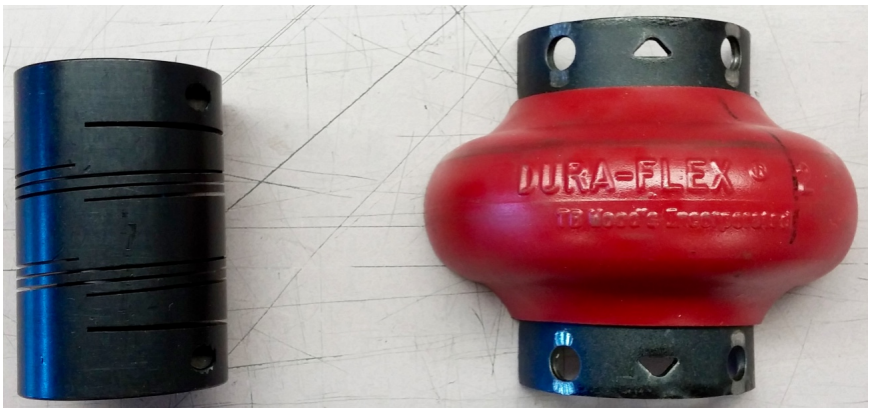

Figure 2.68: Single and double piece flex coupling units.

These slip rings are mated to the shaft below the drive pulley using flex couplings. Flex coupling is a lightweight element that absorbs torsional vibration and shock loading. They are generally composed of elastomeric material or precisely machined flexures on a cylinder. They are not designed for taking large steady loads, rather they facilitate mating concentric rotating shafts within 5 degree of angular misalignment. Figure 2.68 shows two such couplings. The one on left is a Rocom manufactured single piece unit, while one on the right is a TB Woods manufactured elastomeric unit, available as two half pieces, to be secured on to a hub. The elastomeric flex coupling are easy to install and replace and two such units are currently in use at the rotor test stand.

2.8.2 Data Acquisition Hardware

National Instruments SCXI system (Fig. 2.69) is used for signal conditioning and data acquisition. It consists of a 12 slot SCXI - 1001 chassis capable of housing various modules. These modules are selected for specific uses. SCXI - 1102C is used to acquire analog input voltages, SCXI - 1112 for thermocouple inputs and SCXI - 1520 for strain gage inputs. NI USB 6251 is used for Analog-to-digital conversion and NI PCI 6713 is used for analog voltage output.

Figure 2.69: NI SCXI Data acquisition hardware.

The slip rings lines are connected to the BNC breakout panel (Fig. 2.70), which is in turn wired to various modules. Depending on the type of sensor or measurement, the data lines are connected to appropriate modules. A PC running LabVIEW programming environment is used to interface with the hardware and process the data for review and storage. Table 2.10 summaries the capability of the current data acquisition setup.

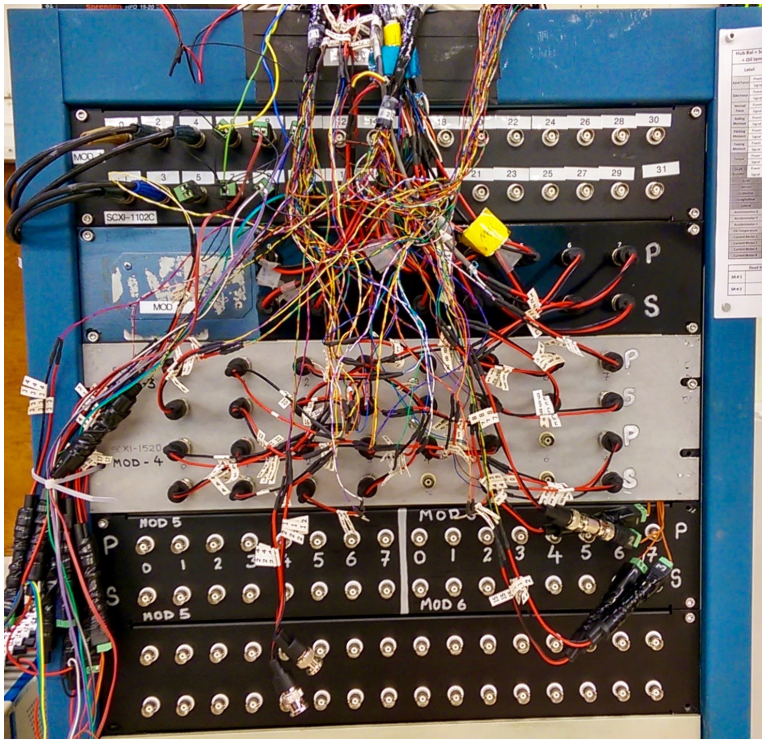

Figure 2.70: BNC Breakout panel.

Table 2.10: Summary of data acquisition system channel capability.

Module	Channels	Capability
USB - 6251	80	ADC, 16 bits, 1.25 Million Samples/s
SCXI - 1520	40	Strain, load, torque, and pressure sensors
SCXI - 1102C	32	Analog input voltages
SCXI - 1112	8	Thermocouples
PCI - 6713	8	Analog output voltages
SCXI - 1001	chassis	12 slot housing SCXI modules

2.8.3 Data Acquisition Software

LabVIEW (Laboratory Virtual Instrument Engineering Workbench), a visual programming language from National Instruments is used for controlling the data acquisition hardware. It includes extensive support for interfacing various data acquisition hardwares over USB or Serial ports. The programming in LabVIEW has a graphical front panel, that allows to drag and drop various functions and display panels. The back panel is a block diagram where the programmer connects different function-nodes by drawing wires. These wires propagate variables and any node can execute as soon as all its input data become available. The code execution is determined by the structure of a block diagram and it is inherently capable of parallel execution. Multi-processing and multi-threading hardware is automatically exploited by the built-in scheduler. Figure 2.71 and 2.72 present an example of LabVIEW front panel and block diagram.

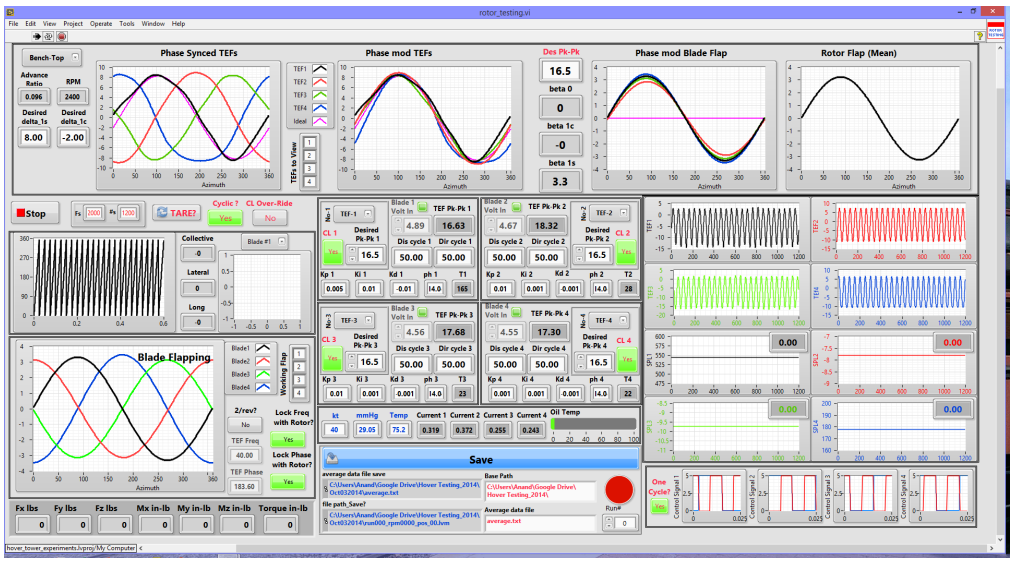

Figure 2.71: LabVIEW front panel.

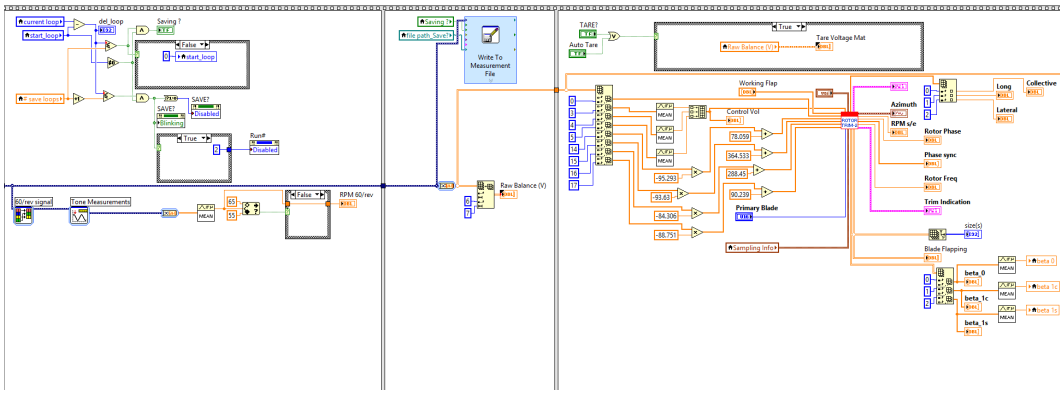

Figure 2.72: LabVIEW block diagram panel.

2.9 Vacuum Spin Chamber

It is essential to test a new design concept, or an on-blade component in rotational environment, under similar centrifugal loads as would be expected on the hover stand. A vacuum chamber allows an enclosed space to carry out such an examination, by subjecting the test specimen under inertial loads only. Figure 2.73 shows the vacuum chamber at UMD. It is a 1-in thick cast iron cylinder, with an internal dimensions of 10-ft diameter and 3-ft height. It is mounted 6 ft above the ground and has two 6-in diameter observation windows. Figure 2.74 shows a typical specimen being examined in the vacuum chamber. It is installed on a rotating beam with a balancing weight. The beam can be spun up to a maximum speed of 1800 RPM. The vacuum environment allows using a low power motor to spin the beam, as only inertial acceleration and frictional loads were to be negotiated.

The vacuum is created by pumping out all the air in the chamber using an electric air pump and a gage pressure of 29.5 in Hg (99% vacuum) can be maintained.

Figure 2.73: Vacuum chamber at University of Maryland.

An Omega PXI-139 pressure transducer is installed in the chamber to monitor the pressure, in addition to a analog pressure gage mounted on the outside of the chamber.

Figure 2.75 shows the drive system for the vacuum chamber. An electric motor is used to spin the rotating beam in the chamber. It can be remotely controlled using a motor controller in the control room. A 60-line Moog manufactured slip ring is also installed to communicate with test specimen (Fig. 2.76). A flex coupling is used to permit up to 5 degree of misalignment in the shaft and the slip ring. A gear-tooth wheel similar to one installed in the hover test stand is also included to measure the rotational RPM. Proper care is taken to ensure that any gaps are vacuum sealed (Fig. 2.77).

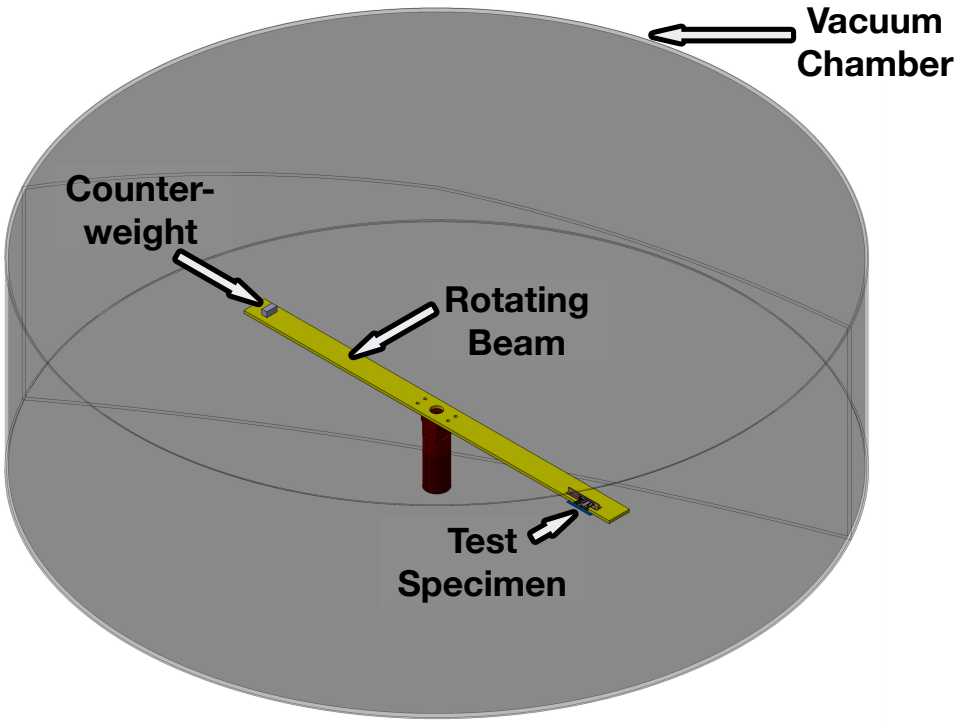

Figure 2.74: Typical specimen testing in the Vacuum chamber.

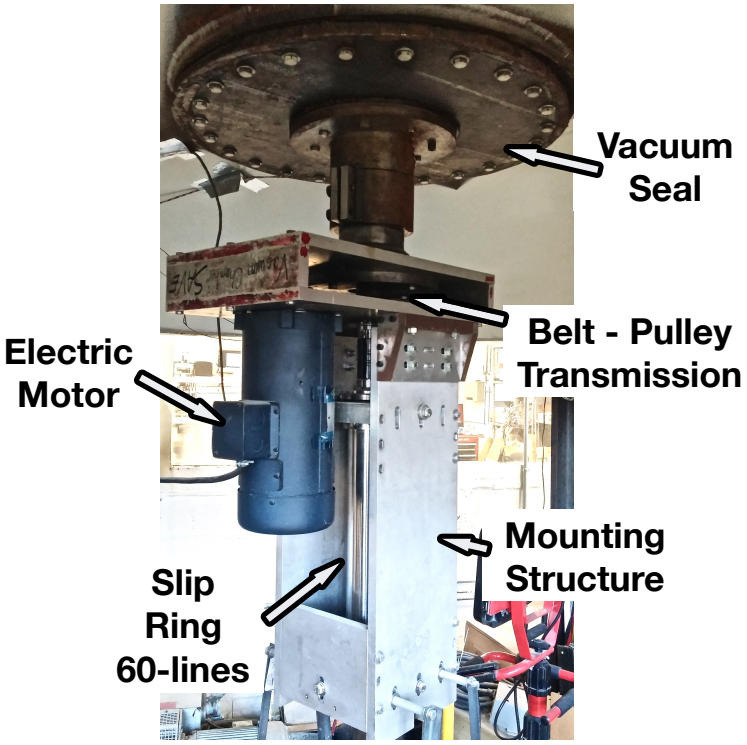

Figure 2.75: Vacuum chamber drive motor and slip ring.

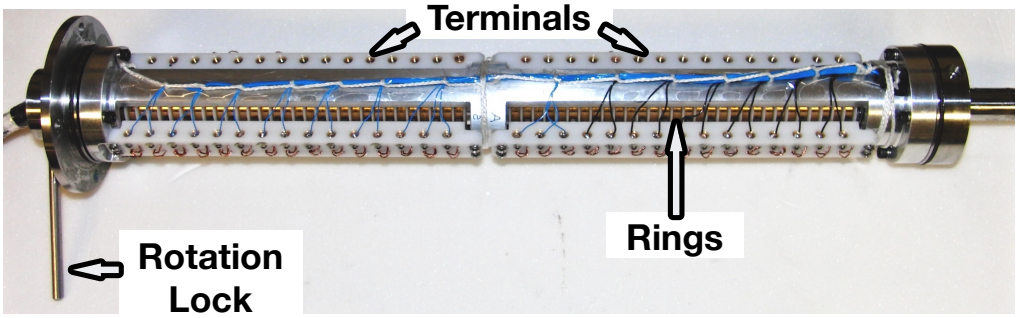

Figure 2.76: Slip ring used in vacuum chamber experiments.

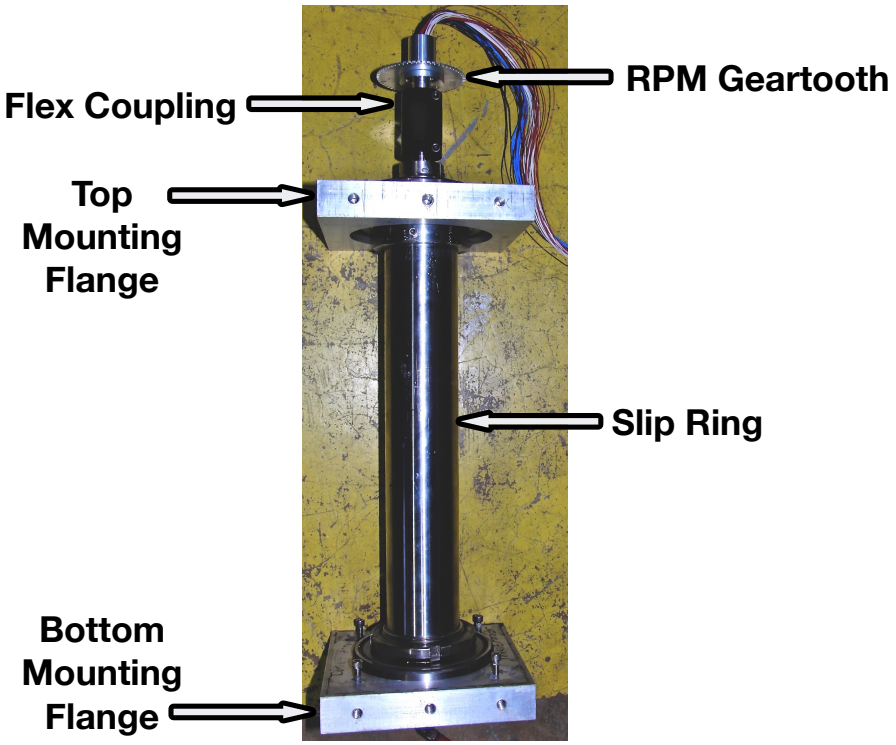

Figure 2.77: Slip ring mounting structure at the Vacuum chamber.

2.10 Glenn L. Marin Wind Tunnel

The Glenn L. Martin Wind Tunnel at the University of Maryland is used to test the Mach-scaled rotor in forward flight conditions. It is a closed circuit tunnel with a rectangular test section 11 ft (3.35 m) wide and 7.75 ft (2.36 m) tall (Fig. 2.78), capable to operating at wind speeds of up to 230 miles per hour.

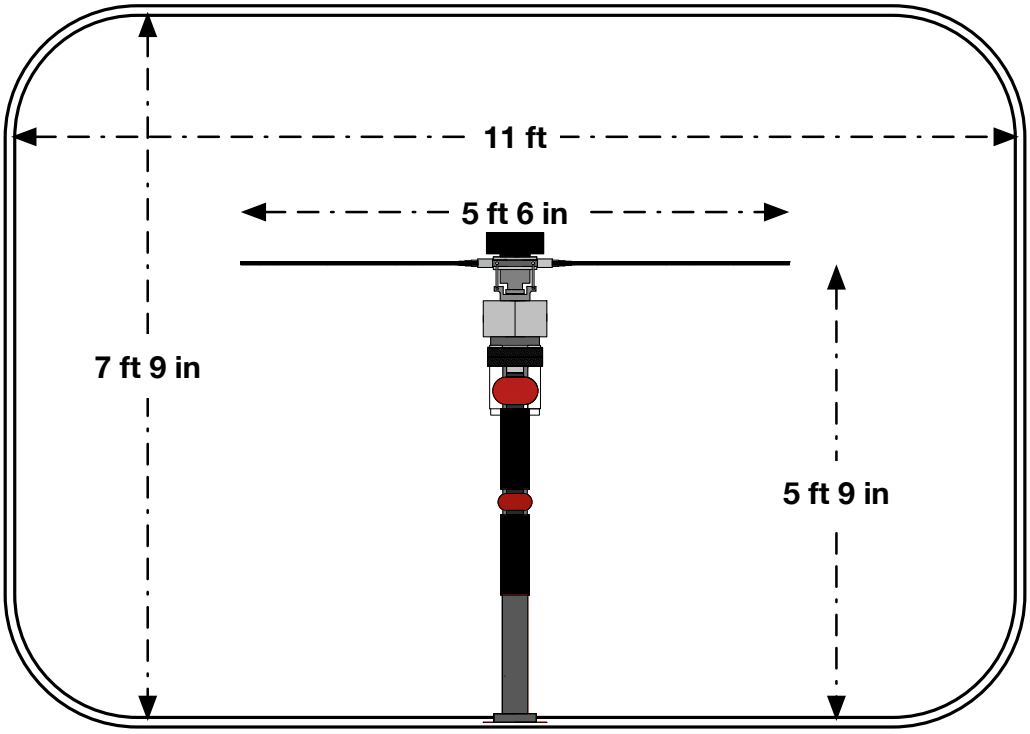

Figure 2.78: Test section dimensions with rotor model installed.

In the wind tunnel, the rotor stand is installed on a tiltable platform, that allows for adjusting the shaft tilt. There manual adjustments can only be made when the test rig is not operating as there is no actuator for making these adjustments during flight. In larger wind tunnels, usually a hydraulic actuator can adjust the shaft tilt. In addition, the wind tunnel balance is locked in order to avoid any softness in the support structure as it can lead to ground resonance like instability.

All the loads measurements are done by the six component hub balance and the torque cell. Figure 2.79 shows the four bladed rotor installed in the wind tunnel.

Figure 2.79: Rotor test stand installed in Glenn L. Martin wind tunnel.

2.11 Other State-of-the-Art Rotor Test Facilities

2.11.1 National Full-Scale Aerodynamics Complex (NFAC)

NASA Ames Research Center houses two of the largest wind tunnels in the world. Largest is an open circuit wind tunnel with a 80- by 120-ft test section [208]. The maximum test section wind speed is about 100 knots. The other is a closed-circuit wind tunnel with a 40- by 80-ft test section, with a peak wind speed capability of 300 knots. Over the years, several rotor aeromechanics testing have been carried out in these tunnels. Both of these facilities employ a common rotor test stand

referred to as Large Rotor Test Apparatus (LRTA) [209, 210].

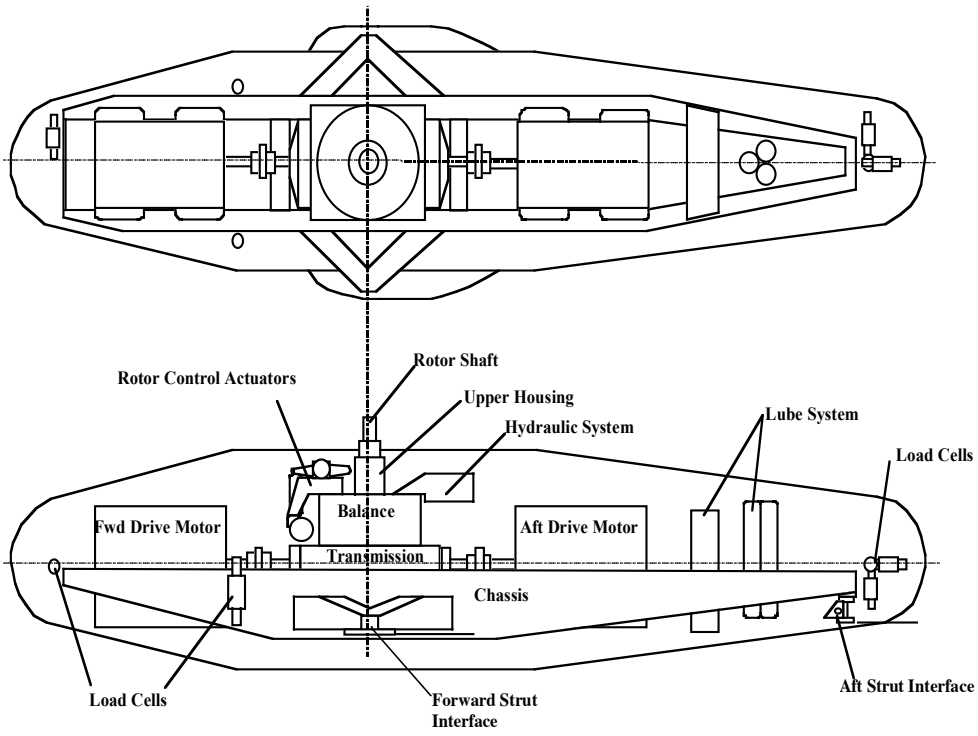

Figure 2.80: Schematic of Large Rotor Test Apparatus at NASA Ames Research Center.

The LRTA (Fig. 2.80) is a multi-purpose special drive and support system designed to test a number of configurations like isolated rotor, conventional helicopter, tilt rotors, tandem rotors, at thrust levels of up to 52,000 lbs, The rotors are powered by two 3000 HP electric drive motors, capable of counter-clockwise or clockwise rotor drive. The drive power is transferred to the rotor shaft by a two stage transmission limiting the maximum rotor speed to 320 RPM and 6000 HP peak shaft power. The LRTA is instrumented with a five component hub balance to measure steady and dynamic rotor loads as well as an instrumented flex-coupling to measure rotor torque. In addition, the fuselage is installed with a six-component load cell system to measure steady fuselage loads. The rotor control system is swashplate

based and can provide primary control using linear high authority low-speed electric actuators as well as higher harmonic control (0 - 25 Hz) using a limited authority high bandwidth rotary-hydraulic actuators. Finally, the output shaft assembly has a replaceable mating arrangement to accommodate a number of rotor systems like articulated, bearing-less or hingeless rotors. The LRTA is mounted on three adjustable struts from the wind tunnel floor, allowing to set the model at desired pitch or roll orientation.

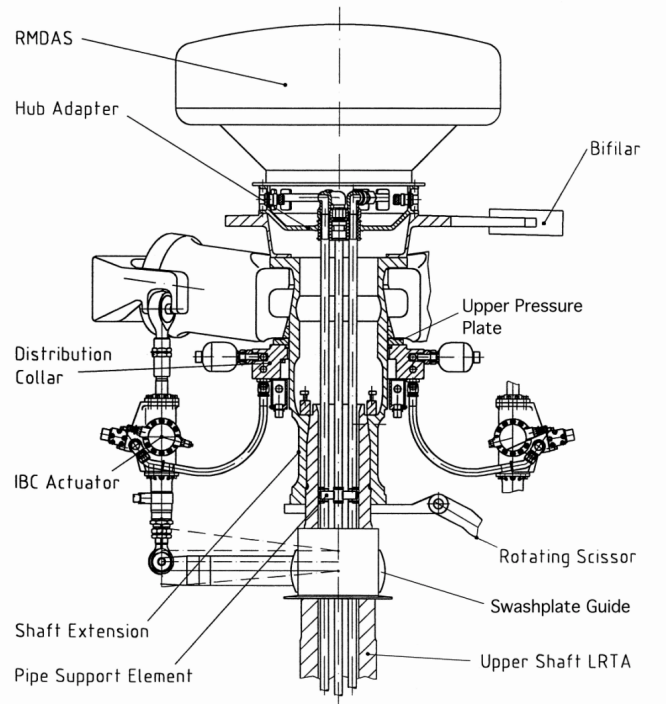

Figure 2.81: Schematic of rotating hardware used with Large Rotor Test Apparatus at NASA Ames Research Center.

A Rotor Mounted Data Acquisition System (RMDAS) [211] is used to acquire, digitize, and store rotor based rotating frame measurements (Fig. 2.81). The proximity of the data acquisition system to the on-blade sensors and transducers ensures high signal - noise ratio for the data. The RMDAS consists of two concentric mod-

ules, each capable of supporting 64 transducers, by providing excitation, filtering, amplification, signal offset and digitization. The data is stored on the unit and is transmitted wirelessly to the control station at a preset bandwidth. The tunnel specific data, rotor data and other safety parameters are all monitored in-real time to ensure that the rotor is operating at the desired test condition.

2.11.2 NASA Langley Transonic Dynamics Tunnel (TDT)

Although full-scale testing of rotor models is the closest approximation to flight tests, the cost and effort to operate these full-scale facilities is phenomenal. In such a situation, it is justified to test a properly scaled down model of the actual rotor, and carryout aeroelastic examination. The choice of scaling is based on similarity parameters and test objectives, which are discussed in detail in following sections.

The Transonic Dynamics Tunnel is a closed-loop, continuous-flow tunnel with a 16- by 16-ft test section, capable of operating at a range of Mach number, from near zero to Mach 1.2. Rotor models with up to 10-ft diameter rotors can be tested in this test section. Typically, the tunnel is used to test roughly 1/5th scaled rotor models. In general, either the tip Mach number or the Froude number of the scaled rotor can be matched to the full-scale rotor. However, a unique capability of the TDT is the ability to control the density of the test medium using heavy gas (R-134a). This allows to match simultaneously the tip Mach number as well as the Froude number of the scaled model to the full-scale rotor.

The rotor test rig used at this facility is referred to as Aeroelastic Rotor Ex-

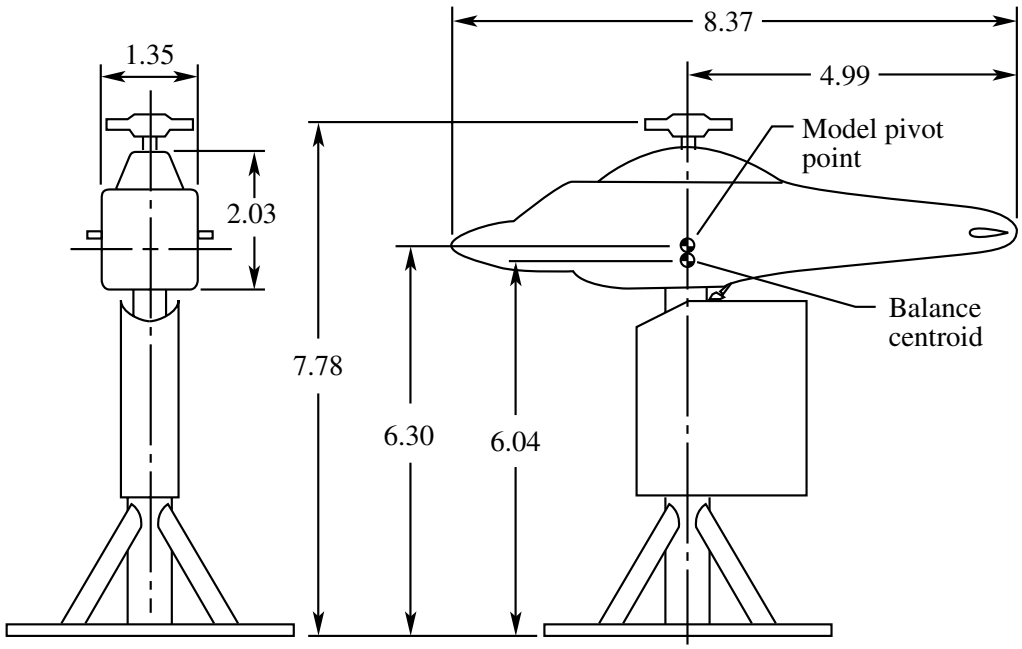

Figure 2.82: Schematic of Aeroelastic Rotor Experimental System at NASA Langley Transonic Dynamics Tunnel.

perimental Setup (ARES) (Fig. 2.82). It is powered by a water-cooled variable frequency synchronous electric motor rated at 47 HP at 12,000 RPM. A two-stage, belt-driven transmission system is used to drive the rotor shaft to boast the available shaft power, and reduce the rotor speed. The rotor is control by a swashplate actuated by three independent hydraulic actuators. In addition, a single hydraulic actuator controls the shaft-tilt of the rotor. The main shaft is so designed to easily accommodate three available rotor hub types: teetering, articulated or hingeless.

A six-component strain-gage based fixed frame balance is placed under the rotor to measure the hub loads and moments. In addition to the tunnel parameters, rotor azimuth position, rotor speed, blade motions, fixed frame accelerations and

pitch link loads are continuously monitored and recorded. A 30-channel slip ring is used to transfer all rotating-system data to the fixed system. An additional high-voltage slip ring is also available to power any rotating frame actuators. Finally, the rotor controls and drive system are enclosed in a streamlined fuselage, and care is taken to structurally isolate it from the rotor system to ensure that body loads are not registered by the hub balance.

Further details about NASA TDT and ARES testbed are included in [212–215].

2.11.3 Co-axial Rotor Test Rig at University of Texas - Austin

Recently, a Mach scale co-axial rotor test rig has been operationalized at University of Texas - Austin [216,217]. The coaxial transmission consists of synchronous serpentine belts and toothed pulleys driven by a 100 HP hydraulic motor. The transmission is mounted on a support column such that the lower rotor plane is 4.32 m above ground. The rotors have a diameter of 2.032 m, and consist of four, constant chord, untwisted blades with a VR12 airfoil profile. Each rotor hub is mounted on a modified ATI Omega 160 6-axis, strain-gage based load cell, enabling measurement of individual rotor loads in the rotating frame. The load cell signals are conditioned and amplified in the rotating frame before passing through slip rings, enhancing the signal to noise ratio.

Additional measurements include fixed-frame accelerations motor torque and power, 1/rev trigger signal and a 60 per revolution optical encoder. Hub loads and accelerations are acquired.

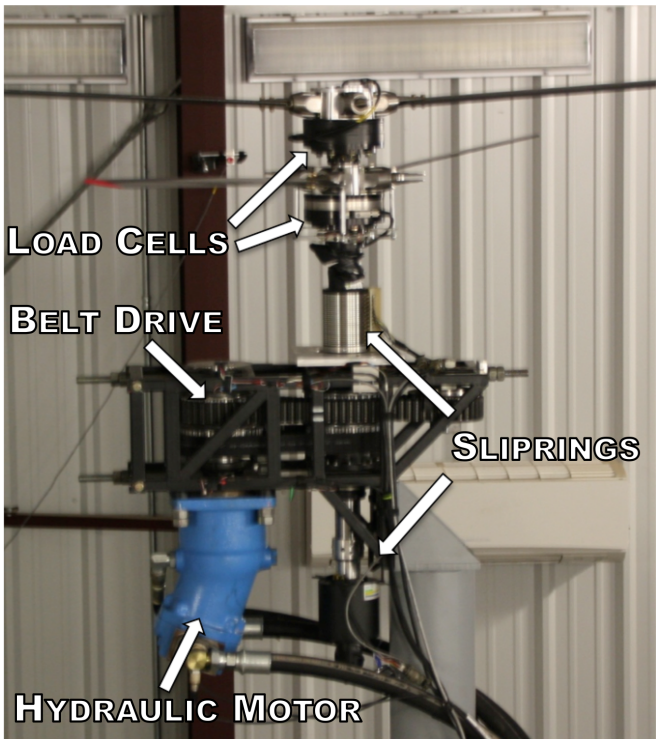

Figure 2.83: Co-axial rotor test facility at University of Texas Austin.

2.11.4 Rotor Testing in DNW Wind Tunnel

Higher harmonic control Aero-acoustics Rotor Test (HART) has been a prominent model scale testing activity in Europe. It has been a large collaborative between German DLR, French ONERA, NASA Langley, and the US Army Aeroflightdynamics Directorate (AFDD). The testing was carried out at with a 40%-geometrically and aero-elastically scaled model of a Bo-105 main rotor in the open-jet anechoic test section of the German-Dutch Wind-tunnel (DNW).

The DNW is the world's largest acoustic wind tunnel and has outstanding aerodynamic and acoustic properties with low background noise. It has a 6.0 by 8.0 m open-jet configuration test section, where flow velocities of up to 80 m/s (262.5 ft/sec or 155 knots) can be reached. The tunnel also has excellent flow qualities,

since the flow uniformity is quite high and the unsteady disturbance amplitude is quite low over the total testing velocity range.

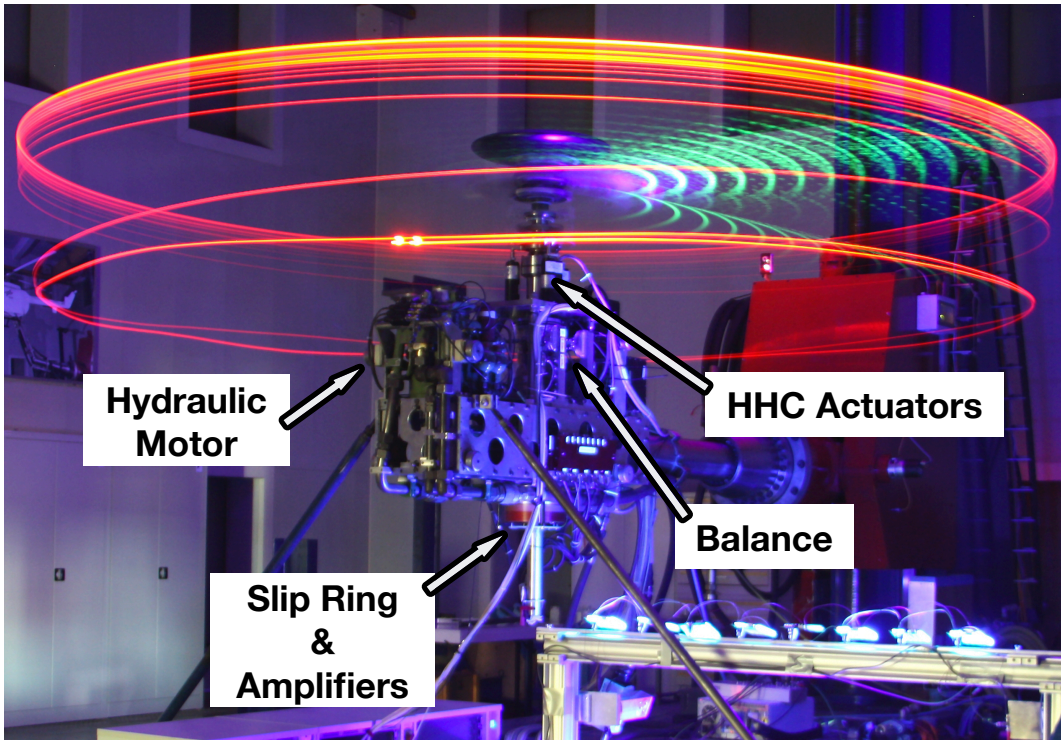

Figure 2.84: Rotor hub at DLR.

The rotor test stand [218] referred to as ROTEST (Fig. 2.84) is designed for model rotors with a maximum diameter of 4 m to provide good correlation with the corresponding full-scale rotor. The test facility consists of the drive system, the rotor balance, the control system, and the measuring system. The rotor is powered by an axial hydraulic motor connected by hydraulic lines to a remotely located electric drive pump. The hydraulic motor drives the rotor shaft by a tooth belt and has a performance of 130 kW at a maximum rotational speed of 1050 RPM. ROTEST is able to support different hubs for hingeless rotors like the Bo-105 as well as for articulated rotors. The rotor hub is mounted on a five-component

rotor balance, that measures the pitching and rolling moments of the rotor and the horizontal, lateral, and vertical forces. For a separate measurement of static and dynamic load components, the balance contains load cells and piezo-resistive transducers connected to the transmission rods in a serial arrangement. The rotor power is measured by a torque tube mounted between the upper and lower part of the rotor shaft.

The rotor control is realized by a swashplate system consisting of three electrodynamic actuators attached to the fixed system, the swashplate, and the rotating blade pitch rods. The computer controlled actuators provide collective and cyclic blade pitch control by adjusting the non-rotating part of the swashplate. Potentiometers at the blade roots measure the actual incidence angles of all rotor blades during rotation. The actuators for the swashplate control can be exchanged for electro-hydraulic HHC (Higher Harmonic Control) actuators to give the corresponding HHC inputs to the rotor blades. The measuring system provides data from both the body fixed sensors and the instrumentation in the rotating system of the rotor. It consists of miniaturized amplifiers in the rotating frame and a 256-channel slip ring system with a maximum frequency of 10 kHz. It allows to pre-amplify a large number of low-level sensor signals such as bending, torsion and in particular pressure distributions at the rotor blade with high resolution, before transmitting them as analogue signals to the fixed system.

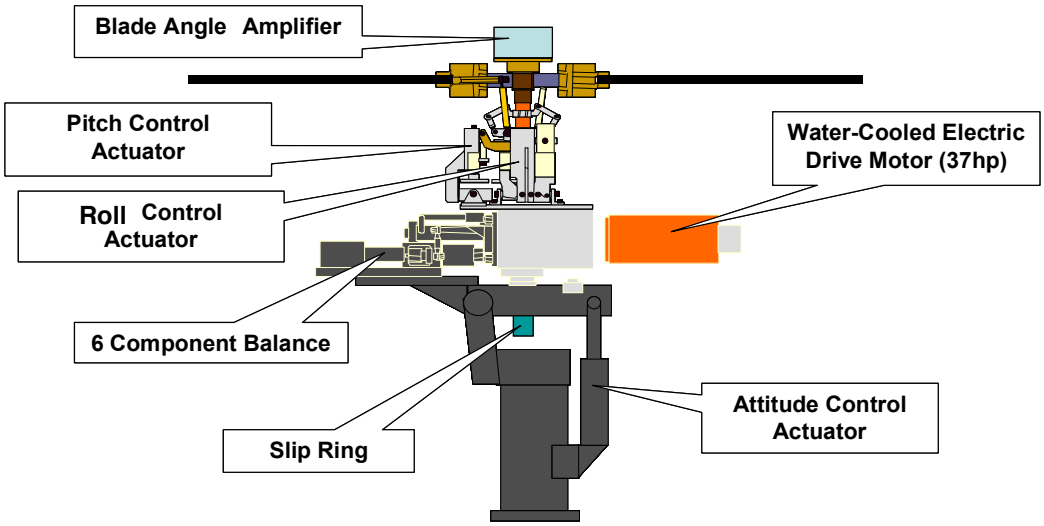

Figure 2.85: Schematic of rotor test stand at Japan Aerospace Exploration Agency.

2.11.5 Rotor Testing at JAXA

Model scale rotor tests are carried out at Japan Aerospace Exploration Agency (JAXA) [219] Low-speed Wind Tunnel. It is a closed circuit tunnel with a 6.5- by 5.5-m test section and a maximum wind velocity of 70 m/s (157 mph, 136 kts). The rotor test rig is referred to as JAXA Multi-purpose Rotor Test Stand (JMRTS) (Fig. 2.85). This rotor test stand was designed to drive different types of rotors in the wind tunnel for measuring aerodynamic and acoustic characteristics of the rotors. A typical configuration is a rotor with four 1.021 m radius, rectangular blades connected to the rotor head by hinges to allow flapping, lead-lagging and feathering motions. The wing section of the blade is NACA0012 with a chord length of 6.5 cm. The linear twist angle for the blades is -8 degree/m. The rotor shaft angle can only be changed together with the fuselage attitude. Rotor is driven with a water-cooled electric motor with a maximum output of 37 hp. Hall-sensors are placed at

the hinges to directly measure the flapping, lead-lagging and feathering angles. A six-component balance is used to measure hub forces and moments. The shaft angle can be adjusted by an attitude control actuator. The rotor system is mounted with a strut to place the rotor in the centre of the test section.

Chapter 3: **Bench Top Testing**

3.1 Introduction to Brushless DC Motor and Controller

Brushless DC motors are electromagnetic actuators, producing mechanical torque in response to electrical current. Figure 3.1 shows various components of a typical brushless DC motor. The copper winding stator encloses a permanent magnet shaft. This shaft is held in-place by a set of low friction radial bearings. A compact planetary gear-head is also installed on the output end of the motor shaft to mechanically augment the torque output from the motor. The stator-rotor assembly is protected by a stainless steel casing. Figure 3.2 presents the transverse view off the brushless DC motor, showing the relative position of each component.

One of the primary difference between the brushed and brushless DC motor is the means by which the motor windings are energized. In conventional DC motors, a ring and brush assembly is used to power the rotating copper winding ensuring continuous rotation of the shaft. This process is termed as commutation. In contrast, there is no commutation hardware in the brushless DC motors, instead they are electronically commutated using a motor controller. The controller energizes the copper windings based on the position of the magnetic rotor in relation to the stator windings. The operating principle of brushless commutation is discussed next.

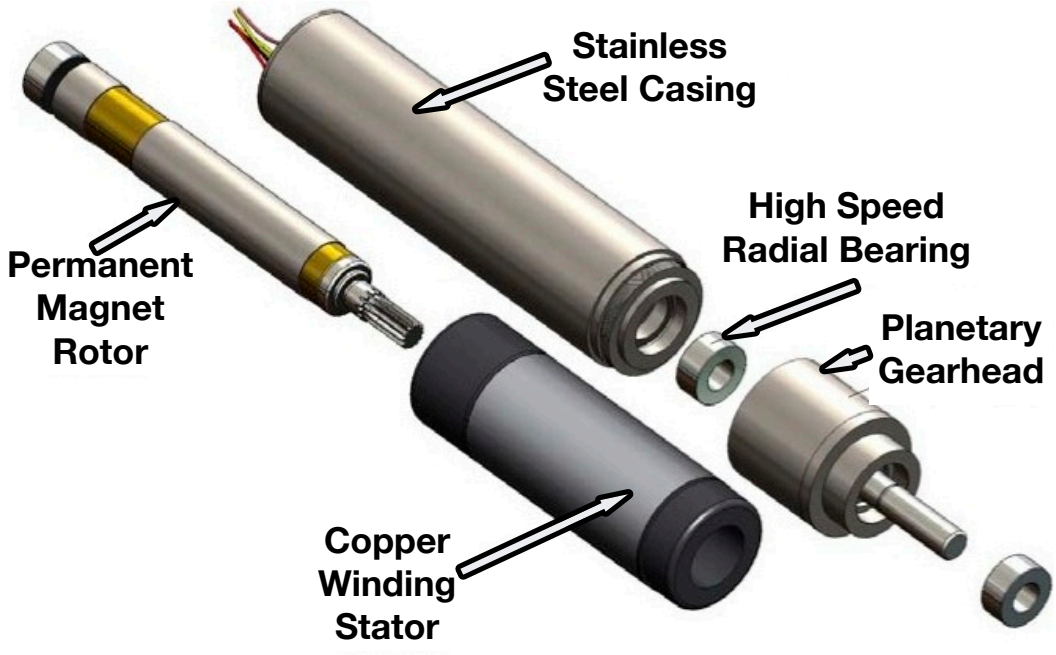

Figure 3.1: Components of a typical brushless DC motor.

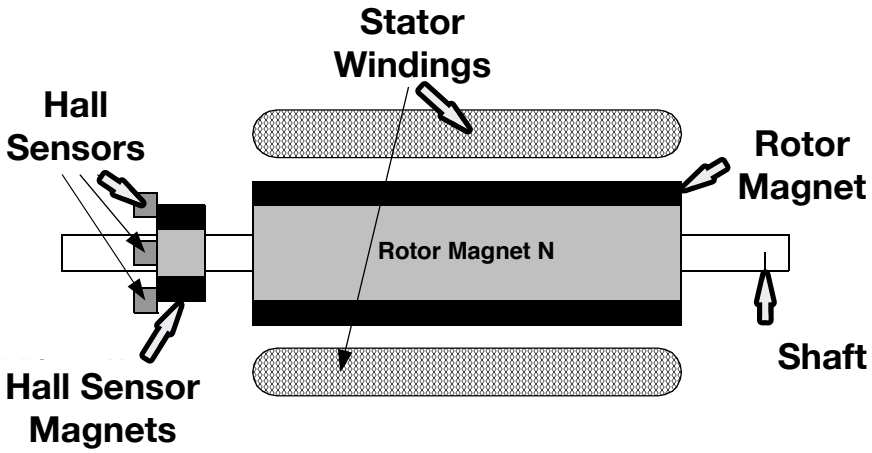

Figure 3.2: Transverse view of a typical brushless DC motor.

3.1.1 Operating Principle

For brushless DC motors, the magnetic field generated by the stator and the permanent magnet shaft rotate at the same frequency. Torque is produced because of the interaction between the magnetic fields generated by the stator coils and the permanent magnets. Ideally, the peak torque occurs when these two fields

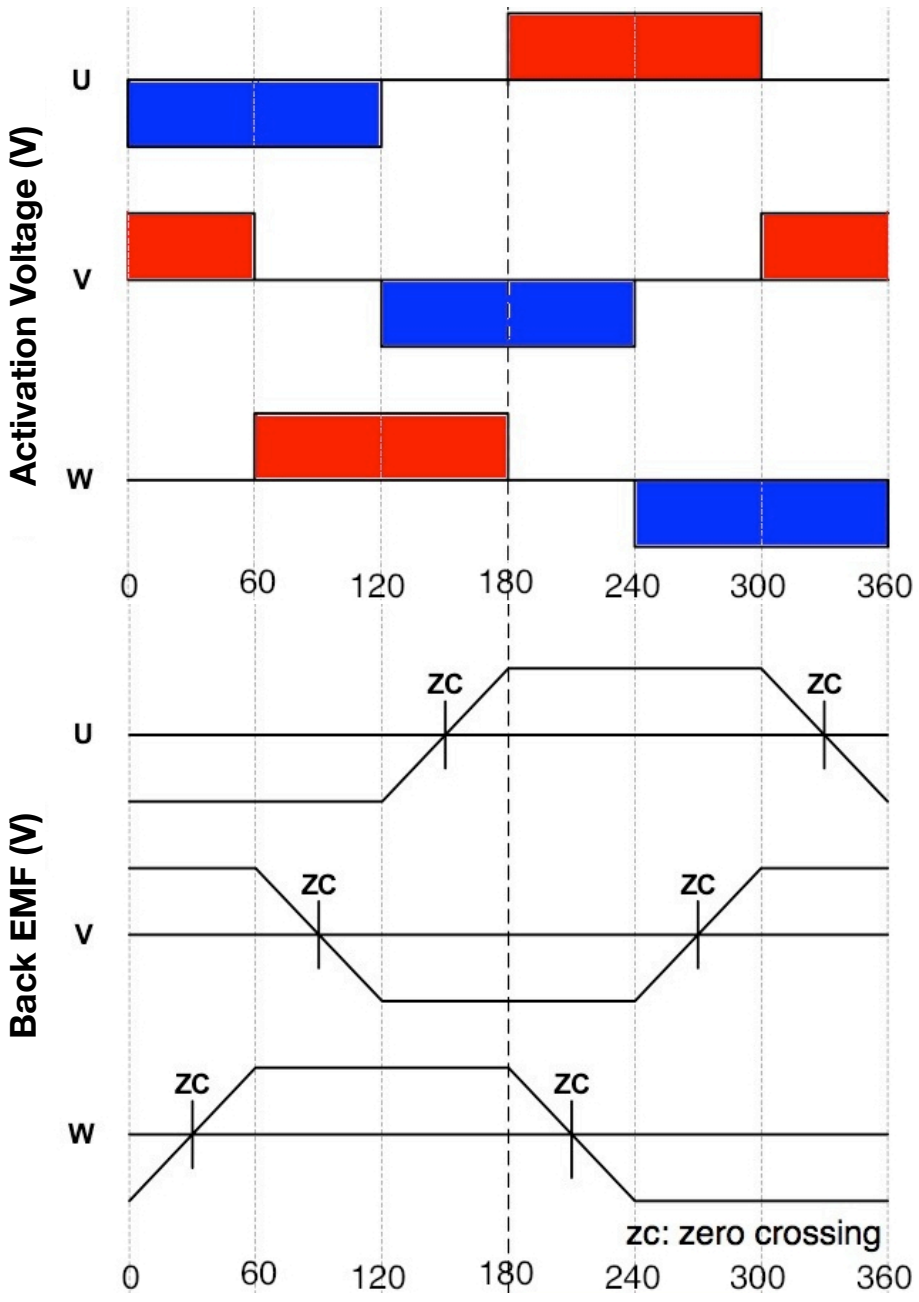

Figure 3.3: Winding excitation based on back EMF monitoring for commutation.

are at 90 degree to each other and falls off as the fields move together in phase. In order to keep the motor running, the magnetic field produced by the windings need to shift position, as the shaft moves to catch up with the stator field. The sequence of energizing the windings so as to keep the motor in motion is often

termed as commutation. For controlling the brushless DC motors, the knowledge of the position of the motor shaft is required. It can be achieved either by using Hall sensors or by monitoring the back-emf in the motor windings.

For the present application, sensor-less commutation was performed by the motor controller. Consider the sequence in Fig. 3.3. For the motor shaft motion from zero to 60 degree, one of the windings (U) is energized to positive power, the second winding (V) is powered negatively and the third (W) is in a non-energized condition. The rotor position is determined using the progression of the back-EMF in the unpowered winding (W). The controller evaluate the zero crossing of the back-EMF and commute the motor current after a speed dependent pause (30 degree after EMF zero crossing). Back EMF is proportional to the speed of rotation. When stalled or at low speed, the voltage signal is too small and the zero crossing cannot be detected precisely and special algorithms are required to run the motor [220].

3.1.2 Maxon Motor and Controller

Maxon EC-10 [221] precision brushless DC motor was evaluated as an on-blade actuator. It was 10 mm (0.394 in) in diameter, 26 mm (1 in) long and capable of providing 1.5 N-mm (13.27 lb-mil) of continuous torque. It was rated at 8 W and weighed 15 g (0.53 oz). A 4:1 planetary gear-head [222] was installed on the motor, weighing an additional 6.7 g (0.24 oz). A sensor-less commutation controller AECS 35/3 was used to drive the motor. Figure 3.4 shows brushless DC motor and motor controller. Fig. 3.5 shows the internal components of the EC-10 motor.

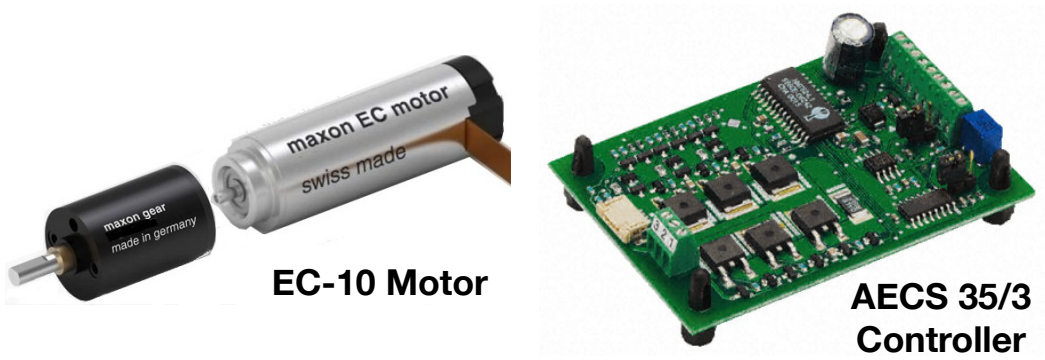

Figure 3.4: Maxon EC-10 motor with 4:1 gear-head and AECS 35/3 controller.

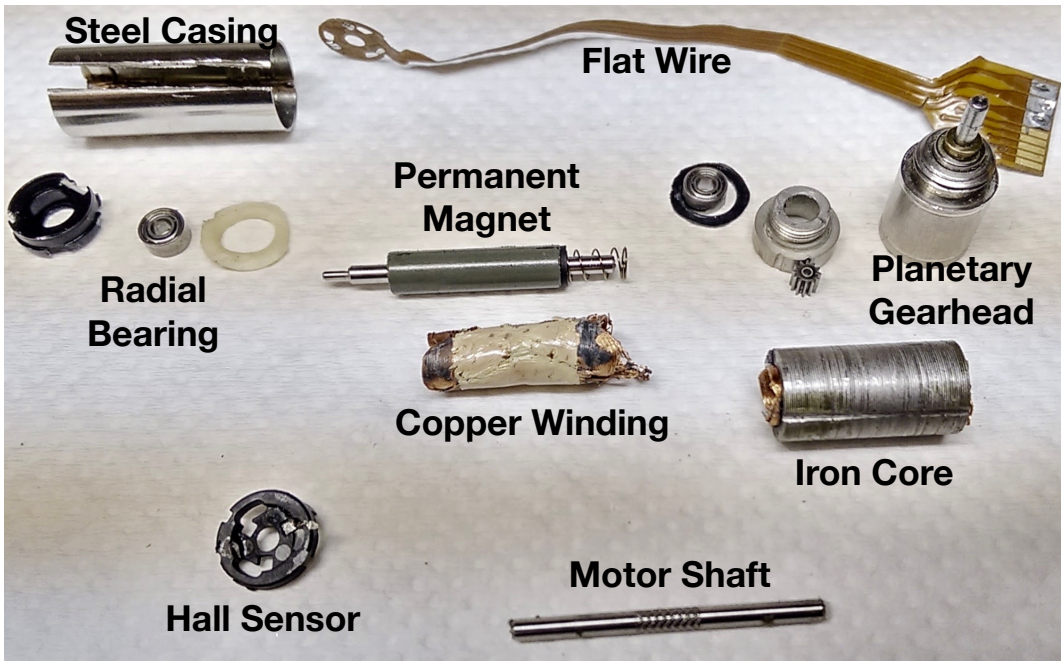

Figure 3.5: Internal components of a Maxon EC-10 motor.

The AECS (Analogue EC Controller Sensorless) [223] is a 1-quadrant EC amplifier for controlling electronically commutated brushless DC motors. Motor shaft position sensors were not required, rather the back-EMF was monitored for commutation. These controllers could be used for a wide range of input DC voltage range (8-35 V). The maximum continuous current was limited to 5 A. Motor speed could be set to predetermined value, or regulated using a built-in potentiometer. A

speed monitoring output could also be used to read motor speed. It also provides for logic based controls namely: *Brake* input allows the motor shaft to slow down to a halt, the *Direction* input adjusts motor direction, and the *Disable* input can interrupt the power supply to the motor. These controls were used to precisely manipulate the motor output to obtain desired flap amplitudes as will be discussed in Section 3.2. The winding excitation is controlled by integrated power MOS-FET power stages which provide for a high efficiency controller performance.

3.1.3 Maxon EC-10 Motor Characterization

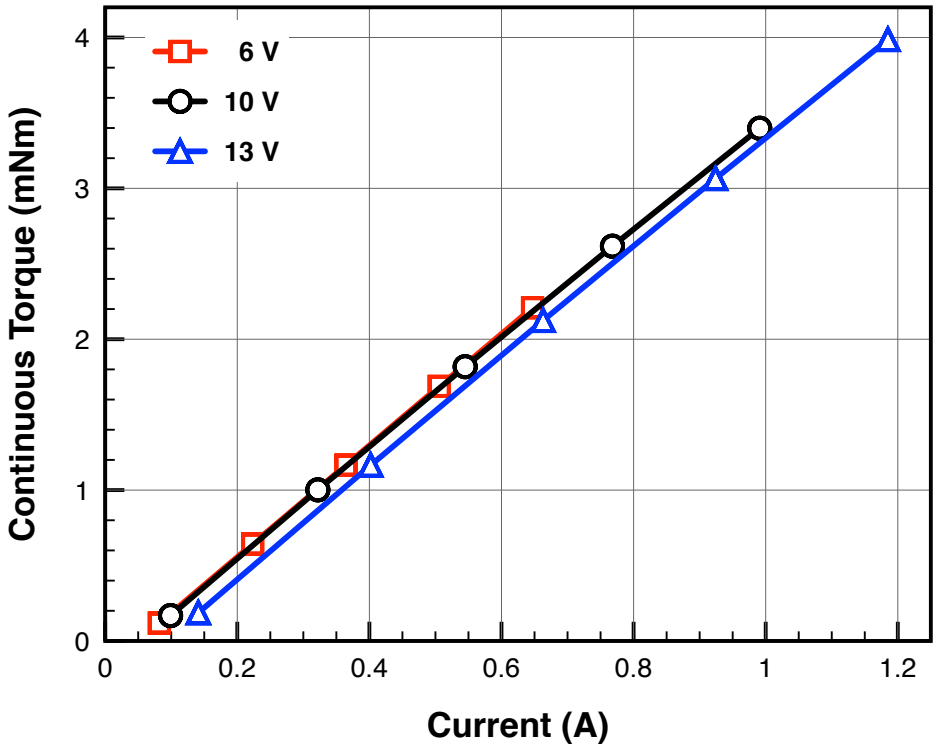

Figure 3.6: Maxon EC-10 motor torque-current characteristics.

A Magtrol MicroDyne hysteresis dynamometer and Yokogawa WT3000 power analyzer were used to characterize the EC-10 brushless DC motor. A full rpm

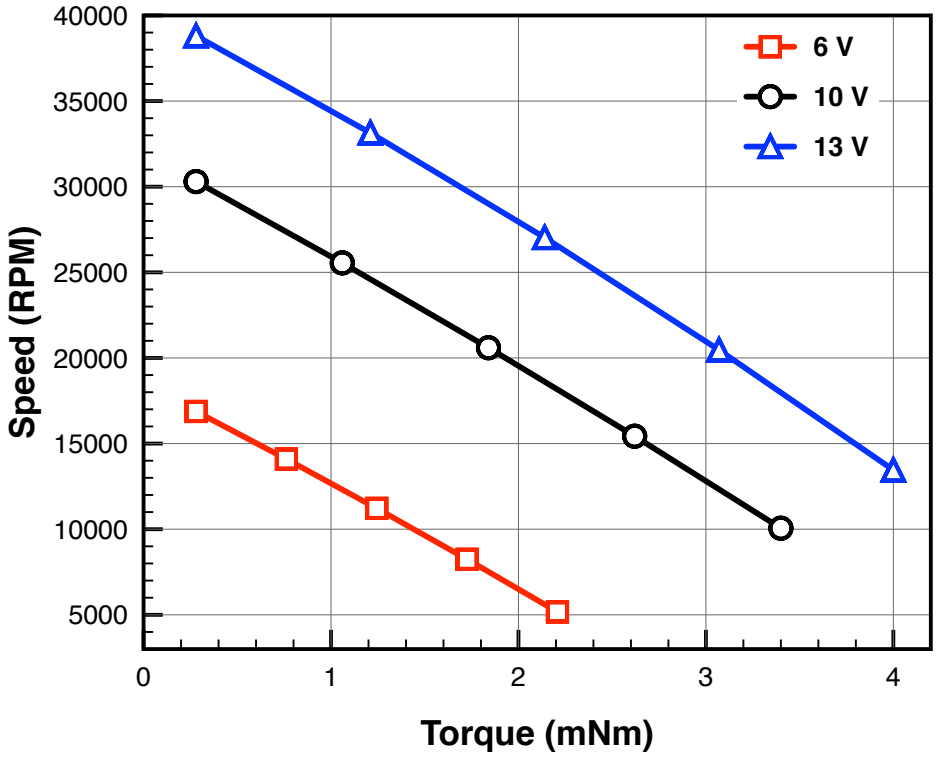

Figure 3.7: Maxon EC-10 motor speed-torque characteristics.

ramp, from free-run to locked rotor, was conducted for various motor input voltages. Motor torque, shaft rpm and winding currents were precisely recorded. Details of the experimental setup and procedure are included in [224].

At a given input voltage, the motor shaft rotates at the rated speed. The potential difference between the back EMF and the supply voltage is sufficient for the motor to draw the rated current and deliver the rated torque (Fig. 3.6). As the motor is driven beyond the rated speed, back EMF increases, which decreases the potential difference across the winding, thereby reducing the current drawn. This, in turn results in a drooping torque. At maximum shaft speed, the supply voltage is equal to the sum of the back EMF and the losses in the motor, and both the current and torque are equal to zero.

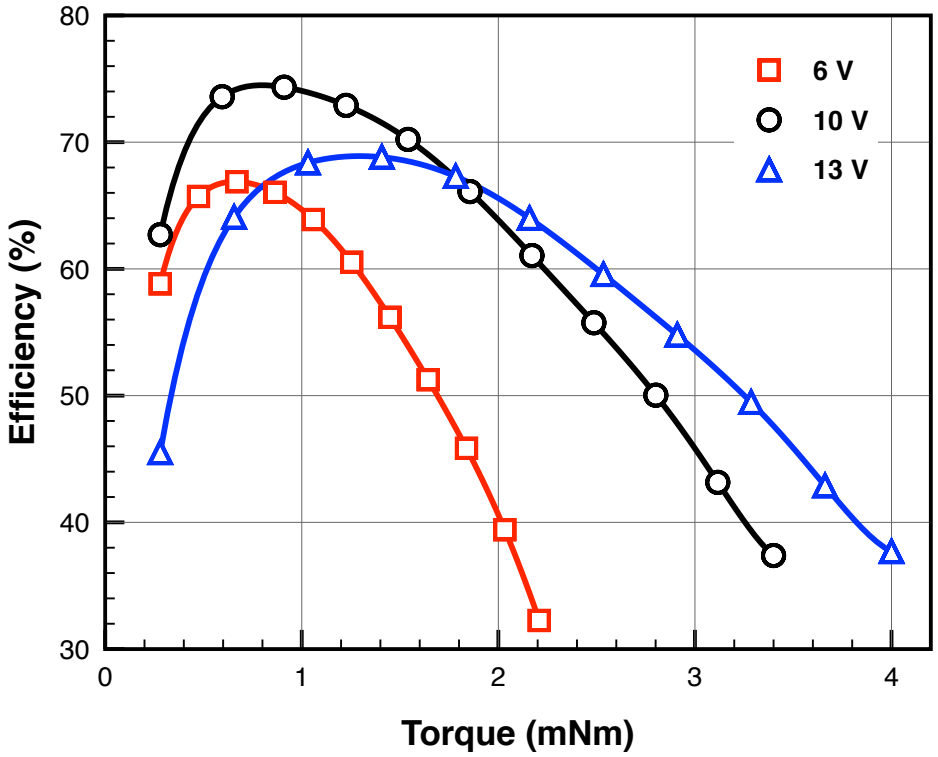

Figure 3.8: Maxon EC-10 motor efficiency characteristics.

Figure 3.6 is also referred to as motor torque characteristic and the slope of this plot is termed as torque constant (mNm/A). Figure 3.7 shows the mechanical behavior of the EC-10 motor at two input voltages, and the slope of this plot is termed as speed - torque gradient (rpm/mNm). Both the no-load speed and stall speed increase with increasing input voltage. For a given load torque, higher the input voltage, higher is the output speed (RPM). Finally, Figure 3.8 plots the motor efficiency at various input voltages. The peak motor efficiency was observed only when it was operated at rated speed and voltage, all other operating conditions had a lower efficiency.

To get a better understanding of the brushless dc motor, an electro-mechanical simulation model of the motor was developed [225–230]. Each stator winding con-

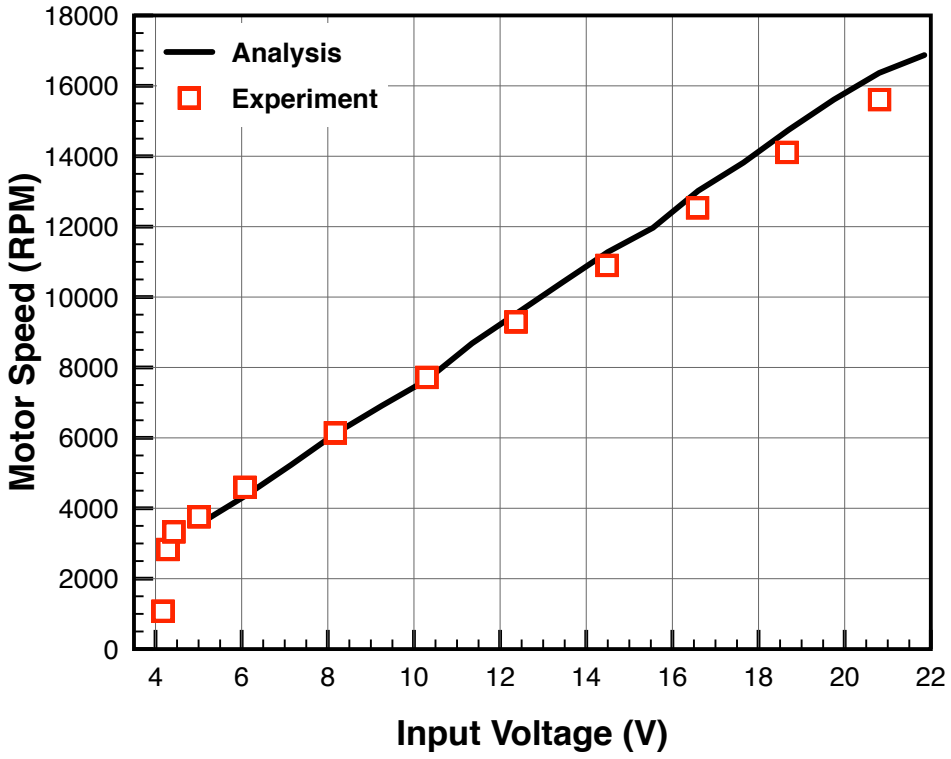

Figure 3.9: Maxon EC-10 motor speed-torque characteristics.

sisted of a series connection of a resistor and an inductor with a voltage source representing back EMF. The electrical characteristics of the motor were represented by Eqs. 3.1 and mechanical characteristic by Eq. 3.2.

$$\begin{aligned} v_{ab} &= R(i_a - i_b) + L\frac{d}{dt}(i_a - i_b) + e_a - e_b \\ v_{bc} &= R(i_b - i_c) + L\frac{d}{dt}(i_b - i_c) + e_b - e_c \\ v_{ca} &= R(i_c - i_a) + L\frac{d}{dt}(i_c - i_a) + e_c - e_a \end{aligned} \tag{3.1}$$

$$T_e = k_f\omega_m + J\frac{d}{dt}\omega_m + T_L \tag{3.2}$$

where v is the phase-to-phase voltages, i is the phase current, and e is the phase back-EMFs in the three phases a, b and c. Also, R is the phase resistance, L is the phase inductance, T_e is the electrical torque, T_L is the load torque, J is the

motor shaft rotational inertia, k_f is the friction constant and ω_m is the motor speed (RPM). The back EMF was assumed to be trapezoidal as well [227].

Figure 3.9 shows the comparison of the analysis with the measured data for Maxon EC 10 motor operating under no-load. The motor startup region at low voltage was not modeled in the analysis, good correlation was obtained at voltages above 5 V.

Brushless DC motors are compact, have high torque output, high efficiency, and long operating life [231], and demonstrate superior dynamic response and noiseless operation, making them highly suited for use as on-blade actuator applications where space and weight are critical factors.

3.2 Actuator Control Strategy

Brushless DC motors have been typically used to deliver continuous shaft rotations in response to the input voltages. However, to use these motors as on-blade actuators for rotor primary control, it is required to switch the direction of motor shaft rotation at frequency corresponding to 1/rev (up to 40 Hz) on the Mach scale rotor. Four-bar mechanisms have been traditionally used for converting the rotational motion to oscillatory (flap up-down) motion, but their output is limited to a pre-determined constant amplitude.

For the current research, a control strategy to actuate the flap at any desired frequency and amplitude was developed. Both the frequency and the amplitude of the flap motion were electronically controlled. The AECS motor controller was

capable of controlling both the motor speed as well as the direction of the motor shaft rotation. The direction of the motor shaft rotation was based on the logic level at the direction input terminal. The frequency of the direction logic input controlled the flap frequency and the flap amplitude was controlled by motor input voltage.

In addition to commanding the direction of the motor shaft rotation, the motor input power was disabled (turned off) for a part of the flap cycle. Using the scheme shown in Fig. 3.10, the motor was enabled when the flap deflects away from the mean position (O to A and O to B) and disabled for the rest of the cycle. The aerodynamic restoring moment would passively bring the flap back to the mean position (A to O and B to O). Further, by controlling the motor off-time (duty cycle of the disable logic signal), the amount of energy input to the motor was controlled. Controlling the input voltage and the input power to the actuator allowed for a precise control of the flap amplitude, and helped in lowering the operating motor temperature especially under high load conditions.

An on-blade actuator would operate under high centrifugal loads. Further, testing of a Mach scale rotor, imposes additional demands of scaled up centrifugal loads. To ensure its use as an on-blade actuator, the motor was systematically evaluated to ascertain its structural integrity, performance and repeatability for a range of test conditions.

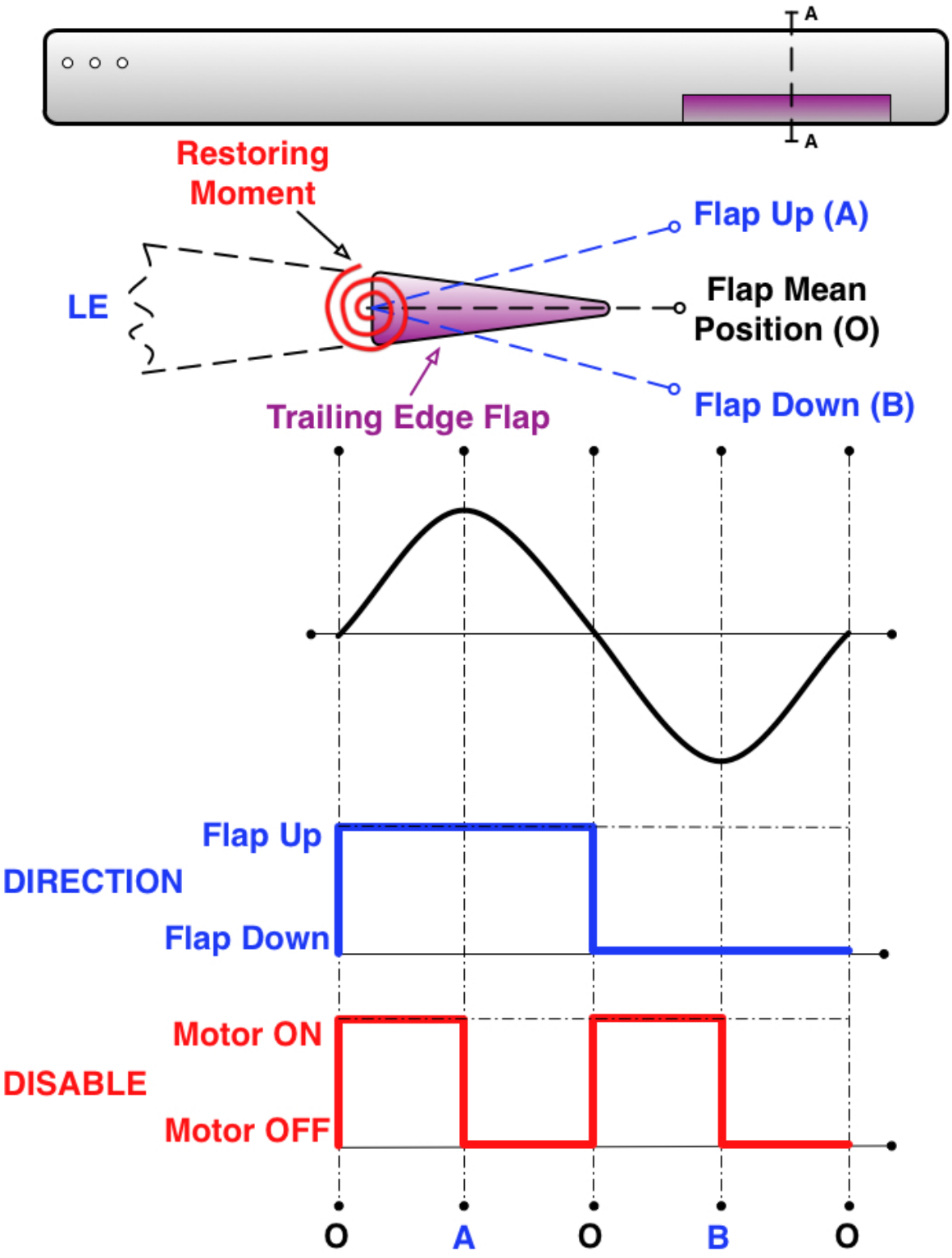

Figure 3.10: Motor driven trailing edge flap control scheme.

3.3 Bench Top Testing

A motor test stand (Fig. 3.11) was designed to evaluate the actuator and the control scheme on the bench top. Motor response to switching direction at 40 Hz (1/rev for the Mach scale rotor) was observed. The aerodynamic loading was simulated using a set of pre-strained torsion springs (Fig. 3.12). The brushless DC motor was mounted on a reaction torque cell to measure the torque output from the motor.

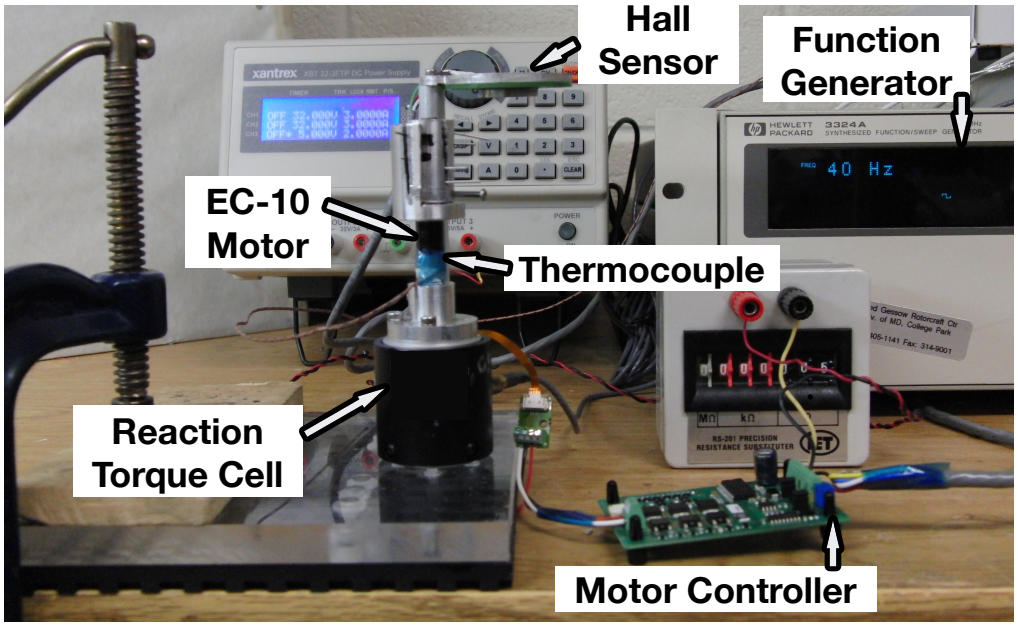

Figure 3.11: Bench top motor test stand.

Torsion springs provided a simulated aerodynamic torsion stiffness of 5.11 N-mm/deg (45 lb-mil/deg). Melexis rotary position Hall sensor was used to record the angular deflection. It is a contact-less rotary position sensor and detects the absolute angular position of a small diametrically polarized magnet attached co-axial with the shaft of the motor. The motor casing temperature and the electrical

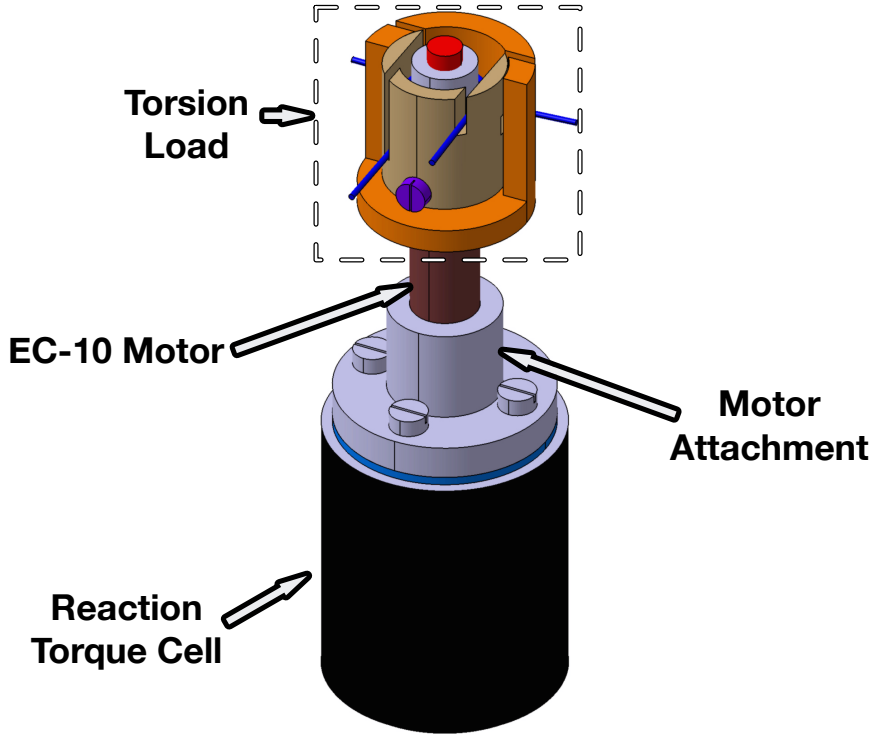

Figure 3.12: Detailed view of Bench top motor test stand.

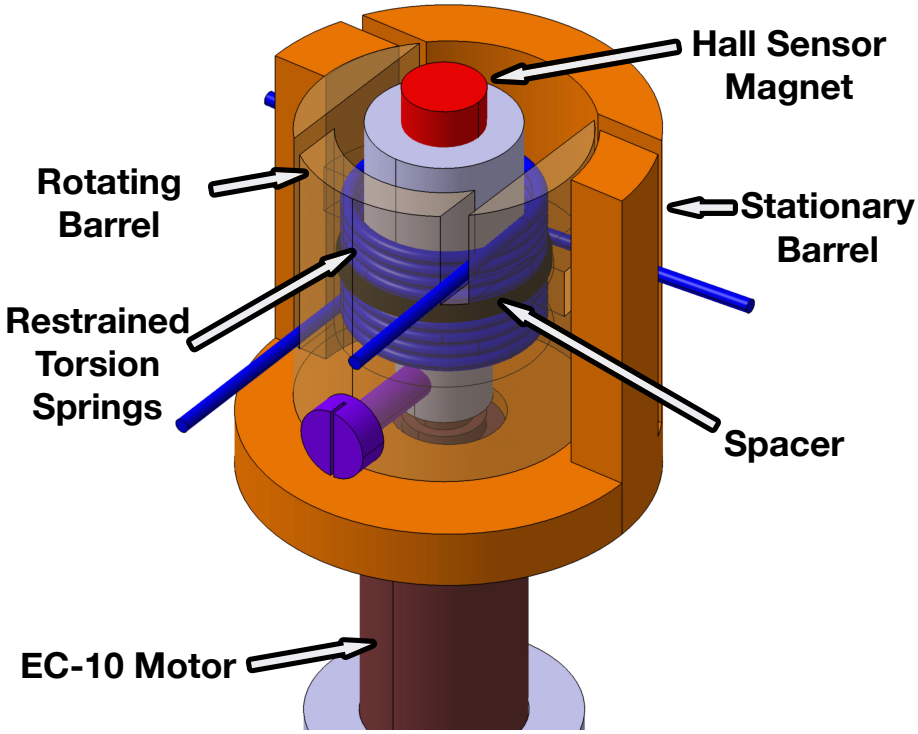

Figure 3.13: Detailed view of actuator torsion loading apparatus.

power consumed by the motor were also monitored.

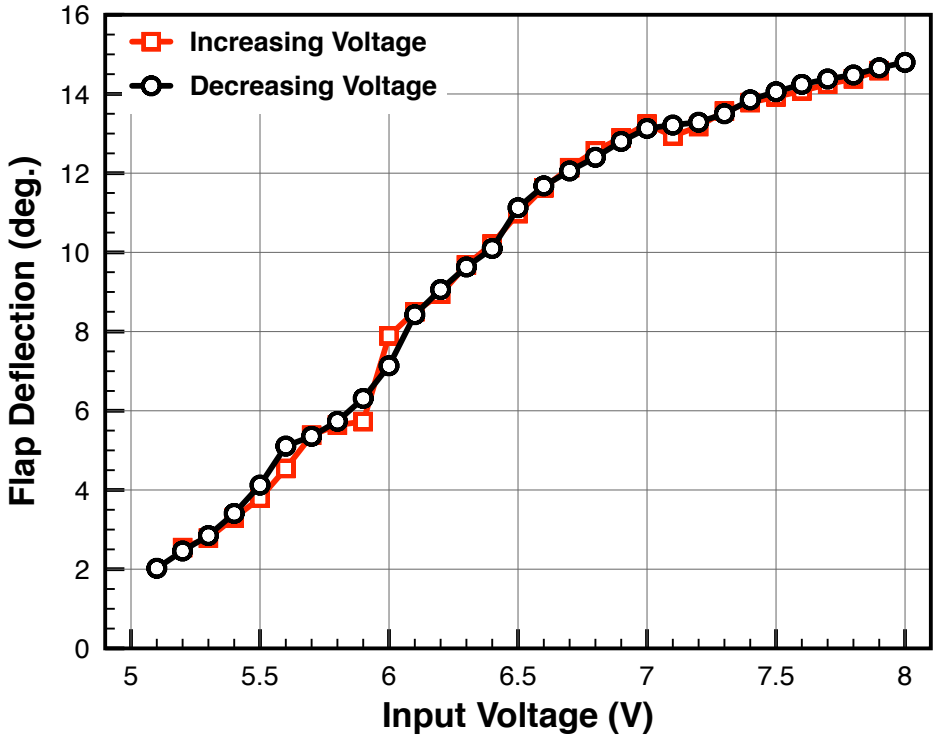

Figure 3.14: Half peak-peak flap amplitude on bench top, 40 Hz flap frequency.

Figure 3.14 shows the flap amplitudes obtained on bench top at 40 Hz actuation frequency. A range of flap amplitudes was obtained by varying the input voltage field. A 30 degree peak-to-peak amplitude was obtained and repeatability was established. Further, a steady flap mean position (Fig. 3.15) was maintained at various flap amplitudes. Figure 3.16 shows the temperature history for motor operating at peak amplitude and 40 Hz actuation frequency. The motor operated for extended time with no observable degradation in performance. Figure 3.17 shows smooth and consistent flap motion at 40 Hz flap frequency. Bench top tests clearly showed that the maxon EC-10 motor had enough control authority to actuate the flap and provided large amplitudes at the required flap frequency.

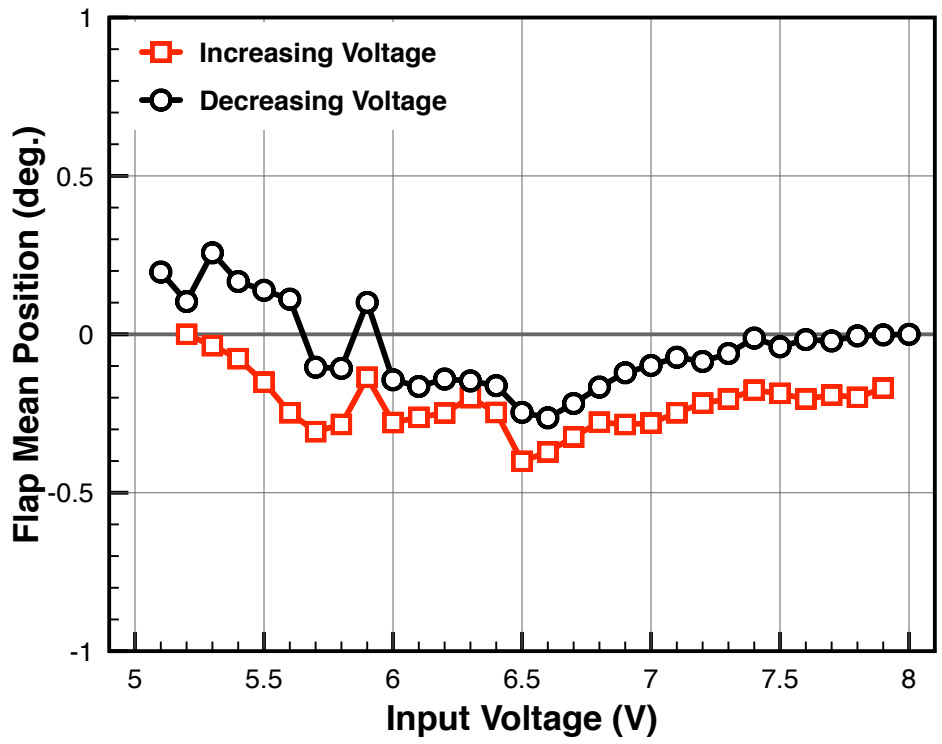

Figure 3.15: Flap mean position, 40 Hz flap frequency.

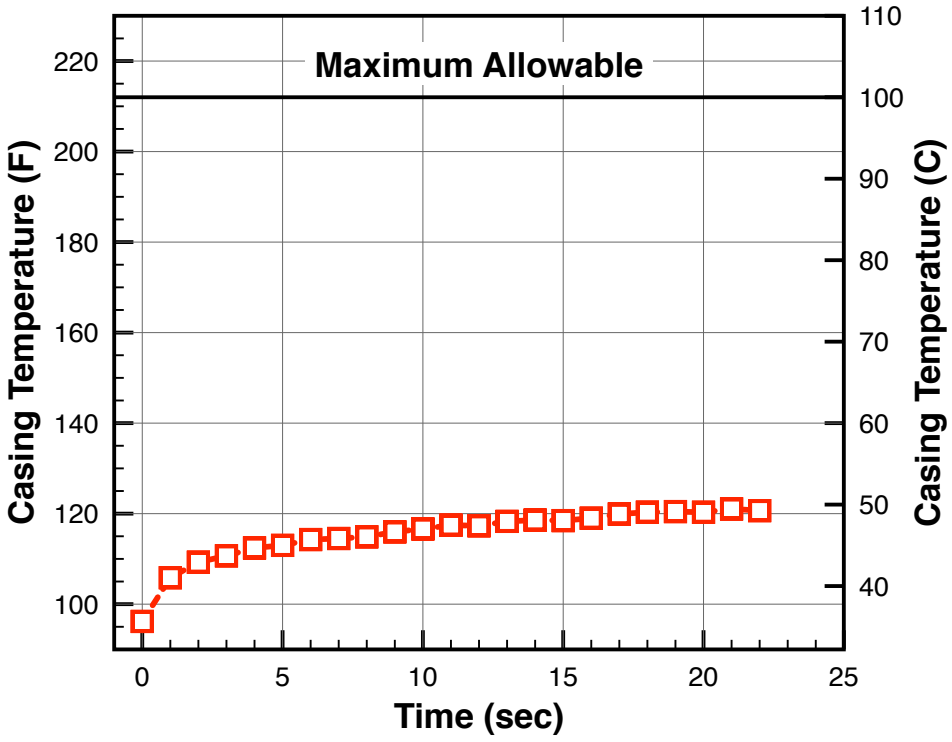

Figure 3.16: Motor casing temperature history for flap operating at peak amplitude.

3.4 Effect of Temperature on Motor Performance

The motor temperature is one of the most critical parameters affecting the motor performance. As the temperature increases, the winding resistance will increase based on the temperature coefficient of the copper winding. Also, the the magnetic flux density of the permanent magnet rotor decreases with increase in temperature. These are the two major parameters that dictate the motor performance at elevated temperatures.

The motor characteristics as provided by manufacturer or obtained experimentally are constant strictly only at the ambient temperature the motor was evaluated. As the load on the motor increases, the stator windings consume more current, which heats the copper windings increasing the the coil resistance. An increase in the winding temperature from 25 degree C to 75 degree C causes the winding resistance to increase by nearly 20% [232]. Mathematically, this manifests as decrease in torque and voltage constants. Physically, increase in operating temperature leads to an increase in the no-load motor speed and decrease in the motor output torque.

Additionally, the permanent magnet becomes weaker at higher temperatures (up to 10% decrease at 75 degree C depending on the material properties of the magnet). This effect is reversible, if maximum temperature ratings are not exceeded. However, higher resistance in stator coils and lower magnetic strength in the rotor, reduces the torque output of the motor.

Overall, a decrease of up to 30% in motor output power could be expected from a motor operating at 125 degree C compared to baseline performance a 25

degree C ambient temperature [233].

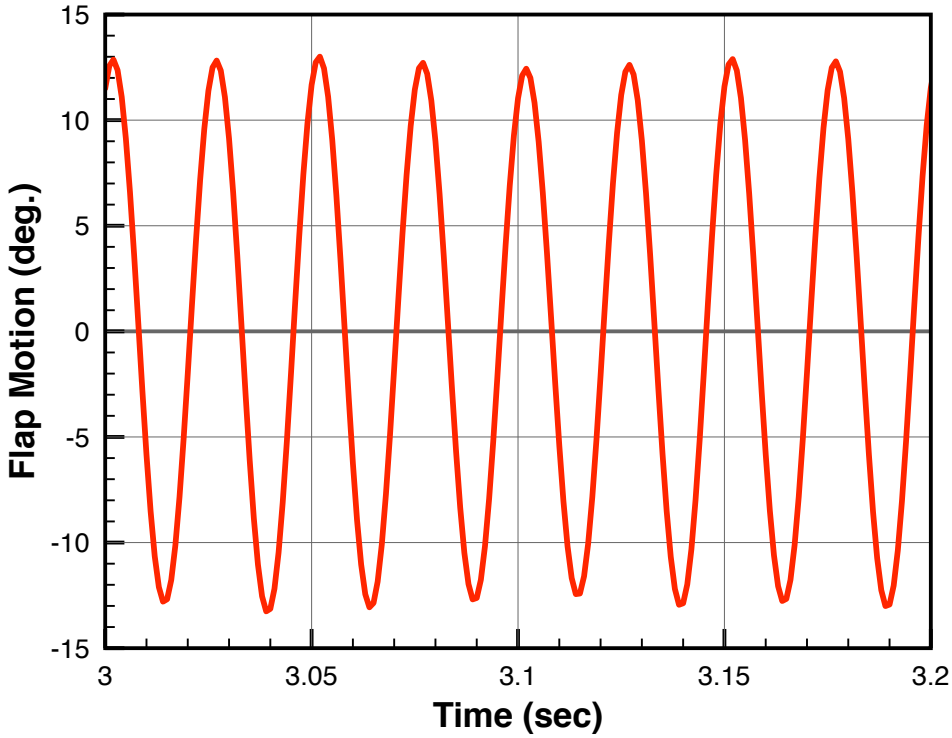

Figure 3.17: Time history of flap motion at 40 Hz flap frequency.

The maximum operational temperature is about 125 degree C for the motors used. If the winding temperature exceeds this limit, winding leakage current may cause a winding breakdown resulting in irreversible damage to the motor. To prevent any irreversible damage, the casing temperature was constantly monitored and kept below 100 degree C.

3.5 Comparison of Maxon EC-10 motor with PZT-5K4 Piezobender

A bench-top experiment was setup to compare the performance of the two actuators namely, 8-layer PZT-5k4 piezo-bender and Maxon EC-10 brushless motor with 4:1 gear-head. The piezo-bender actuator was assembled in-house. The number of layers, width of each layer, size of each layer among other parameters were optimized to ensure maximum d_{31} performance from the piezo-bender. The details of the piezo-bender optimization, assembly and performance are available in [186].

Both the piezo-bender and the brushless DC motor were used to actuate a flap at 40 Hz and were loaded under the same torsional stiffness of 45 mil-lb/deg (5 mNm/deg). using spring loads. The actuators can be compared on the basis of output energy per unit weight. The results are in Table 3.1.

It was observed that the brushless DC motor produced about six times more energy output per unit weight compared to the piezo-bender. This is directly an indication of the torque capability of the actuators; larger the torque output greater would be the capacity to negotiate the aerodynamic and inertial load moments on the trailing edge flap. The piezo and motor driven flaps have different mechanisms to transfer the output to the flap from the actuator. It is to be noted that this test doesn't include the inefficiencies due to respective mechanisms. Also, at model scale rotors, although both the actuators weigh about the same, the center of mass of piezo actuator is further aft of quarter chord compared to that DC motor. This leads to a heavier rotor with piezo actuated flaps as compared to a rotor with motor actuated flaps.

Table 3.1: Comparison of piezobender and brushless DC motor operating at 40 Hz.

	Piezobender PZT-5k4	Maxon EC-10 motor
Load torque	45 mil-lb/deg.	45 mil-lb/deg.
Max. half peak-peak amplitude	6°	15°
Output power	120.8 mil-lb/s	740.2 mil-lb/s
Actuator weight	16.6 g	17 g
Output energy/weight	0.45 W/kg	2.68 W/kg
Ratio	**1.0**	**6.0**

Chapter 4: **Design of Motor - Flap System**

A well designed mechanism to transfer the motion from the actuator to trailing edge flap was central to the success of a swashplateless rotor. The on-blade components on a sub-scale rotor were under large g-loads due to scaled up rotational speeds. In addition, the internal volume in the blade was limited. The challenge was to design a compact, lightweight and sturdy mechanism capable of operating under high g-loads, while resulting in minimum drag penalty from exposed parts. The design process was iterative, and major design milestones are discussed next.

4.1 Evolution of Motor - Flap System Design

Figure 4.1 presents the first generation of the motor-flap system design. The main purpose of the mechanism was to transfer the motion from the motor gearhead to the flap and incorporate about a 3:1 gear reduction. The oscillatory motion from the motor shaft was converted to push-pull motion of the flap rod by means of a shaft attachment. The shaft attachment connected to the motor at one end and has an eccentric hole on the other end, causing flap rod to push-pull on the flap mount in response to the back and forth motion of the motor shaft. The flap mount pivots about the hinge axis, producing the flap motion. Figure 4.2 shows the major

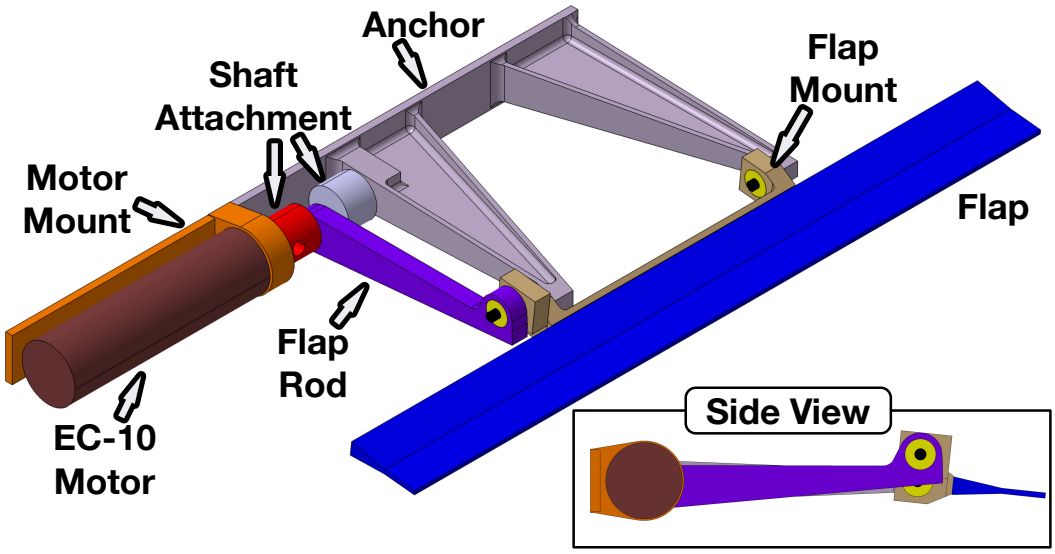

Figure 4.1: Motor-flap system - version 1.

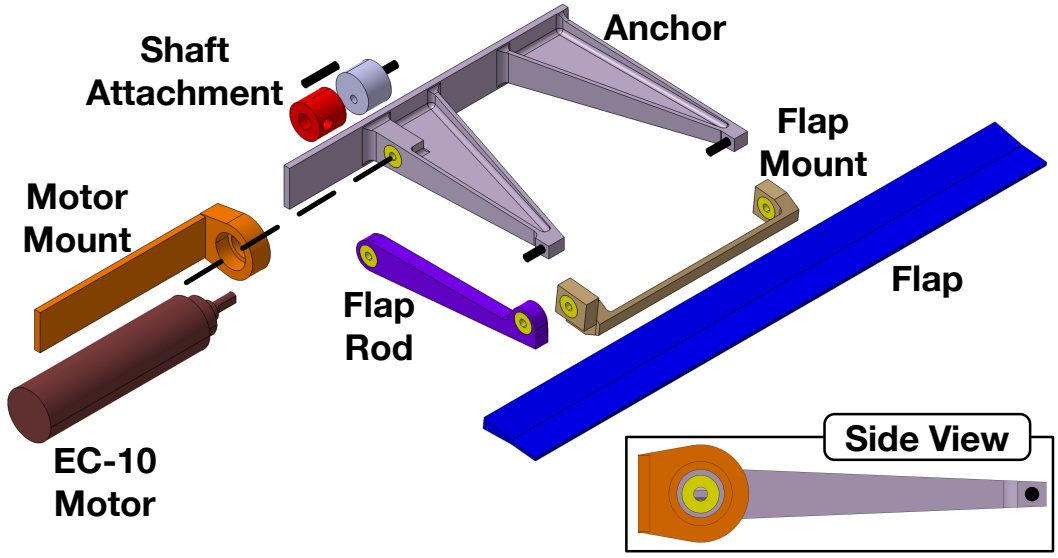

Figure 4.2: Components of motor-flap system - version 1.

components of the first version of the motor-flap system.

Upon testing it was realized that one of the critical areas was the alignment between the motor mount and the anchor. In addition to possibility of misalignment during assembly, the centrifugal force acting on the motor has the tendency to exaggerate this flaw. This was detrimental to smooth operation of the system.

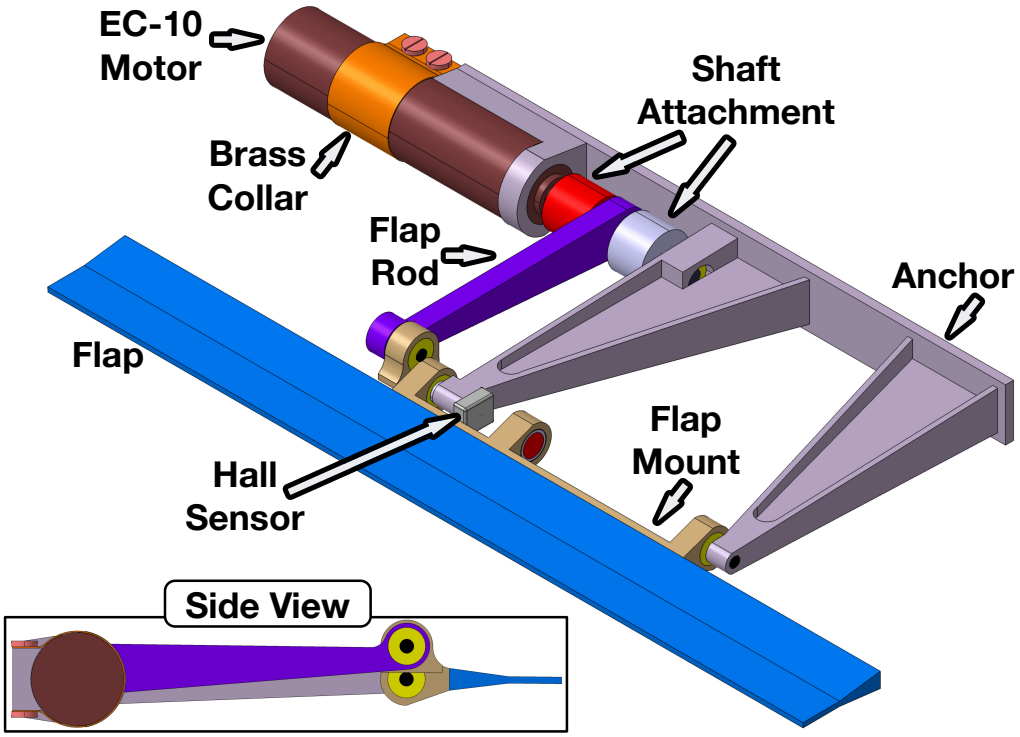

Figure 4.3: Motor-flap system - version 2.

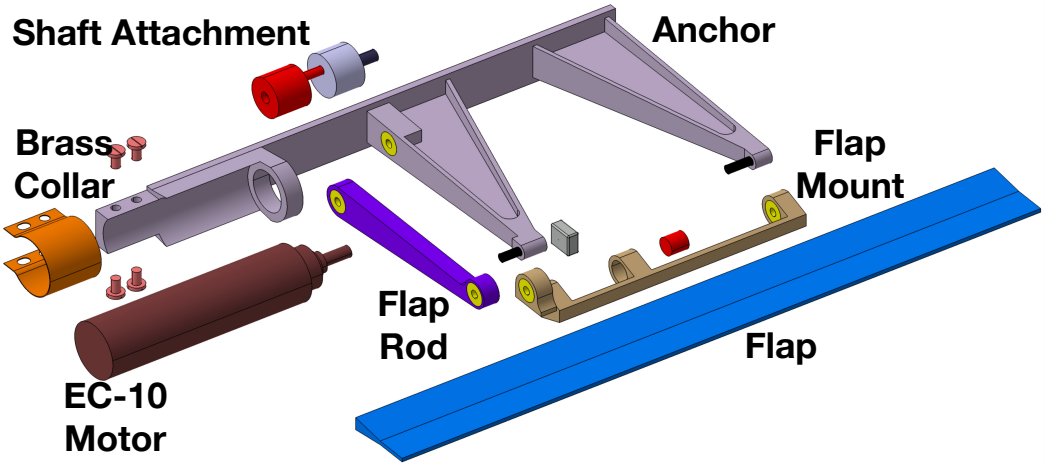

Figure 4.4: Components of motor-flap system - version 2.

The second iteration of the motor-flap system (Fig. 4.3) attempted to remedy the misalignment issue, by manufacturing the anchor and motor mount out of a single stock of metal. This eliminated possibility of misalignment while being assembled. In addition, the motor mount was designed with a cusp to better accommodate

the motor, as well as use the aluminum anchor as heat shield for the motor. A brass collar was also used to retain the motor in place while under centrifugal loads. This significantly reduced any misalignments under rotation. Figure 4.4 shows the major components of the second version of the motor-flap system.

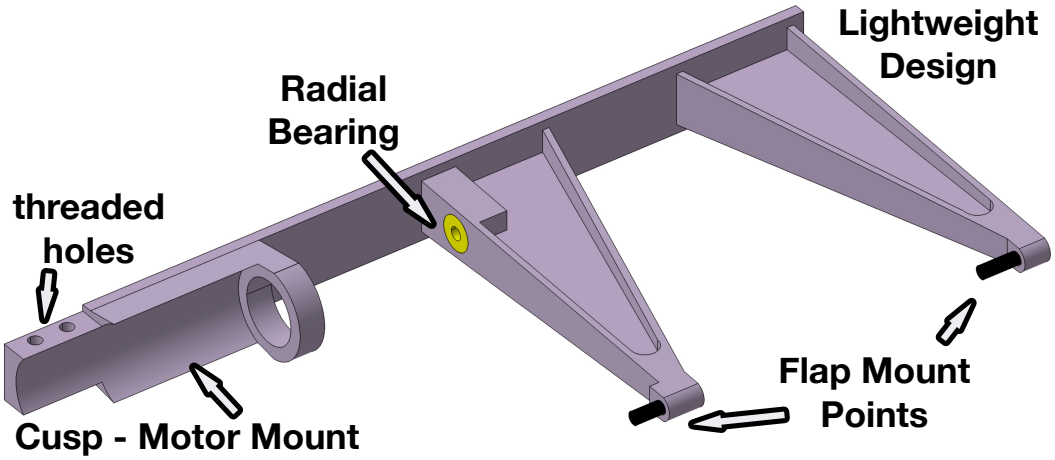

Figure 4.5: Anchor design details.

A lightweight aluminum anchor was designed to bond to the blade spar (Fig. 4.5). The anchor had a cusp to closely conform to the motor profile. The motor was screwed into the anchor and a thin layer of thermal paste was applied between the motor and the anchor cusp to ensure thermal conductivity at all times. This ensured that the whole aluminum anchor (an excellent heat conductor) acted as a heat sink for the motor. A thin brass shim supported the motor at the rear end, and kept the motor from misaligning under the centrifugal loads.

Figure 4.6 shows the final motor-flap system. A thrust bearings was placed in-line with the motor shaft to offload the centrifugal load on the permanent magnet rotor. Additional radial bearings were placed co-axial with the motor shaft to ensure low friction operation and alignment of the motor shaft and flap rod. Figure 4.7

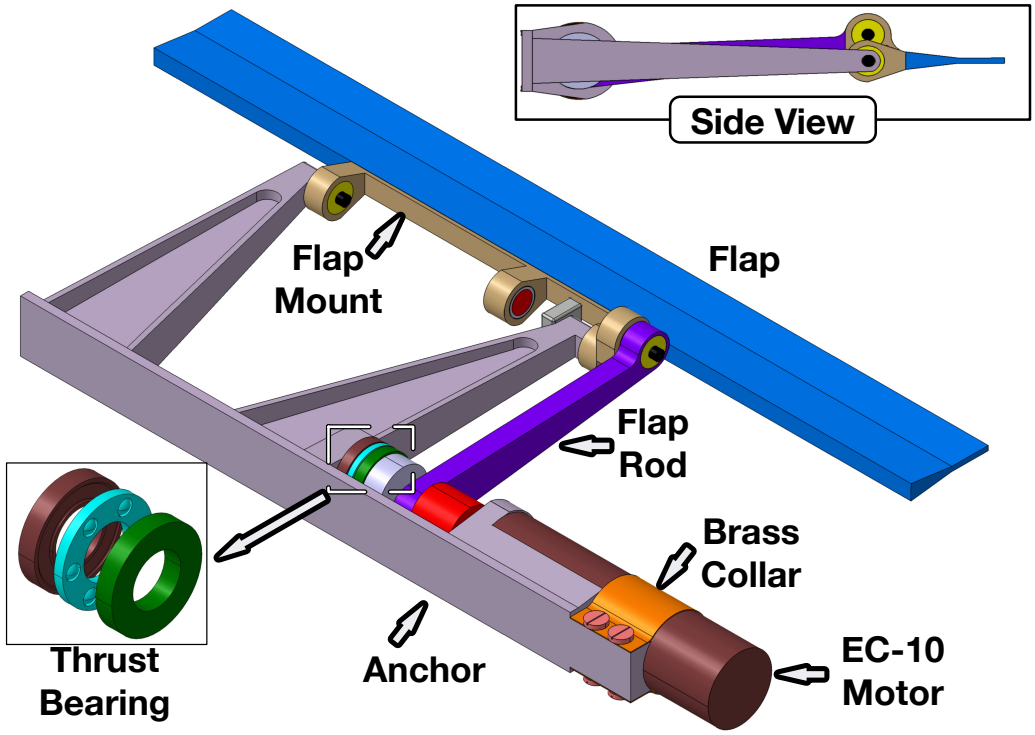

Figure 4.6: Motor-flap system - version 3.

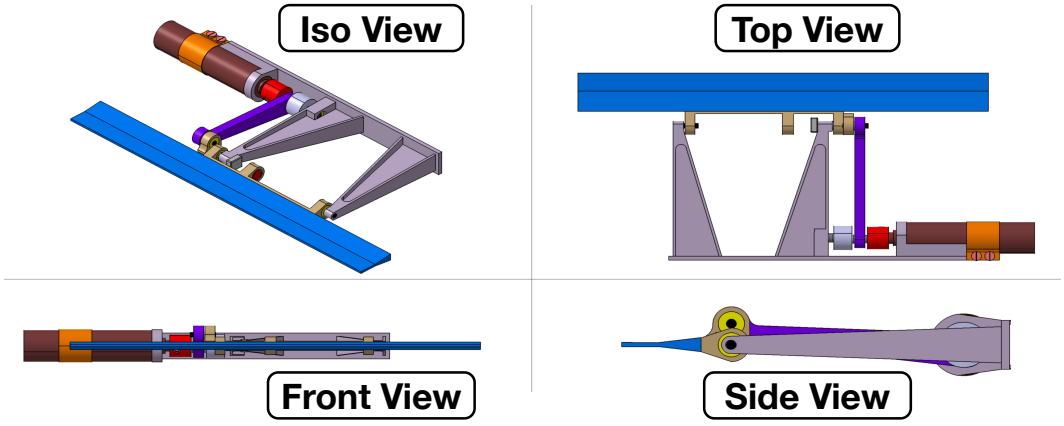

Figure 4.7: Multiple views of the final motor-flap system.

shows multiple views of the system and the complete weight breakdown of the motor-flap system is in Table 4.1.

Figure 4.8 shows conceptually the motor-flap system incorporated in the composite rotor blade and Fig. 4.9 shows the side view of the motor-flap system in the rotor blade. For the most part the system is well within the profile of the blade. At

Table 4.1: Weight breakdown of the motor-flap system.

Components	Weight (g)
Actuator	17
Flap anchor	6.8
Flap	3.2
Flap rod	1.2
Radial Bearings	1.1
Thrust Bearings	1.0
Flap mount	0.8
Shaft attachment B	0.7
Shaft attachment A	0.6
Brass shim	0.3
Hall magnet	0.2
Micro-washers	0.1
Miscellaneous	0.7
Total	**34**
% of Blade Weight	**11.2%**

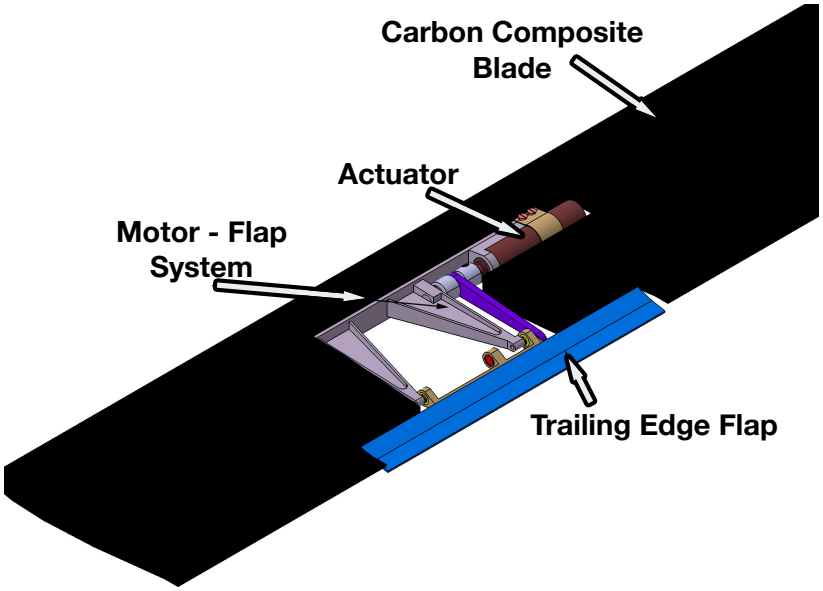

Figure 4.8: Isometric view of motor-flap system in the blade.

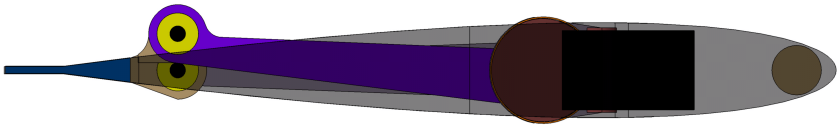

Figure 4.9: Side view of the motor-flap system in the blade.

the trailing edge, the space is especially limited and the flap mount extrudes outside the blade profile. Also, the frequency and the amplitude of the flap motion were electronically controlled by commanding the motor controller and were not limited by the design of the mechanism.

This system was next evaluated in the rotating frame, first in the vacuum chamber and then on the hover tower. The design of the motor-flap system was carried out iteratively. Several design changes were implemented as a result of testing under various loading conditions. The aim of these iterations was to achieve an optimum configuration, with minimal weight and enough strength to maintain the alignment of various components under centrifugal and aerodynamic loading.

4.2 Comparison of Flap Waveform with Analytical Results

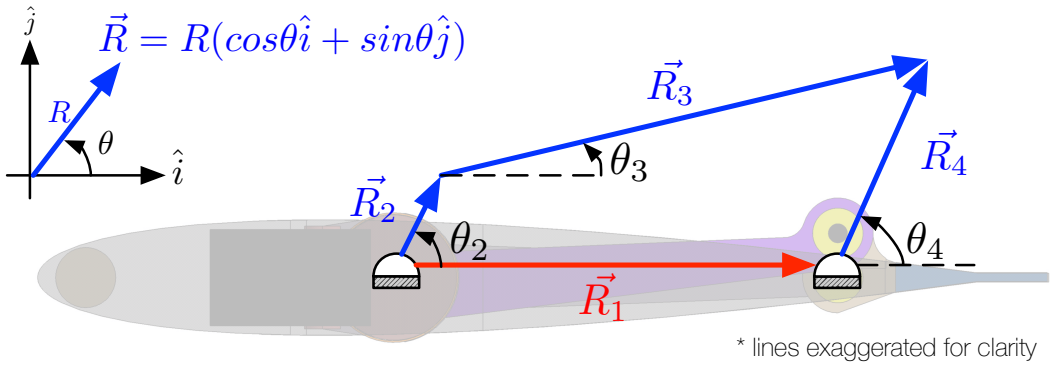

Figure 4.10: Four bar based analysis of motor - flap system.

The waveform output from the motor-flap system was analyzed using four-bar analysis. Figure 4.10 is the pictorial representation of the system. The vector equation of motion shown in Eq. 4.1 and the component equations shown in Eqs. 4.2 were used for the mathematical formulation.

$$R_2\left(cos\theta_2\hat{i} + sin\theta_2\hat{j}\right) + R_3\left(cos\theta_3\hat{i} + sin\theta_3\hat{j}\right) = R_1\hat{i} + R_4\left(cos\theta_4\hat{i} + sin\theta_4\hat{j}\right) \quad (4.1)$$

$$R_2cos\theta_2 + R_3cos\theta_3 = R_1 + R_4cos\theta_4$$

$$R_2sin\theta_2 + R_3sin\theta_3 = R_4sin\theta_4 \quad (4.2)$$

Figure 4.11 shows the input - output response of the four bar system. The input is delivered as a oscillating input from the brushless DC motor and the output is the oscillatory motion observed at the trailing edge flap. As discussed before, the mechanism incorporates about 3:1 reduction gear ratio. This was also observed in Fig. 4.11. Figure 4.12 compares the output from the mechanism to ideal sine wave. Although not identical, the trailing edge flap motion is close to a sinusoidal motion.

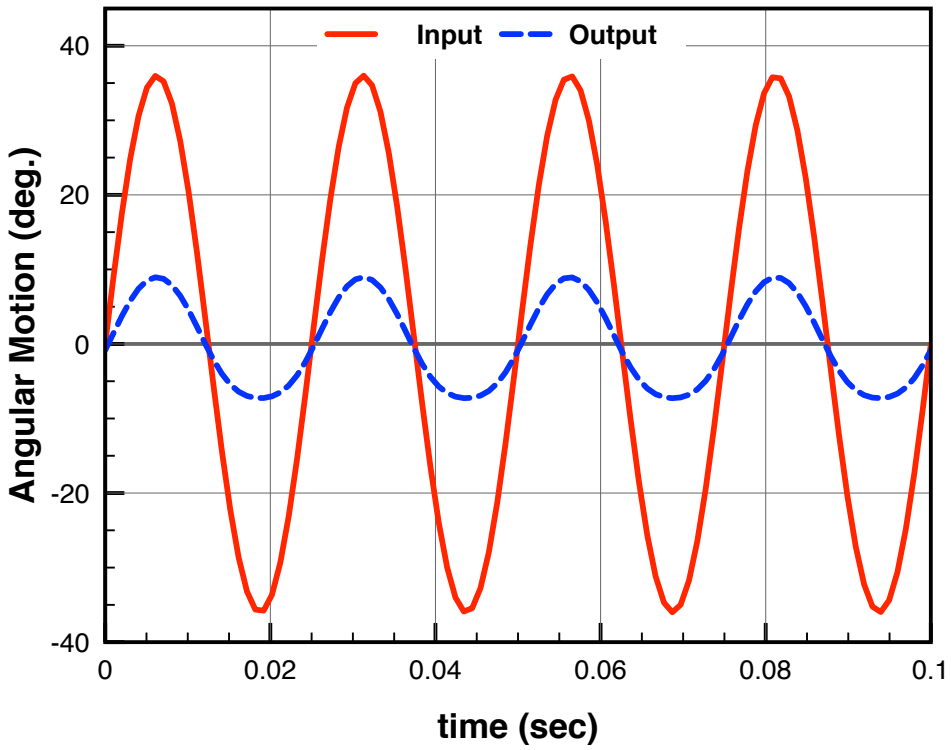

Figure 4.11: Analysis of input and output of motor-flap system.

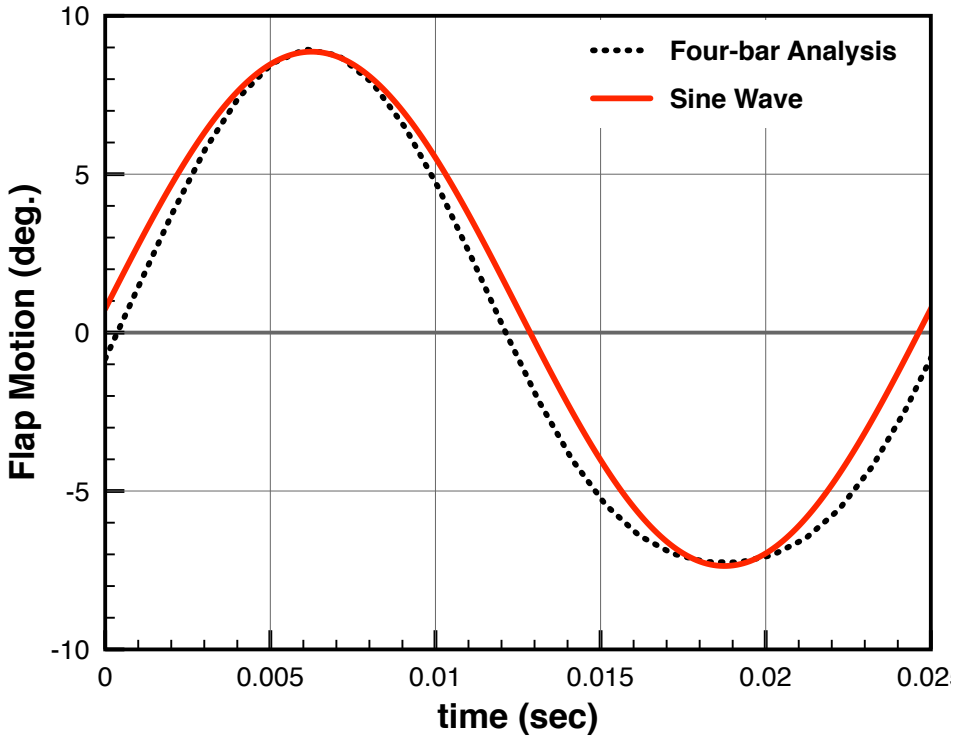

Figure 4.12: Comparison of output waveform from motor-flap system with sine wave.

4.3 Finite Element Analysis of the Motor - Flap System

The flap anchor was the most complicated part of the motor-flap system. It was designed to sustain multiple number of loads. A finite element analysis of the anchor was carried out in CATIA. The 3D CAD model was imported in the structural analysis workbench and the anchor was subjected to loads (Fig. 4.13) calculated at maximum load condition at 2400 rotor RPM.

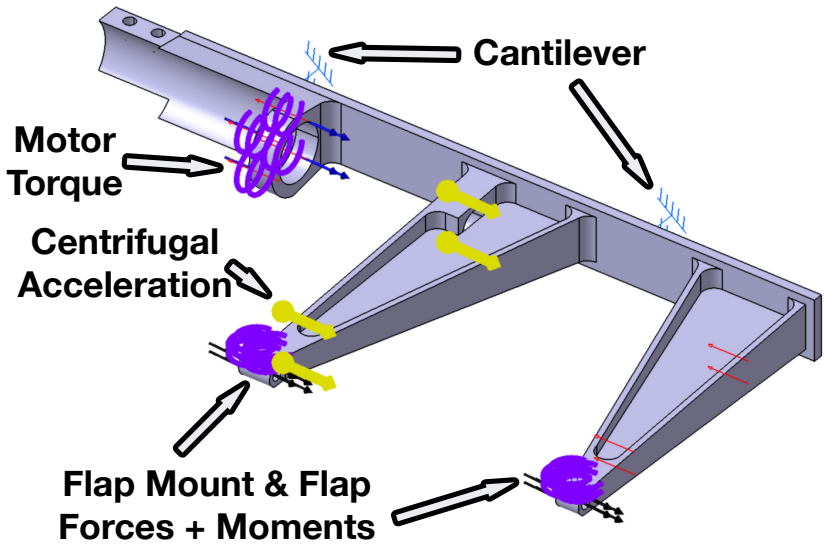

Figure 4.13: Loads on the flap anchor.

(a) The centrifugal load was applied as an acceleration field at the center of gravity of the anchor.

(b) The centrifugal force on the flap mount and trailing edge flap applied loads and moments at the flap mount points.

(c) The lift force on the trailing edge flap applied load on the flap mount point.

(d) The centrifugal load due to the motor was applied on the motor attachment point.

(e) The motor output torque was applied at the attachment point as well.

(f) The hinge moment from the trailing edge flap and moment due to lift on the flap were relieved by the bearings and hence not applied on the anchor.

(g) The pitching moment produced due to trailing edge flap deflection was reacted at blade root, about the soft pitch link, and was not applied at the anchor.

The entire geometry was discretized in 8566 elements and 16214 nodes, using parabolic structural elements. Figure 4.14 shows the mesh on the anchor as well as deformation under applied load. The maximum in-plane deformation was observed to under 10 mils (0.25 mm) and maximum out of place deformation was less than 2 mils (0.05 mm).

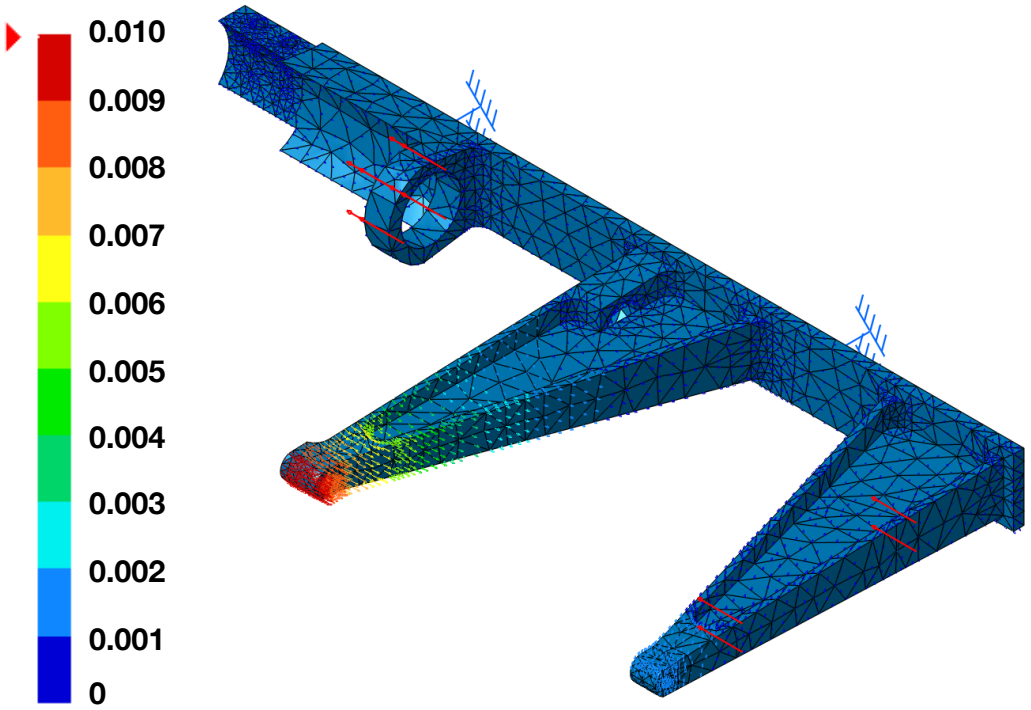

Figure 4.14: Finite element analysis of the flap anchor.

Chapter 5: **Vacuum Chamber Testing**

Once the suitability of the actuator was established on the bench top, evaluation under centrifugal load was systematically performed in the ten feet diameter vacuum chamber (Fig. 5.1). Testing in a vacuum spin chamber allowed to isolate the aerodynamic and inertial forces on the actuator. As a precursor to evaluating the motor as an actuator, the structural integrity of motor-only and then the motor-flap system under centrifugal load was evaluated. Once the structural integrity was established, the actuator control scheme was tested with motor-flap system operating under centrifugal load.

Figure 5.1: 10 feet diameter vacuum chamber at University of Maryland.

5.1 Motor-only under Centrifugal Load

Figure 5.2 shows the characteristic curve for the Maxon EC-10 motor. This curve was obtained by measuring the motor output rpm at various input voltages with no load on it. The linear region of the characteristic curve was used to compare the performance of the motor at various loads. The motor-gear-head combination was mounted on a rotating arm, 30 in from the rotation center (85% span location on the Mach scale rotor) in the vacuum chamber (Fig. 5.3). A motor input voltage sweep was performed at various centrifugal loads, and the motor shaft rpm and casing temperature were recorded.

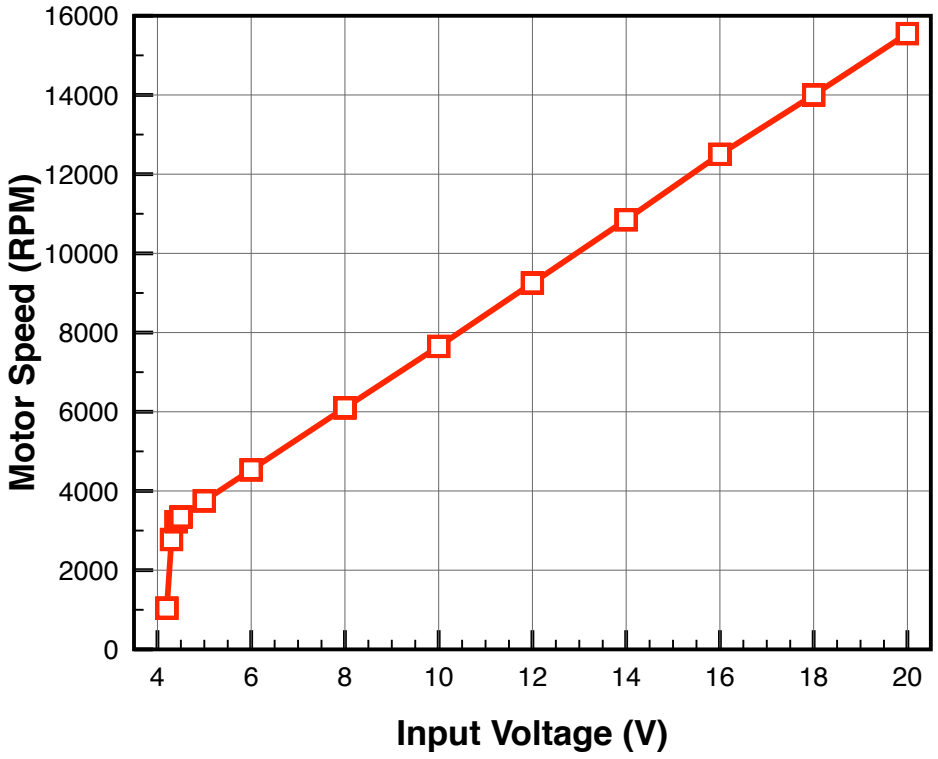

Figure 5.2: Variation of motor output at various input voltages operating under no centrifugal load.

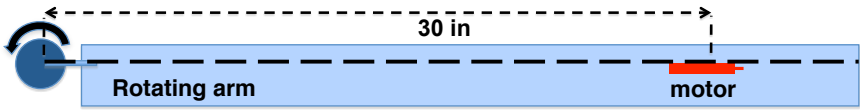

Figure 5.3: EC-10 motor mounted on the rotating shaft in vacuum spin chamber.

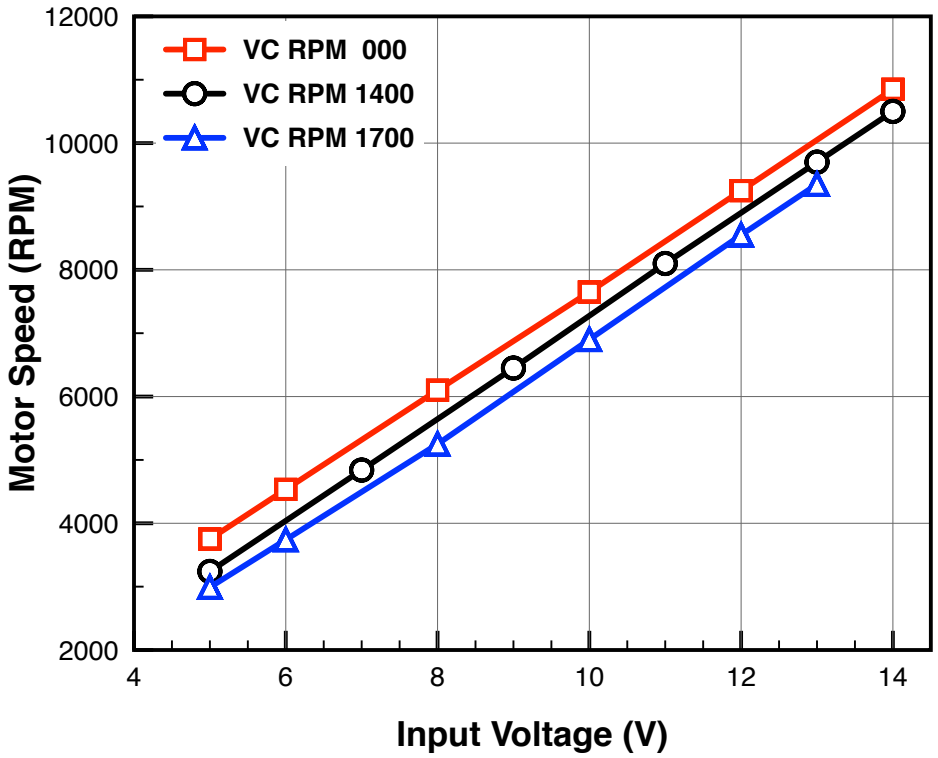

Figure 5.4: Motor rpm versus input voltages under various centrifugal loads.

Figure 5.4 shows motor performance at various centrifugal loads (vacuum chamber RPMs). Motor rpm increases linearly with input motor voltage and is consistent for various centrifugal loads. Also, it was observed that as the centrifugal load increases, the motor rpm falls slightly. The permanent magnet shaft in the brushless dc motor was supported in position by a set of radial bearings. This could be due to friction in the radial bearings operating under high axial loads. Overall, the motor operated smoothly under centrifugal loads.

5.2 Motor-Flap System under Centrifugal Load

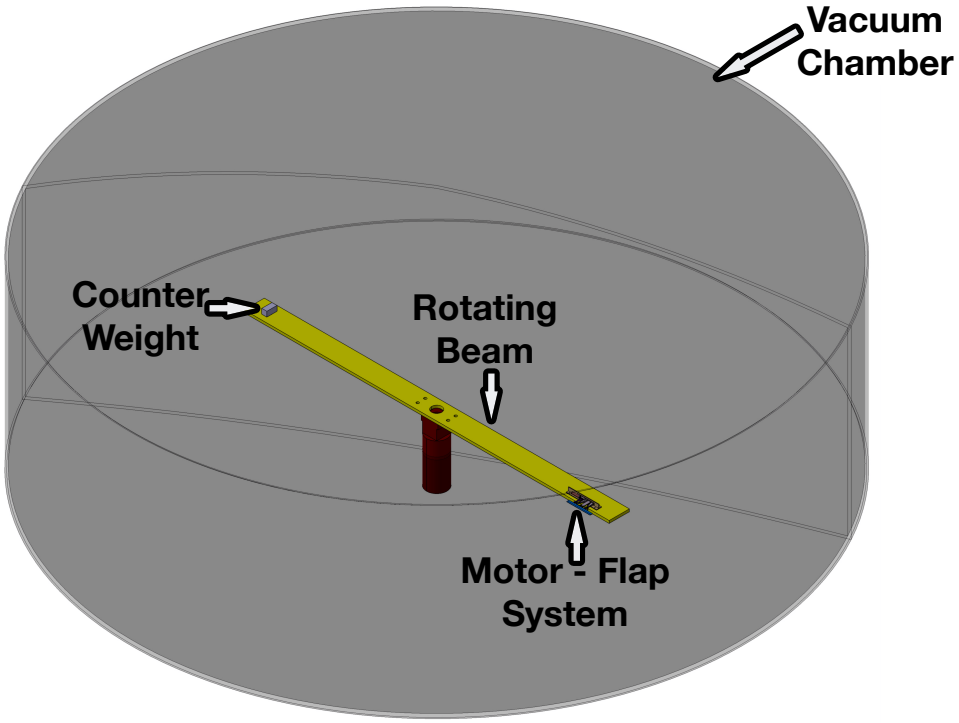

Figure 5.5: Motor-flap system mounted on rotating shaft in vacuum spin chamber.

Figure 5.5 shows the motor-flap system mounted in the vacuum spin chamber. Two Hall sensors were used to measure the angular position of the flap at both near and far end of the flap mount as shown in Fig. 5.6. Initially, the motor was operated continuously in one direction (with no oscillations), and the motion from the flap mechanism was observed. Figure 5.7 shows flap motion under centrifugal load, the rotational motion from the motor is converted to flap motion by the flap mechanism. The motor-flap mechanism performed very well. Both the near and far Hall sensors showed similar flap motion. This proved that the trailing edge flap was torsionally stiff and the flap motion was consistent along the flap span. Henceforth, only one Hall sensor was used to measure the flap motion.

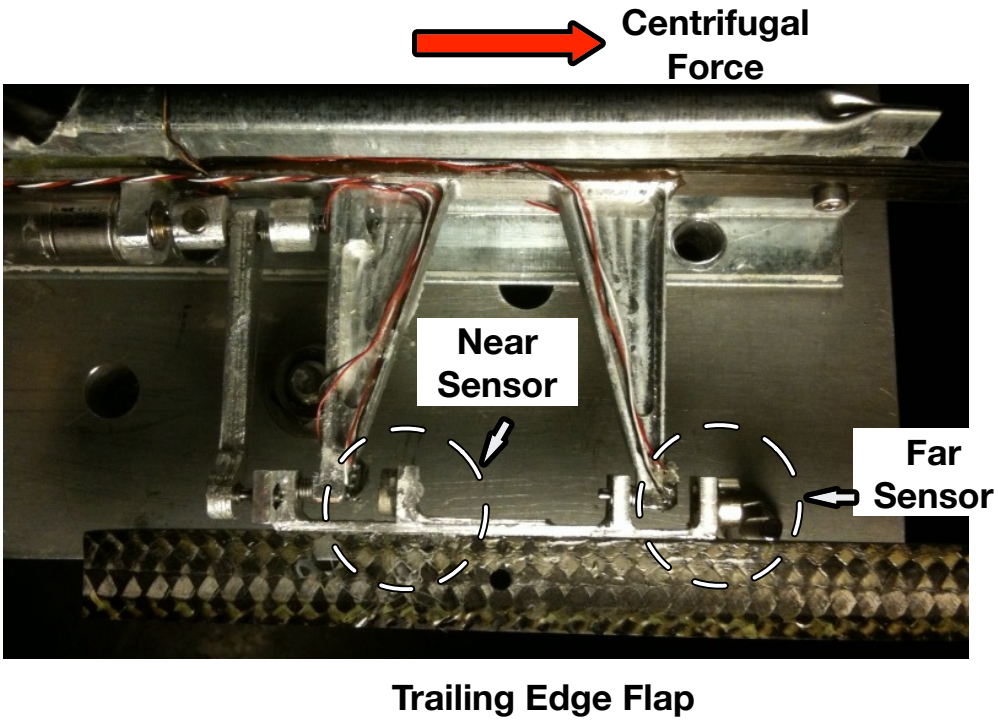

Figure 5.6: Close-up view of the motor-flap system in vacuum spin chamber.

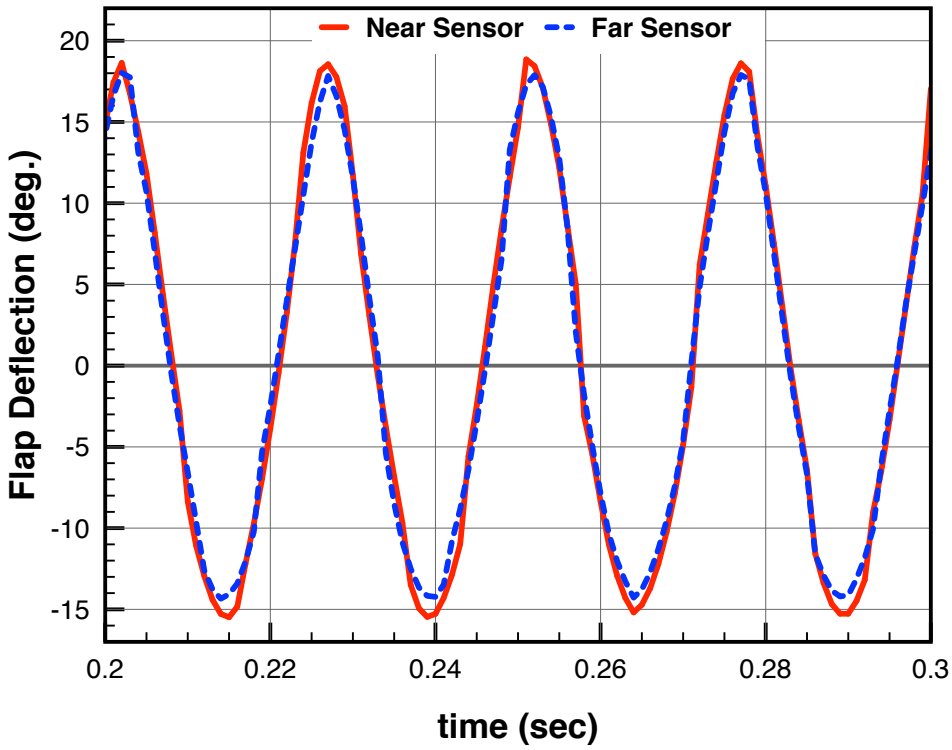

Figure 5.7: Flap motion in vacuum spin chamber at 800 RPM.

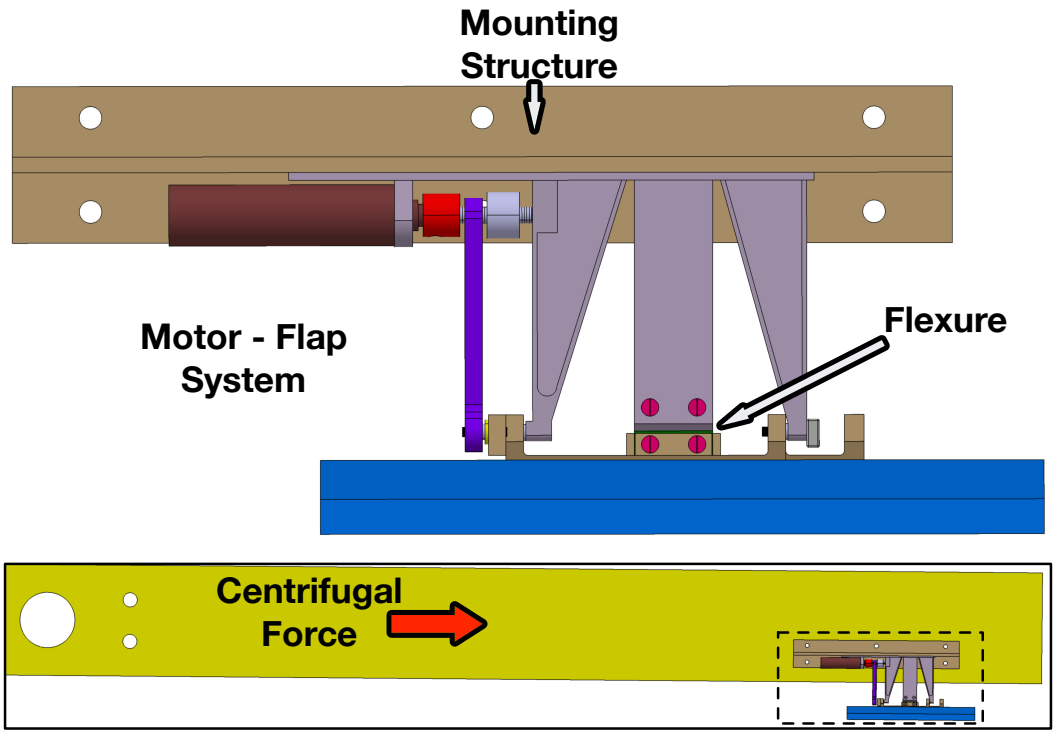

Figure 5.8: Motor-flap system with flexure in vacuum spin chamber.

Next, the actuator control strategy discussed in Section 3.2 was implemented with motor-flap system in the vacuum spin chamber. Figure 5.8 shows the system mounted on a rotating beam in the vacuum chamber. Torsion stiffness (0.90 N-mm/deg (8 lb-mil/deg)) was provided by a flexure to simulate the aerodynamic loading. Figure 5.9 shows the experimental evaluation of the torsional stiffness of the flexure element.

Figure 5.10 show the flap amplitude obtained at 40 Hz actuation frequency at zero and 1200 rotor rpm. Consistent operation was observed, however due to the enclosed environment in a vacuum chamber, there was inadequate cooling of dc motor and sharp temperature rise with increasing input voltage was also observed (Fig. 5.11). The motor heating became an issue, especially under high loading

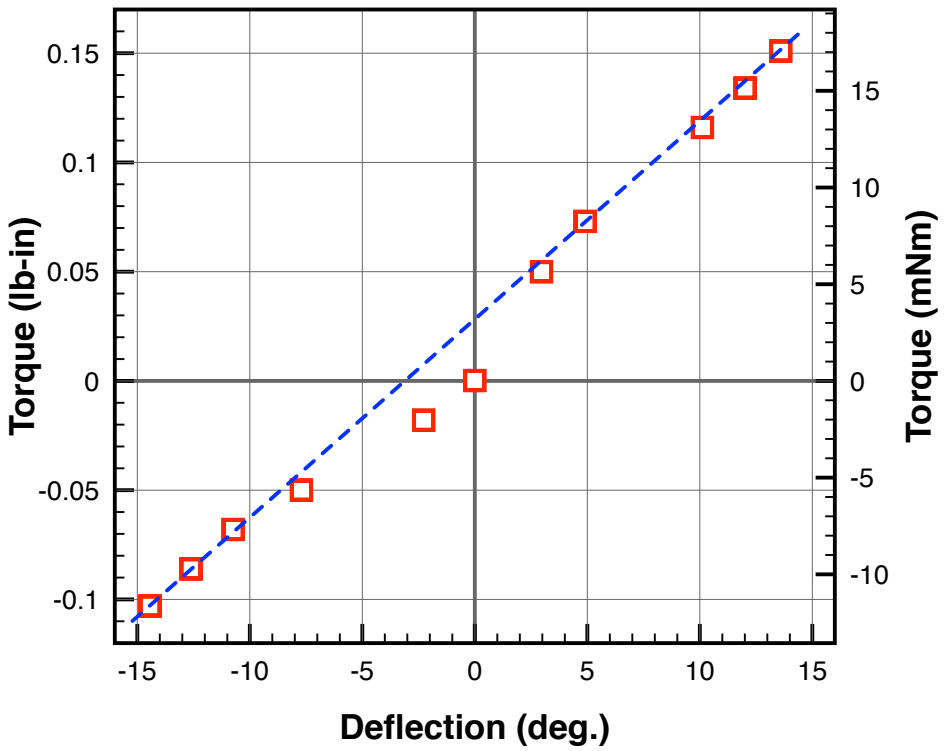

Figure 5.9: Torsional stiffness of the flexure element in the motor-flap system.

conditions (high vacuum chamber rpm) and input voltages. This imposed an upper bound on the flap amplitude obtained at 1200 rpm. This may not be an issue when testing on the hover tower as better motor cooling is possible. The mechanism operated satisfactorily in the rotating environment under high g-loads and motor actuation was successfully accomplished for different rotational speeds.

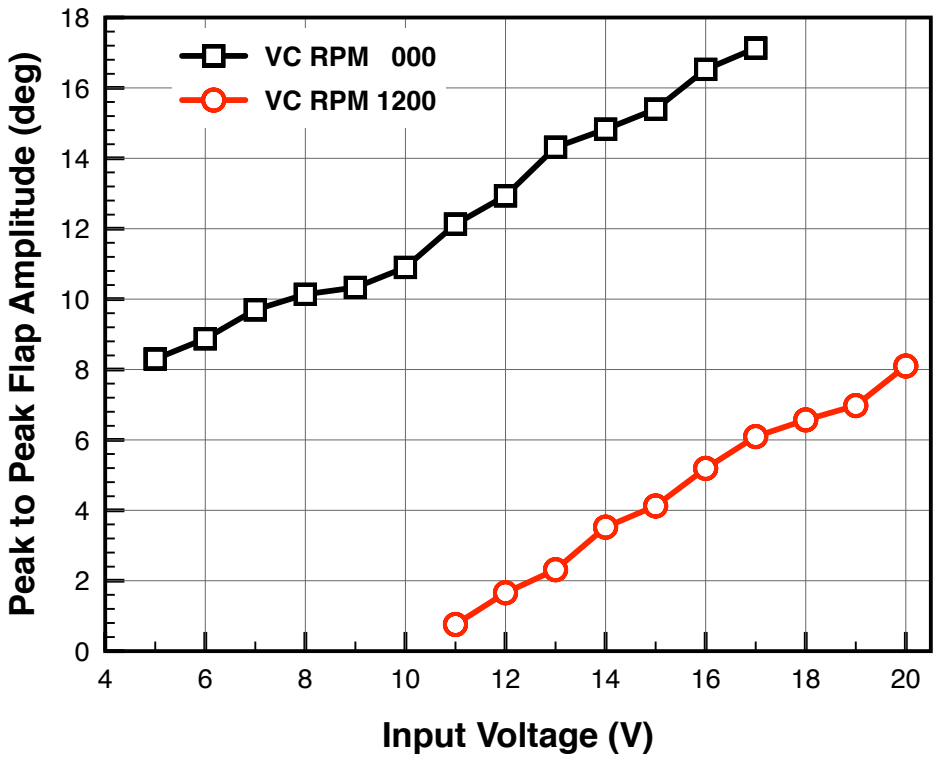

Figure 5.10: Peak-peak flap amplitude at 40 Hz actuation in vacuum.

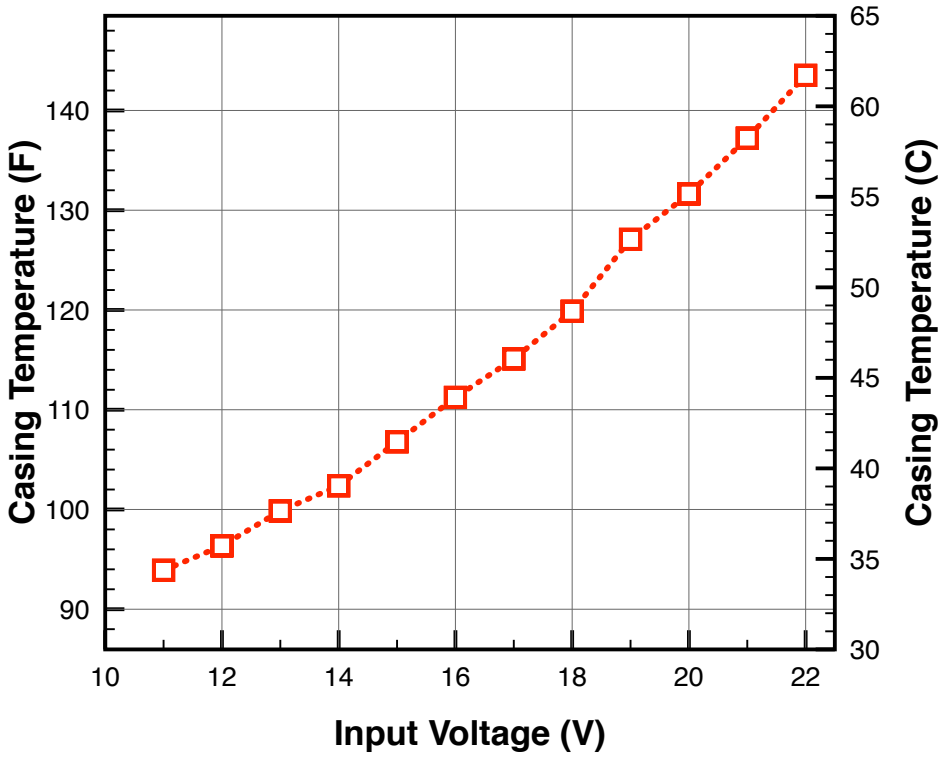

Figure 5.11: Motor casing temperature at 1200 rotor rpm in vacuum.

Chapter 6: **Fabrication and Structural Testing of Active Blade**

6.1 Composite Blade Fabrication

A composite rotor with NACA 0012 profile and a no twist, no taper, rectangular planform was manufactured. The components of a composite rotor blade are presented in Fig. 6.1. The blade was designed to take centrifugal load due to rotation, bending and torsion loading due to airloads. Design on each component is discussed next.

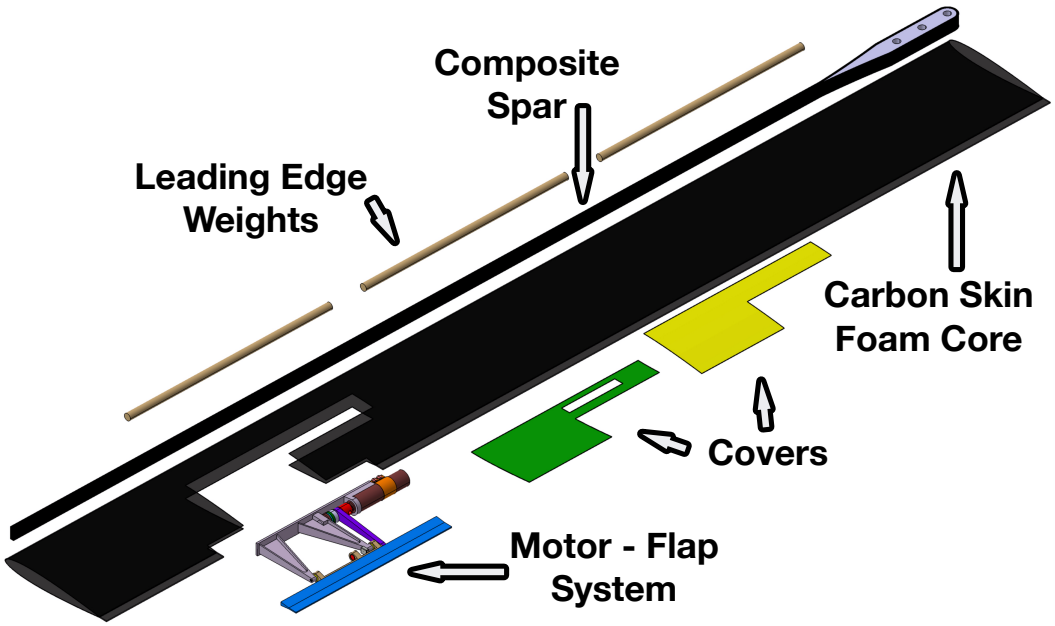

Figure 6.1: Components of a composite rotor blade with an active trailing edge flap.

6.1.1 Composite spar

Spar was a primary load carrying member, it was designed to be the primary member for carrying centrifugal and bending loads. The spar could either be made as a D-spar closed section member or a flat open section design. The D-spar provides better leading edge shape and can take larger loads. However, its complicated to layup and to simplify fabrication, a flat spar design was chosen. Once manufactured it was tested to ensure safe operation under centrifugal loads.

The composite spar was composed of 16 layers of IM8 unidirectional graphite-epoxy fibers, wrapped around an aluminum root insert with attachment holes for blade grip. The fabrication process is listed below:

1. Machine the aluminum root insert with the attachment holes.

2. Cut 8 strips of unidirectional Graphite-Epoxy (0.32 in x 58 in) using a 0.32 in wide aluminum stencil.

3. Use Frekote [234] to coat the mold at least four times, allowing the coat to dry between consecutive applications.

4. Wrap the root insert in film adhesive (FM300 [235]) such that the tips of the adhesive strip come together at the tip of the insert.

5. Using the mold to keep the graphite-epoxy strips lined up, wrap the strips around the root insert and form the spar. Make sure the strips are pulled tightly around the root insert.

6. Once all the eight straps are finished, trim off excess material such that the spar fits within the mold. The length should be slightly longer than 28 in, but not too long. Excessive length could lead to bowed spar once cured.

7. Place spar in mold and close at multiple points using C-clamps.

8. Cure it in the oven at 350 F (177 C) for 60 minutes. The cure cycle is based on FM300 cure cycle.

9. Once cured, clean up the spar and sand down to 28 inches length and 0.32 in wide.

10. Wrap a 1.5 in wide piece of graphite epoxy perpendicularly around the spar where the strips come together at the tip of the aluminum. This is to eliminate de-lamination near the insert tip.

11. Repeat the curing process and this concludes the spar fabrication.

The spar provides for a stiff mounting location for motor-flap system components. A specimen was fabricated and tested in the MTS material testing machine (Fig. 6.2) under tensile loading. Figure 6.3 presents the results from the spar extension testing. Some initial fiber re-adjustment was observed followed by failure of the cross-strap at the neck of the root insert at about 18500 N (4150 lbf) load. A complete failure of the composite spar was observed at about 20000 N (4250 lbf) load.

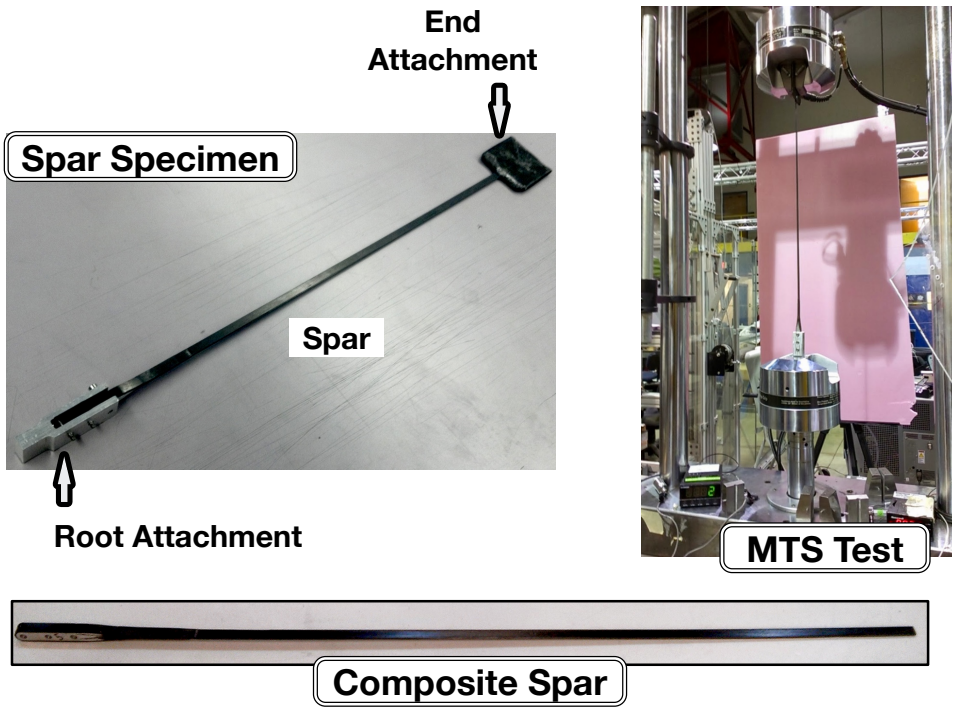

Figure 6.2: Fabrication and testing of composite spar.

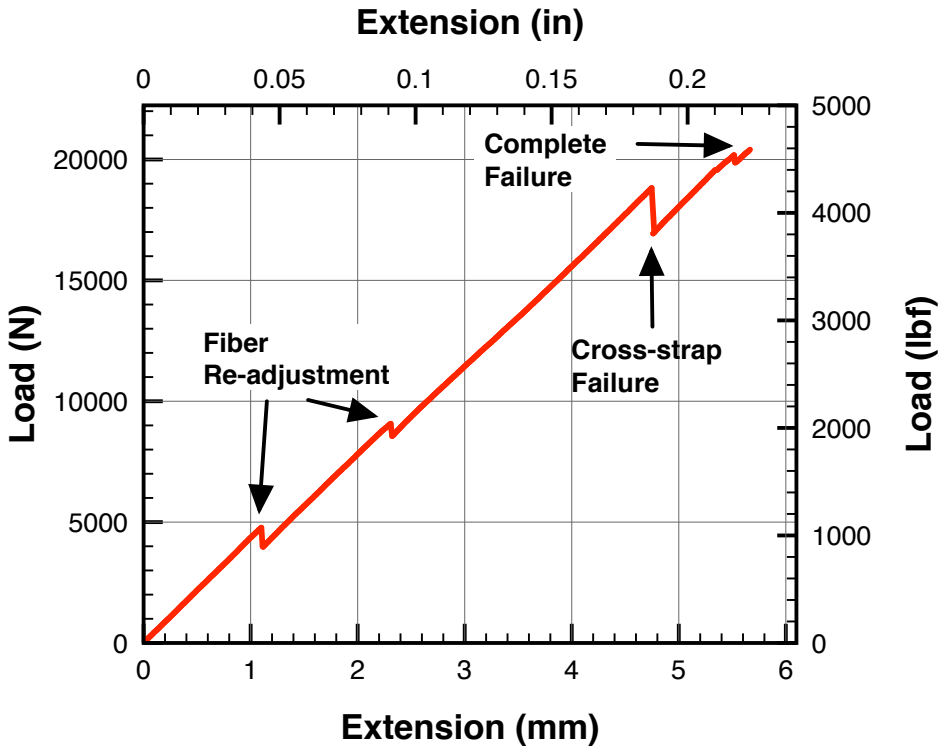

Figure 6.3: Extension test of composite spar.

6.1.2 Leading edge weights

Leading edge weights were required to place the chordwise c.g. at the quarter chord location. Since the space was limited in the nose of the blade, a high density material weights were required. Discrete Tungsten-Carbide rods were used as leading edge weights. These rods were commercially available in two, four and six inches pieces and could be secured better in the blade. Using multiple rods rather than a single unit leading edge weight helped in better integration of these weights in the blade structure.

6.1.3 Foam core

Rohacell [236] foam was used to form the core of the blade. The core needed to be lightweight at the same time be dense enough to provide shape and hold internal components such as leading edge weights. Medium density Rohocell-51 was chosen as core material for the blades fabricated. Following procedure was followed to prepare the foam core:

1. Cut out rectangular piece of foam with sides of blade radius and chord length.

2. Roughly sand the foam in the shape of the blade and cut a half inch slot, 0.1 in deep to accommodate the wires (Fig. 6.4a).

3. Place a 12-wire ribbon in the foam cavity and secure the foam piece in the blade mold (Fig. 6.4b).

4. Cure in oven at 350 F (177 C) for 60 minutes and obtain foam matching blade profile (Fig. 6.4c,d).

5. Cut the foam core along the quarter chord, separating into leasing edge piece and trailing edge piece. Carefully sand to accommodate the spar between the two foam core parts (Fig. 6.4e).

6. Cut slots in leading edge foam where the tungsten-carbide weights will fit. Wrap the rods in film adhesive and place them snuggly within slot (Fig. 6.4f).

7. Wrap Teflon tape around the motor-flap system slot to prevent it from bonding to the skin. Finally wrap foam pieces and spar in film adhesive (Fig. 6.4g).

6.1.4 Composite skin

IM7/8552 [237] plain weave $\pm$ 45 degree carbon-epoxy skin was used to provide the blade shape and torsional stiffness. A quarter chord skin wrap was closed around the leading edge foam and spar, making it a closed box design. Then a single layer of composite skin was wrapped out (Fig. 6.4h) and the whole assembly was fit inside the blade mold and oven cured at 350 F (177 C) for 60 minutes. Once the blade was cured, an outboard section was cut out (Fig. 6.4i), aft of the spar and the motor-flap system was bonded to the spar. The details of system fabrication and assembly are discussed in next section.

Key parameters of the rotor are included in Table 6.1 and component-wise weight breakdown of the composite blade is listed in Table 6.2.

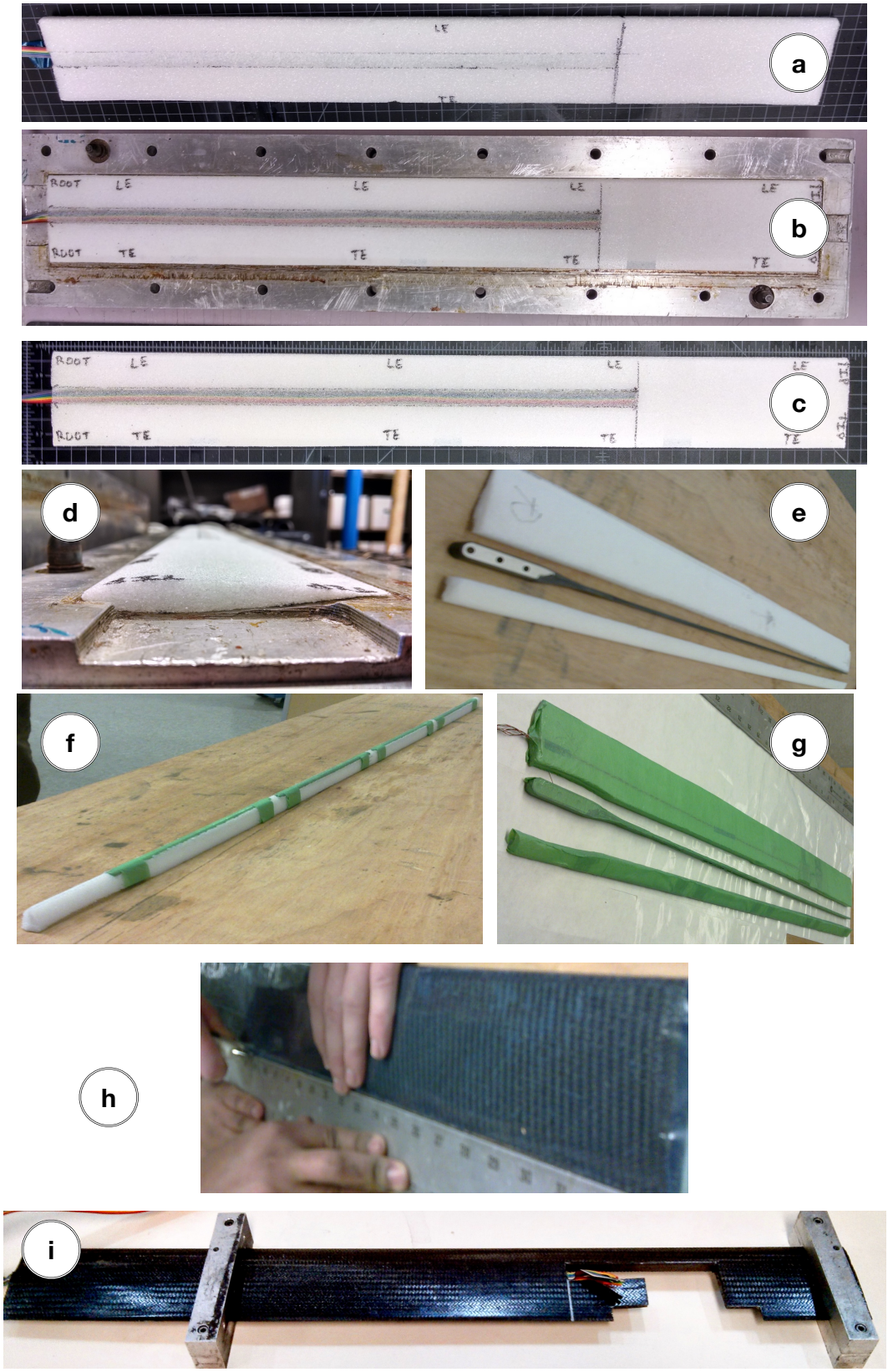

Figure 6.4: Steps for composite blade construction.

Table 6.1: Key parameters of the Mach scale rotor with trailing edge flaps.

Airfoil section	NACA 0012
Rotor radius	33.5 in
Rotor chord	3.15 in
Flap chord	0.47 in (0.15 R)
Flap length	4.5 in (0.14 c)
Flap location	0.75 - 0.89 R

Table 6.2: Weight breakdown of various components of the composite active blade.

Component	Weight (g)	C.G. (%c)	Weight fraction (%)
Carbon-epoxy skin	65.7	39.68	22.5
Uni-graphite composite spar	40.1	25.00	13.7
Motor-flap system	34.0	44.50	11.6
Leading edge skin wrap	16.4	16.67	5.6
Trailing edge foam core	14.2	48.70	4.9
Leading edge foam core	5.1	16.67	1.7
Weight (No LE weight)	175.5	35.17	60.0
Leading edge weights	117.0	5.40	40.0
Total design weight	292.5	23.26	100

6.2 Motor-flap System: Fabrication and Assembly

The components of the motor-flap system were designed in house using CATIA computer aided design software. It was also used to assess the structural strength of the system using a FEM analysis. Once the design was completed, the parts were also machined in house using a CNC milling machine.

Visual Mill was used to generate the CNC codes required to automate the milling process. Aluminum 6061 was used as stock. The machine process involved facing down the stock to dimensions, milling in the CNC machine, manual drilling and threading operations, followed by finishing cuts. Anchor took the most time to machine as it was the most intricate and critical of all the components. Figure 6.5 shows stepwise design and fabrication of flap anchor.

Once machining was completed, steel rods and radial bearings were installed in the components. The anchor was bonded to the spar of the rotor blade using a high strength high temperature film adhesive. Also, flap mount was bonded to trailing edge flap using same high strength film adhesive. Once the anchor was attached to the spar, flap mount with the flap was installed, followed by shaft attachments and flap rod. A thin shim was bonded between the flap element and the main blade body to minimize air gap. Finally, the brushless DC motor was installed by screwing it into the motor mount. A brass collar was used to further brace the motor to the anchor.

Figure 6.6 shows motor-flap system being integrated into the composite blade. A thermocouple was bonded to motor casing for temperature monitoring and a Hall

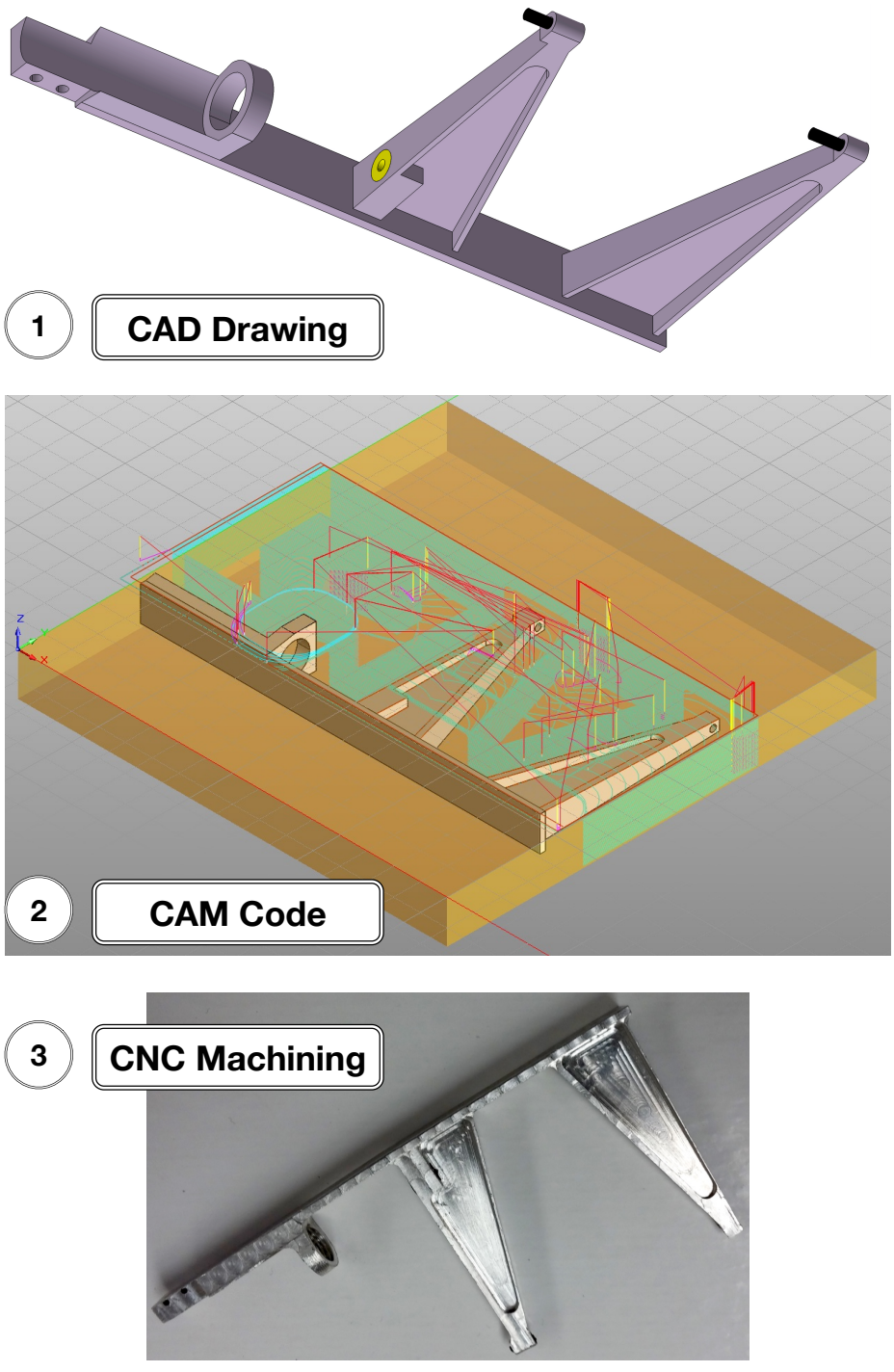

Figure 6.5: Steps for manufacturing flap anchor.

sensor was installed on the flap mount to record trailing edge flap deflections. Covers were then taped on to top and bottom surfaces to close off the cavity. A wood putty

was used to smooth out any rough surfaces, improving blade finish and reducing skin drag. The final blades are presented in Fig. 6.7.

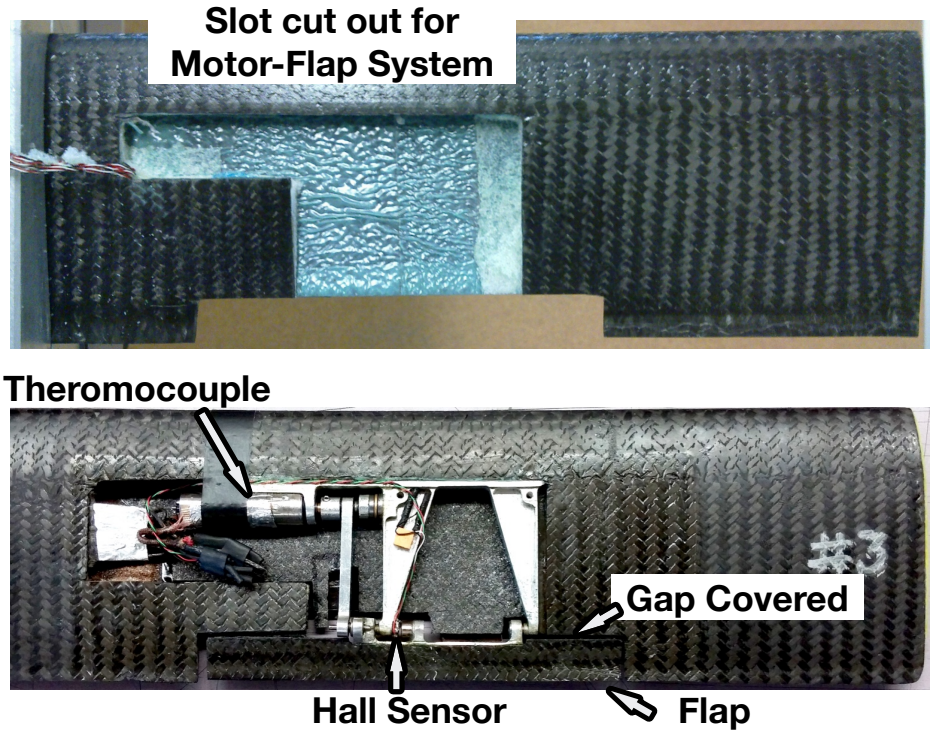

Figure 6.6: Integrating motor-flap system in the blade.

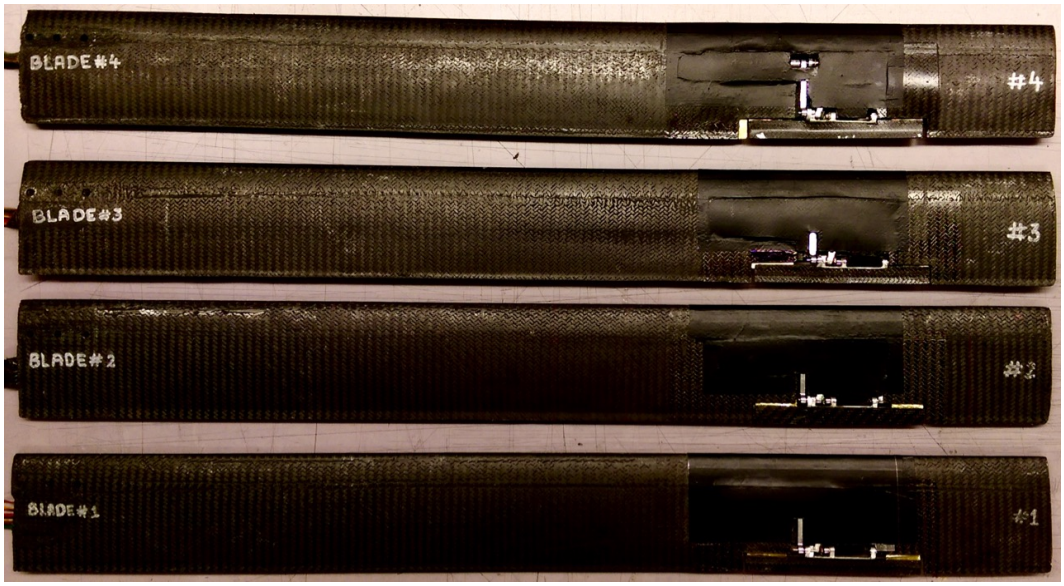

Figure 6.7: Completed composite blades active rotor.

6.3 Mass Balancing and Inertia Matching

It was essential to precisely locate the chordwise and spanwise center of gravity (c.g.) of the blades. In general, the chordwise c.g. of each blade was required to be at or slightly ahead of the aerodynamic center of the blade (quarter chord location). This was to avoid any aeroelastic instability that might occur during wind tunnel tests, especially when the torsional stiffness of the rotor was reduced. Figure 6.8 shows the setup to measure the chordwise c.g. location of the blade. The blade was balanced on a smooth steel rod, and the c.g. location was precisely measured using calipers (± 0.001 in accuracy). This chordwise c.g. was also tested with blade rotated about its spar, flipping the top and bottom surface, and an average value was used.

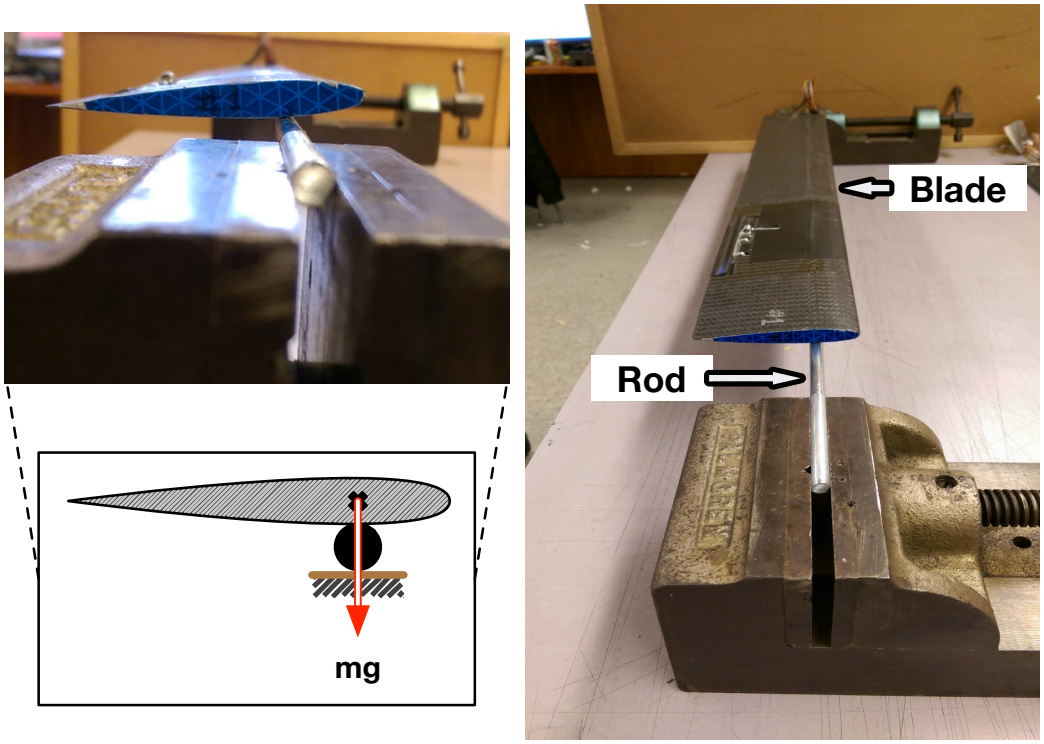

Figure 6.8: Setup for chordwise c.g. measurement.

For the spanwise balance, sets of opposing blades (1 & 3 and 2 & 4) were balanced on a see-saw teeter to ensure that the center of gravity is at the center of rotation. Usually a piece of tape was sufficient to correct for any imbalances. Spanwise balancing reduces rotor vibrations and also makes them less susceptible to any structural excitations during rotor spin up. Once they were spanwise balanced, spanwise c.g. location was found for each of the blade. Figure 6.10 shows the setup for measuring the spanwise c.g. of a blade. The spanwise c.g. location was found to be within $\pm$ 0.5%R for each of the blades.

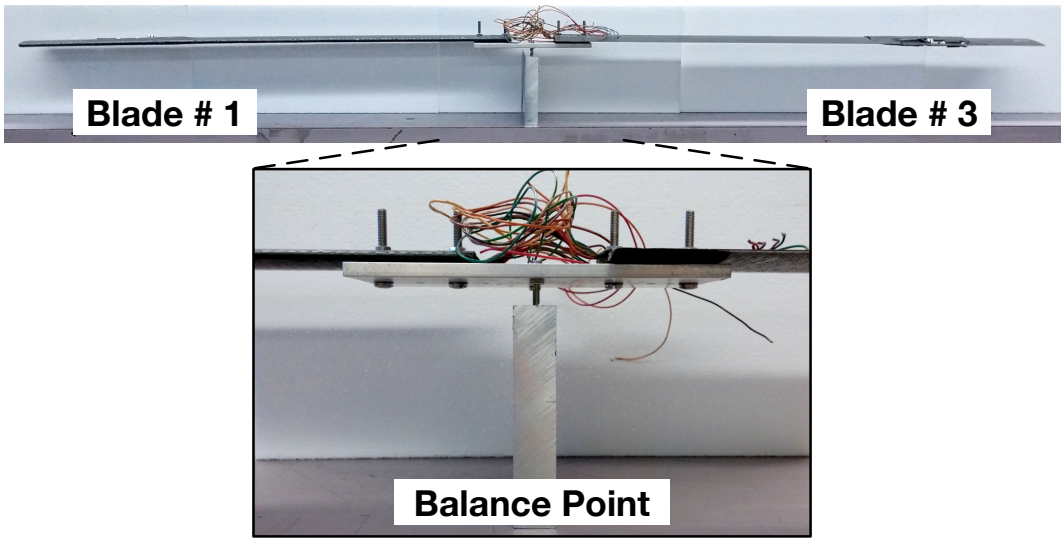

Figure 6.9: Setup for spanwise blade balancing.

In addition, an effort was made to match the flap inertia of the blades as well. The blade with grip was suspended on a set of low friction radial bearings in a support structure. The blade was then swung and the oscillations were recorded using a hall sensor at the hinge. Based on the time period of the oscillations, mass and spanwise c.g. of the blade, blade inertia was experimentally obtained. This method was first checked using a uniform aluminum beam with known properties.

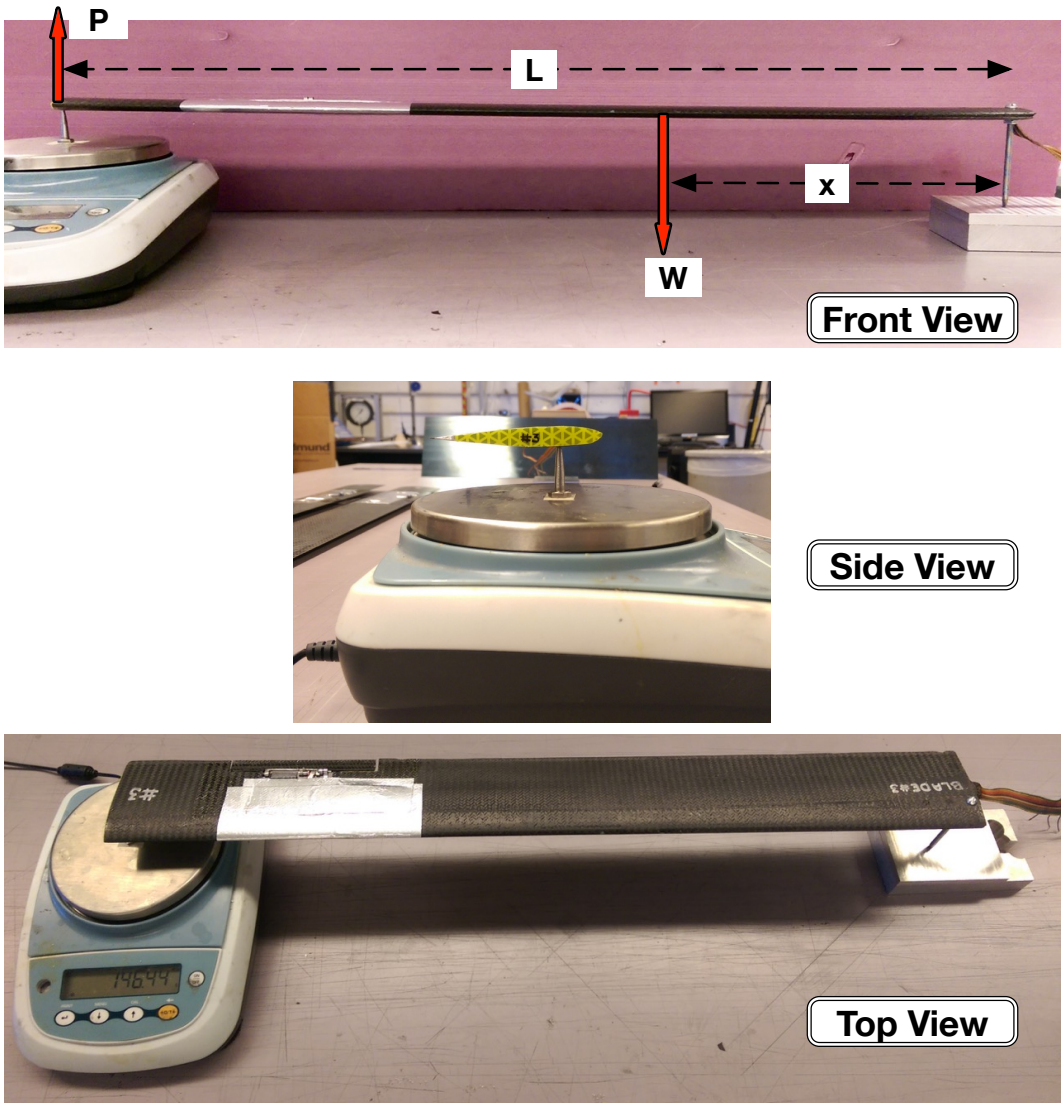

Figure 6.10: Setup for spanwise c.g. measurement.

The experimental results obtained were within 3% of the theoretical calculations. For each blade, small weights were embedded ahead of the spar to match the moment of inertia. Table 6.3 lists the measured properties for all the blades. The finished blade weight was within 5% and chordwise c.g. was within 0.5%c of the design values. This highlights the tight tolerances and repeatability in the fabrication and integration process.

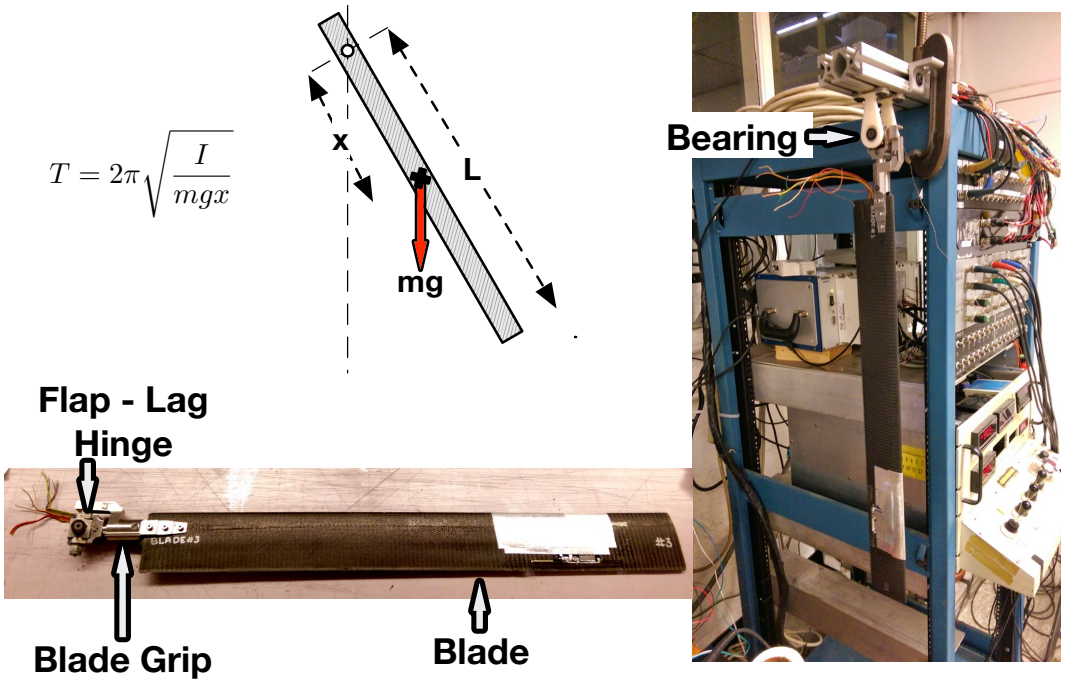

Figure 6.11: Setup for blade flap-wise inertia measurement.

Table 6.3: Blades weight, c.g. and inertia comparison.

	Weight (g)	Chordwise C.G. (%c)	Spanwise C.G. (%R)	Flap Inertia ($kg-m^2$)
Design	292.5	23.3	–	–
Blade 1	304.3	23.7	50	0.0642
Blade 2	304.7	23.2	52	0.0641
Blade 3	304.2	23.7	51	0.0641
Blade 4	304.5	23.4	50	0.0643

6.4 Structural Testing of Blades

Experiments were carried out to measure the bending and torsional stiffness of the blades. A rotor blade was considered as a beam in bending (Fig. 6.12) and as a rod in torsion (Fig. 6.13) and analyzed as shown in Eqs. 6.1, 6.2 and 6.3.

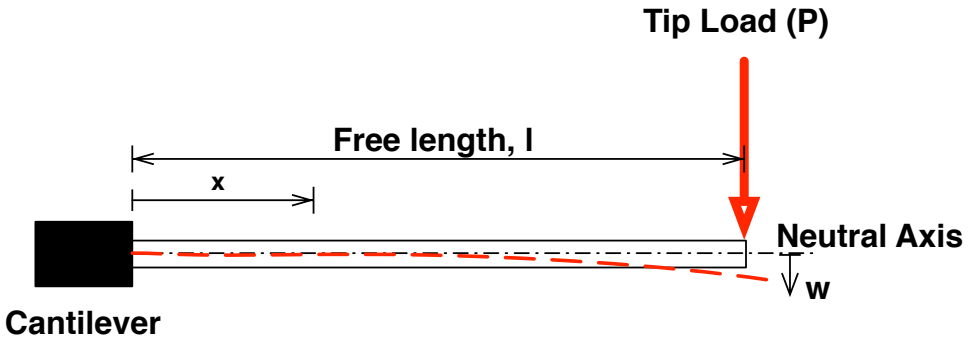

Figure 6.12: Blade as a beam in bending.

$$\frac{d^2w}{dx^2} = \frac{M}{EI} = \frac{P(l-x)}{EI} \tag{6.1}$$

$$\begin{aligned} \theta_b = \frac{dw}{dx} &= \frac{P}{EI}\left[lx - \frac{x^2}{2}\right] \\ \Rightarrow \qquad EI &= \frac{P}{\theta_b}\left[lx - \frac{x^2}{2}\right] \end{aligned} \tag{6.2}$$

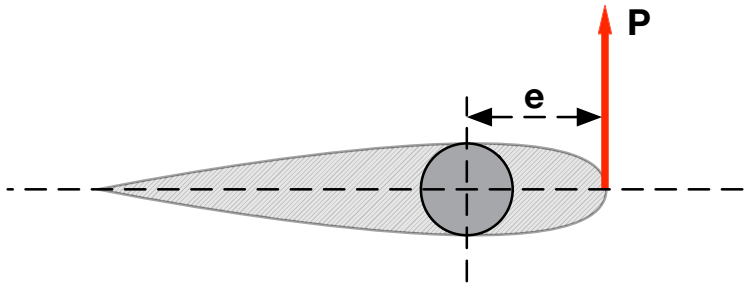

Figure 6.13: Blade as a rod in torsion.

$$Torque(Pe) = GJ\frac{d\phi}{dx} \quad \Rightarrow \quad GJ = \frac{P}{\phi}ex \tag{6.3}$$

6.4.1 Testing using mirror method

A loading setup (Fig. 6.14) was designed and fabricated to load the blade in bending and accurately record the force applied.

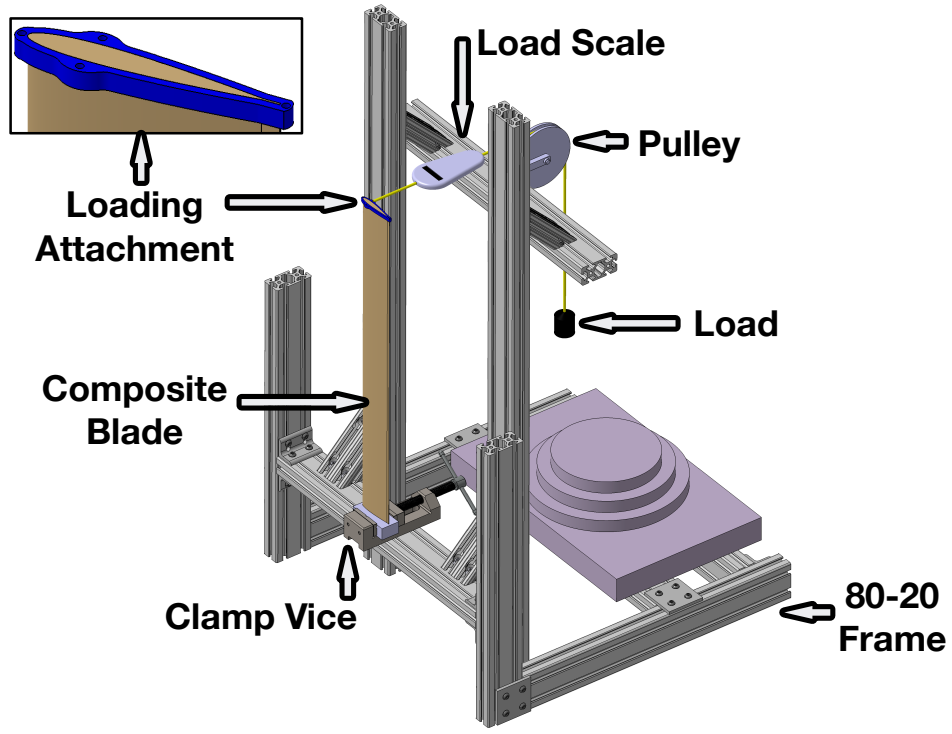

Figure 6.14: Drawing of the loading structure for blade testing.

To obtain the bending slope ($\frac{dw}{dx}$), three mirrors, one close to root, second near the mid-span and third close to blade tip, were placed on the spar of the blade. Laser light was pointed at the mirror and the reflection from the mirrors was recorded on a screen. The motion of the reflected dots with various bending loads was traced on a screen. The screen was placed at least 20 feet from the blade to magnify the small bending slope angles (Fig. 6.15). Additional mirrors were placed along the chord of the blade to measure the blade twist angle. Figure 6.16 shows the loading setup as well as an output trace on the screen.

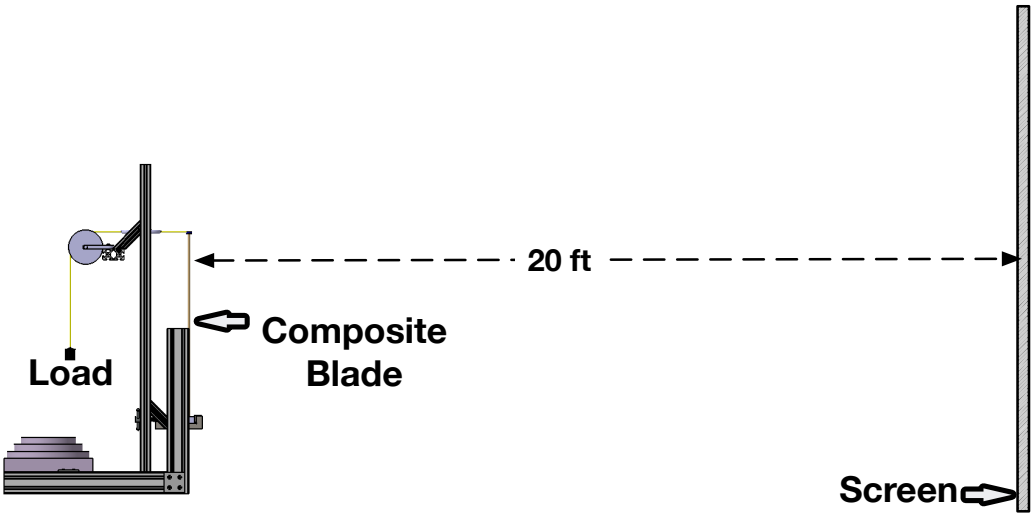

Figure 6.15: Drawing of the loading structure for blade testing.

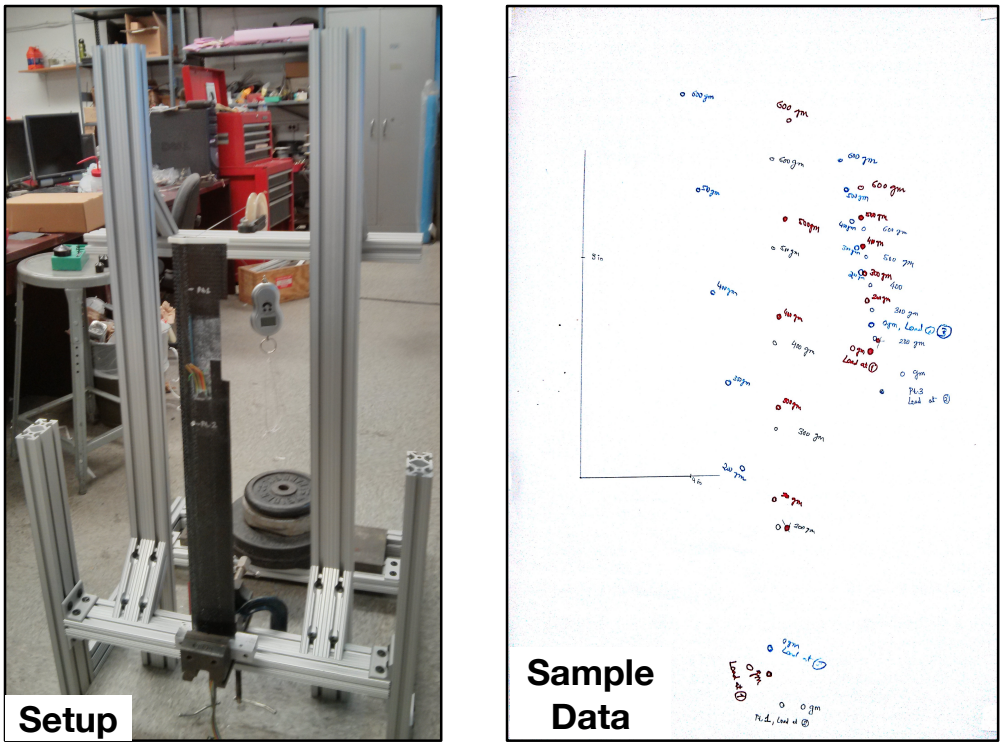

Figure 6.16: Drawing of the loading structure for blade testing.

As shown in Fig. 6.17, for pure bending the reflected light marker on the screen moves in a vertical direction and for pure torsion, along a horizontal line. Further details about the method are included in [238].

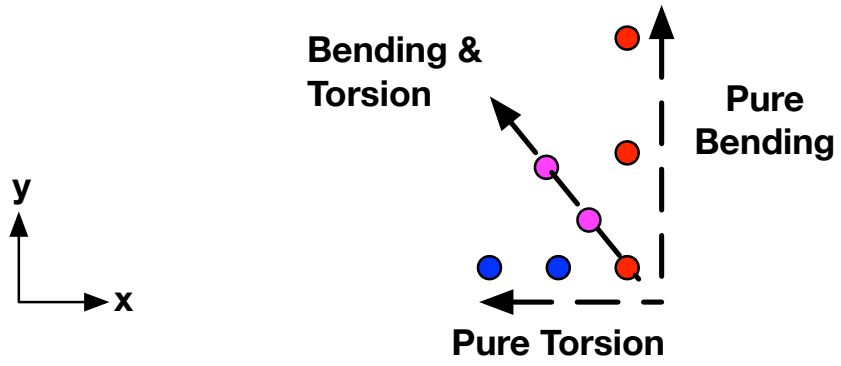

Figure 6.17: Sample output from the mirror-laser method.

Figures 6.18 and 6.19 present the bending slope at various loads. The bending stiffness of the blade was calculated to be 32 $\pm$ 0.5 Nm^2. Figure 6.20 presents the torsion angle for load applied at leading and trailing edge of the blade tip. Torsional stiffness of the blade was calculated to be 34 Nm^2/rad and shear center at 24.9%c chord location.

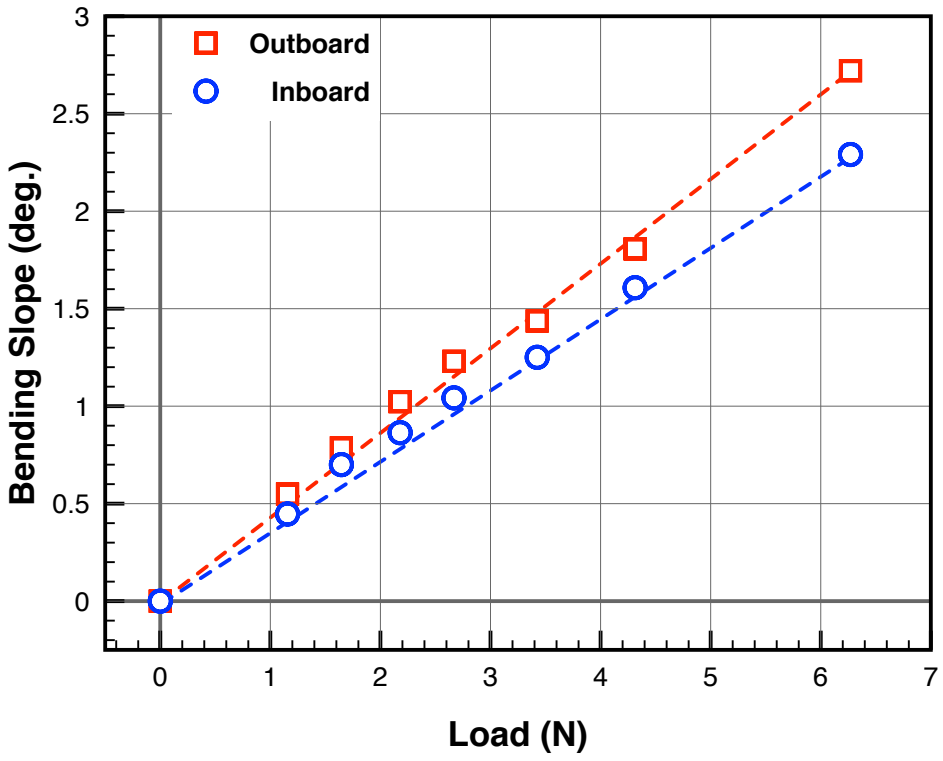

Figure 6.18: Beam bending at two station under various loads.

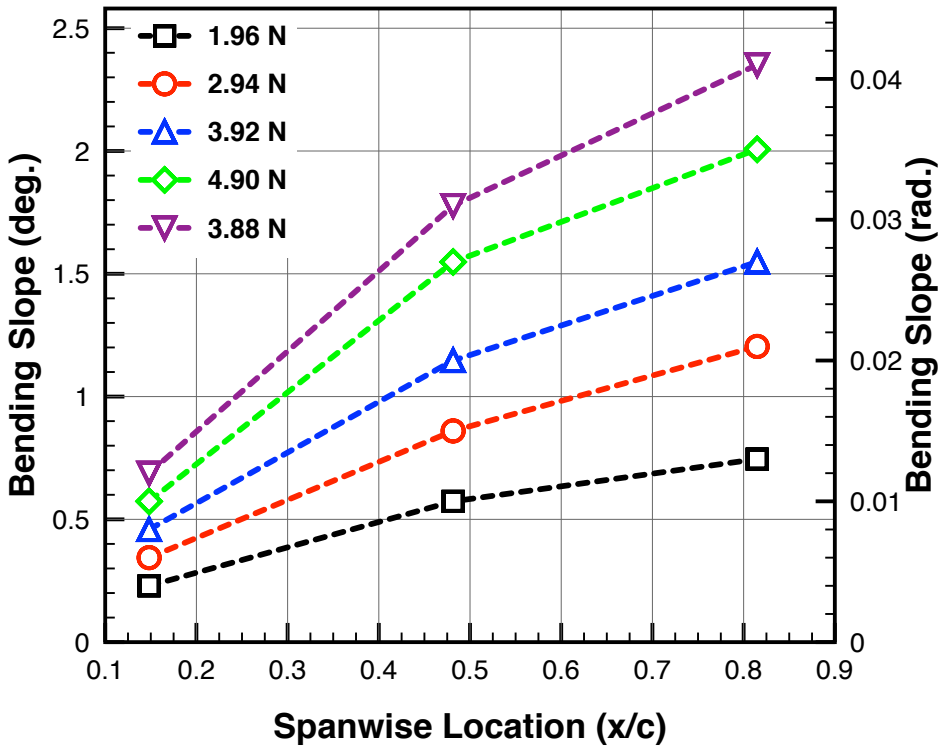

Figure 6.19: Beam bending at three spanwise location under various loads.

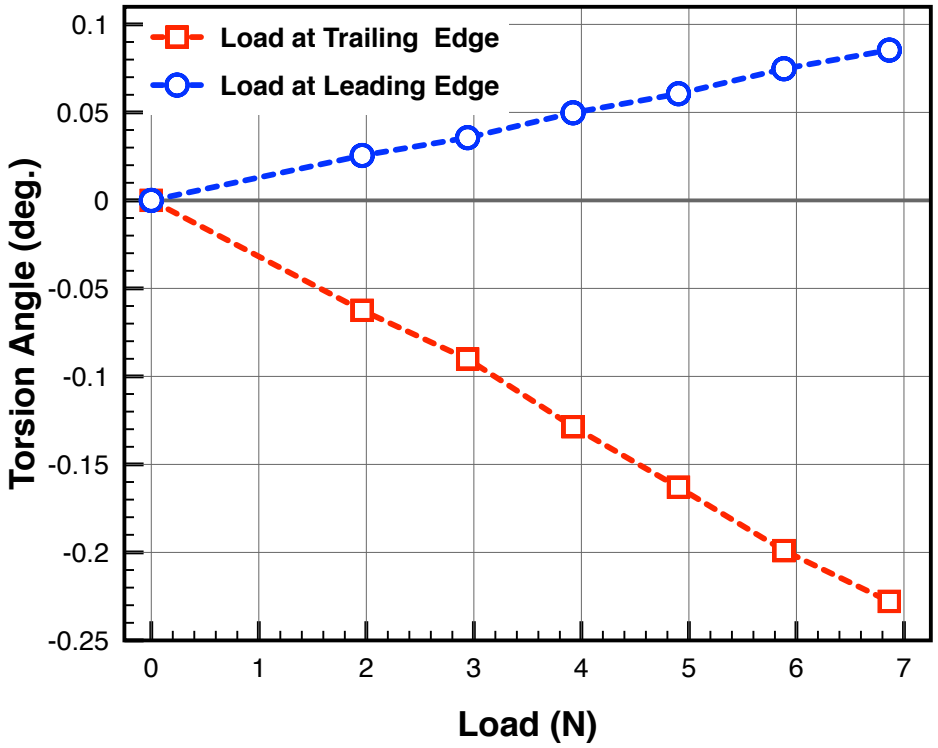

Figure 6.20: Blade under torsion load.

6.4.2 Testing using Vicon motion capture system

A major drawback of the mirror method was that only a limited number of mirrors could be tracked. To get a distribution of the properties, closely placed mirrors would be required. Manual simultaneous tracking of mirrors would be cumbersome. Vicon motion capture system eliminates the need for manually tracking the markers.

Figure 6.21: Blade with Vicon markers.

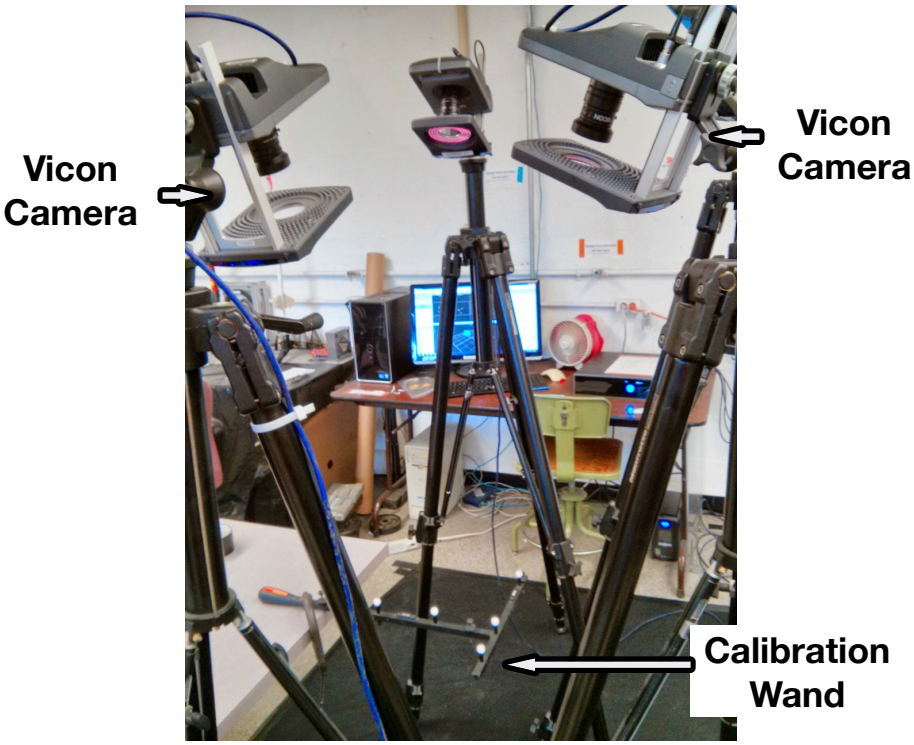

Figure 6.22: Vicon camera setup with calibration wand.

A number of reflective markers were placed on the blade surface (Fig. 6.21) and multiple specialized cameras extract markers localization by triangulation (Fig. 6.22). Figure 6.23 shows various spanwise and chordwise markers tracked by the system.

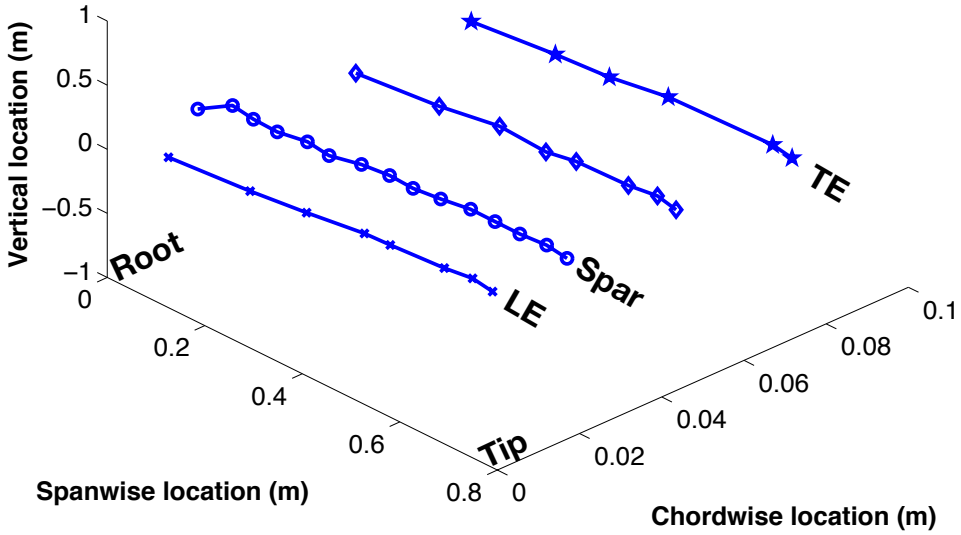

Figure 6.23: Marker placement on blade as measured by Vicon.

The blade was cantilevered at root and a reference marker was placed at the root as well to monitor cantilever root deflections. The deflections along the spar under various tip bending loads is presented in Fig. 6.24. These deflections were then used to calculate bending slope (Fig. 6.25) and curvature (Fig. 6.26), using a central difference formulation. Finally, bending stiffness distribution (Fig. 6.27) could be calculated (Eq. 6.1). This process was repeated for each of the four blades and bending stiffness distribution was calculated (Fig. 6.28).

Further, torsion loads were applied at the blade tip and chordwise deflections were used to calculate the twist angle, twist rate and shear center. The cut-out in the blade to accommodate the motor-flap system primarily affected the torsion stiffness at the sections outboard of the cut location.

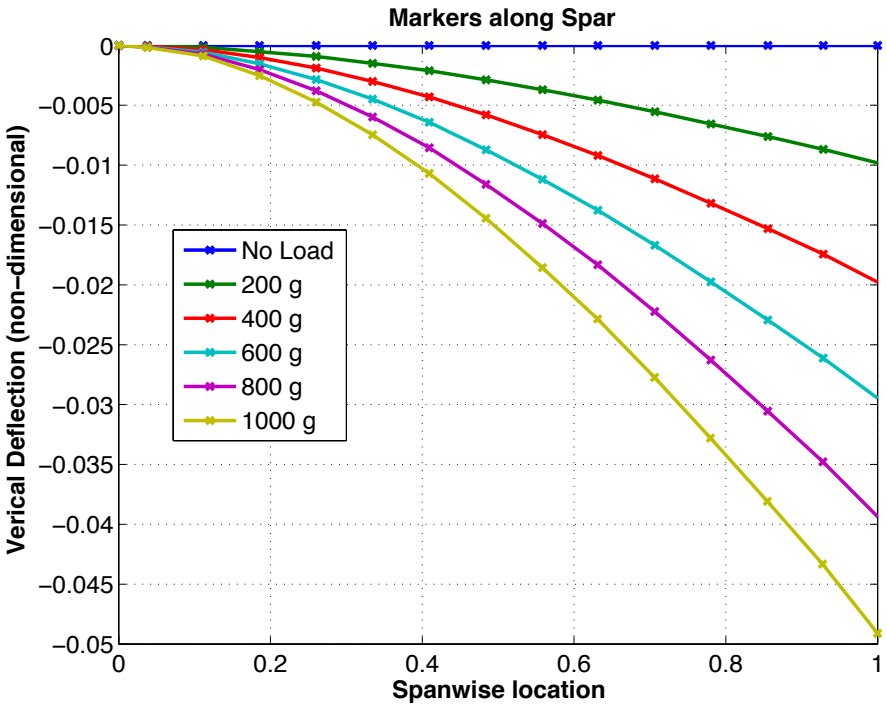

Figure 6.24: Blade bending deflection.

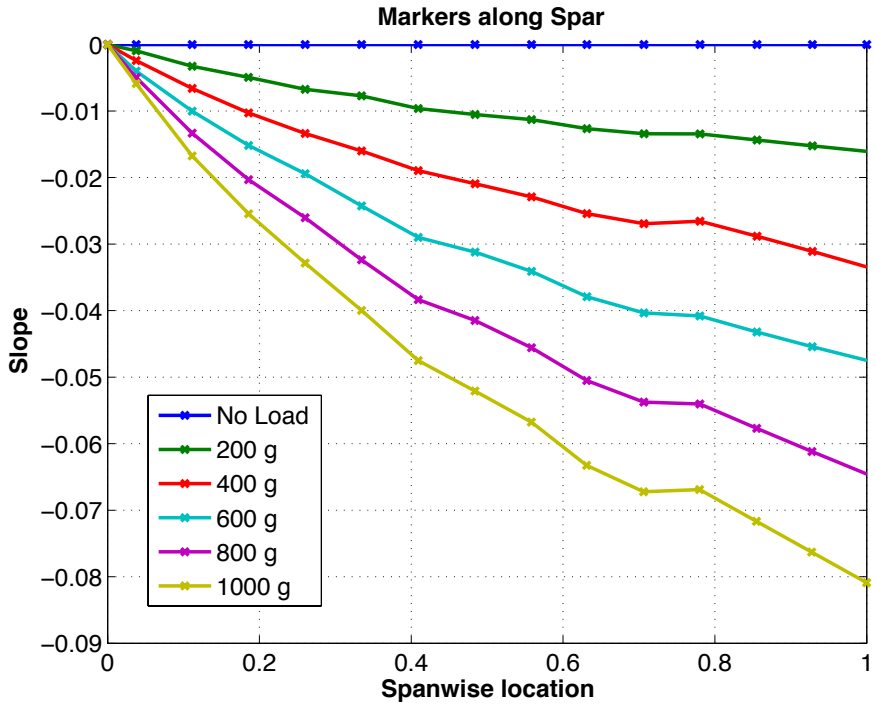

Figure 6.25: Blade bending deflection slope.

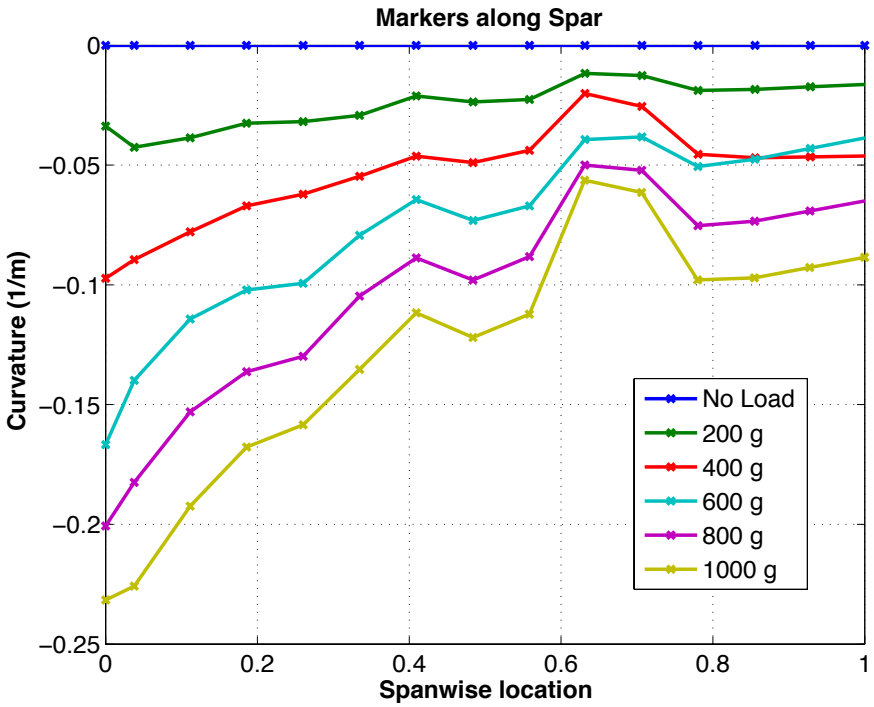

Figure 6.26: Blade bending curvature.

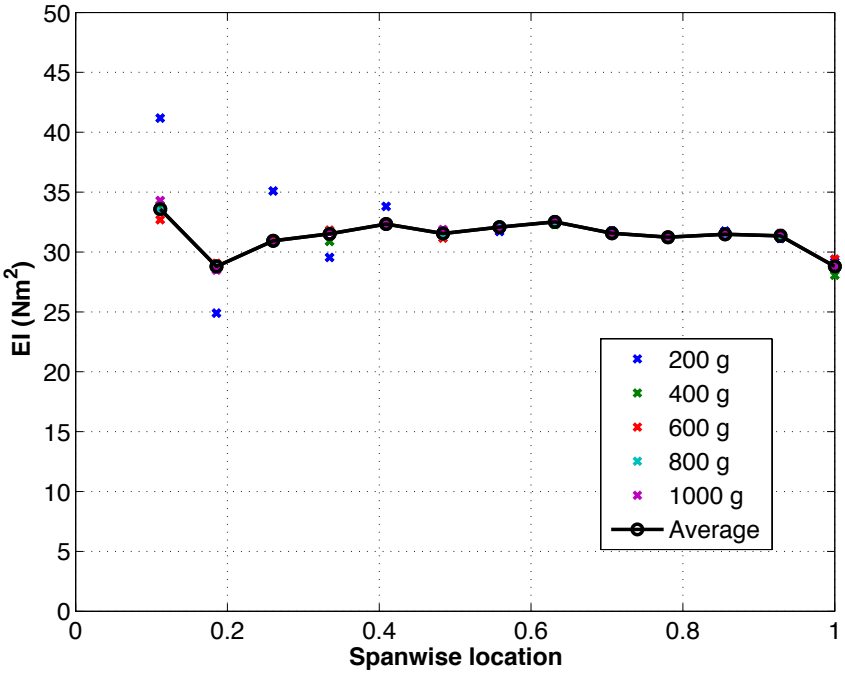

Figure 6.27: Blade bending stiffness at various loads.

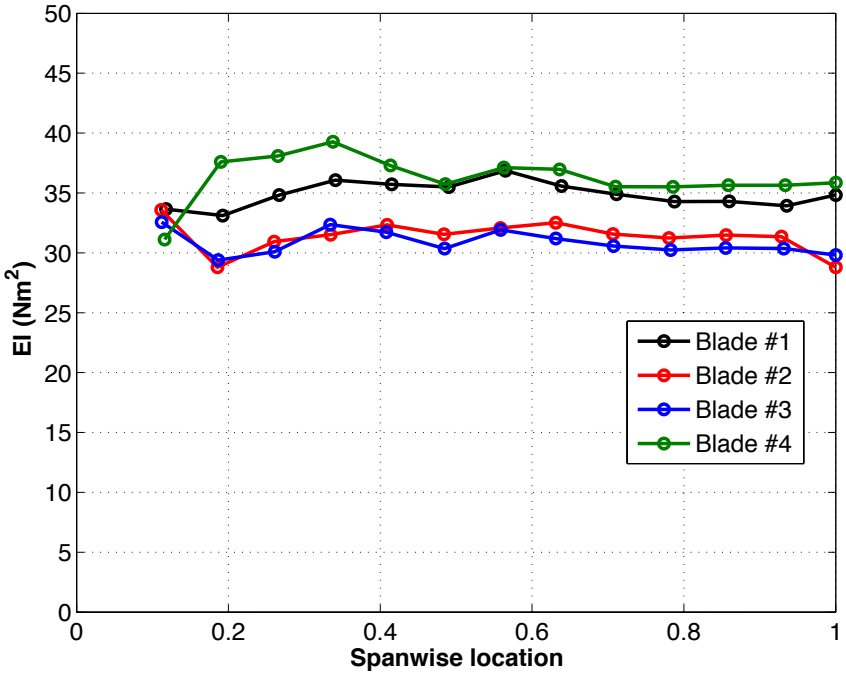

Figure 6.28: Blade bending stiffness at various loads for all blades.

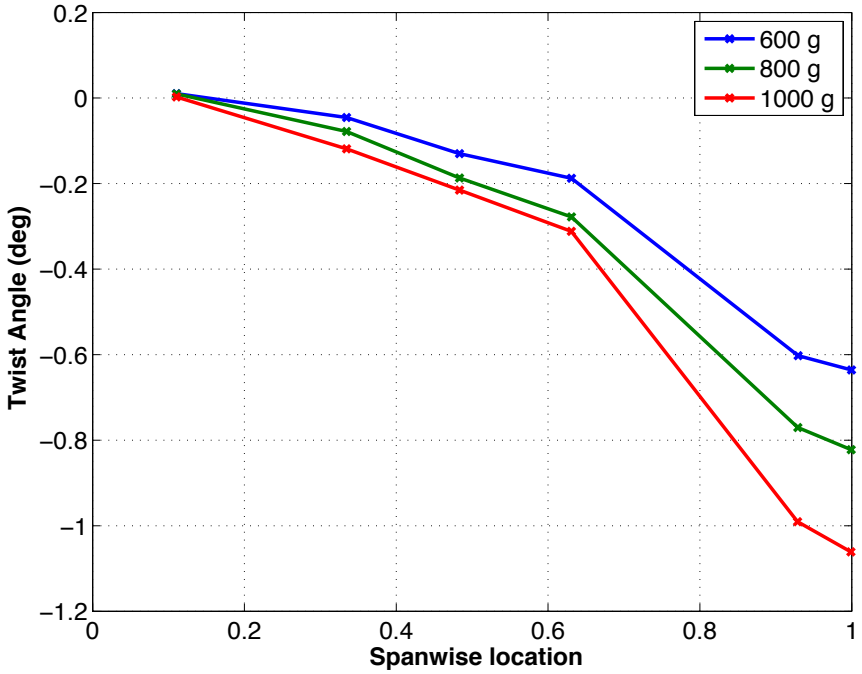

Figure 6.29: Blade torsion angle.

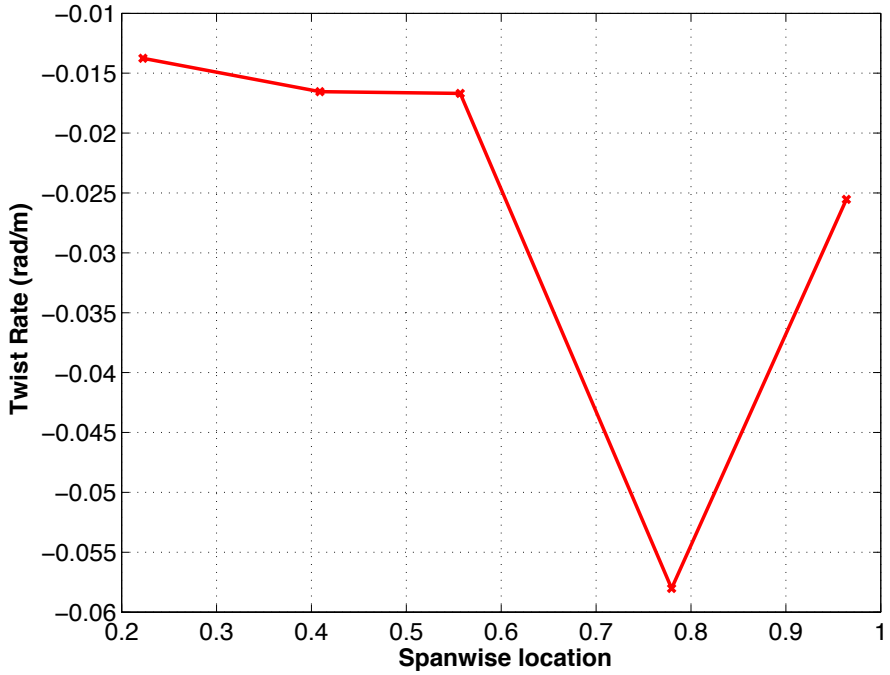

Figure 6.30: Blade torsion twist rate.

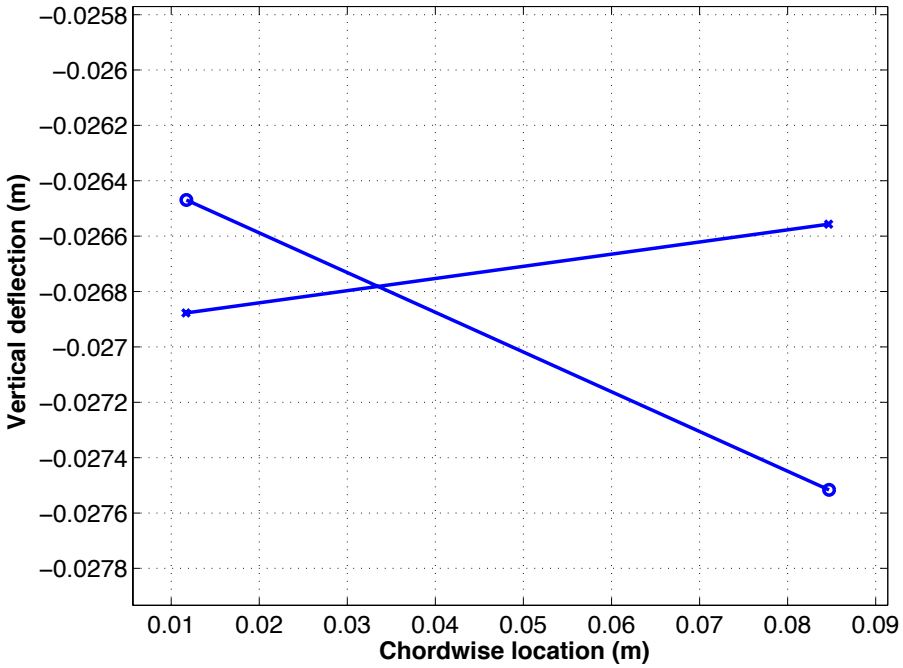

Figure 6.31: Blade torsion shear center.

Finally, chordwise bending loads were applied and in-plane deflections were recorded. Blades were found to be an order of magnitude stiffer in-plane compared to out-of-plane bending loads. Table 6.4 summaries the stiffness properties of all the four blades.

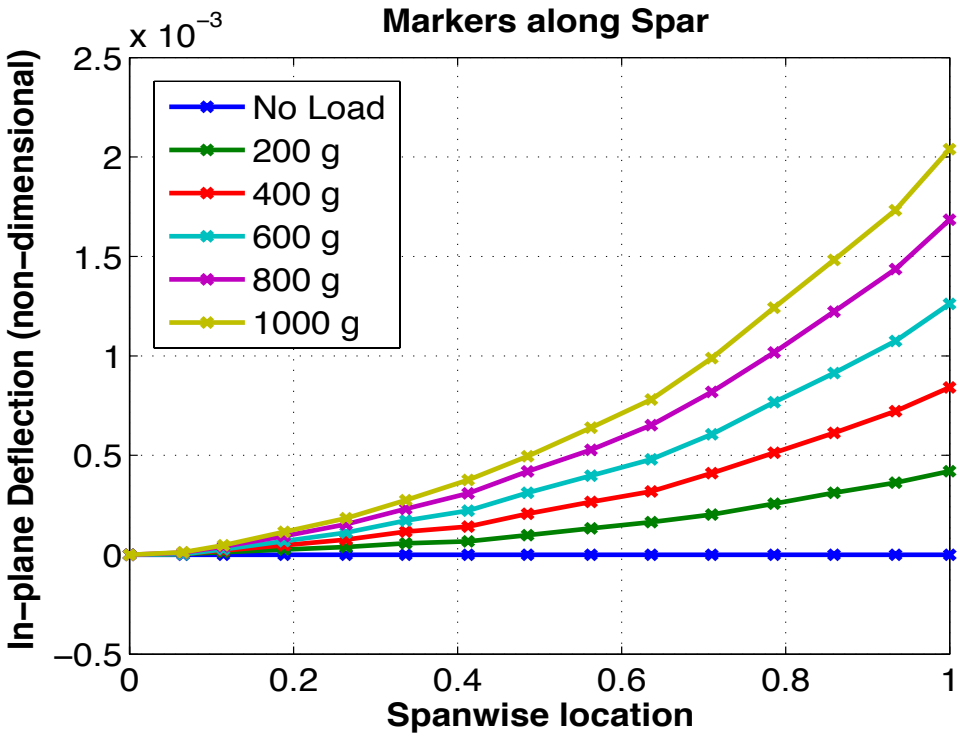

Figure 6.32: Blade chordwise bending deflection.

Table 6.4: Blade flap-wise, chord-wise and torsional stiffness.

Stiffness	Blade 1	Blade 2	Blade 3	Blade 4
EI - flap-wise (Nm^2)	35	32	32	36
EI - chord-wise (Nm^2)	690	725	721	689
GJ - torsional (Nm^2/rad)	38/24	38/24	38/24	38/24

6.4.3 Comparison of mirror and Vicon based methods

A number of studies [239, 240] were conducted at the rotorcraft lab with an aim to access the repeatability and accuracy of measuring stiffness properties using Vicon motion capture system. These also attempted comparison of Vicon method with mirror method as well.

The choice between these two methods was based on speed of implementation and accuracy of measurements. Mirror method proved to be more accurate of the two and its accuracy could be further improved by using higher intensity lasers and increasing the separation between the test article and screen. However, the implementation and data collection process was cumbersome and time consuming. With increasing numbers of mirrors, manual tracking becomes time prohibitive.

For the Vicon method, the speed of implementation and data acquisition from tracking a large number of markers was swift and convenient. As long as good baseline calibrations of the camera system and blade deflections greater than one mm could be achieved, the error in stiffness measurements was limited to 5%. Also, repeatable results were easily achieved using Vicon method.

Chapter 7: **Hover Tower Testing**

Once operation of the motor-flap system was demonstrated under rotation in the vacuum chamber, hover testing was carried out next to evaluate the system under both aerodynamic and inertial loading. A Mach scale composite rotor, with motor-flap system incorporated, was fabricated and tested in hover.

7.1 Experiments with Stiff Pitch Link

For initial experiments in hover, the blade pitch was constrained, as the objective was to establish adequate trailing edge flap operation. The actuator was operated at various input voltages and the flap amplitude output was observed. The flap frequency was fixed at 40 Hz, to test for the highest 1/rev frequency the flaps would need to operate at. Further, a feedback system was implemented to command the flap at desired operation amplitude. Before spinning the blades in hover, it was ensured that the chord-wise c.g. of the blade was slightly ahead of the quarter chord and that the span-wise c.g. of the two-bladed rotor was at the center of rotation. The trailing edge flaps Hall sensors were calibrated. Figure 7.1 shows the calibration setup using a laser based deflection measurement sensor. Figure 7.2 and Table 7.1 present the calibration for all the four trailing edge flaps.

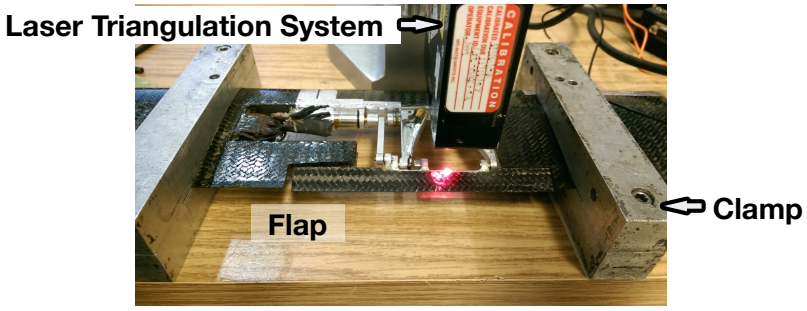

Figure 7.1: Trailing edge flap deflection calibration setup.

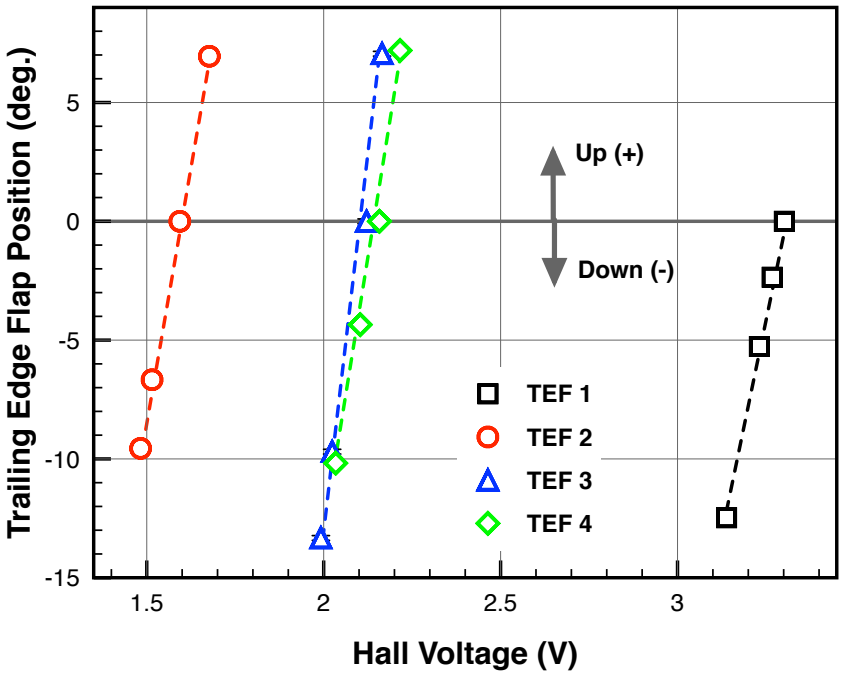

Figure 7.2: Trailing edge flap deflection calibration.

Table 7.1: Calibration co-efficeints for trailing edge flaps.

Deflection (deg.)	Slope	Intercept	R^2 value
TEF 1	76.989	-254.08	0.999
TEF 2	84.824	-135.24	0.999
TEF 3	113.830	-240.25	0.991
TEF 4	93.860	-201.53	0.989

7.1.1 Open Loop Trailing Edge Flap Control

For the open loop tests, the trailing edge flap amplitude at a fixed rotor rpm was recorded. The rotor collective was set at 4 degree for these hover experiments. An input voltage sweep was carried out and flap frequency was fixed at 40 Hz. The motor casing temperature was constantly monitored to ensure actuator operation didn't exceed desired temperature range.

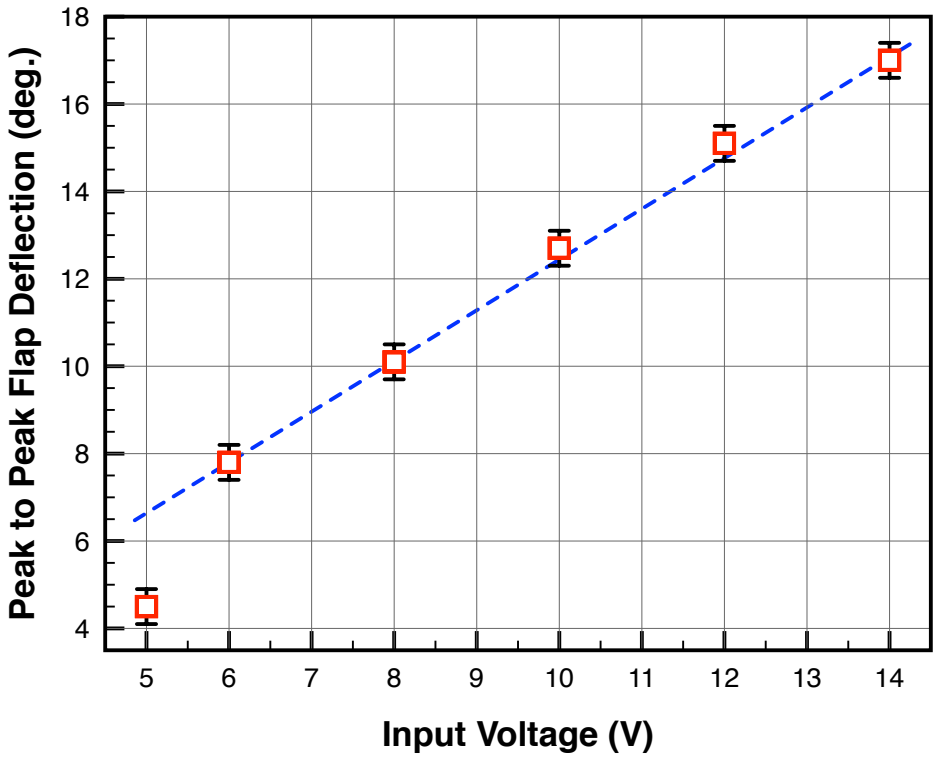

Figure 7.3: Peak-peak trailing edge flap deflections at 1900 RPM in hover at 40 Hz.

Figure 7.3 presents the peak-to-peak flap amplitude at 40 Hz obtained for various motor input voltages at 1900 rotor rpm. Large flap amplitudes were observed with flap operating under centrifugal, inertial and aerodynamic loads. Repeatability was demonstrated with increasing and decreasing input voltages (Fig. 7.4) at 1800

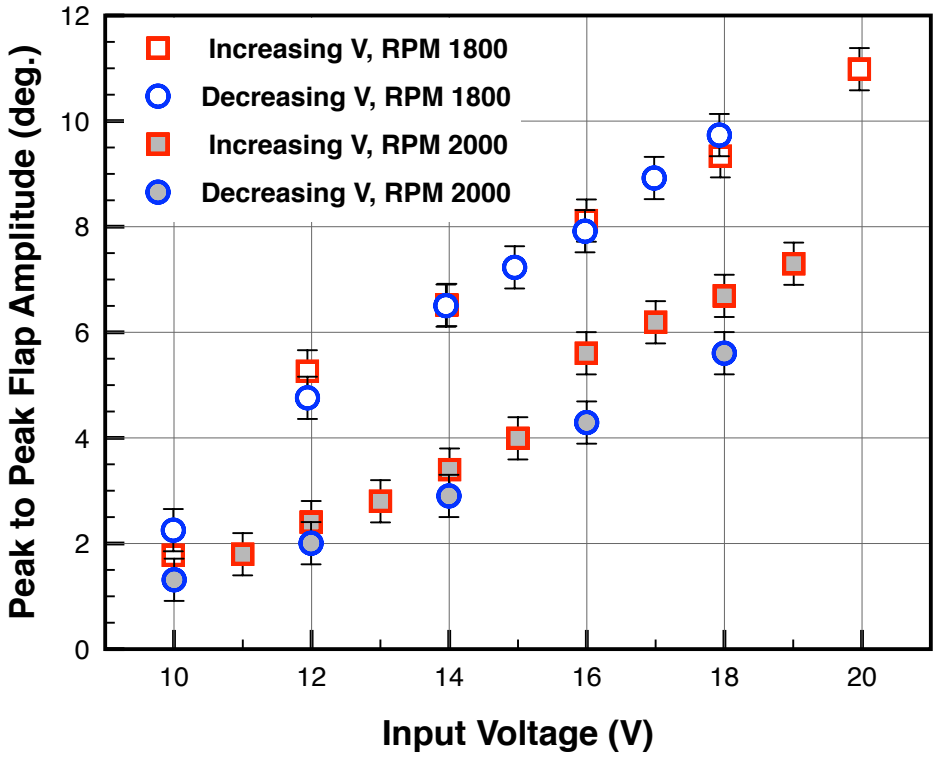

Figure 7.4: Repeatability in trailing edge flap operation at 40 Hz.

and 2000 rotor RPM. The motor casing temperature stayed within the allowable limits.

Figure 7.5 shows the trailing edge flap motion observed from the motor-flap system integrated in the blade in hover at 2000 rotor rpm, with flap operating at 40 Hz. The motion was smooth and a peak-to-peak amplitude of 15 degree was observed. Also, the trailing edge flap waveform was close to the ideal sinusoidal shape.

Figure 7.6 shows the effect of blade root collective on the trailing edge flap deflection from motor-flap system. Consistent operation was observed and for the blade collectives tested, negligible effect on trailing edge flap deflections were observed.

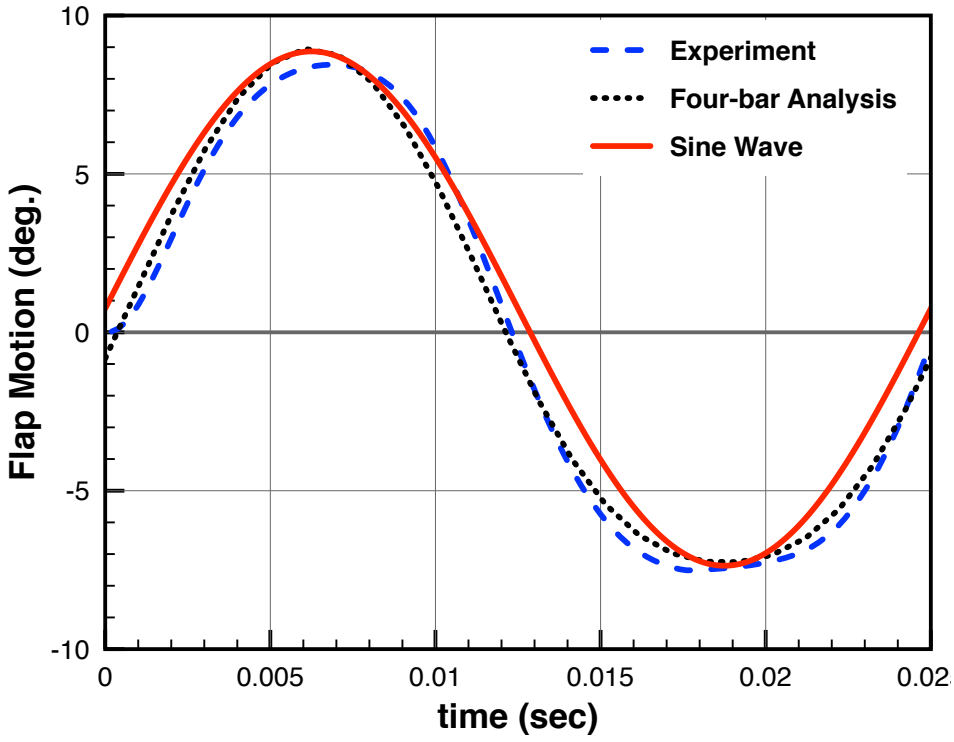

Figure 7.5: Time history of flap motion at 2000 RPM in hover.

Next, the effect of centrifugal load was studied. Figure 7.7 presents trailing edge flap deflections obtained at a number of rotor speeds. The motor-flap system configuration and blade root collective were kept unchanged, to highlight the effect of centrifugal loads. Centrifugal force is the major load on motor flap system, for a given motor input voltage, the flap deflection obtained decrease with increasing rotor speeds.

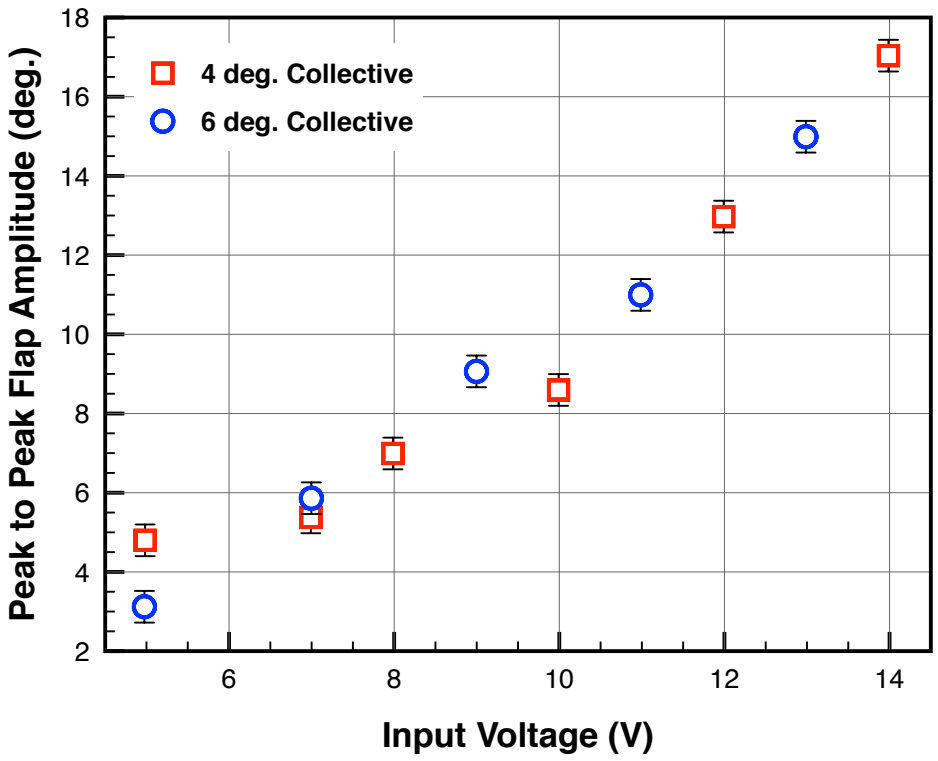

Figure 7.6: Effect of rotor collective on trailing edge flap deflections.

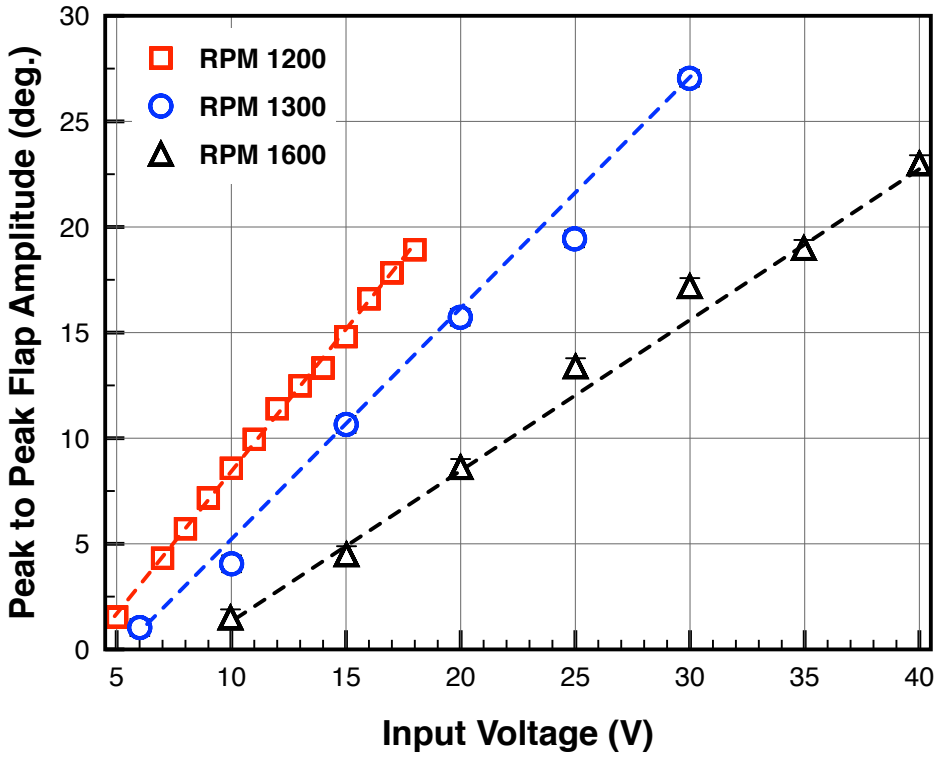

Figure 7.7: Effect of rotor speed on motor-flap system output.

7.1.1.1 Improvements in Motor-Flap System

During the development and testing process, several updates to the motor-flap mechanism were made with the aim of improving the output flap amplitude for given input power. The design of various iterations was discussed in detail in Section 4.1 and Fig. 7.8 summarizes the major versions of the motor flap system.

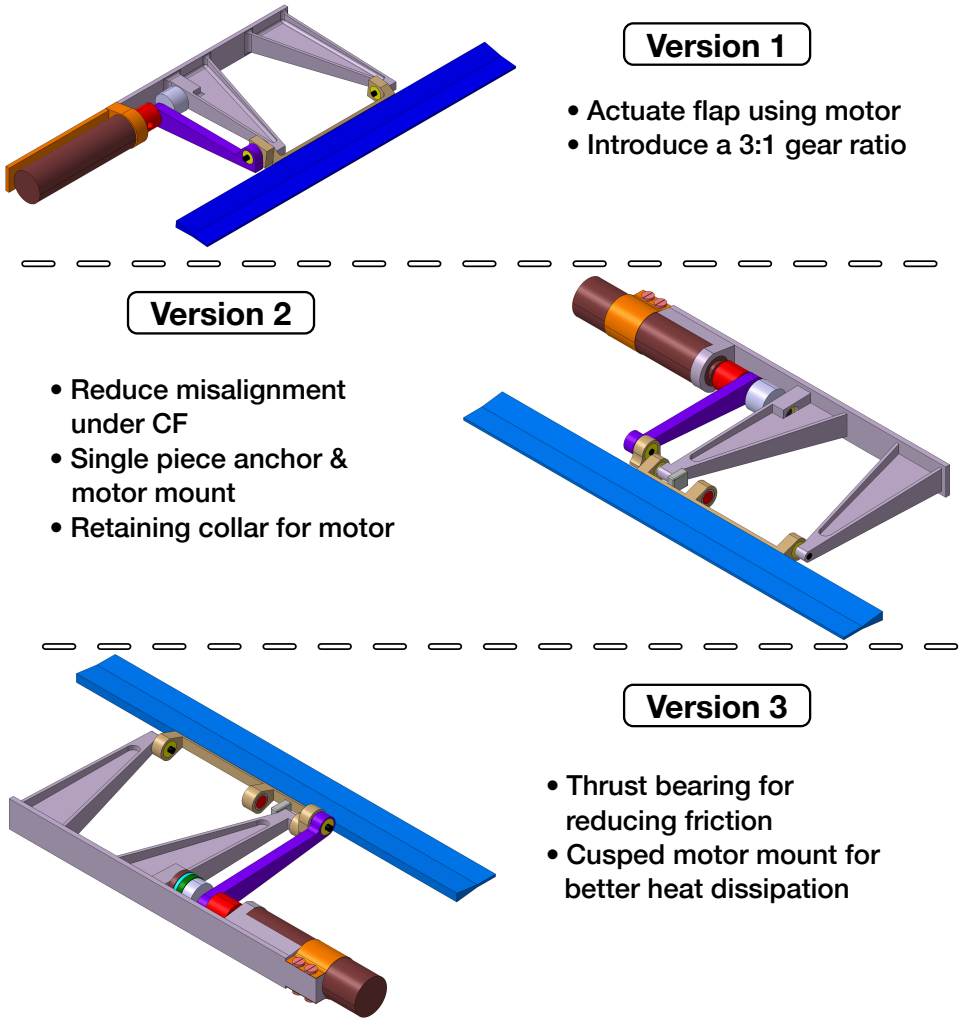

Figure 7.8: Evolution of motor-flap system design.

Aside from the effect of centrifugal load on the motor itself, the various other moving parts in the motor-flap system experienced high load too. This resulted

in increased frictional losses and wear and tear in the parts. As the operational rotor speed envelope of the system was expanded, several modifications were made to the motor-flap system to ensure consistent operation, starting with increasing the alignment of various parts. A small misalignment in the system would magnify under centrifugal loads leading to large losses. To remedy this issue, the motor holder and flap anchor were machined from single stock. These improvements are presented in Fig. 7.9. Better alignment lead to lower frictional losses, and for same rotor speed and input voltage, a higher trailing edge flap deflection was obtained. Repeatability in operation was also established (Fig.7.10), which was essential for on-blade actuator performance.

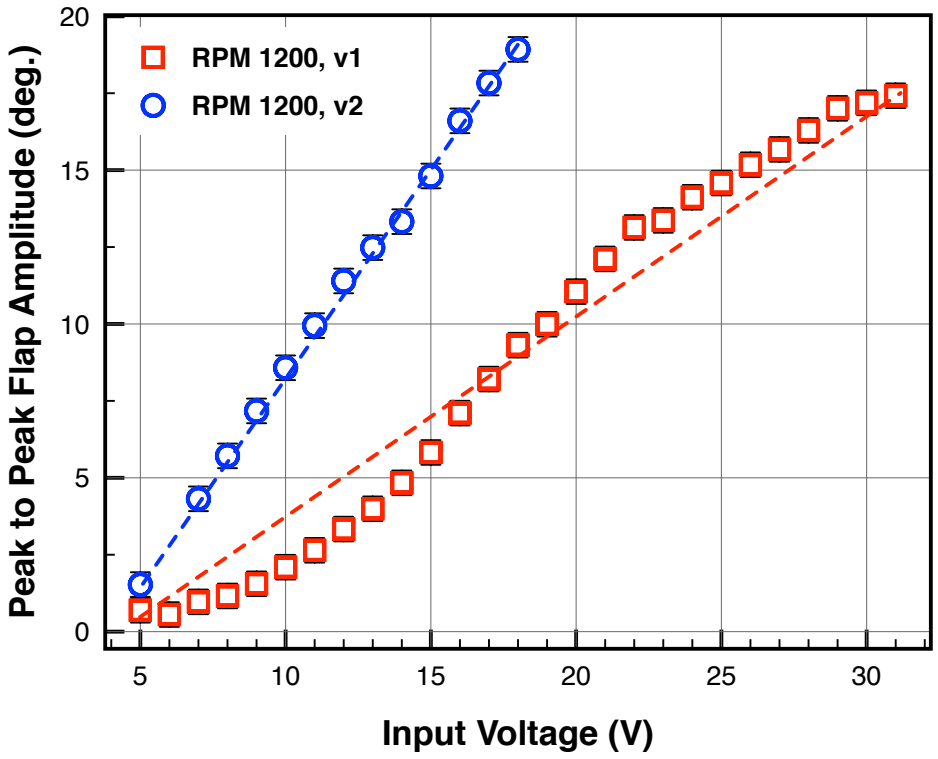

Figure 7.9: Comparison of motor-flap system versions 1 and 2.

As the motor-flap system operational envelope was expanded to higher rotor

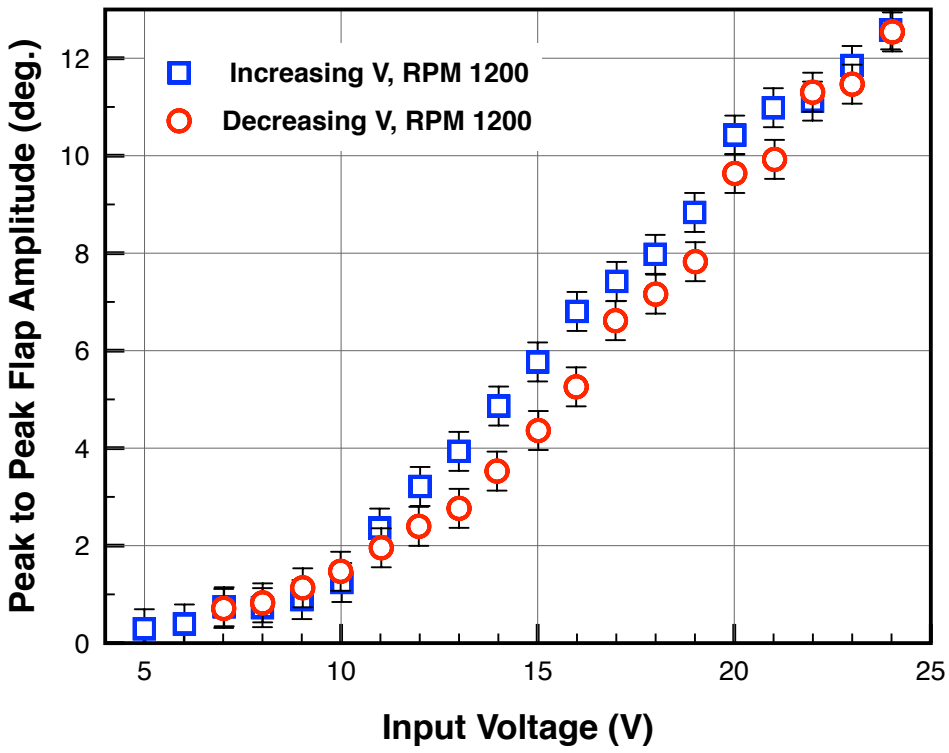

Figure 7.10: Repeatability in trailing edge flap operation version 2.

RPMs, it was observed that centrifugal loading had strong effect on trailing edge flap deflections obtained. This observation motivated in adding a thrust bearing to the motor-flap system. Additional radial bearings were placed to better negotiate the loads and thrust bearing was added to reduce the friction between the motor output and the flap rod. These changes greatly contributed in improving the system as shown in fig. 7.11.

At this point, the composite rotor blade with motor-flap system has been tested at rotor speeds of up to 2000 RPM. These tests establish that the motor-flap system could provide large flap amplitudes operating under high g-loads. This would be critical for achieving rotor trim using trailing edge flaps.

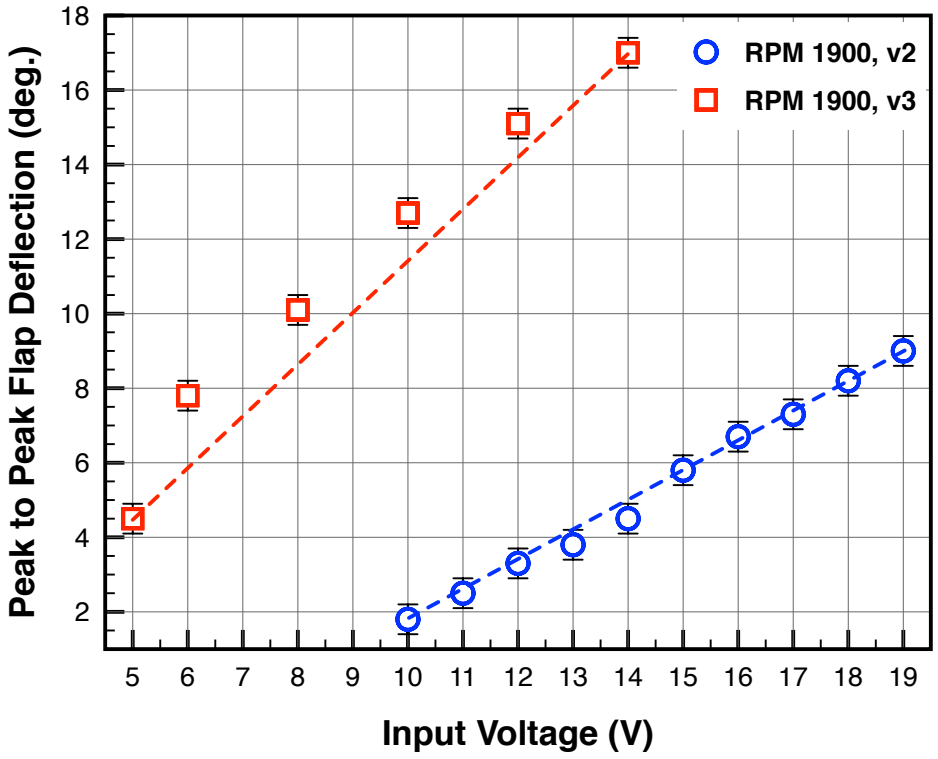

Figure 7.11: Comparison of motor-flap system versions 2 and 3.

7.1.2 Closed Loop Trailing Edge Flap Control

For the open loop tests, the emphasis was placed on achieving repeatable large peak-peak flap amplitudes. Once the open loop flap operation on the hover tower was established, a single-input-single-output PID based controller for the flap amplitude was implemented. Instantaneous flap position from the Hall sensor was fed to the controller and that commanded the motor input voltage. Figure 7.12 is the pictorial representation of the controller.

Figure 7.13 shows the controller maintaining a desired peak-peak flap amplitude of 3 degree at 40 Hz flap frequency. The rotor was spun to 1200 RPM and certain open-loop flap amplitude from the system was obtained. At this point, the

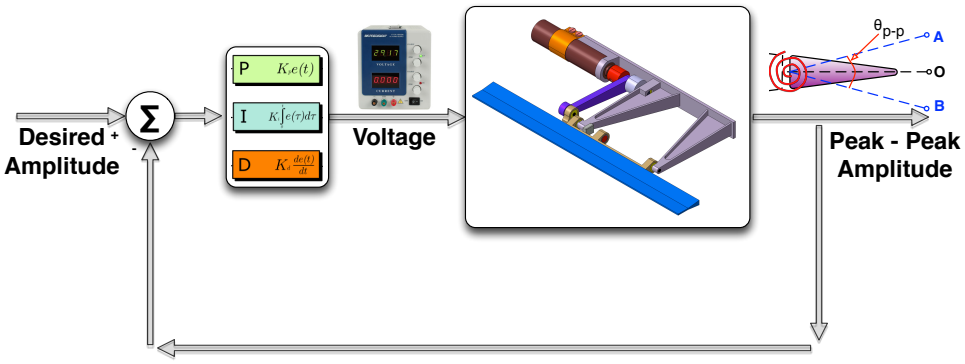

Figure 7.12: Closed loop PID controller.

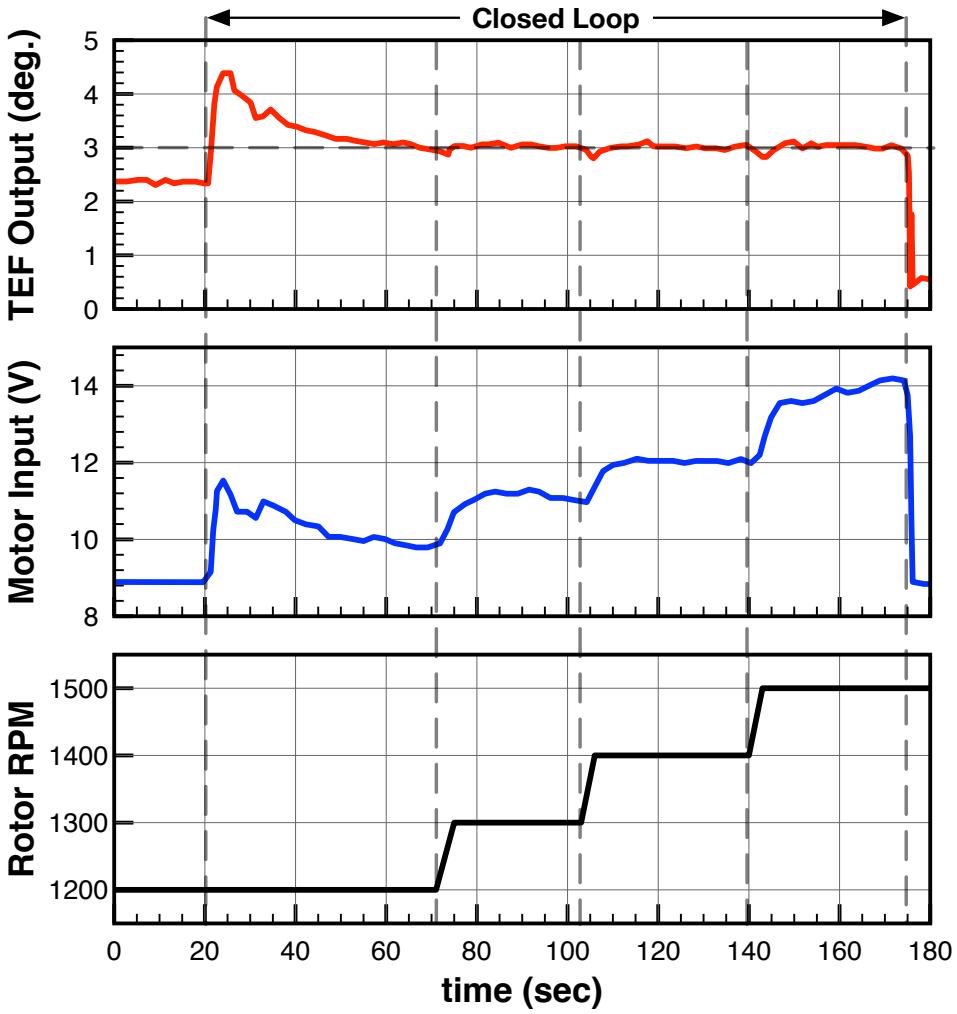

Figure 7.13: Closed loop controller performance at various rotor speeds.

PID feedback controller was switched on, which adjusted the input voltage to produce the desired flap amplitude. Further, as the rotor speed was increased from 1200 to 1500 RPM, the controller was able to steadily hold the flap amplitude at the desired level. To further examine the performance of the controller, another experiment was conducted, where the rotor speed was held steady at 1200 RPM and the controller was required to operate the flap at various desired flap amplitudes (Fig. 7.14). These experiments demonstrated consistent and repeatable controller operation.

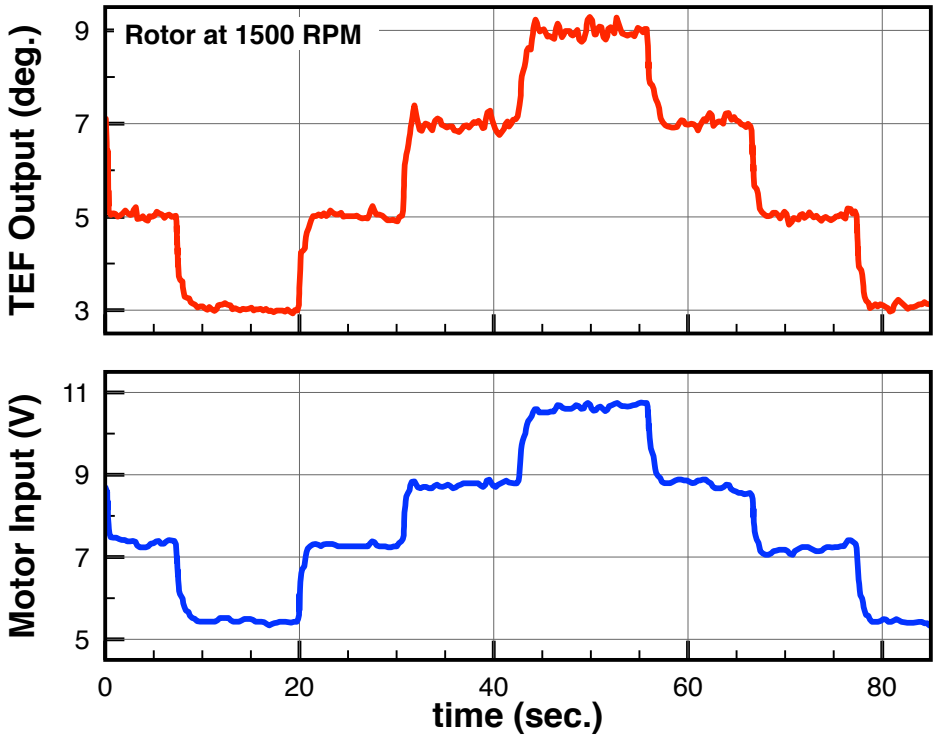

Figure 7.14: Closed loop controller performance at 1200 rotor RPM.

In addition to commanding the peak-to-peak flap amplitude, it was desired to control the mean position of the trailing edge flap as well. Figure 7.15 shows the flap mean position control being implemented. The peak-peak amplitude was

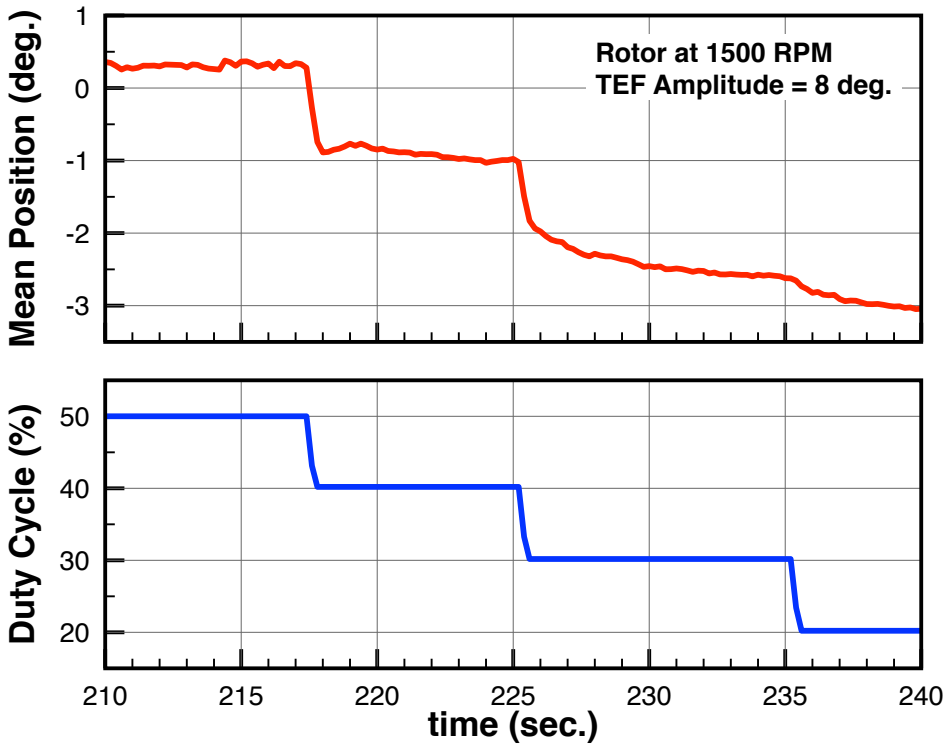

Figure 7.15: Flap mean position control at 1500 rotor RPM.

maintained at 8 degree, the rotor speed was held at 1500 RPM and the flap was operated at 40 Hz. By changing the duty cycle of the direction signal, the flap output was biased. Thus, changing the duty cycle from 50% (balanced/equal flap up and down) to 40% and lower, the flap mean position is changed. The closed loop on amplitude ensures that the peak-peak value remains unchanged. A limited mean position control was demonstrated by this experiment.

7.2 Experiments with Soft Pitch Link

7.2.1 Mechanism of Moment Trailing Edge Flap

Consider an active blade at a pitch setting (θ) with no trailing edge flap deflection (Fig. 7.16). An upward trailing edge flap deflection reduces the effective local camber, reducing local lift ($-\Delta L_1$) but producing a nose up pitching moment ($+\Delta M_1$). The blade pitch increases in response to this moment to reach a new pitch angle ($\theta + \Delta\theta$) until moment equilibrium is established. This pitch change produces an additional lift (ΔL_2) increasing the overall lift on the blade. Thus the immediate response of an upward trailing edge flap deflection is a decrease in local lift, but the response of the blade is to pitch nose up, causing an increase in the overall blade lift.

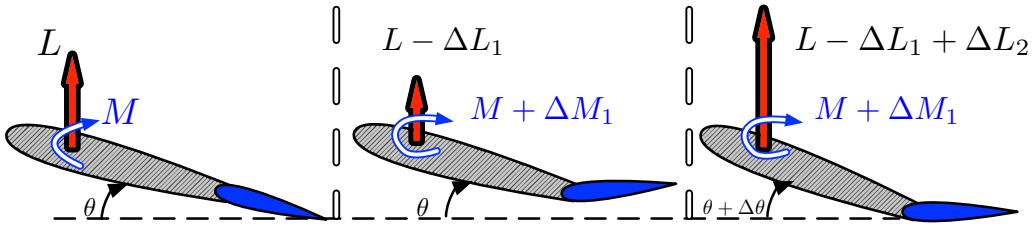

Figure 7.16: Mechanism of blade pitching using a moment trailing edge flap.

7.2.2 Design and Calibration of Soft Pitch Link

The aim of swashplateless rotor experiments was to demonstrate blade pitching in response to the moments created by deflecting trailing edge flaps. For these experiments, the blade was assumed to be rigid in torsion, instead the softness in

pitch was provided by replacing the stiff pitch links in the hub (Fig. 7.17) with a new unit whose stiffness could be tuned to a value as desired (Fig. 7.18). A set of radial pitch bearings in the blade grips allowed for low-friction motion of the blade about the pitch axis.

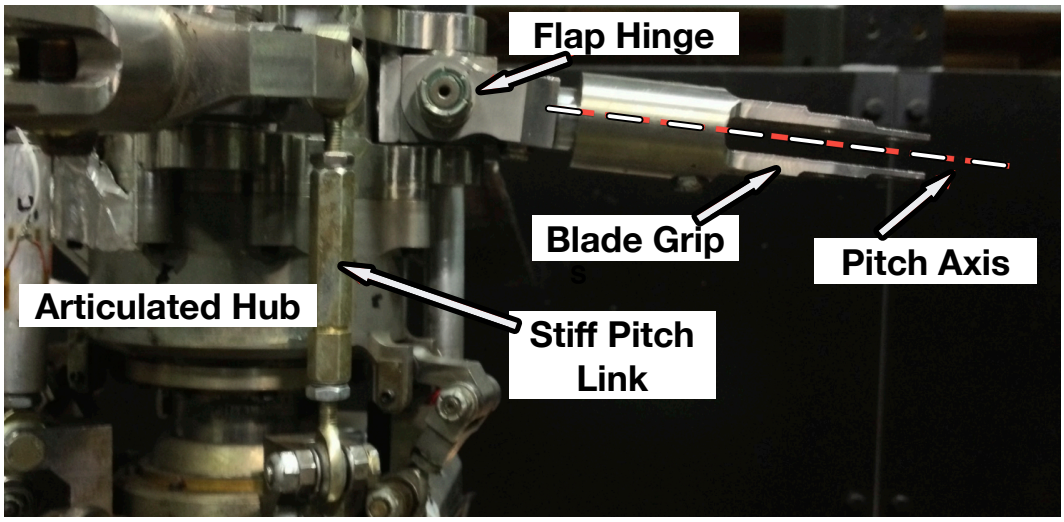

Figure 7.17: Stiff pitch link on an articulated rotor hub.

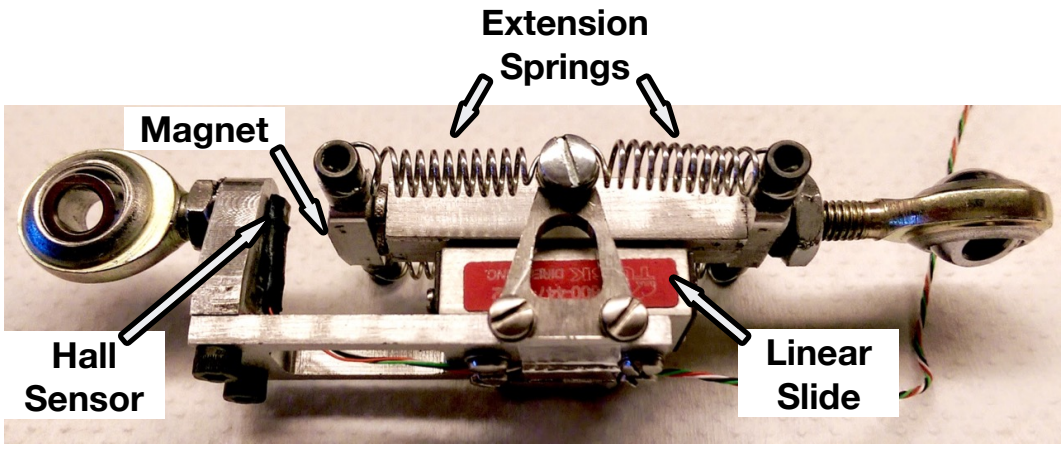

Figure 7.18: Soft pitch link with extension springs for frequency tuning.

The soft pitch link consisted of sets of extension springs mounted on a frictionless linear slider. The spring stiffness were chosen to obtain the desired pitch

stiffness. The travel of the pitch link is calibrated for blade root pitch angle using a Hall sensor. Figure 7.19 shows the calibration setup on the hover stand. A moment arm was used to torque the rotor blade at root. The blade angular motion was measured using inclinometer as well as the blade root pitch sensor. The extension springs used in the slip ring were carefully calibrated independently on the bench top as well.

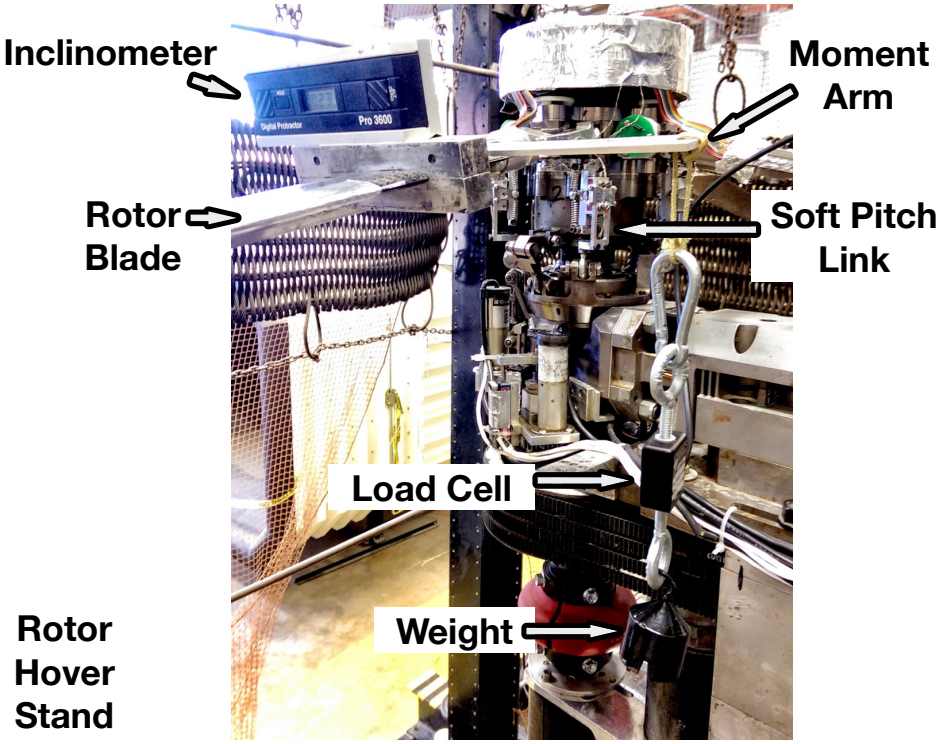

Figure 7.19: Soft pitch calibration setup on the hover stand.

Figure 7.20 shows the soft pitch link response to load torque. All the pitch links were demonstrated to have similar torsional stiffness. For different operational conditions, extension springs were replaced to achieve the desired torsional stiffness.

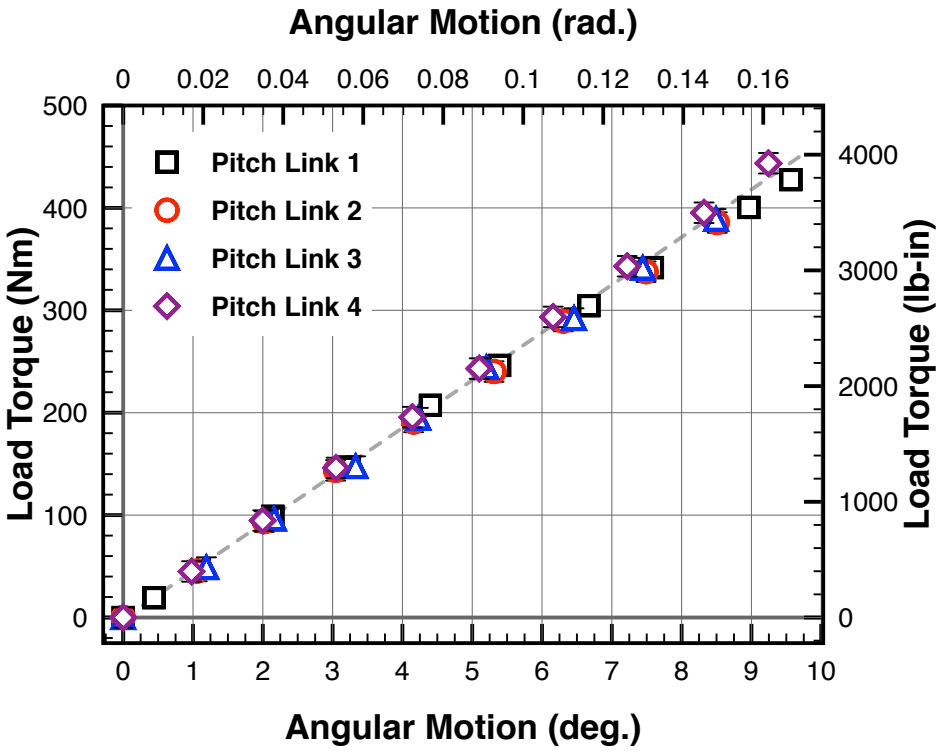

Figure 7.20: Calibration curve for soft pitch links.

7.2.3 Blade Root Pitch Response

To achieve a desired pitch setting for the rotor at operational rpm, the blade pitch had to be preset before rotation, termed as blade indexing. This essentially required setting the blade root pitch at a high positive angle, the nose down pitching moment from the rotating blade reduces this angle. The index angle depends on blade properties, operation rpm and the pitch spring stiffness. For these experiments, the index angle was set so as to achieve a blade pitch of about 4 degree at 1200 rotor rpm with a pitch spring stiffness of 1.9/rev.

Figure 7.21 shows the time history of the blade root pitching motion in response to trailing edge flap inputs at 1/rev (25 Hz) at 1500 rotor rpm in hover.

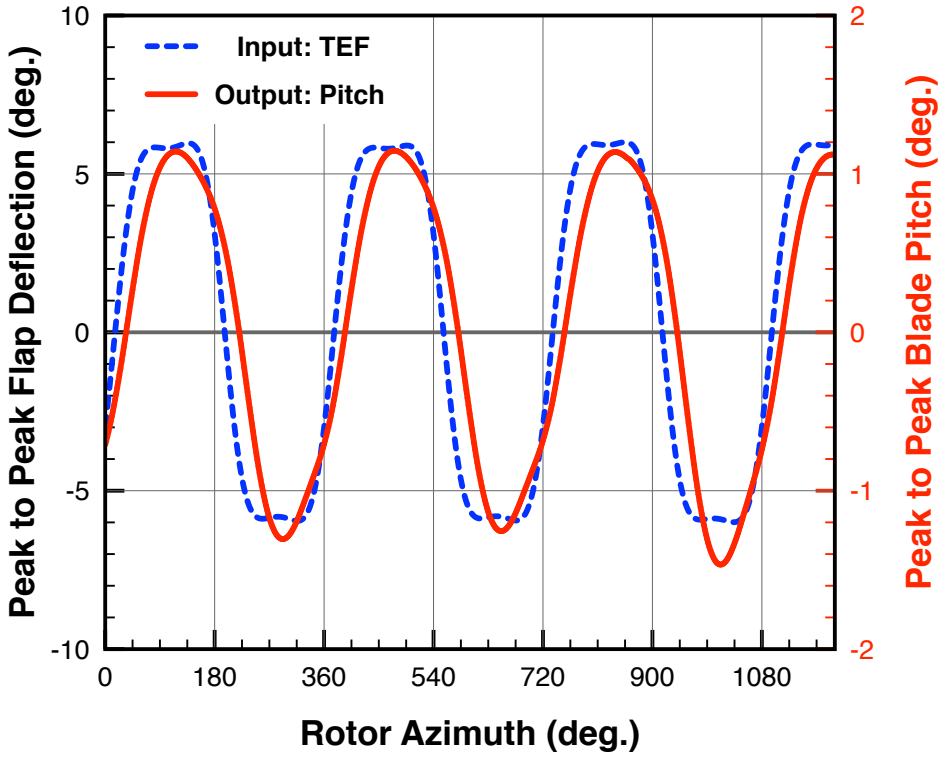

Figure 7.21: Time history of blade pitch response to trailing edge flap input at 1500 RPM, 25 Hz flap frequency, 1.55/rev pitch stiffness.

The root pitch stiffness is at 1.55/rev. The blade pitch follows the trailing edge flap input with a delay. Smooth trailing edge flap and blade pitching mechanism was observed.

Further, a sweep of various trailing edge flap amplitudes was carried out and the blade pitch response was recorded. The trailing edge flap input could be thought of as a combination of a steady deflection (i.e., collective trailing edge flap) and oscillating flap deflections (i.e., cyclic trailing edge flap). The cyclic flap was operated at 1/rev frequency, 20 Hz for 1200 rotor rpm and 25 Hz for 1500 rotor RPM.

Figure 7.22 shows the effect of steady flap deflections on the root pitch of the blade. Due to indexing, when the trailing edge flap is aligned with the trailing edge of the blade, the root pitch is about 4° at 1200 rotor rpm. Upwards trailing edge

flap deflection (positive) increased the blade pitch and downwards trailing edge flap deflection (negative) decreased the blade pitch. Similar trend was observed at 1500 rotor rpm. Since the pitch spring is softer for 1500 rpm case, the flattening produced by spinning the rotor is greater than at 1200 rotor rpm. Further, the slope of change in blade collective with change in trailing edge flap collective seems to be similar for both the rotor speeds.

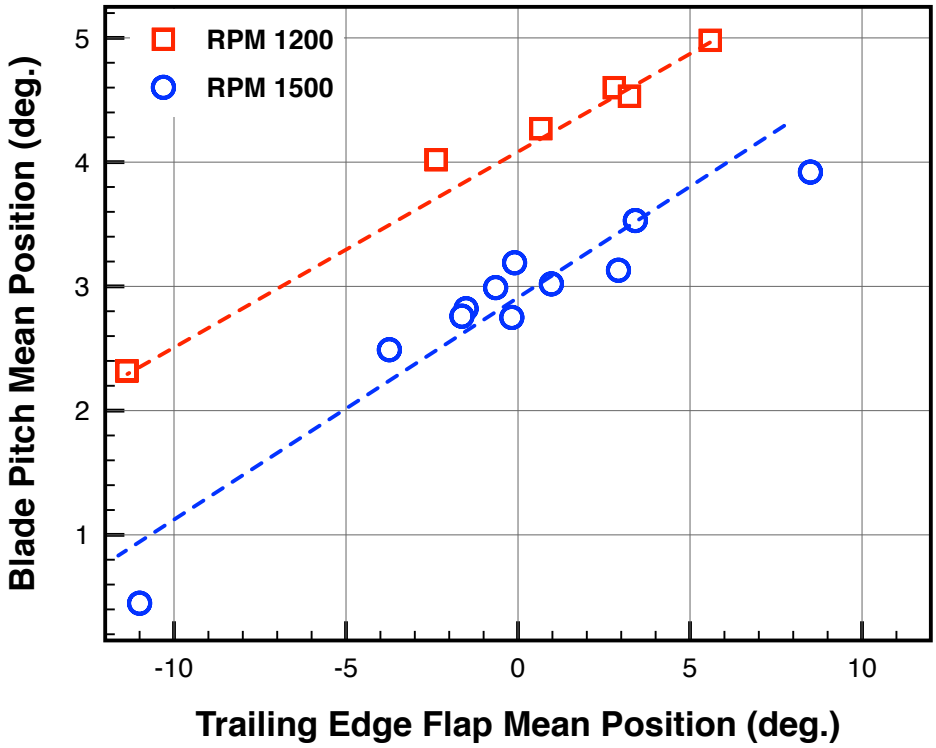

Figure 7.22: Blade root collective angle response to trailing edge flap collective, pitch stiffness of 1.9/rev at 1200 RPM and 1.55/rev at 1500 RPM.

Figure 7.23 presents the cyclic response of the blade pitch to trailing edge flap inputs. For low trailing edge flap inputs, the blade pitch response is comparably small. This could be due to frictional losses in the radial bearings and linear slider in the soft pitch link As the flap amplitudes were increased, large blade pitch angles were recorded. At 1500 rotor rpm, 18 deg. peak-peak flap cyclic produced 8 deg.

peak-peak blade root pitch cyclic. These experiments demonstrated the effectiveness of trailing edge flaps in producing blade pitching.

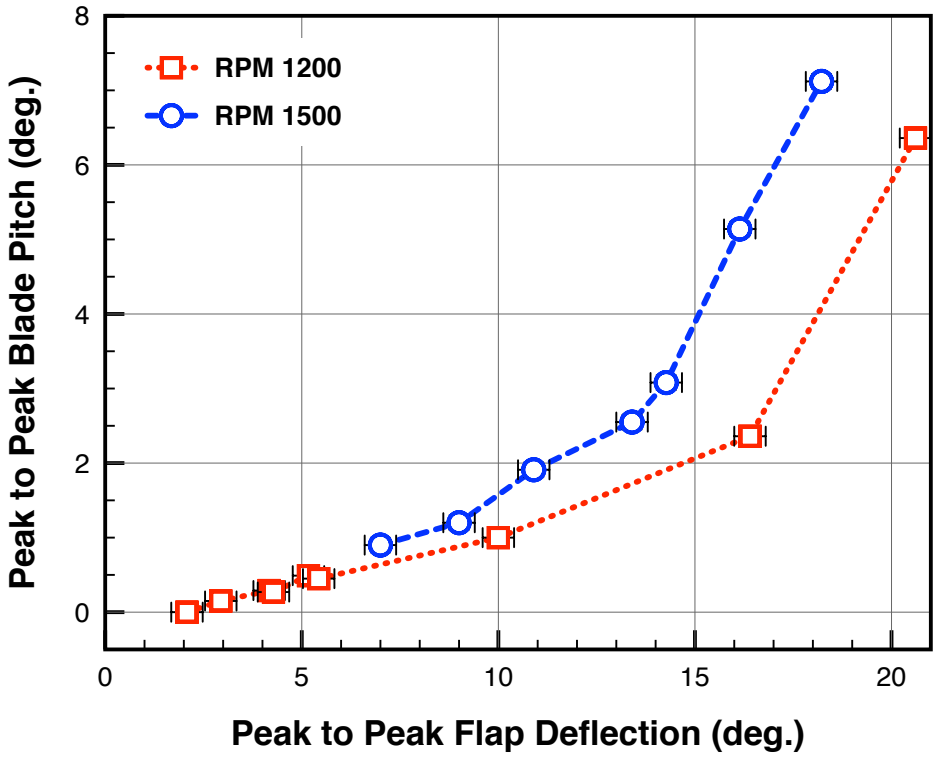

Figure 7.23: Blade root cyclic angle response to trailing edge flap cyclic, pitch stiffness of 1.9/rev at 1200 RPM and 1.55/rev at 1500 RPM.

Chapter 8: **Wind Tunnel Testing**

Once the active blade operation was established on the hover test stand, the suitability of the active trailing edge flaps in trimming the rotor in forward wind speed was assessed. Wind tunnel trim could be understood as adjusting the blade pitch to minimize cyclic blade flapping at desired rotor thrust condition. Conventionally, swashplate pitch actuators were used to trim the rotor by directly commanding the blade root cyclic pitch. A swashplateless trim using trailing edge flaps involved commanding trailing edge flaps and the resulting pitching moment pitched the blade about the root.

When using the torsionally soft rotor, it is important to ensure the blade chord-wise c.g. is at or ahead of quarter-chord to avoid any aeroelastic instability. The test facility and installation procedure is first explained, followed by active blade track and balance. The active rotor was systematically tested, first with stiff pitch links the motor-flap operation was verified under various rotor RPMs and wind speeds. A baseline swashplate trim control inputs were also recorded. Finally the torsional stiffness was reduced to 2/rev and swashplateless wind tunnel rotor trim was attempted using motor operated trailing edge flaps.

8.1 Installation Procedure

The rotor test stand as used for hover test and described in Section 2.1 was moved to the Glenn L. Martin wind tunnel for forward flight testing. The wind tunnel is a closed circuit tunnel with a rectangular test section 11 ft (3.35 m) wide and 7.75 ft (2.36 m) tall, capable to operating at wind speeds of up to 230 miles per hour (102 meters per second). The details of the wind tunnel are described in Section 2.10.

The installation and calibration checklist for the rotor test apparatus in the wind tunnel is listed below:

1. Install the rotor stand in the test section. Make sure that the shaft tilt is zero. The mounting structure for the rotor test stand is shown in Fig. 8.1.

2. Connect the two slip ring cables, the balance and swashplate controls cables.

3. Connect the cables to the control box and the data acquisition system.

4. Setup the acquisition and control computer, motor controllers and the dc power supplies.

5. Check if the LabView VI reads all the channels. If not, there is a loose or broken connection.

6. Make sure that the shaft encoder calibrated to correct azimuth location. calibration procedure is detailed in Section 2.4.2. Also, ensure that the sensor is aligned to correct azimuth setting.

(a) Using the two wind tunnel walls, set the rotor at zero azimuth. Measure the distance between the blade lag hinge and the two walls. Zero azimuth is equidistant from both the walls.

(b) Loosen the screws holding the encoder and adjust it to read zero azimuth.

(c) Once adjusted to zero azimuth, make sure to tighten the screws holding the encoder.

7. Calibrate the swashplate control angles. The calibration process and curve was included in Section 2.4.4.

(a) Mount the two axes inclinometer setup on blade grip number one.

(b) Use the stiff pitch links and set blade number one at zero blade pitch and zero blade flap angles.

(c) Record in an excel sheet, the control voltages and the pitch angle at 0, 90, 180 and 270 degree azimuth locations. At each azimuth, ensure that the blade flap angle is zero.

(d) At least five cases of setting the swashplate at various orientations by moving the collective and cyclic controls are needed.

(e) Cover the entire collective and cyclic travel range.

(f) Be careful of the travel limits on each control.

8. Calibrate the blade pitch sensors.

(a) Ensure the blade is at zero azimuth location and zero blade flap.

(b) Loosen the nuts holding the stiff pitch link and turn it to change the length, which changes the blade root pitch.

(c) Calibrate the pitch sensor for each blade for a range of +15 to -5 degree using procedure detailed in Section 2.4.3.

9. Calibrate the blade flap sensor.

   (a) Set the blade root pitch at zero and blade at zero azimuth location record the blade flap angle.

   (b) Record the bottom most angle, -2, -1, 0, +1, +2 and +5 deg. flap angle.

   (c) Follow the calibration procedure in Section 2.4.3.

10. Calibrate the blade lag sensors.

    (a) Set the blade root pitch and flap at zero and blade at zero azimuth location record the blade flap angle.

    (b) Use the wind tunnel walls to calibrate the lag angle, using the procedure detailed in Section 2.4.3.

11. Check the calibration of the trailing edge flap deflection angles.

12. Connect all the channels to the slip ring terminals as per chart in Fig. 8.5 and 8.7.

13. Finally, use the shaft inclination turnbuckle and set the shaft tilt at desired angle. For the results presented here the shaft tilt was set at two degree forward.

Figure 8.3 shows the active rotor mounted in the wind tunnel test section. Figure 8.4 shows the view of the control room at the wind tunnel.

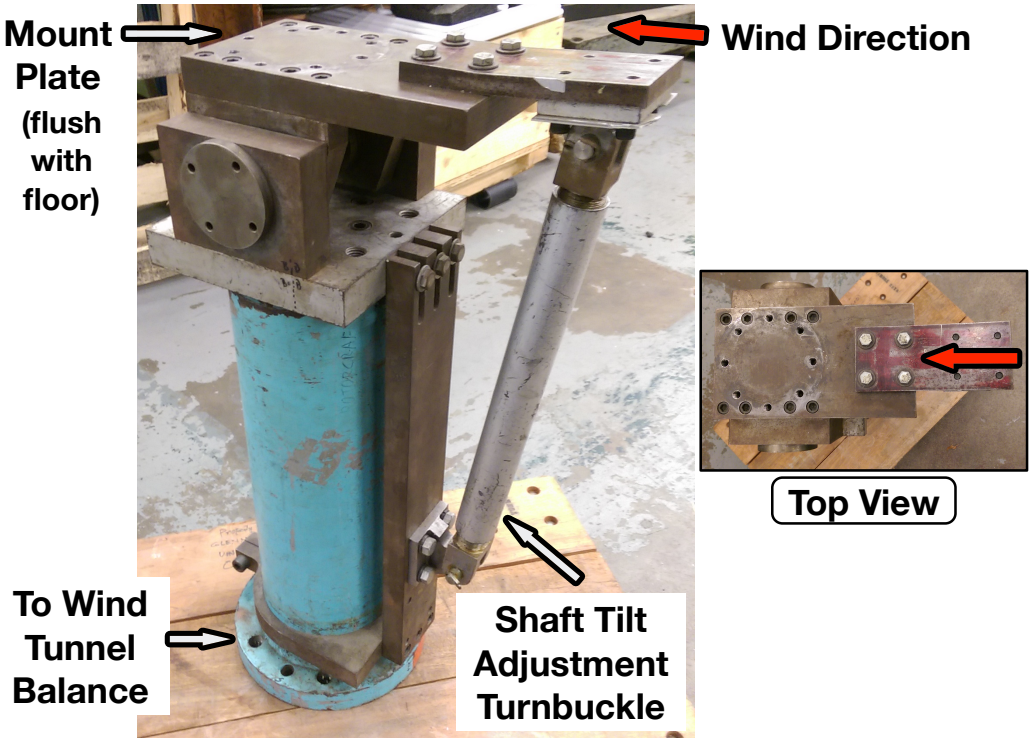

Figure 8.1: Mounting structure for rotor test stand in the wind tunnel.

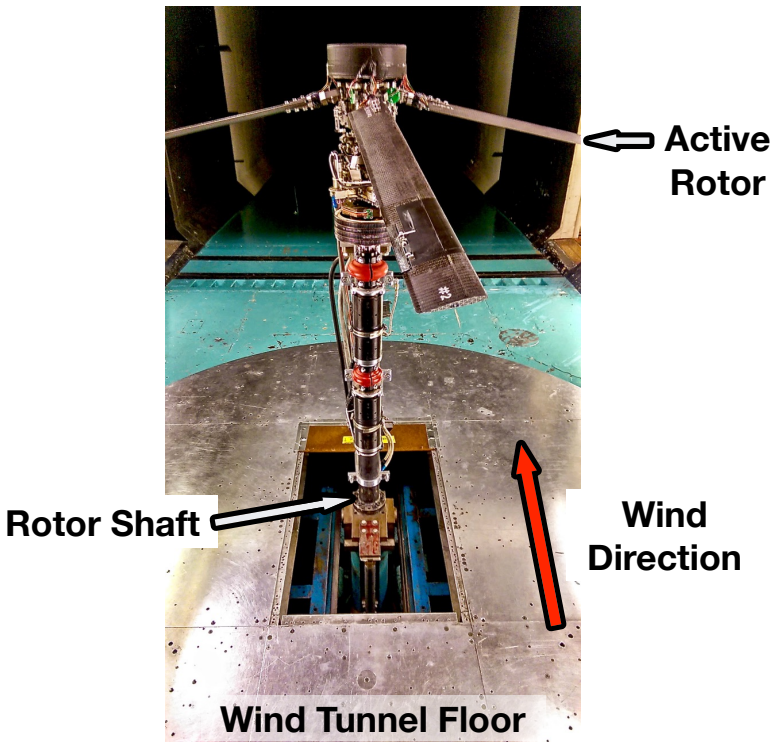

Figure 8.2: Rotor test stand mounted in the wind tunnel.

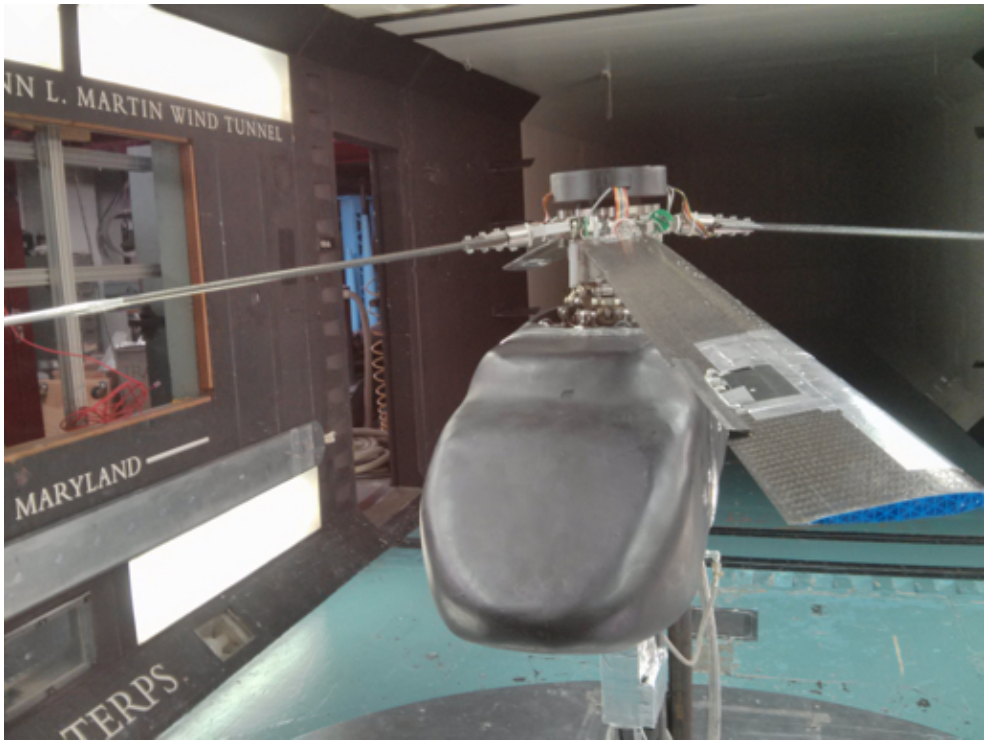

Figure 8.3: Rotor test stand installed in Glenn L. Martin wind tunnel.

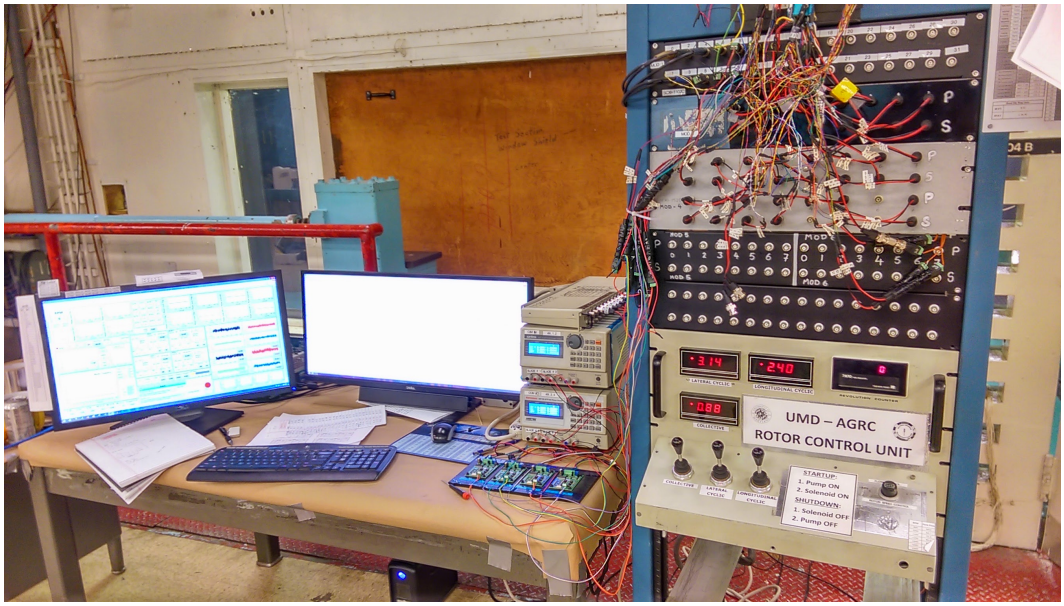

Figure 8.4: View of the control room at Glenn L. Martin wind tunnel.

Hub Bal + Swash Ctrls + Hub Accel + Oil temp + Motor Currents			
Label		DAQ Ch #	scale
Axial Force	Power	MOD 2: ai0	3m to -3m
	Signal		
Side Force	Power	MOD 2: ai1	5m to -5m
	Signal		
Normal Force	Power	MOD 2: ai2	3.5m to 1m
	Signal		
Rolling Moment	Power	MOD 2: ai3	5m to -5m
	Signal		
Pitching Moment	Power	MOD 2: ai4	1m to -4m
	Signal		
Yawing Moment	Power	MOD 2: ai5	5m to -5m
	Signal		
Torque	Power	MOD 2: ai6	0 to -15m
	Signal		
Shaft Encoder	Power	MOD 2: ai7	shaft encoder
	Signal		
1/rev		MOD 1: ai0	5 to -500m
60/rev		MOD 1: ai1	5 to -500m
Collective		MOD 1: ai2	3 to 0
Longitudinal		MOD 1: ai3	3 to 1.5
Lateral		MOD 1: ai4	4 to 2
Accelerometer X		MOD 1: ai5	3 to 0
Accelerometer Y		MOD 1: ai6	3 to 0
Accelerometer Z		MOD 1: ai7	3 to 0
Oil Temperature		MOD 8: ai4	100 to 20
Current Motor 1		MOD 1: ai8	1 to -1
Current Motor 2		MOD 1: ai9	1 to -1
Current Motor 3		MOD 1: ai10	1 to -1
Current Motor 4		MOD 1: ai11	1 to -1

Dead Slip Ring Lines	
SR # 1	6, 51
SR # 2	1, 18, 49

Rotor Torque + Blade Flap + Pitch				
SR # 1 Ch #	Label		DAQ Ch #	scale
1	Torque	Red : V +	MOD 2: ai6	0 to -15m
2		Black : V -		
3		Green : S +		
4		White : S -		
45	Blade Flap # 1 SR # 2	Red : V +	MOD 3: ai0	5 to -500m
46		Black: Gnd		
47		White : S +		
48		Black: Gnd		
9	Blade Flap # 2	Red : V +	MOD 3: ai1	5 to -500m
10		Black: Gnd		
11		White : S +		
12		Black: Gnd		
13	Blade Flap # 3	Red : V +	MOD 3: ai2	5 to -500m
14		Black: Gnd		
15		White : S +		
16		Black: Gnd		
17	Blade Flap # 4	Red : V +	MOD 3: ai3	5 to -500m
18		Black: Gnd		
19		White : S +		
20		Black: Gnd		
53	Pitch # 1	Red : V +	MOD 3: ai4	5 to -500m
54		Black: Gnd		
55		Green : S +		
56		White: Gnd		
57	Pitch # 2	Red : V +	MOD 3: ai5	5 to -500m
58		Black: Gnd		
59		Green : S +		
60		White: Gnd		
61	Pitch # 3	Red : V +	MOD 3: ai6	5 to -500m
62		Black: Gnd		
63		Green : S +		
64		White: Gnd		
33	Pitch # 4	Red : V +	MOD 3: ai7	5 to -500m
34		Black: Gnd		
35		Green : S +		
36		White: Gnd		

Figure 8.5: Channel labels of hub sensor connections for active rotor experiments.

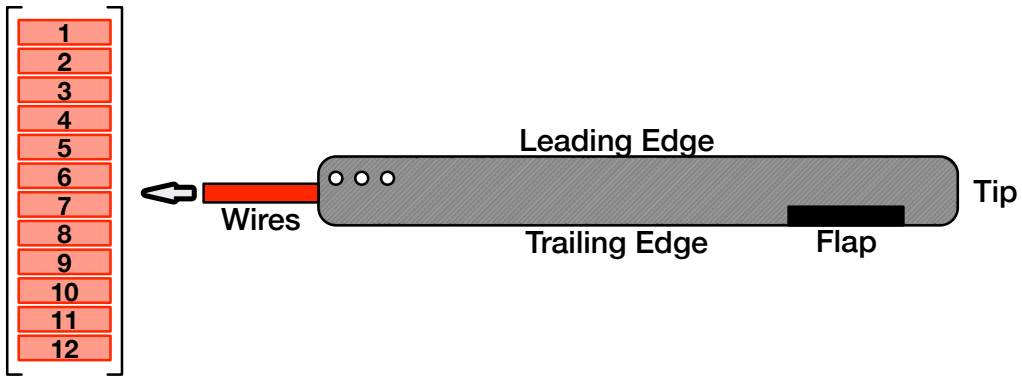

Figure 8.6: Blade wire labeling convention.

Active Blades + Soft Pitch Links							
Ch #		Blade Wire	Label		DAQ Ch #	scale	ohm
Blade # 1 SR # 1 (11 wires only)	41	2	Motor W1		xx	xx	4.0 / 4.0
	42	3	Motor W2				
	43	4	Motor W3				
	45	7	TEF Angle	Red : Power +	MOD 4: ai0	5 to -500m	in:8.8M / out:31M
	46	9		Black, White : Gnd			
	48						
	47	11		Green : Signal +			
	49	6	TC +	White	MOD 8: ai0	80 to 20	2.5
	50	5	TC -	Red			
Blade # 2 SR # 1	25	3	Motor W1		xx	xx	3.8 / 3.8
	26	4	Motor W2				
	27	5	Motor W3				
	29	6	TEF Angle	Red : Power +	MOD 4: ai1	5 to -500m	in:8.8M / out:23M
	30	8		Black, White : Gnd			
	32						
	31	7		Green : Signal +			
	7	1	TC +		MOD 8: ai1	80 to 20	2.5
	8	2	TC -				
Blade # 3 SR # 2	33	3	Motor W1		xx	xx	3.8 / 3.8
	34	4	Motor W2				
	35	5	Motor W3				
	37	7	TEF Angle	Red : Power +	MOD 4: ai2	5 to -500m	in:8.5M / out:25M
	38	6		Black, White : Gnd			
	40						
	39	8		Green : Signal +			
	41	1	TC +		MOD 8: ai2	80 to 20	3.4
	42	2	TC -				
Blade # 4 SR # 2	17	6T	Motor W1		xx	xx	3.9 / 3.8
	20	7T	Motor W2				
	19	8T	Motor W3				
	21	8B	TEF Angle	Red : Power +	MOD 4: ai3	5 to -500m	in:9.7M / out:28M
	22	7B		Black, White : Gnd			
	24						
	23	6B		Green : Signal +			
	15	4T	TC +		MOD 8: ai3	80 to 20	2.8
	16	5T	TC -				

Figure 8.7: Channel labels of on-blade connections for active rotor experiments.

8.2 Rotor Track and Balance

The procedure for blade chordwise, spanwise and flap-wise inertia matching was detailed in Section 6.3. The final table for matched rotor blades is reproduced in Table 8.1.

Table 8.1: Blades weight, c.g. and inertia comparison.

	Weight (g)	Chordwise C.G. (%c)	Spanwise C.G. (%R)	Flap Inertia $(kg-m^2)$	Tip Color –
Blade 1	304.3	23.7	50	0.0642	Blue
Blade 2	304.7	23.2	52	0.0641	Silver
Blade 3	304.2	23.7	51	0.0641	Yellow
Blade 4	304.5	23.4	50	0.0643	Orange

Once the blades are mounted on the hub, the rotor tracking was carried out. Reflective tapes on the blade tips are illuminated by a light strobe synced to rotor frequency and phase. The blade root pitch was adjusted to ensure all the blade tips are in a plane within half blade thickness. Tracking procedure described in Section 2.6 was used.

8.3 Active Rotor in Forward Flight with Stiff Pitch Link

Preliminary wind tunnel testing was performed with the rotor stiff in torsion. The aim was to establish active flap performance in forward wind speed.

Figure 8.8 shows the trailing edge flap amplitudes obtained at various operating conditions. For each test condition, the flap was synced with rotor and excited at 1/rev flap frequency. Two important observations were made from these results. First, for a given rotor speed, the trailing edge flap performance was not strongly affected by forward wind speed. Second, for a given forward wind speed, increasing centrifugal load results in decreased flap amplitude for same input power. This was as expected from the hover experiments.

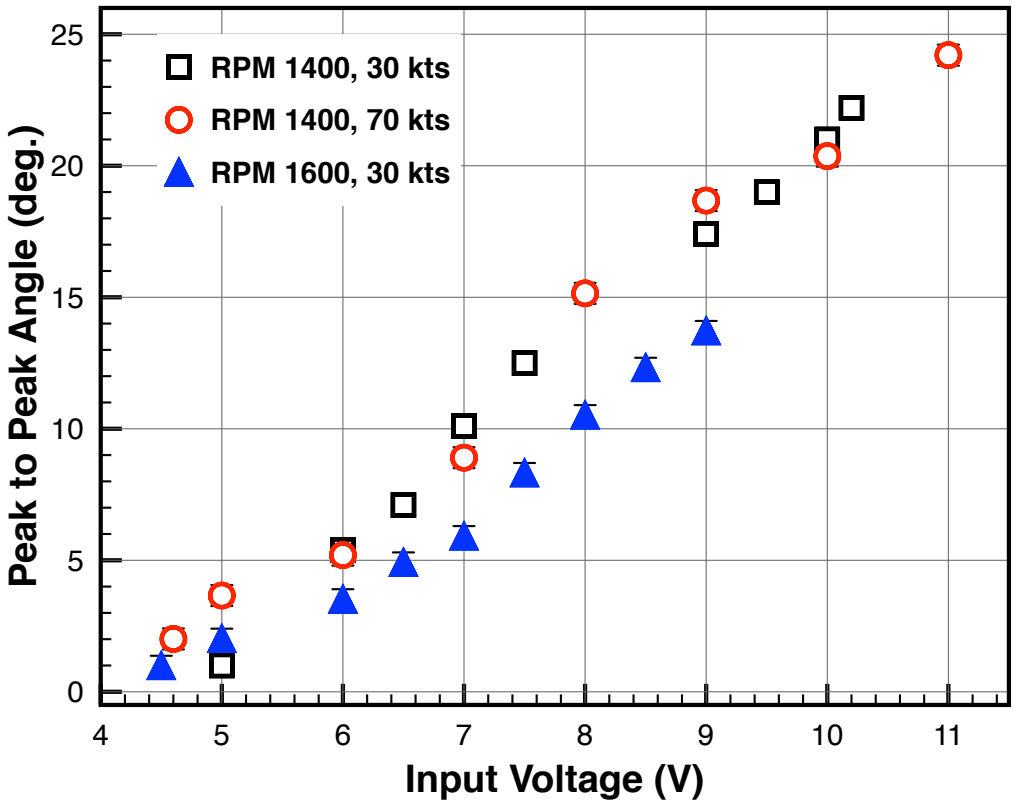

Figure 8.8: Trailing edge flap amplitude at 40 Hz for various rotor speeds and wind speed.

8.4 Rotor Trim Algorithm

The objective of wind tunnel trim was to counter the cyclic blade root flapping. This ensures that the rotor thrust was always aligned with the rotor shaft and only coning was observed in the blade flap motion.

8.4.1 Conventional Swashplate Rotor Trim

For conventional swashplate rotors, the trim was achieved by adjusting the cyclic blade pitch inputs to the rotor via the swashplate. Hall position sensors were installed at the blade flap hinge.

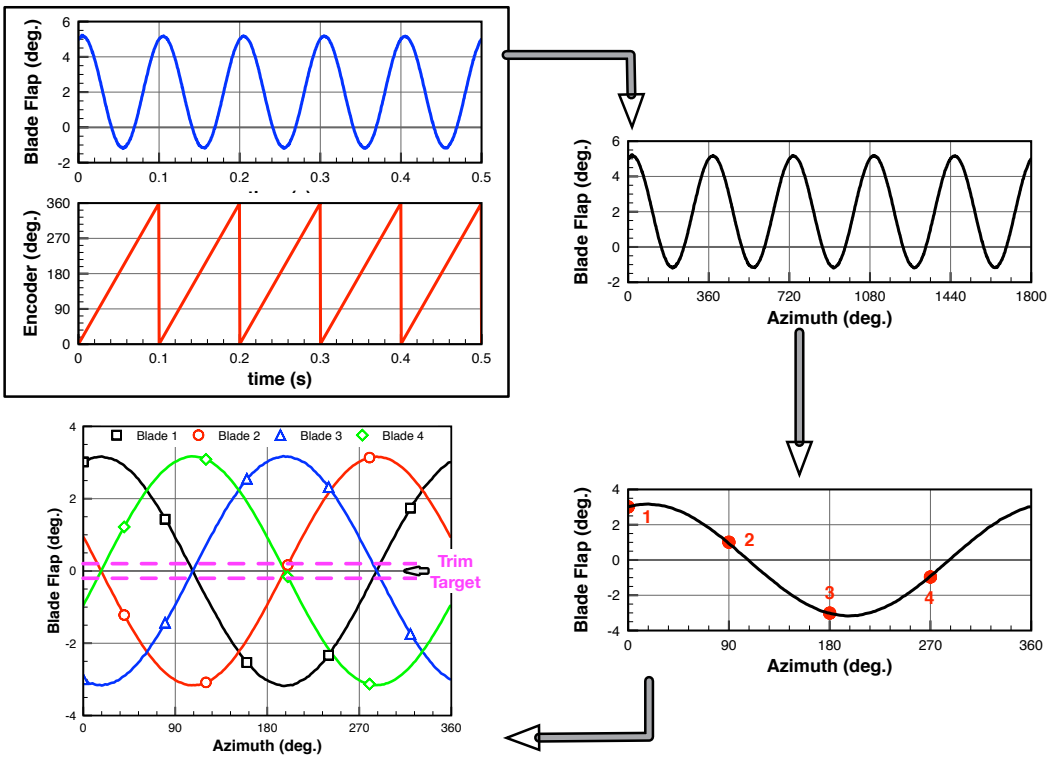

Figure 8.9: Trim procedure using swashplate controls.

The blade flapping and rotor azimuth data was used to resolve the flap motion

in terms of rotor azimuth. In each data acquisition cycle, a number of rotor revolutions were captured. These multiple revolution data was then averaged to generate a phase resolved blade flap motion. The blade coning angle was removed from the data and longitudinal and lateral cyclic angles were calculated. This process was carried out for all the blades and an averaged lateral and longitudinal flapping angles were calculated for the rotor. Cyclic pitch inputs were then chosen to cancel cyclic flap angles. For an articulated rotor with low hinge offsets, the rotor flap response lags pitch input by about quarter rotor revolution. This phase was introduced at the swashplate by installing the lateral and longitudinal pitch servos 90° offset of the flap locations. This iterative process was carried out until lateral and longitudinal flapping was negotiated to be about zero. Detailed explanation was presented in Section 2.7 and a concise chart is reproduced in Fig. 8.9.

8.4.2 Swashplateless Rotor Trim

For a swashplateless rotor, the controls were the cyclic deflection of the trailing edge flaps. The motion of the trailing edge flaps, produced a blade pitching moment that changed the pitch of the blade. This change in the blade pitch in turn caused change in the blade flap motion. The pre-pitch applied to the blades is carefully set to ensure that each blade reached the same steady pitch angle at the operation rotor speed. The flap mean position was only changed in a limited amount to reject any disturbances, but primarily cyclic pitch control was implemented with motor actuation.

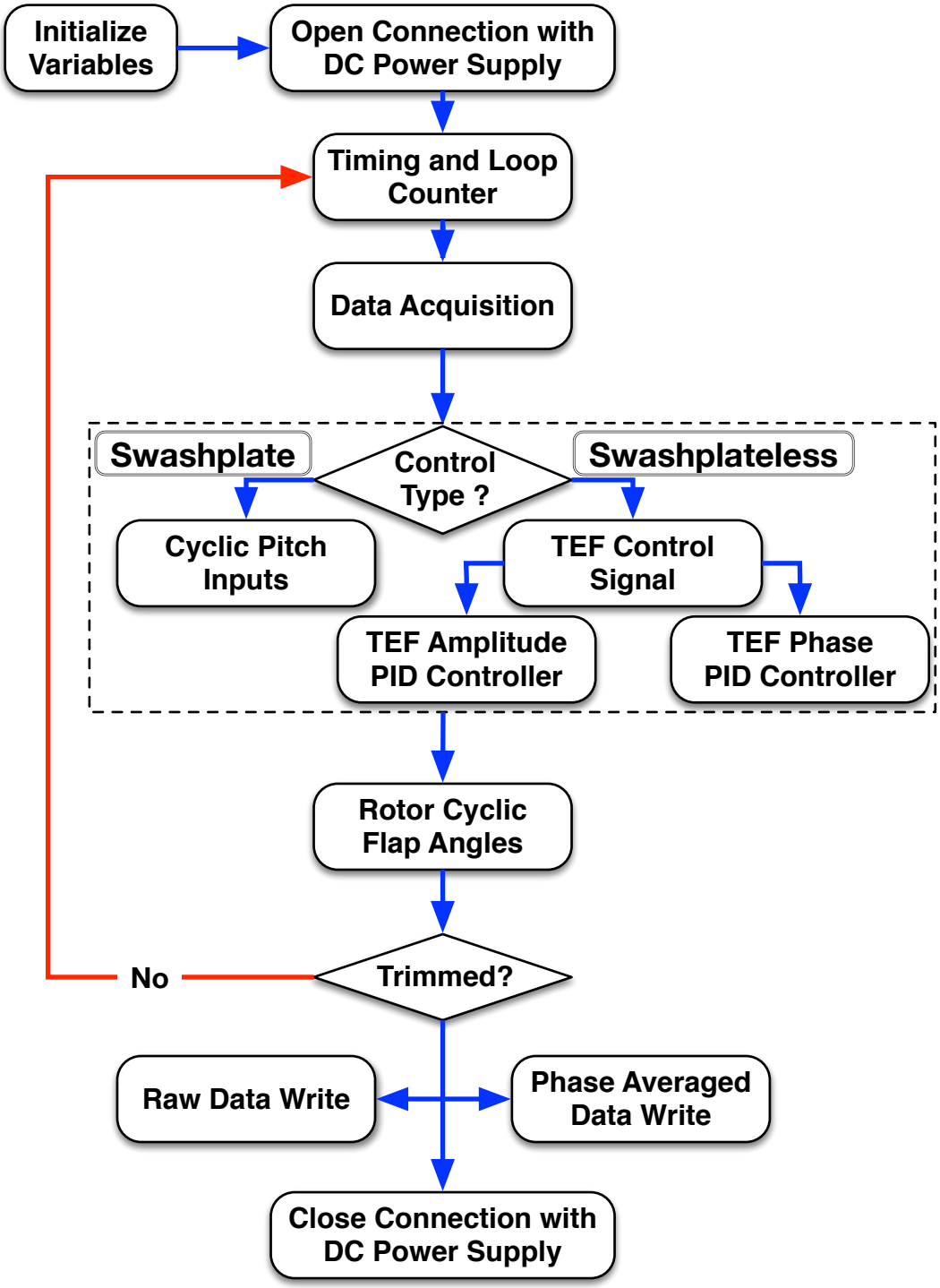

Figure 8.10: Trim procedure using trailing edge flaps.

A closed loop controller was employed to ensure that the trailing edge flaps operated at correct phase difference and in sync with the rotor azimuth. In addition, a closed loop controller maintained the desired trailing edge flap amplitude.

Figure 8.10 shows the flow chart of the control algorithm as implemented in LabVIEW data acquisition and control software. Once the connection with the hardware and power supplies is verified, the data acquisition loop is initiated with collecting data at desired rate. Care was taken to ensure that data for multiple rotor revolutions were captured so any measurement error could be minimized by averaging. The blade root flap data is then processed to calculate the cyclic flapping. Then the trailing edge flap controls are provided to counter these flapping. Closed loop controllers ensure flaps operate at desired amplitude, frequency and phase locking. Once the trim inputs were applied, the data from the six degree of freedom hub balance is processed through a coupled matrix to compute hub loads. Each data acquisition cycle is then phase averaged and written into a separate file that holds the average computed data for each cycle.

8.4.3 Bench-Top Proof of Concept for Swashplateless Trim

Before testing the closed loop trailing edge flap amplitude and phase controllers (TEF controllers) on the hover stand, a bench-top verification was carried out. The four blades were secured on the bench top and were first systematically tested to ensure that they all operate at the desired trailing edge flap amplitude and with the correct phase offset. Also, the flaps were loaded with torsional loads as a simulated

aerodynamic loading. Figure 8.11 shows the TEF controllers maintaining the desired trailing edge flap operation for each individual blade. The target wave (black-solid) was matched as close as possible by the controller on trailing edge flap one (red-dotted-sqaure). The remaining trailing edge flaps were also operated with proper phase offset.

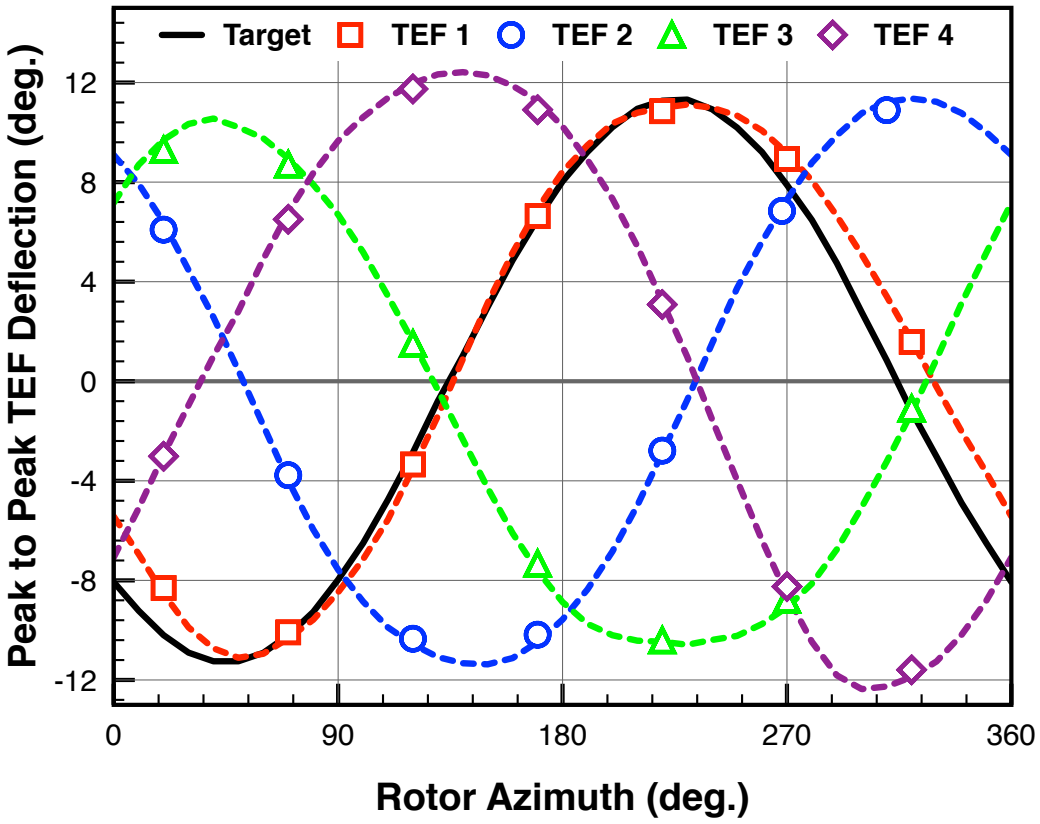

Figure 8.11: Bench top verification of TEF controller.

Figure 8.12 shows the trailing edge flap waveforms phase for two, three and four blade shifted by 90, 180 and 270 degree respectively. This compares the waveform shapes of all the trailing edge flaps deflections. Also, a transfer function based on hover tower experiments with soft pitch link was implemented and blade flap response was simulated for actual trailing edge flap inputs. The trim methodology

discussed in Fig. 8.10 was employed. This allowed to check, on the bench-top, if these flaps would be able to trim the rotor. Once bench-top verification was established, the active rotor was tested in the wind tunnel and swashplateless trim using trailing edge flap inputs was attempted.

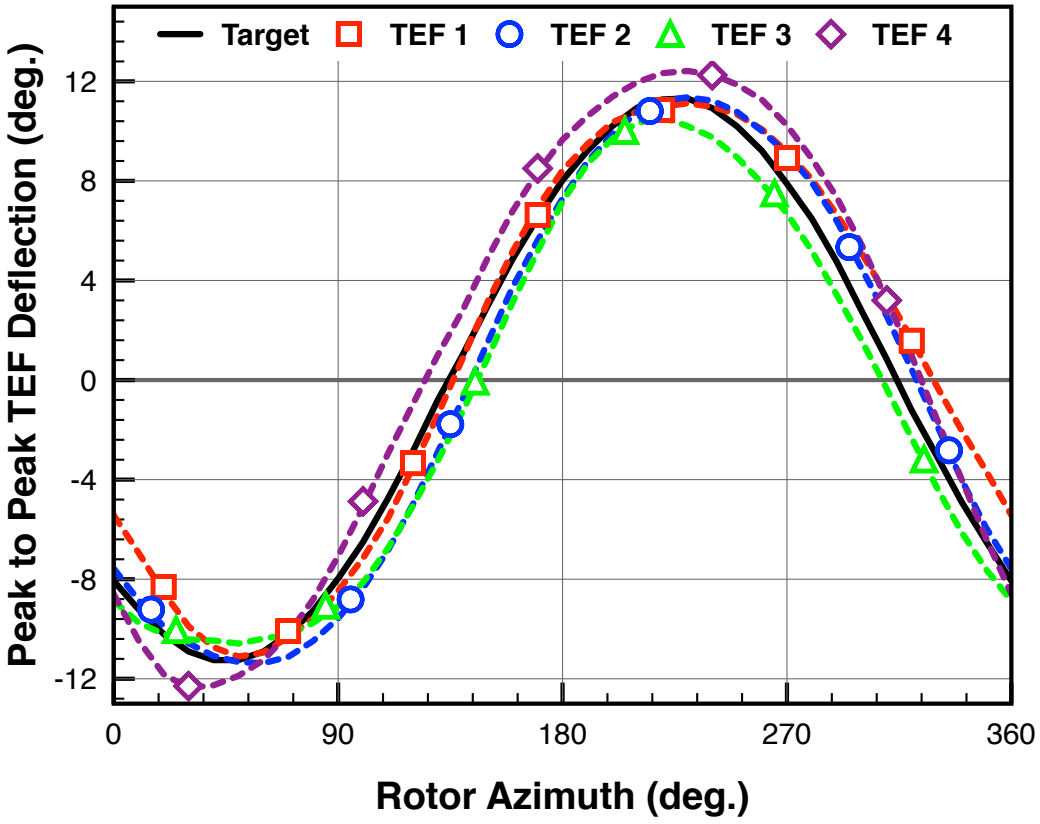

Figure 8.12: Phase shifted TEF waveforms.

8.5 Active Rotor Trim in Forward Flight

Wind tunnel trim implies minimizing the cyclic blade root flapping using cyclic pitch controls. This ensures that the rotor thrust was always aligned with the rotor shaft and only coning (steady blade flap) was observed in the blade flap motion. For swashplateless rotor, the controls were the cyclic deflections of the trailing edge flaps.

The motion of the trailing edge flaps, produced a pitching moment that changed the pitch of the blade. This change in the pitch caused change in the blade flap motion.

The blades were pre-indexed to achieve 2 degree blade pitch at operating RPM. The rotor was first spun to 900 RPM and then the wind was turned on, with gradual increase in the wind speed to 30 mph. Once rotor trim was achieved at 30 mph, the wind speed was increased in steps of 5 mph, progressively trimming the rotor at each wind speed. Once rotor trim was achieved at 50 mph, the wind speed was gradually reduced to zero and finally the rotor RPM was reduced to zero as well. Under no circumstances, should the rotor speed be reduced until the wind has been completely turned off. This ensured rotor and wind tunnel safety while swashplateless rotor trims were attempted.

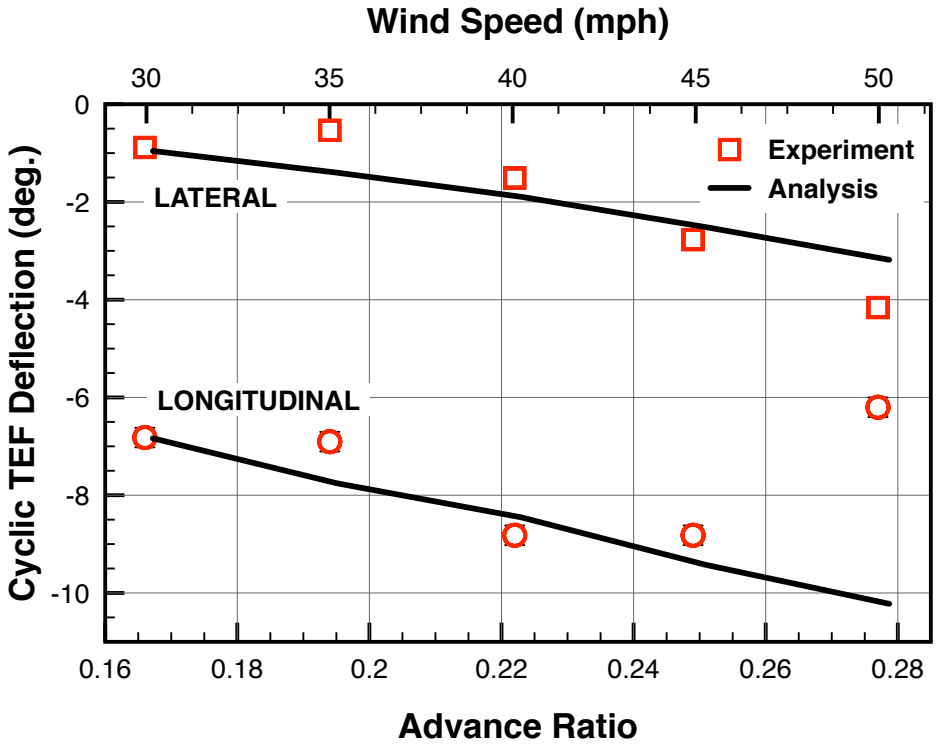

Figure 8.13: TEF deflection for rotor trim at 900 RPM and 2/rev torsion stiffness.

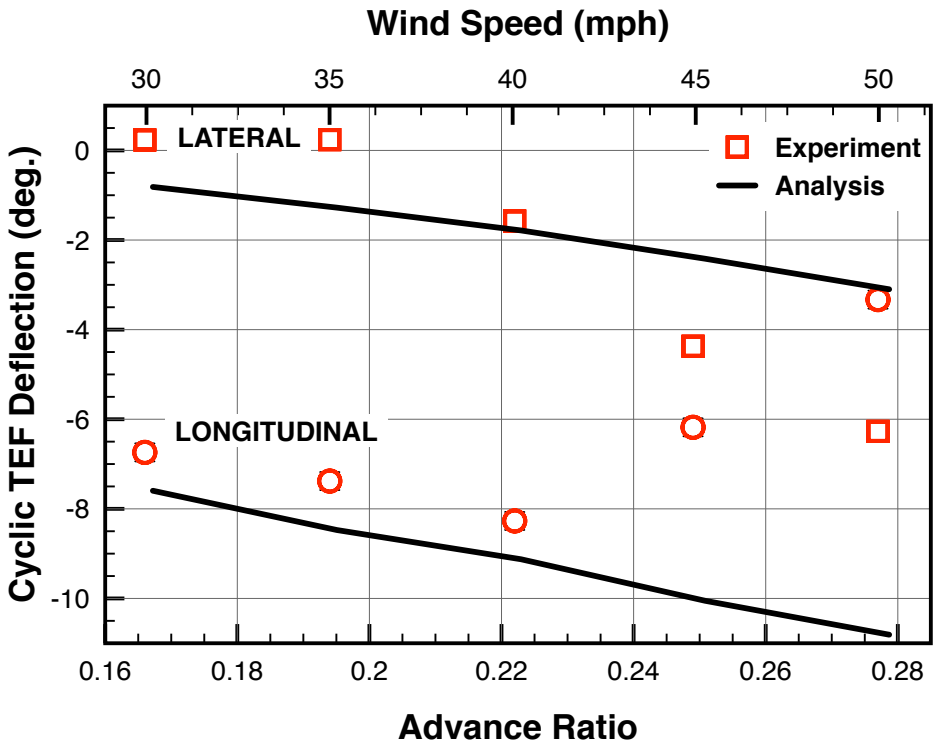

Figure 8.14: TEF deflection for rotor trim at 900 RPM and 1.75/rev torsion stiffness.

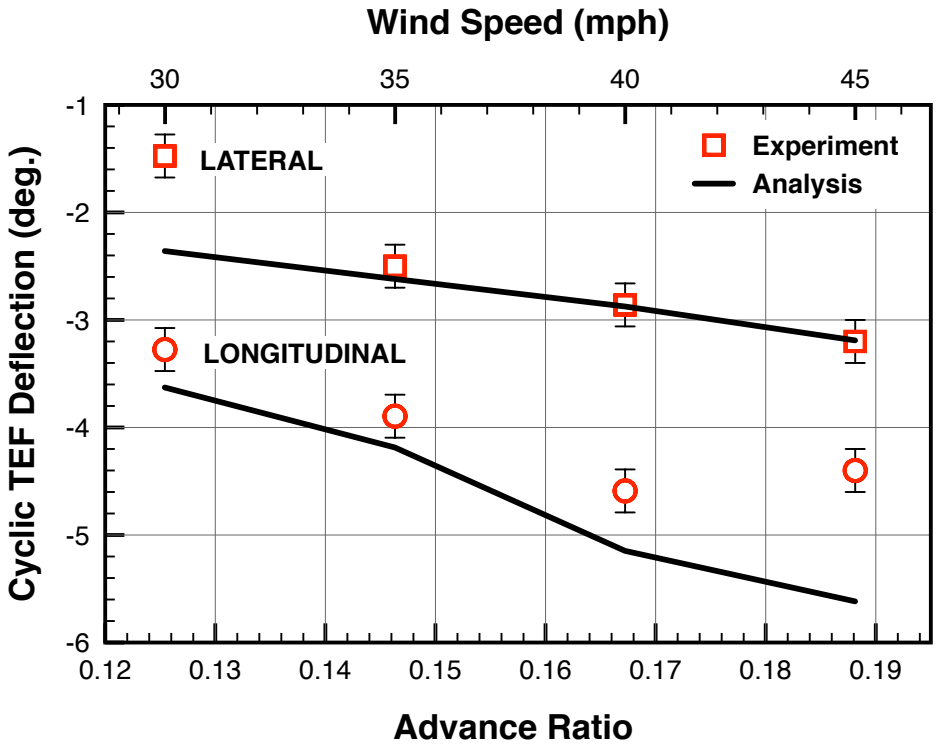

Figure 8.15: TEF deflection for rotor trim at 1200 RPM and 2/rev torsion stiffness.

Figure 8.13 and 8.14 shows the trailing edge flap input required to trim the rotor operating at 900 RPM at various wind speeds (advance ratio is wind speed non - dimensional by rotor tip speed) and with torsional stiffness of 2/rev and 1.75/rev respectively. The symbols are test data and the solid lines are trends predicted by a preliminary analysis. Figure 8.15 shows the cyclic trailing edge flap deflection required to trim the rotor operating at 1200 RPM with 2/rev torsional stiffness. These results show that a swashplateless rotor can be trimmed in wind tunnel using trailing edge flaps, provided the rotor was made torsionally soft compared to conventional rotor.

Figure 8.16 compares the blade root pitch angle required for rotor trim. The swashplate trim case represents the rotor trim achieved using pilot pitch inputs from the control console. The TEF trim case is the swashplateless trim condition. It contains the blade pitch angles, recorded at the soft pitch link, produced as a response to the trailing edge flap deflections. Irrespective of the method by which the rotor trim was achieved, as long as the operating conditions were same, the blade pitch response was similar to one another. Also, these angles were predicted well by simple analysis as well.

Finally, Fig. 8.17 presents the blade pitch response for trimmed flight at various advance ratios. It includes swashplateless trim flight condition data points for rotor operating at 900 and 1200 RPMs. The blade pitch response trends look consistent with advance ratio, larger cyclic pitch was required for higher advance ratios.

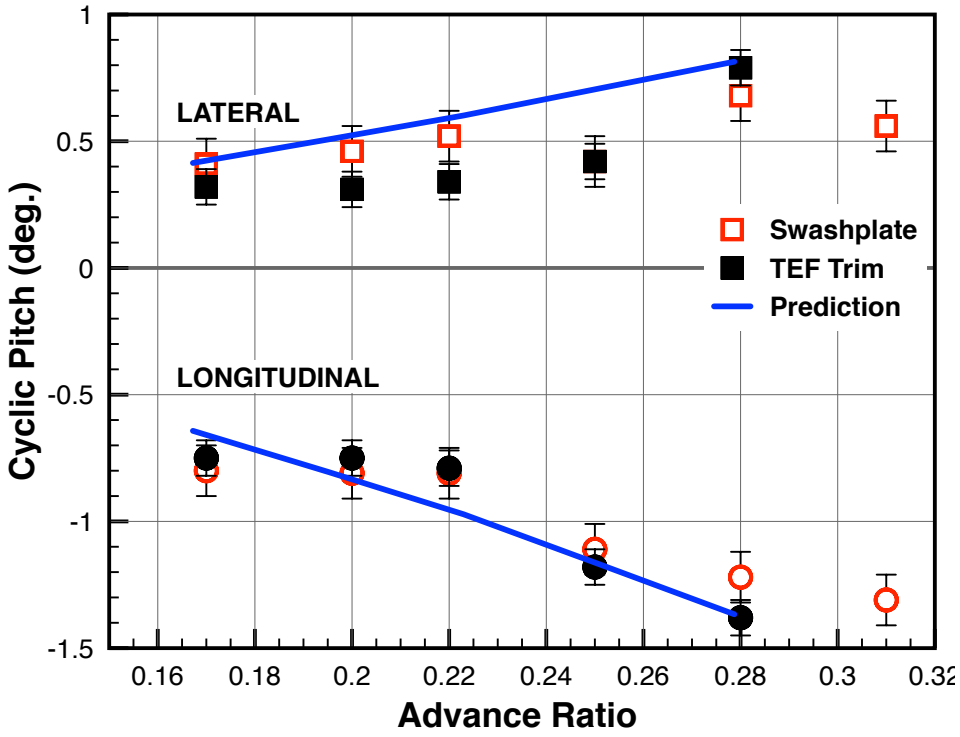

Figure 8.16: Blade root pitch for rotor trim at 900 RPM.

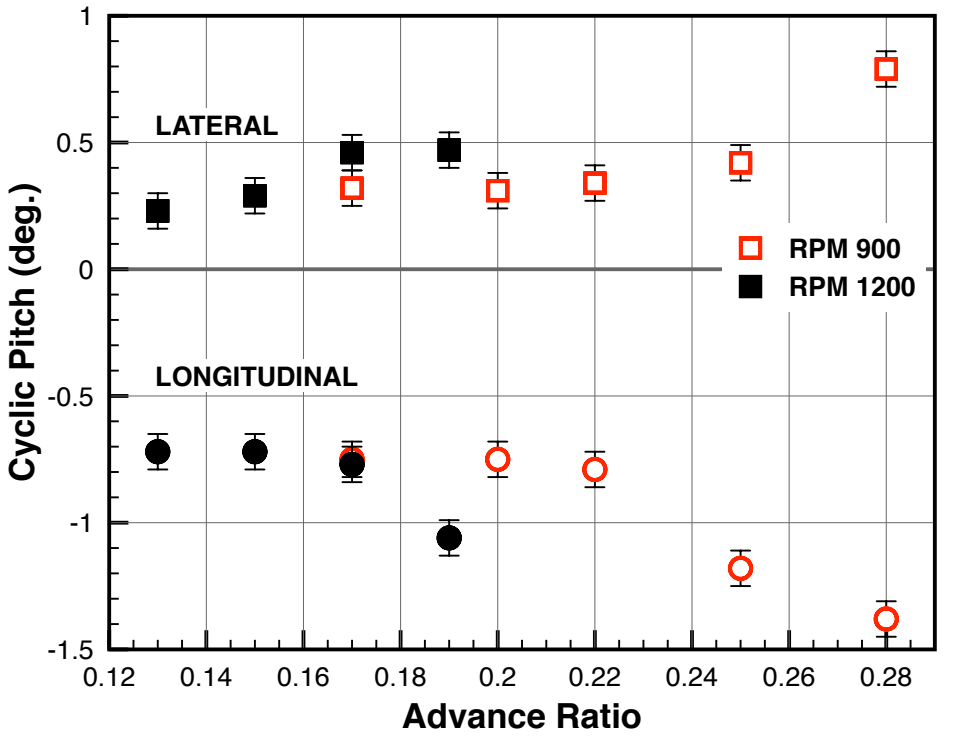

Figure 8.17: Blade root pitch for trimmed rotor at 900 and 1200 RPM.

8.6 Hub Loads Comparison - Swashplate v/s Swashplateless Trim

A comparison the hub loads between swashplate and swashplateless trim rotor is presented here. First with trailing edge flaps inactive and providing pitch inputs through swashplate actuators, baseline loads were recorded. These were then compared with the rotor loads observed in swashplateless trim rotor.

Irrespective of the choice of trim method, the rotor was operating at the same mean thrust level 8.18. Compared to the baseline swashplate trim, the 1/rev normal force loading was lower for the swashplateless trim. These 1/rev loads arise due to blade to blade differences in the rotor system and as such are hard to address using swashplate inputs. Since swashplateless trim using trailing edge flaps allows individual blade control to minimize each blade flapping, these differences can be accounted for and corrective control inputs to minimize them could be achieved. Thus, swashplateless rotor controls were able to better address the loads arising from rotor dissimilarity.

The trailing edge flap input was not a perfect 1/rev sinusoid, but only 1/rev amplitude was targeted. Some amount of higher harmonics were present in the input. So hub load response at higher harmonics was observed as well.

In general, higher in-plane loads (Figs. 8.19, 8.20 and 8.21) were observed for swashplateless trim rotor compared to baseline with conventional swashplate trim. This could be due to the drag of trailing edge flap element operating in a high dynamic pressure region of the blade. Although efforts were made to minimize gaps, however since only a single trailing edge flap was used, larger amplitudes were

required to trim especially at higher advance ratios. This could have contributed to increased sectional drag of different blades and thus an overall higher in-plane force.

Due to the pitching moment (Figs. 8.22, 8.23 and 8.24) induced by the trailing edge flap deflections, a higher 1/rev hub moment was observed. Some response at higher harmonics were also observed.

Finally, torque harmonics are presented in Fig. 8.25. Unfortunately, the baseline values were not correctly recorded during the experiment and hence only swashplateless trim values were included.

These hub load comparisons are to be looked into further details to completely understand the effect of swashplateless trim on these loads.

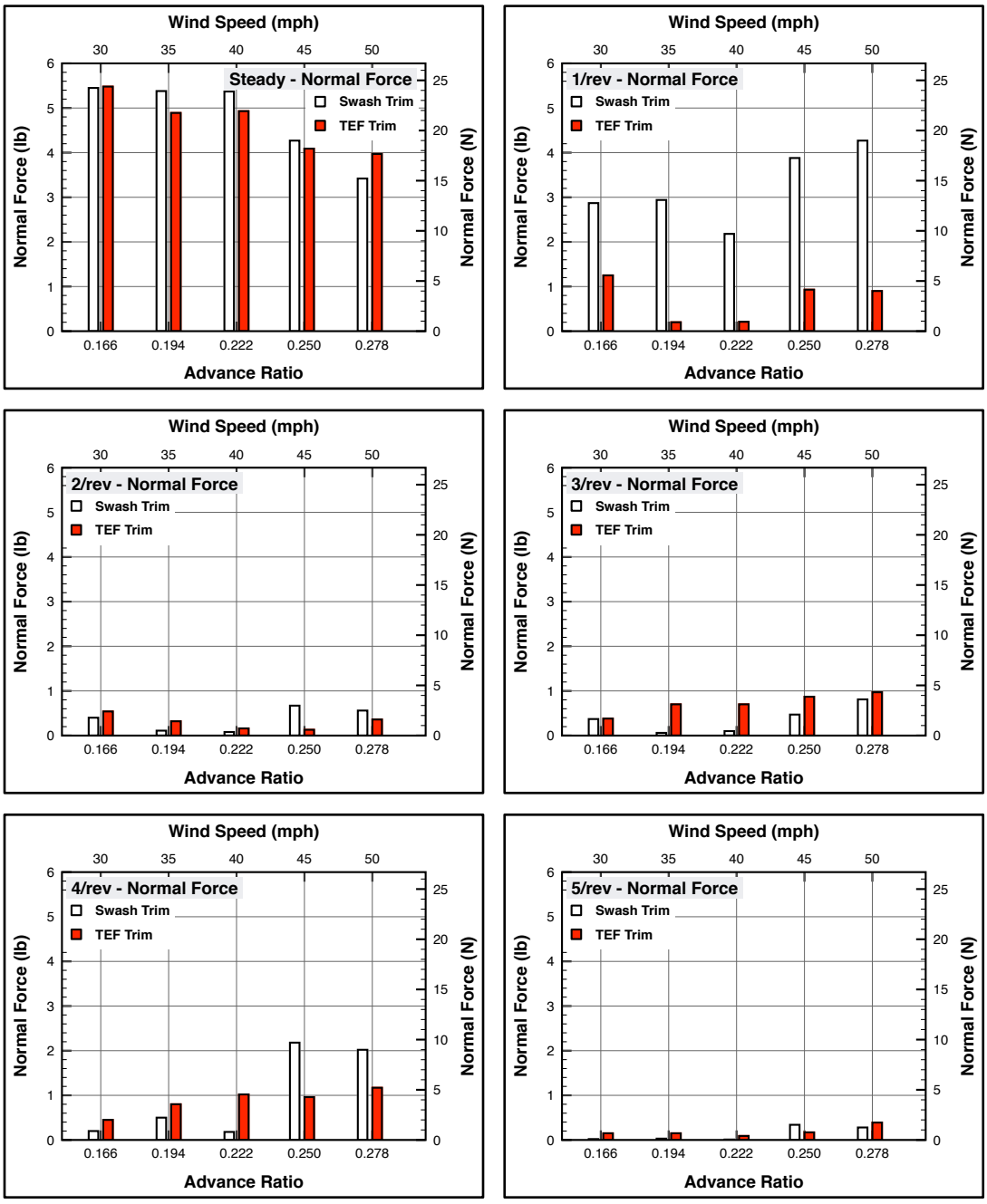

Figure 8.18: Harmonic components of normal hub force at various advance ratios.

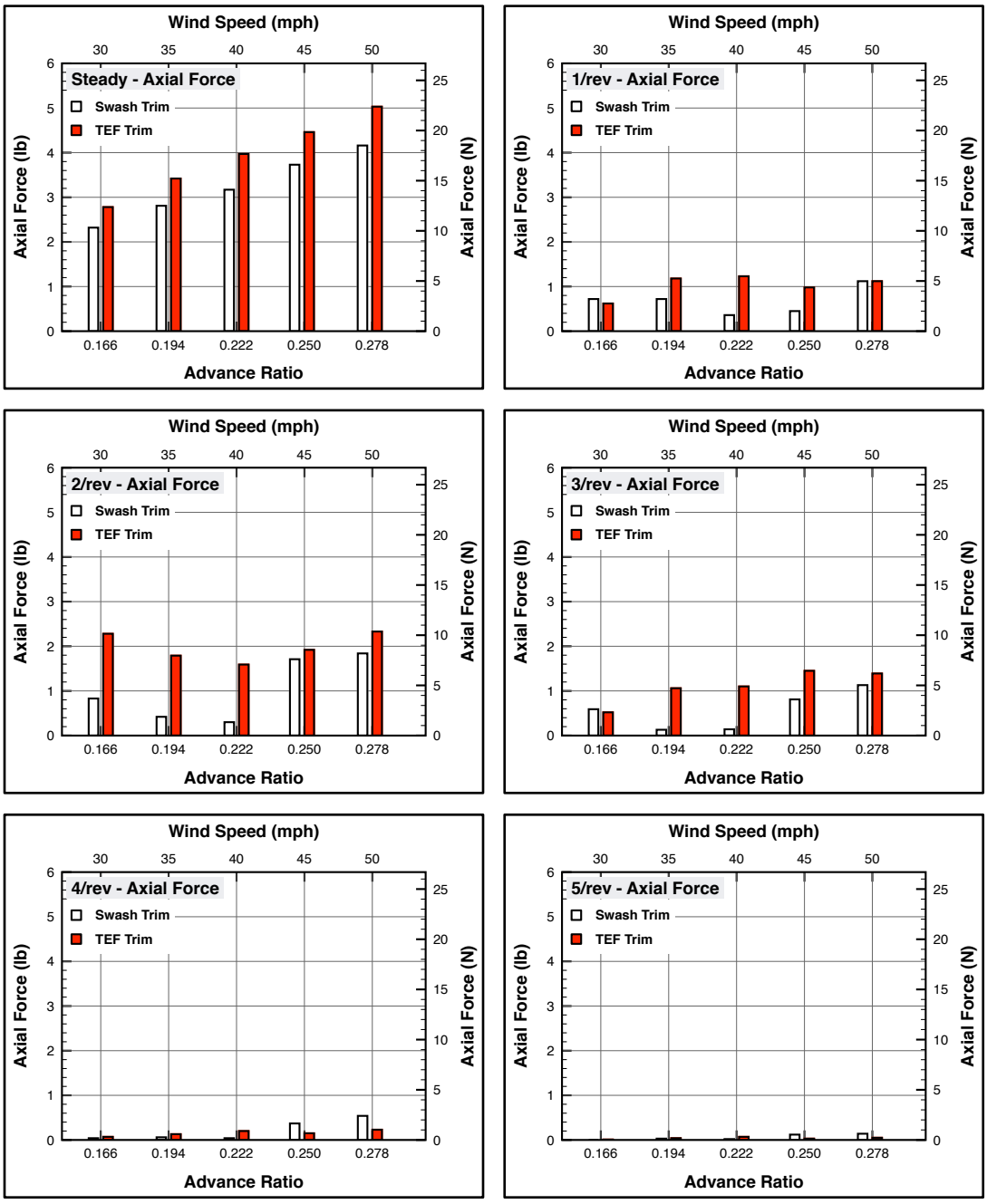

Figure 8.19: Harmonic components of axial hub force at various advance ratios.

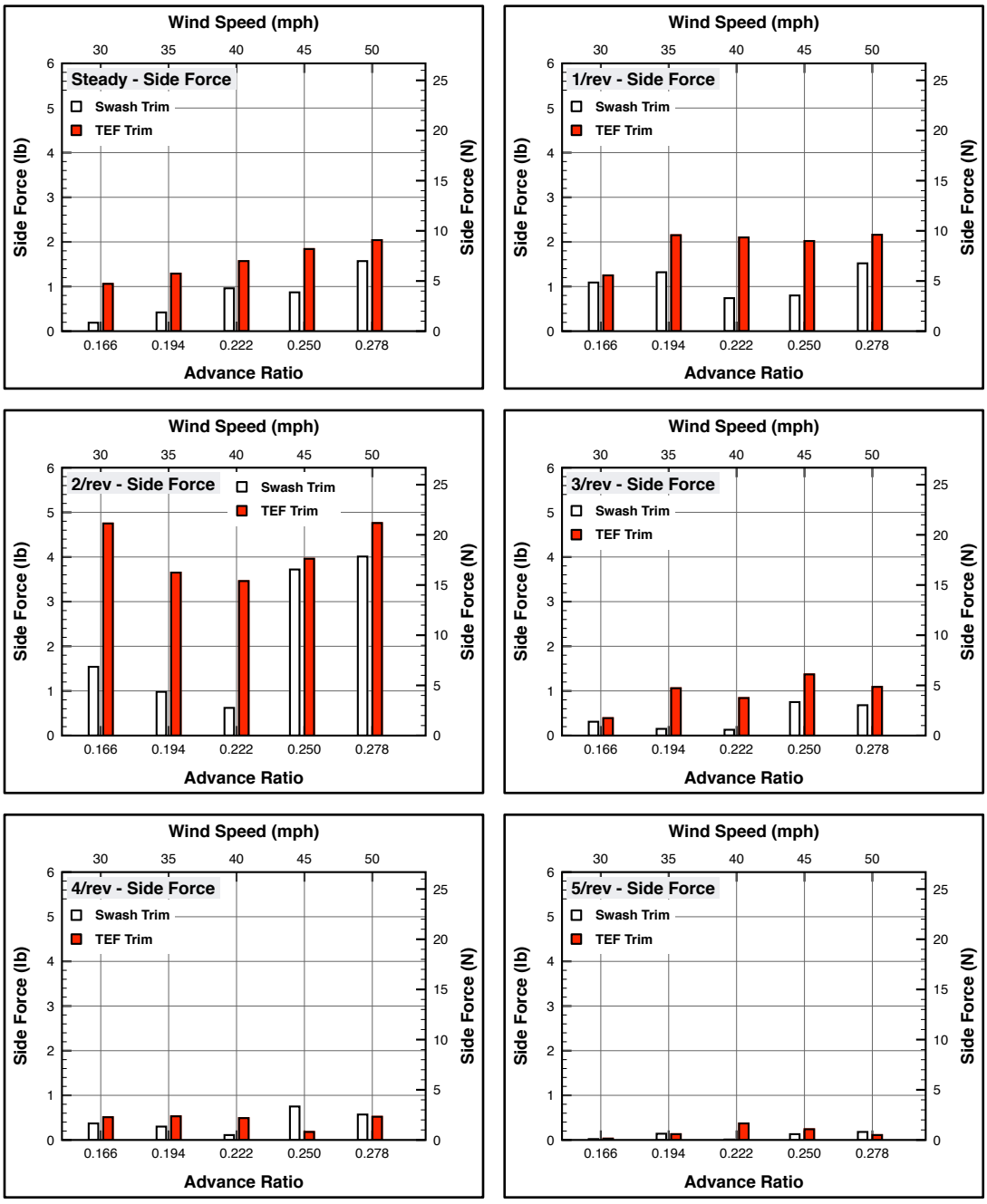

Figure 8.20: Harmonic components of side hub force at various advance ratios.

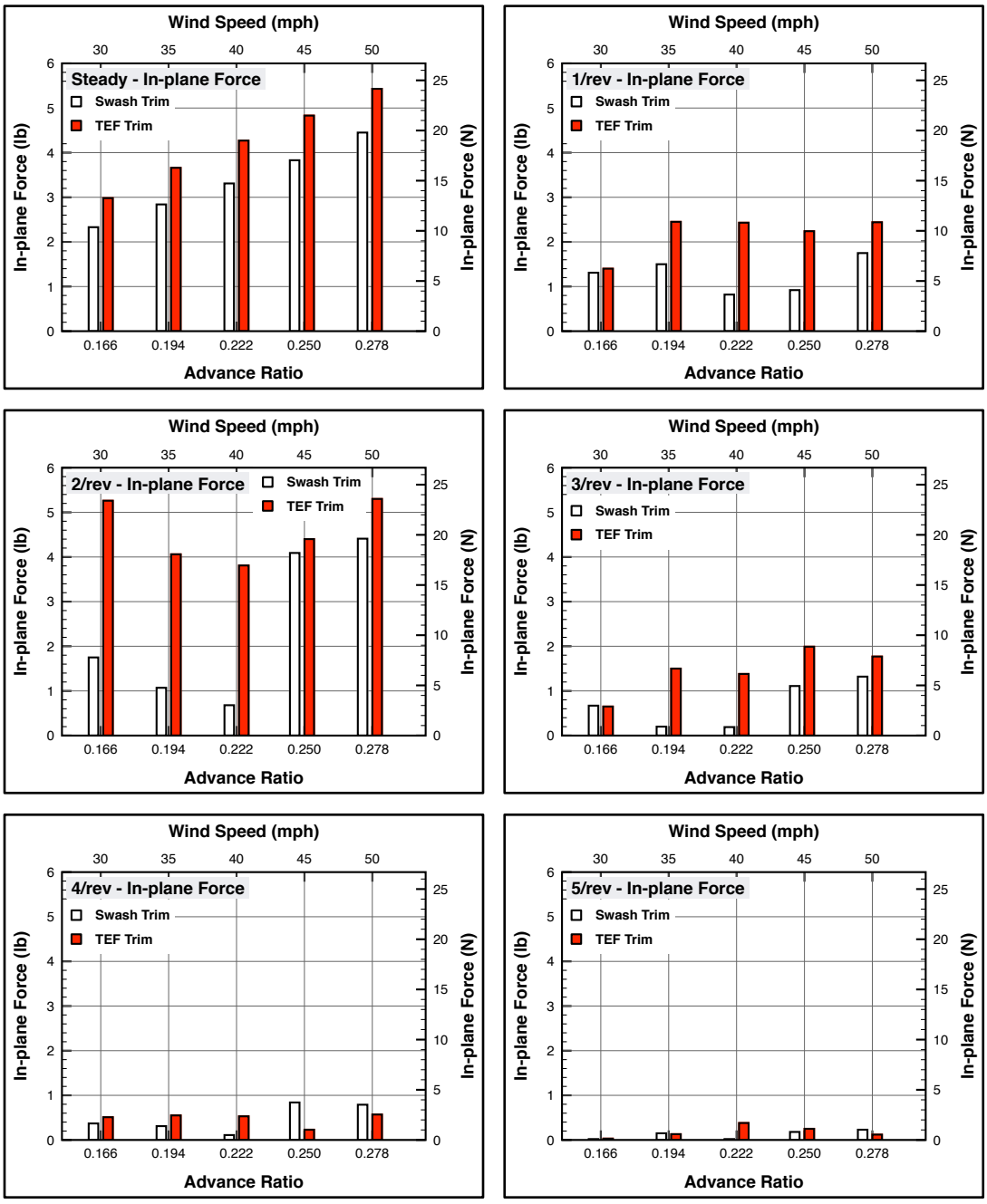

Figure 8.21: Harmonic components of in-plane hub force at various advance ratios.

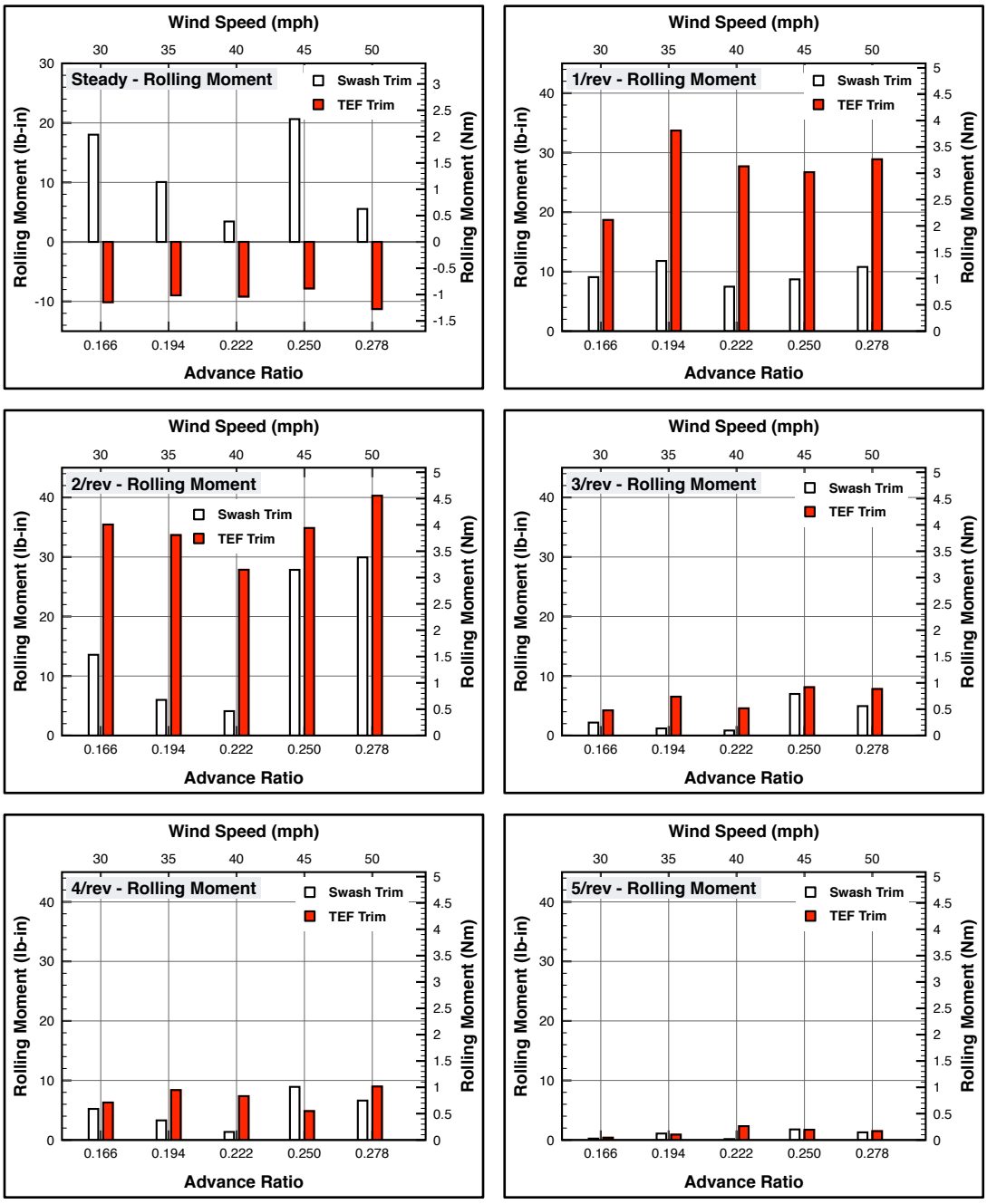

Figure 8.22: Harmonic components of rolling hub moment at various advance ratios.

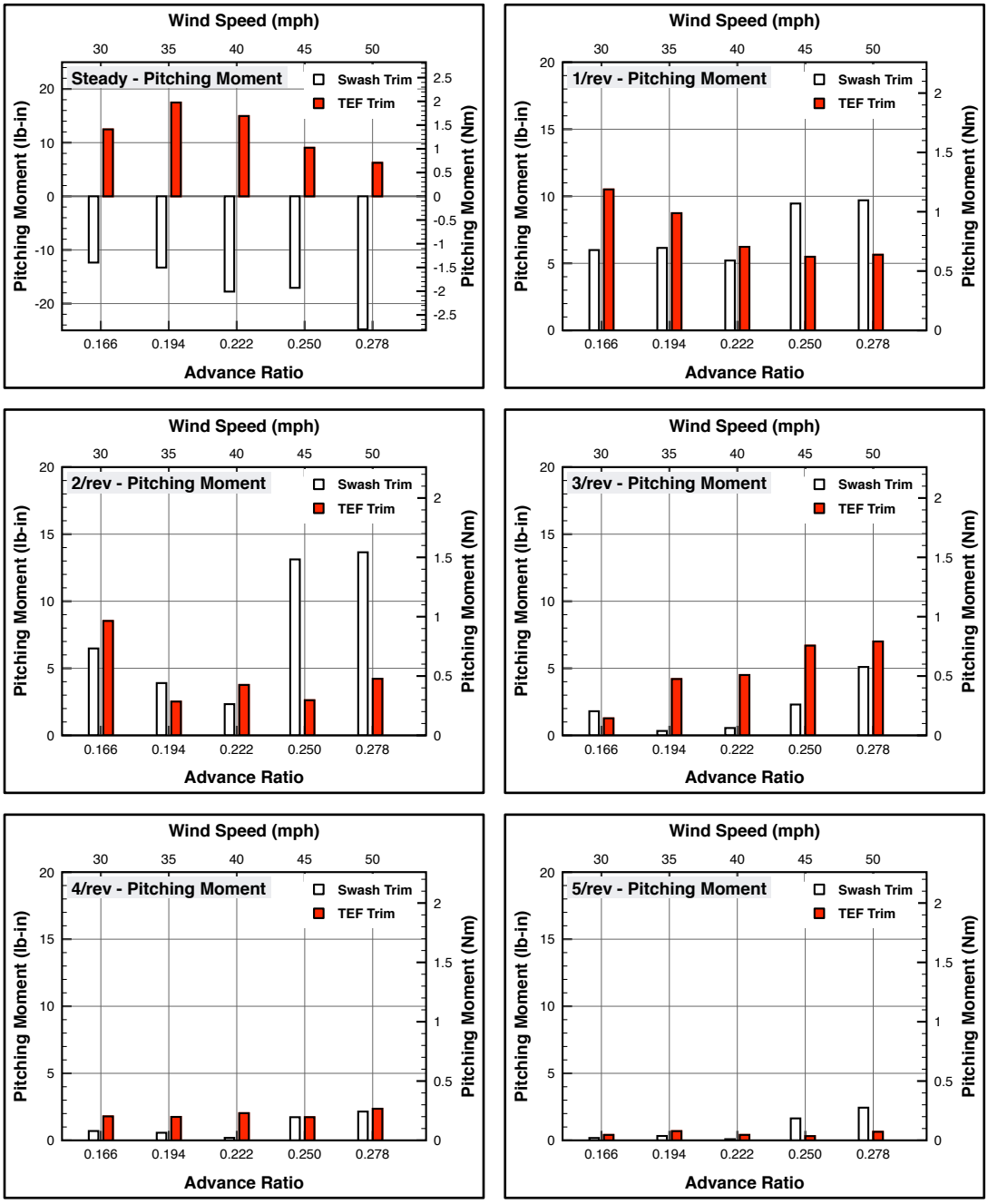

Figure 8.23: Harmonic components of pitching hub moment at various advance ratios.

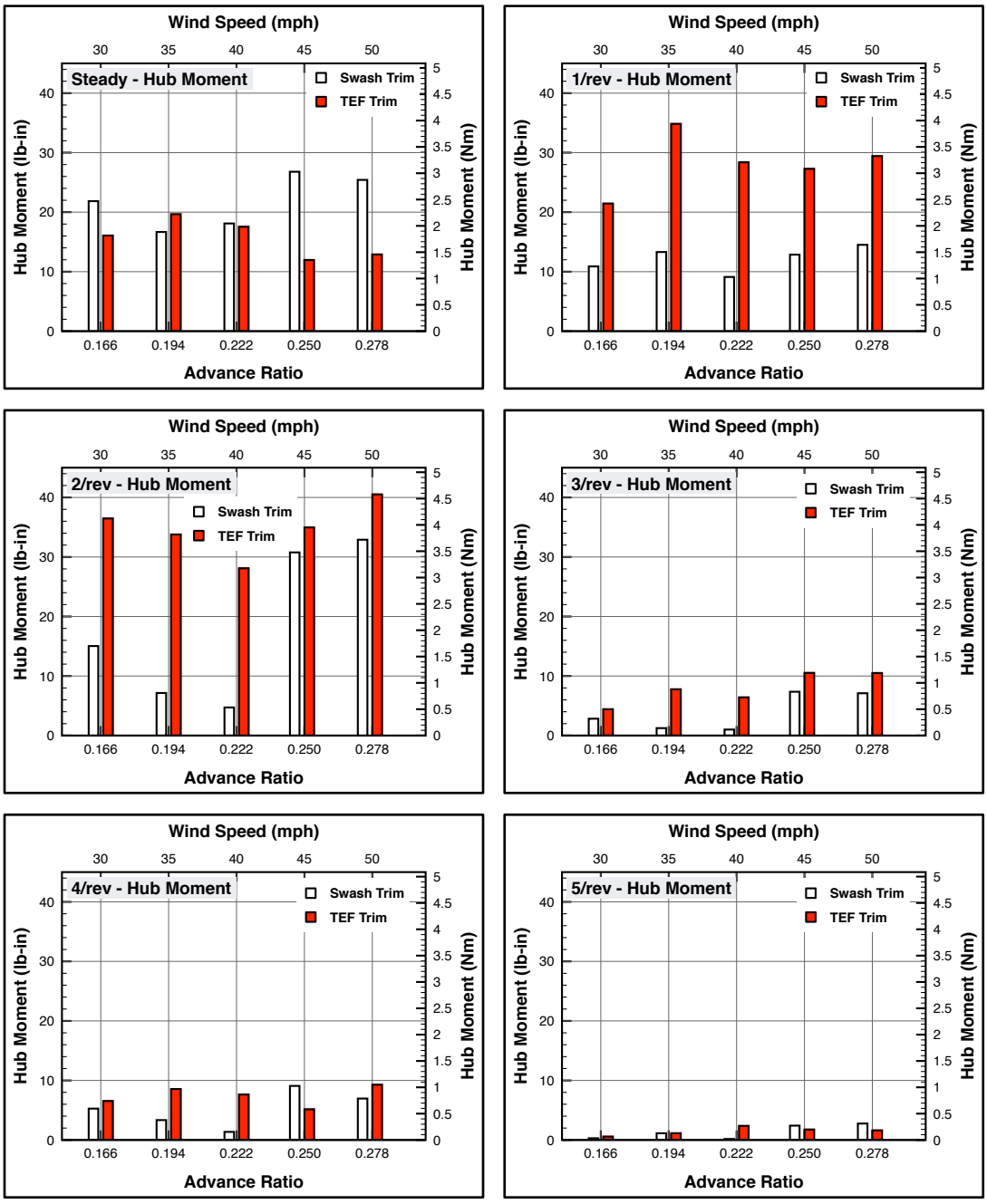

Figure 8.24: Harmonic components of net hub moment at various advance ratios.

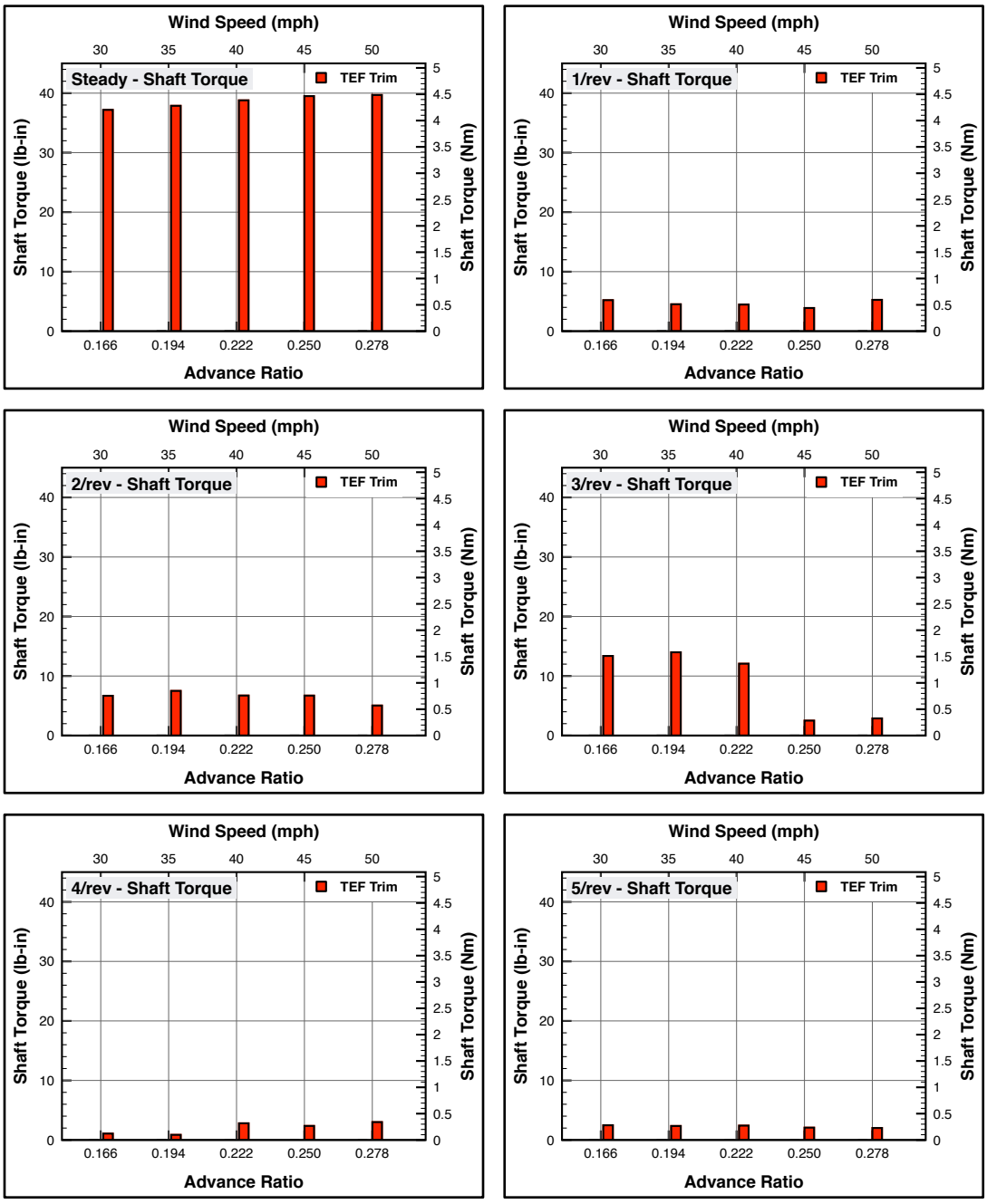

Figure 8.25: Harmonic components of shaft torque at various advance ratios.

8.7 Error Estimates in the Experimental Data

Errors in the experimental data could be thought of as either systematic errors or random errors. Systematic errors could arise due to bias in the measurement technique, experiment procedure or errors in calibrations. Unfortunately, systematic errors cannot be removed by averaging the data, since the bias in measured quantities always skews the data in same direction every time the process is repeated. Only careful experimentation and experience can help in avoiding these errors and as such these errors are hard to quantify.

Random errors arise due to fluctuations in the measurements. These could be introduced due to limited precision of sensors, changes in ambient conditions not accounted for in the measurements and noise in the data acquisition process. These errors can be minimized by repeating the measurement multiple number of times and taking an average value as representative measurement. Frequent baseline data points (referred to as zero readings) were taken and data was appropriately adjusted to negate any errors due to drift in the sensors. Random errors can be statistically estimated by calculating standard deviation of multiple samples. Standard deviation represents the amount of variation of data from the mean value.

Figures 8.26 and 8.27 present the mean data and one standard deviation dispersion of 200 rotor revolutions data samples of trailing edge flap deflections and blade root pitch angles respectively at 1200 RPM and 0.28 advance ratio in the wind tunnel. The maximum error in peak to peak value of trailing edge flap deflection was found to be $\pm$ 0.2 degree and $\pm$ 0.1 degree for blade pitch measurements.

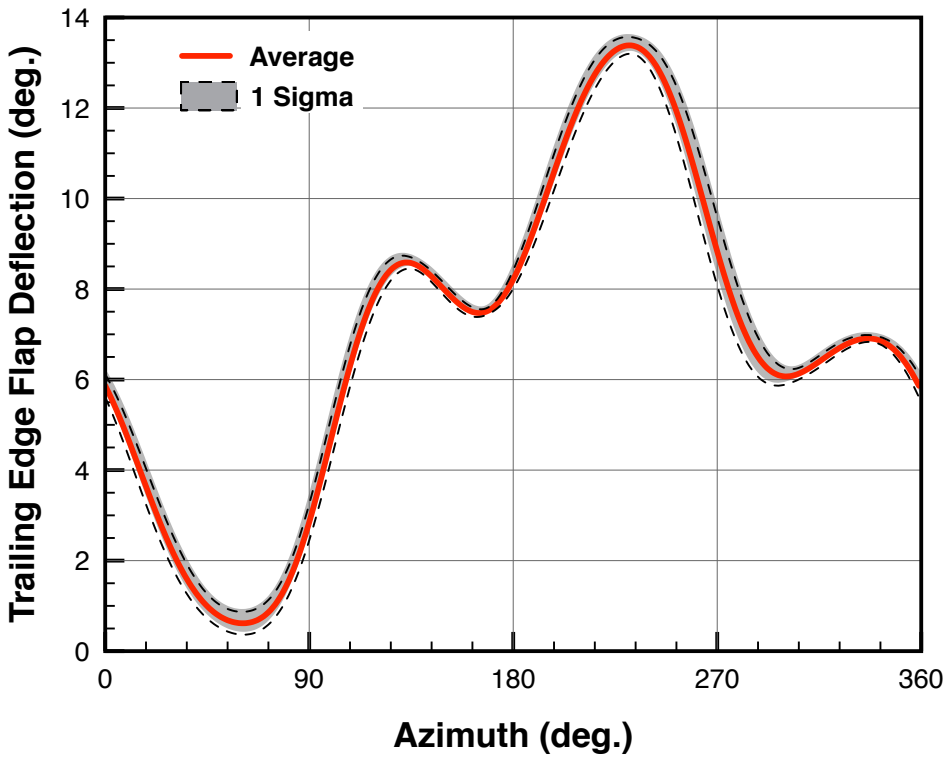

Figure 8.26: Standard deviation in trailing edge flap deflection data.

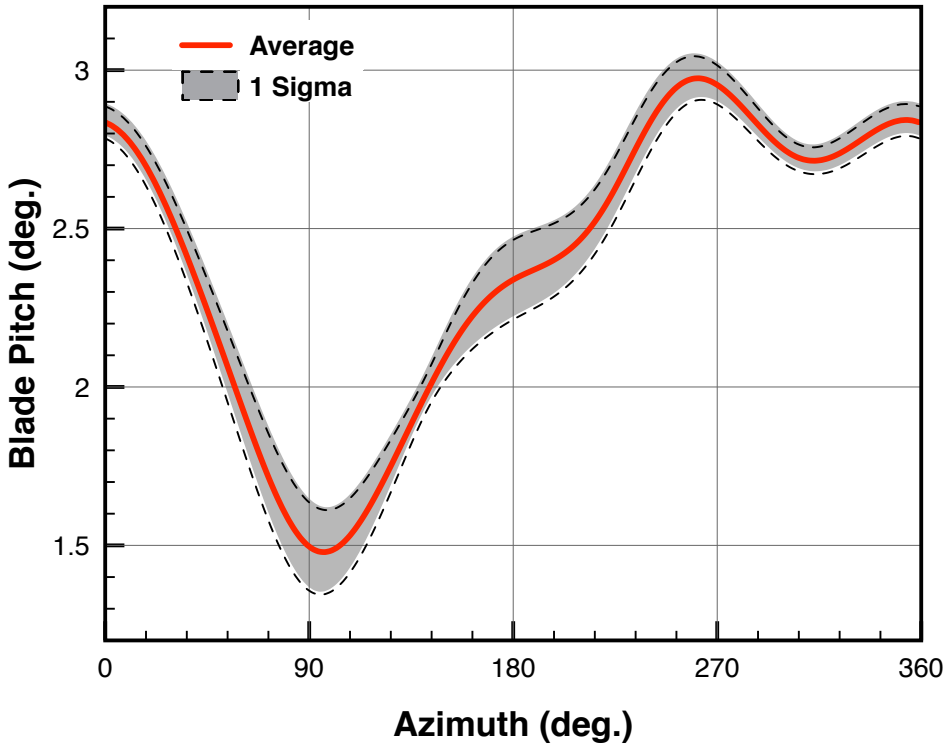

Figure 8.27: Standard deviation in blade pitch data.

8.8 Scalability Assessment for Full Scale Applications

Testing on-blade actuators in the Mach scale rotor presented challenges of limited space and scaled up centrifugal loads. Figure 8.28 presents ratio of g-loads on Mach scale to that on UH-60 rotor calculated at 75% R spanwise location. To match the full-scale centrifugal load, the 6 feet diameter Mach-scale rotor has operate at 800 RPM only.

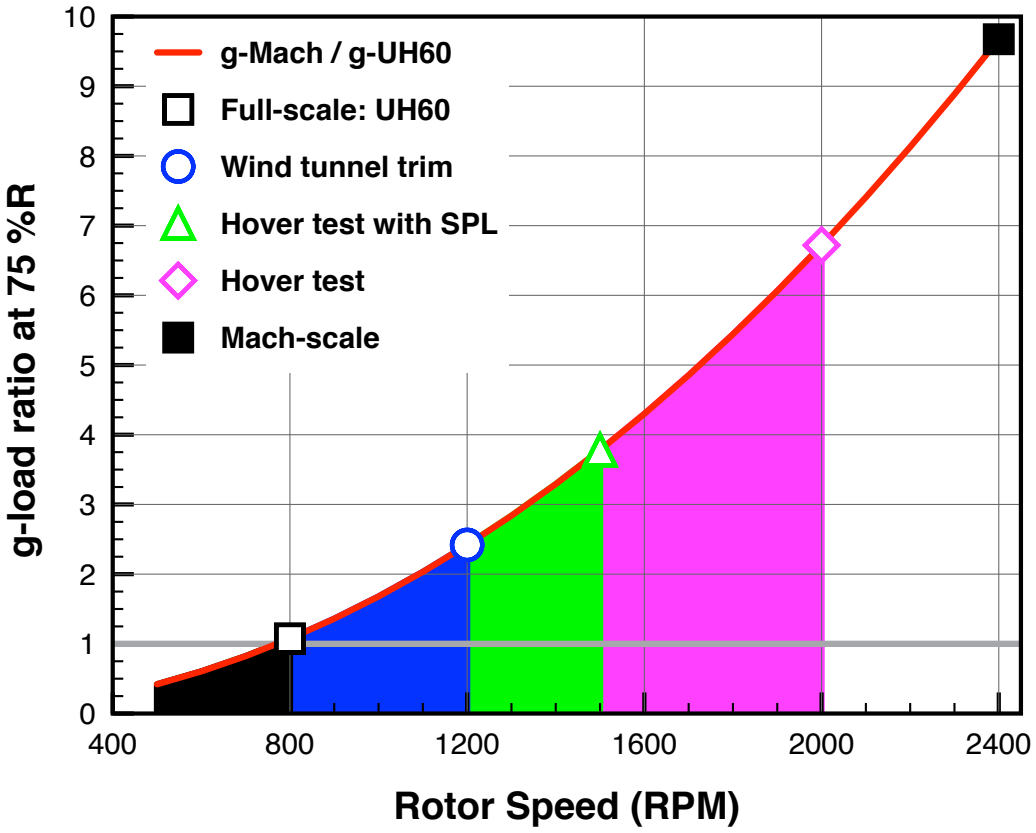

Figure 8.28: Comparison of g-loads.

In the current study, hover testing with stiff pitch links were carried up to 2000 RPM, hover tests with soft pitch links at up to 1500 RPM and wind tunnel trim has been demonstrated at up to 1200 RPM. All the testing on the Mach scale

has been done at g-loads significantly higher than the full-scale g-loads.

For a full-scale rotor, on-blade components experience lower centrifugal load compared to Mach-scale rotor. At the same time, full-scale provides larger internal volume to accommodate bigger actuators and support mechanisms. However, larger actuation authority would be required to drive the active flaps. Figure 8.29 presents the maximum continuous torque output from the brushless DC motor with motor diameter. Each data point is a Maxon precision brushless DC motors, having the same construction and technology as the EC-10 motor evaluated in the current study.

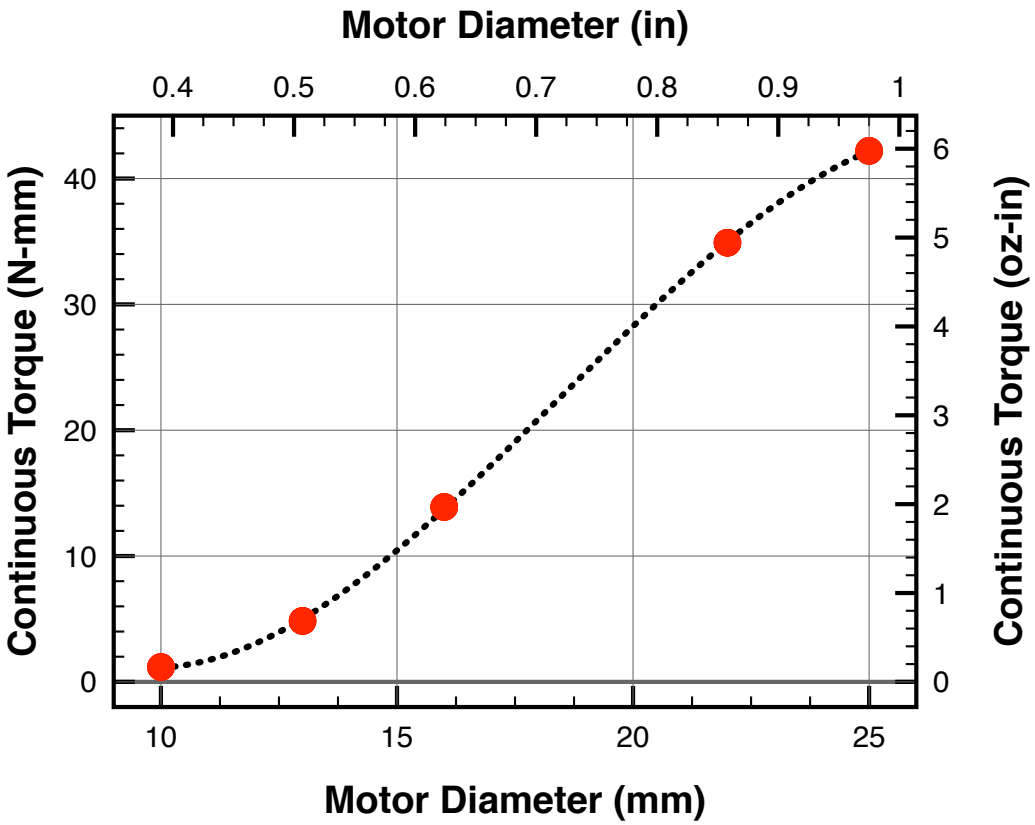

Figure 8.29: Motor torque scaling with diameter.

The data points represent the current off-the-shelf EC brushless motors avail-

able from Maxon. The torque output scales with cube of the motor diameter. The motor weight as well as the motor shaft inertia also scale up. But on full scale rotor, the centrifugal load and the actuation frequency for primary control will reduce and the available space for accommodating actuator would increase.

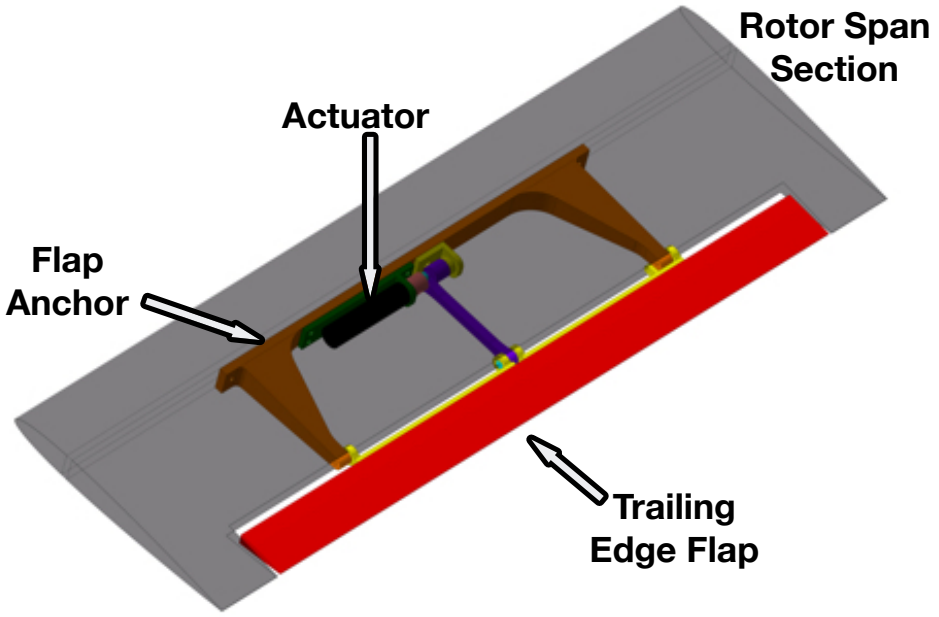

Figure 8.30: Full-scale sectional model for trailing edge flap.

Finally, to explore the scalability of the motor-flap system for full-scale applications, a model with a section of S-434 rotor blade has also been designed. Figure 8.30 shows a section of full-scale blade with a 16 mm diameter Maxon brushless DC motor as actuator. The model is being fabricated and once completed would be tested first in the vacuum chamber under matched centrifugal loads and then in open jet wind tunnel.

Chapter 9: **Summary and Conclusions**

9.1 Summary

The focus of this research was to demonstrate a four blade rotor trim in forward flight using integrated trailing edge flaps instead of using a swashplate controls. A compact brushless DC motor was evaluated as an on-blade actuator, with the possibility of achieving large trailing edge flap amplitudes. A control strategy to actuate the trailing edge flap at desired frequency and amplitude was developed and large trailing edge flap amplitudes from the motor (instead of rotational motion) were obtained. Once the actuator was tested on the bench-top, a lightweight mechanism was designed to incorporate the motor in the blade and actuate the trailing edge flaps. A six feet diameter, four bladed composite rotor with motor-flap system integrated into the NACA 0012 airfoil section was fabricated. Systematic testing was carried out for a range of load conditions, first in the vacuum chamber followed by hover tests. Large trailing edge flap deflections were observed during the hover testing, and a peak to peak trailing edge flap amplitude of 18 degree was achieved at 2000 rotor RPM in hover. A closed loop controller was designed to demonstrate trailing edge flap mean position and the peak to peak amplitude control. Further, a soft pitch link was designed and fabricated, to replace the stiff pitch link and

thereby reduce the torsional stiffness of the blade to 2/rev. This soft pitch link allowed for blade root pitch motion in response to the trailing edge flap inputs. Blade pitch response due to both steady as well as sinusoidal flap deflections were demonstrated. Finally, tests were performed in Glenn L. Martin wind tunnel using a model rotor rig to assess the performance of motor-flap system in forward flight. A swashplateless trim using brushless DC motor actuated trailing edge flaps was achieved for a rotor operating at 1200 RPM and an advance ratio of 0.28. Also, preliminary exploration was carried out to test the scalability of the motor driven trailing edge flap concept. In conclusion, the concept of using brushless DC motors as on-blade actuators, actuating trailing edge flaps has the potential to replace the current mechanically complex swashplate with a hydraulic-free swashplateless system and thereby reduce overall weight and hub drag.

9.2 Conclusions

The objective of the dissertation was to experimentally demonstrate that a swashplateless rotor trim could be achieved. Over the years, several analytical studies have concluded that in-principle a torsionally soft rotor, with blade torsional frequency of 2/rev, could be controlled using trailing edge flap inputs. However, limited stroke from smart material actuators such as piezobenders and piezostacks has been a major limitation in achieving the goal of rotor primary control using Individual Blade Control (IBC). To address this shortfall, compact brushless DC motors were evaluated as on-blade actuators. Systematic evaluation and focussed

design and fabrication efforts were made to integrate Maxon EC-10 brushless DC motor in a Mach scale composite rotor blade and actuate a trailing edge flap. The key conclusions of this research effort are summarized below:

1. Maxon EC-10 brushless DC motor was examined as an on-blade actuator to drive trailing edge flaps. A motor control strategy using Maxon AECS 35/3 controller was successfully implemented, to obtain flap amplitudes instead of rotational motion from the motor, to actuate the trailing edge flap at desired amplitude and frequency. The control scheme allowed precise control of trailing edge flap amplitude and frequency electronically, independent of any motor-flap mechanism.

2. A bench-top test setup was designed, with pre-strained torsion springs to simulate aerodynamic loading, and parameters like flap amplitude, motor current and temperature were monitored. The control strategy developed was implemented and a maximum half peak to peak amplitudes of 15 degree from the motor operating at 40 Hz under simulated torsional loads was obtained. Sufficient actuation moment capability was demonstrated and flap amplitude repeatability was established. Further, no hysteresis in flap amplitude with increasing and decreasing input voltages was observed. Motor temperature was identified as an important parameter affecting actuator performance. The motor was operated at 40 Hz and 15 degree half peak to peak amplitude under torsional load for an extended time. The motor temperature was remained below the allowable limit of 100 degree C.

3. The motor performance was independently tested under centrifugal loads in a ten

feet diameter vacuum chamber. The motor was tested under the same centrifugal loads as it would experience in the the rotor blade. Although, a reduction in motor output was observed with increasing centrifugal load, the motor remained structurally intact and its operation remained consistent.

4. A focussed effort was made to design a compact motor-flap system that could smoothly operate trailing edge flaps under centrifugal loads. Efforts were made to minimized exposed parts and associated drag penalty. The motor-flap mechanism was fabricated and successfully tested in vacuum chamber under various centrifugal loads. The system operated smoothly under the centrifugal loads. However, inadequate motor cooling limited the maximum peak to peak flap amplitude to eight degree at 40 Hz in vacuum chamber at 1200 RPM.

5. A composite rotor was constructed with integrated motor-flap system. In addition to careful composite layup and fabrication process, chordwise and spanwise mass balancing and flap-wise inertia matching were carried out to minimize blade to blade dis-similarities. An experimental setup was designed and manufactured to apply precise bending and torsional loads on the active rotor blades. The blades were then tested and blade deformations were recorded using a Vicon motion capture system. The active blade bending and torsional stiffness were found close to be 32 Nm^2 and 38 Nm^2/rad respectively.

6. For initial experiments in hover, the blade pitch was constrained, as the objective was to establish adequate trailing edge flap operation. The trailing edge flap frequency was fixed at 40 Hz and flap amplitudes at various rotor speeds and

motor input voltages were recorded. The rotor was tested up to 2000 RPM in hover and peak to peak trailing edge flap amplitudes of up to 18 degree were obtained. Motor temperature was well below the critical limit over entire input voltage range. Repeatability in motor-flap system operation was demonstrated with increasing and decreasing input voltages at 1200, 1800 and 2000 rotor RPM.

7. A single-input-single-output PID based controller for the trailing edge flap amplitude and mean position control was implemented. It was successfully demonstrated by holding the trailing edge flap amplitude at desired value with increasing rotor speed from 1200 to 1500 RPM. The controller was also demonstrated to command the motor to achieve desired trailing edge flap amplitudes.

8. A soft pitch link was designed and fabricated to allow lowering the blade torsional stiffness to 2/rev. This allowed the blade root pitch to respond to trailing edge flap inputs. The blade collective and cyclic root pitch control were demonstrated using trailing edge flap inputs instead of conventional swashplate controls. The rotor with soft pitch links tuned to 1.55/rev, was tested to 1500 RPM in hover and peak to peak blade pitch output of up to seven degree at 40 Hz actuation was demonstrated.

9. Wind tunnel demonstrations of swashplateless rotor trim were successfully carried out. A rotor trim algorithm using trailing edge flap inputs instead of swashplate controls was developed. The trim algorithm was implemented and wind tunnel trim of the rotor operating at 1200 RPM and an advance ratio of 0.28 was successfully achieved. The trailing edge flaps were also found effective in addressing

1/rev blade dis-similarities. A lower 1/rev hub normal force was observed for the rotor trimmed using individual blade flaps compared to swashplate trim.

10. Preliminary scaling assessment was carried out and a full-scale sectional model for wind tunnel testing was designed.

9.3 Recommendations for Future Work

The following recommendations are made for extending the current research effort.

(a) Extend the hover testing and wind tunnel demonstration to the design rotor speed of 2400 RPM.

(b) Manufacture an active blade with larger trailing edge flaps to reduce the control input requirements at low advance ratio as well as extend the trim capability to higher rotor loads.

(c) Implement a more effective trailing edge flap mean position control, to add the collective pitch authority to the active rotor system.

(d) Implement a more robust closed loop controller to include a faster loop closure implementation. This would help with better phase locking of control inputs to rotor azimuth.

(e) Use comprehensive analysis to achieve better theoretical predictions of trim inputs required as well as better understanding of the hub loads.

(f) Fabricate and wind tunnel test the full-scale model of motor actuated trailing edge flap system in a non-rotating but high dynamic pressure conditions.

Appendix A: **Technical Drawings**

A.1 RPM Gear tooth

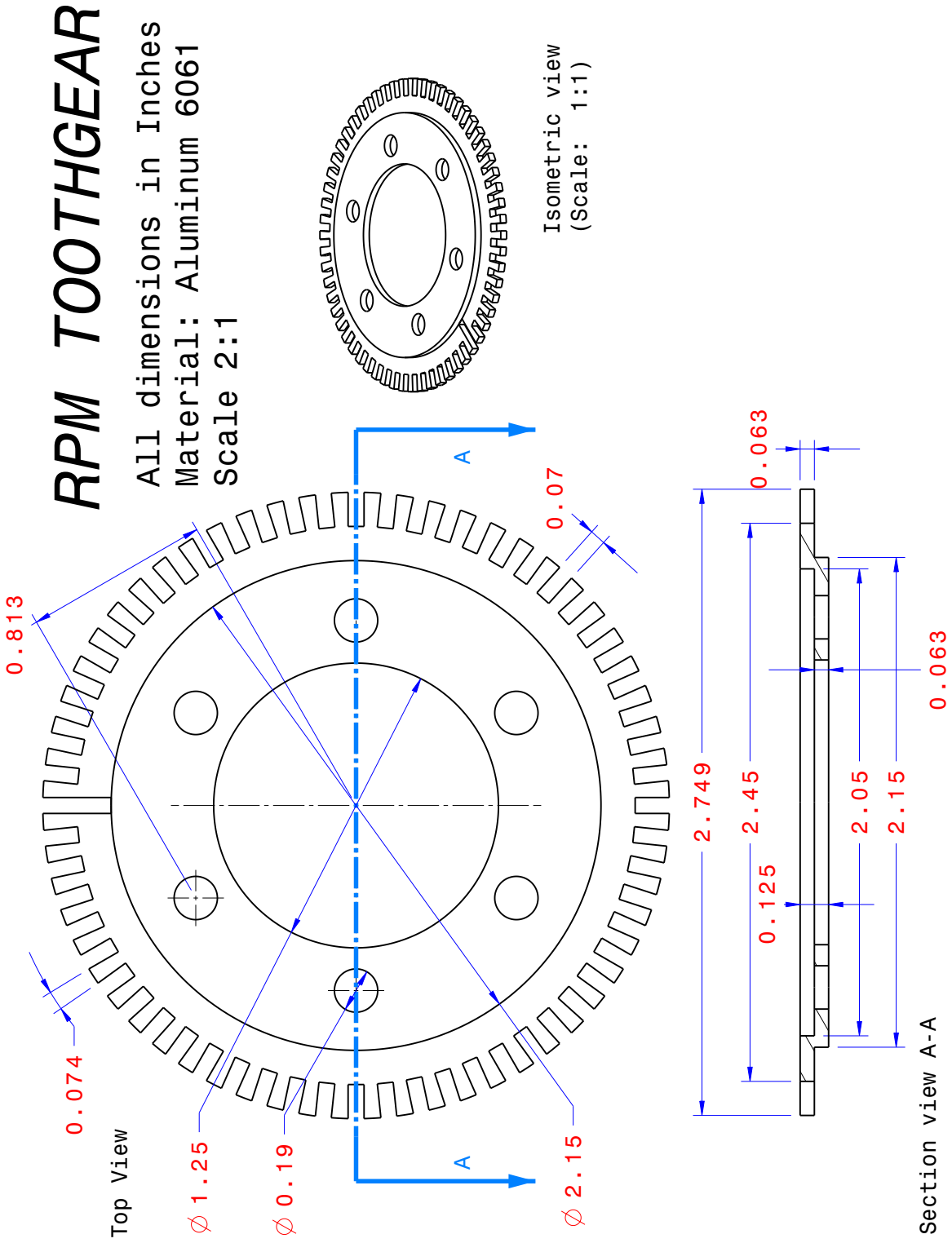

A.2 Torque Membrane

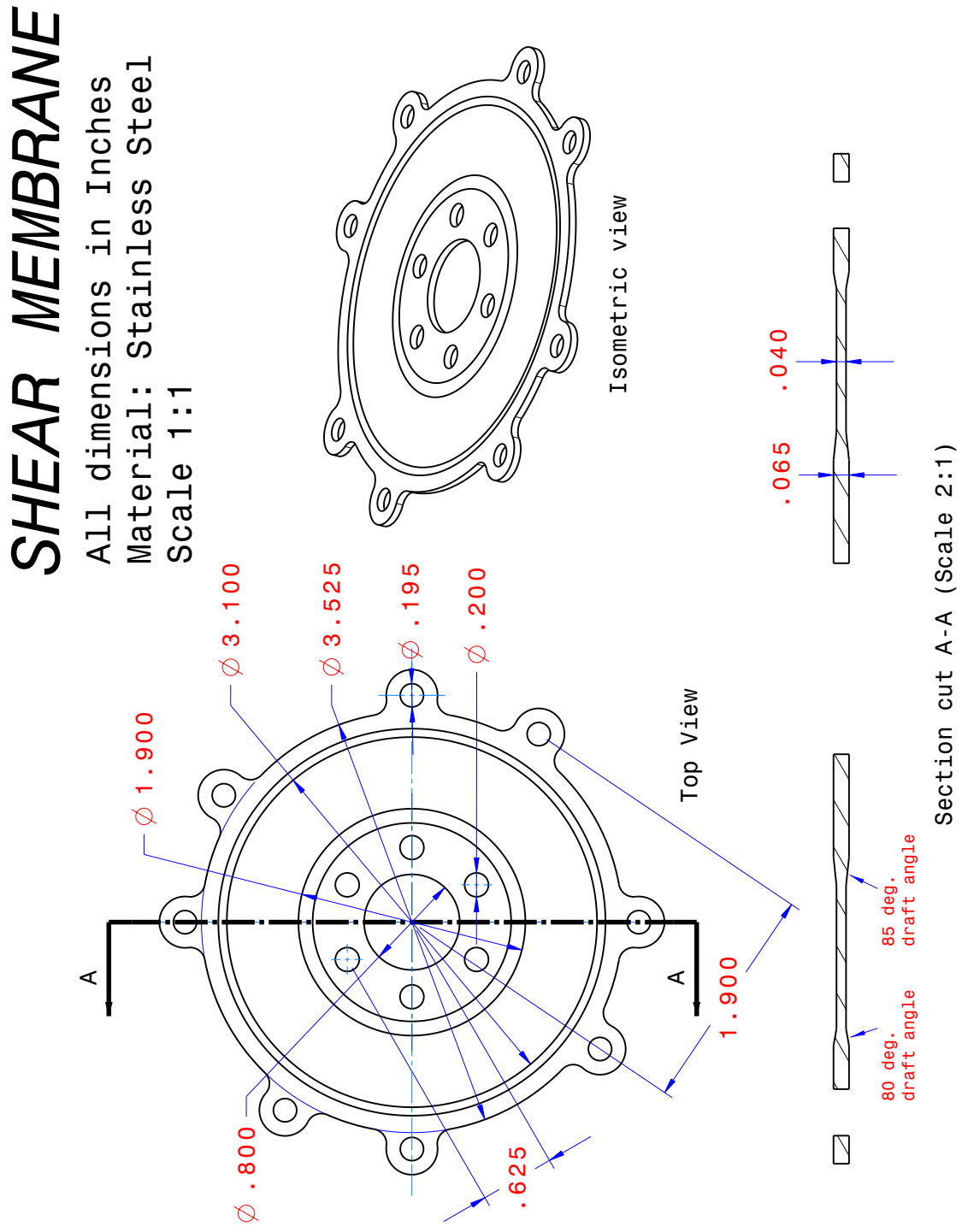

A.3 Fabricast manufactured Signal Slip Ring - 1

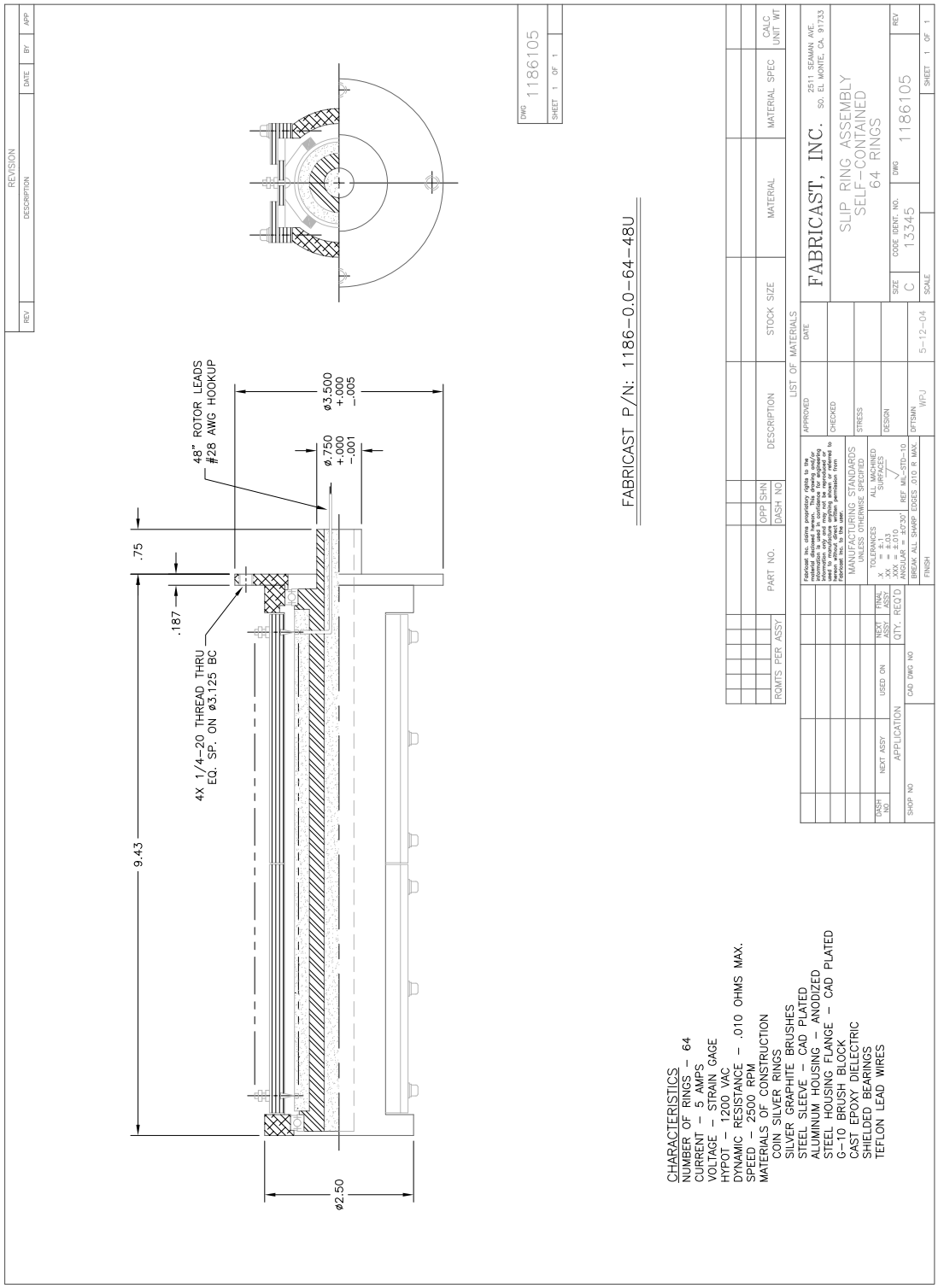

A.4 Fabricast manufactured Signal Slip Ring - 2

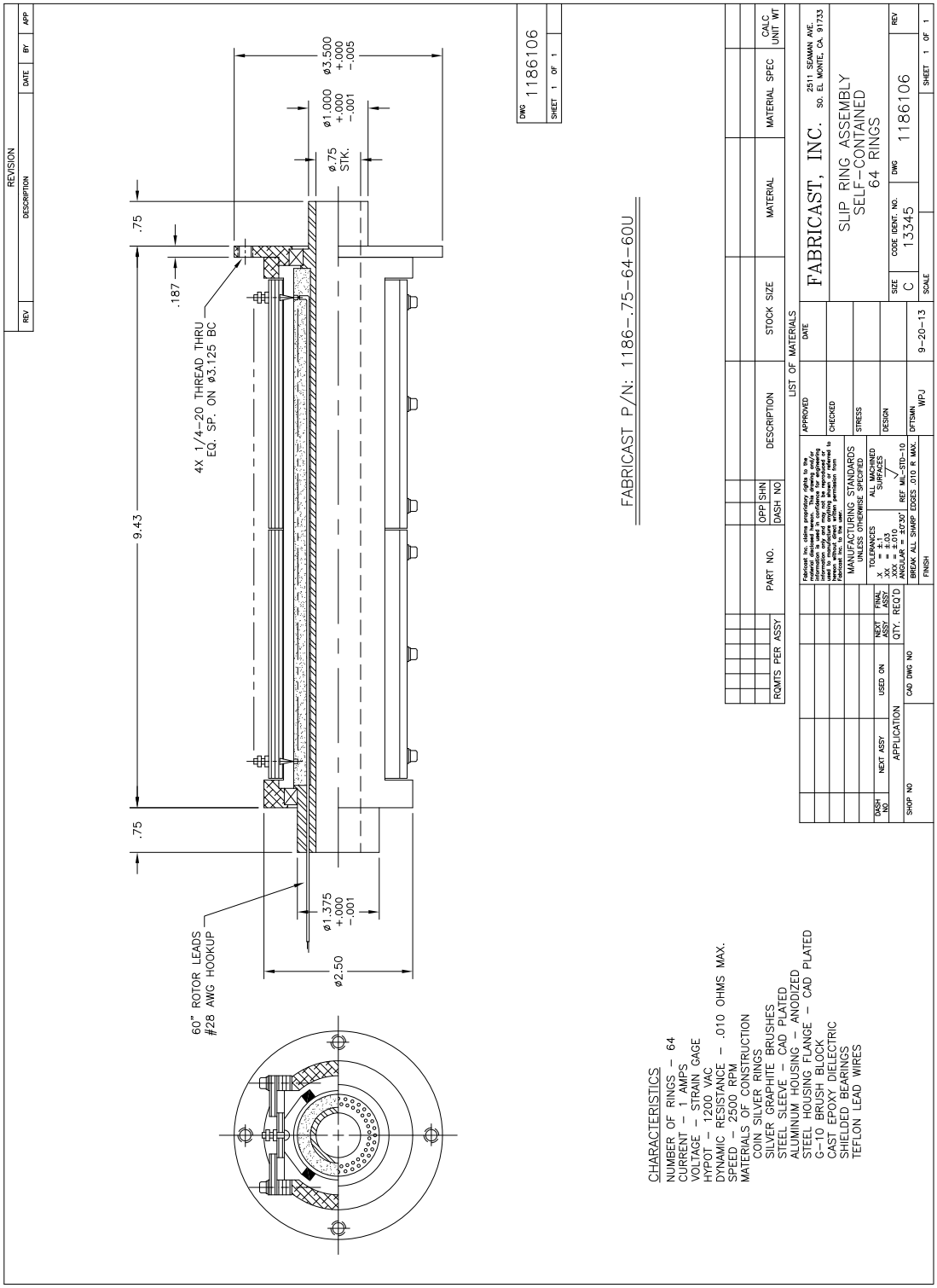

A.5 Fabricast manufactured Power Slip Ring

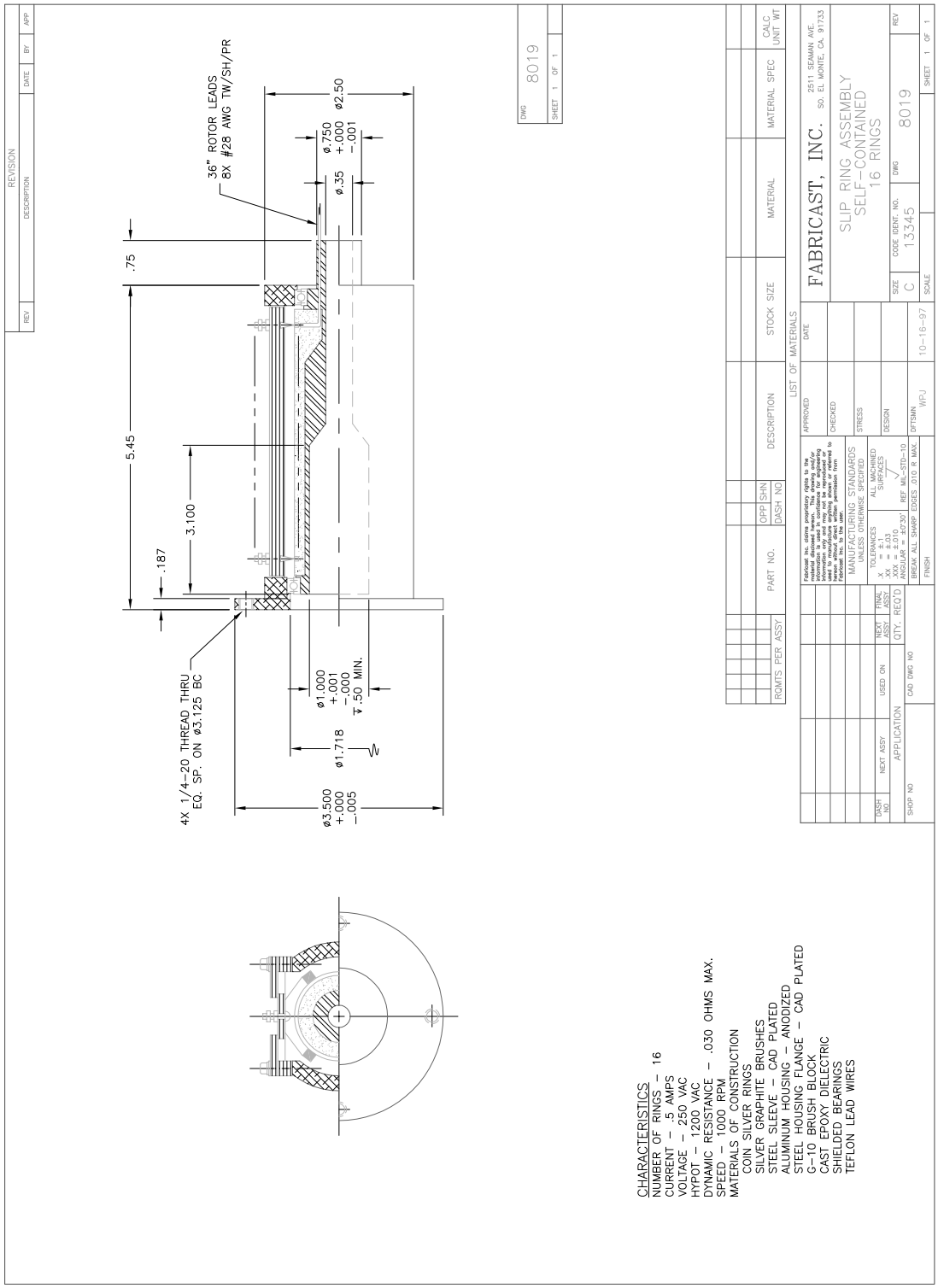

A.6 Composite Blade with Trailing Edge Flap

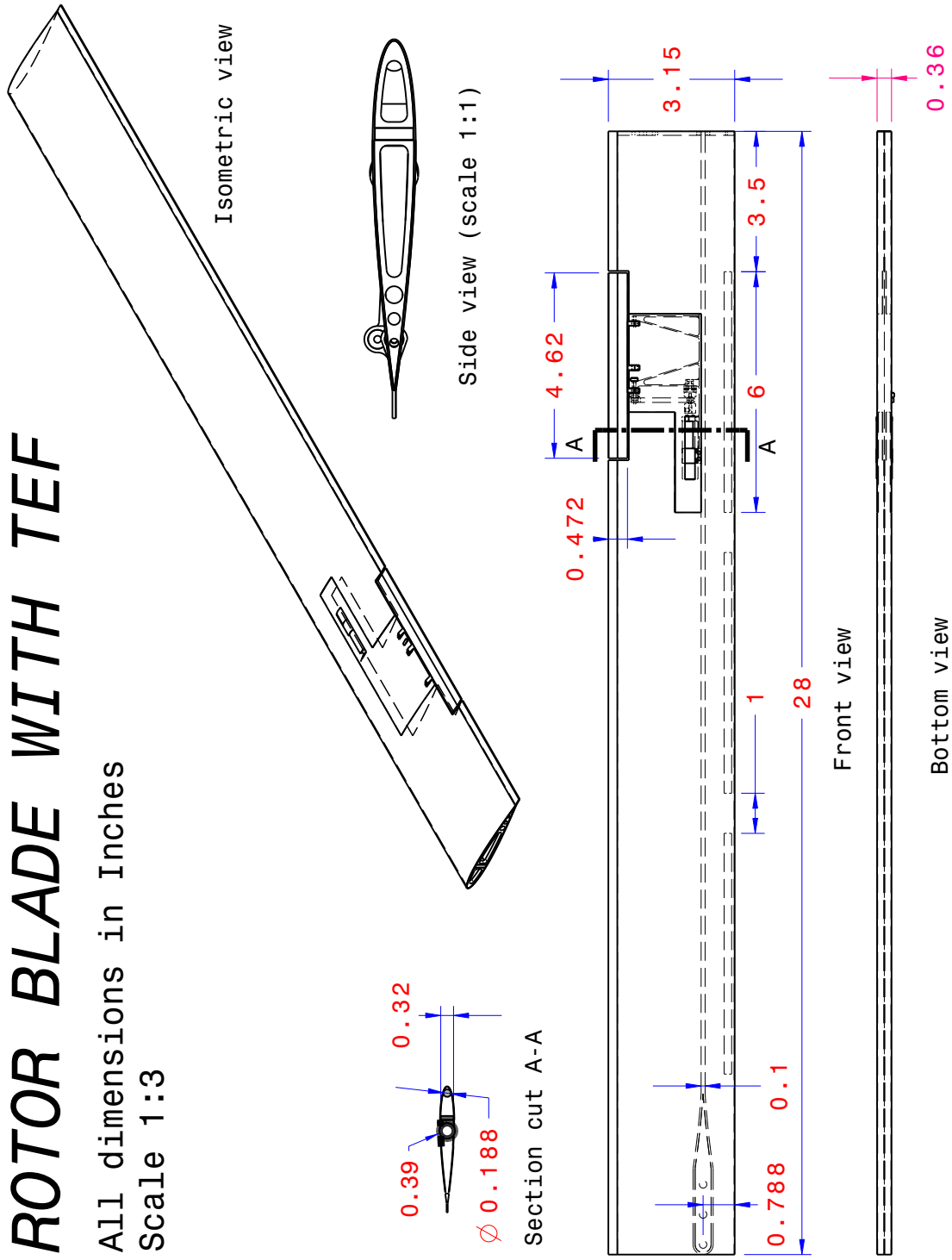

A.7 Top View of Blade Layout

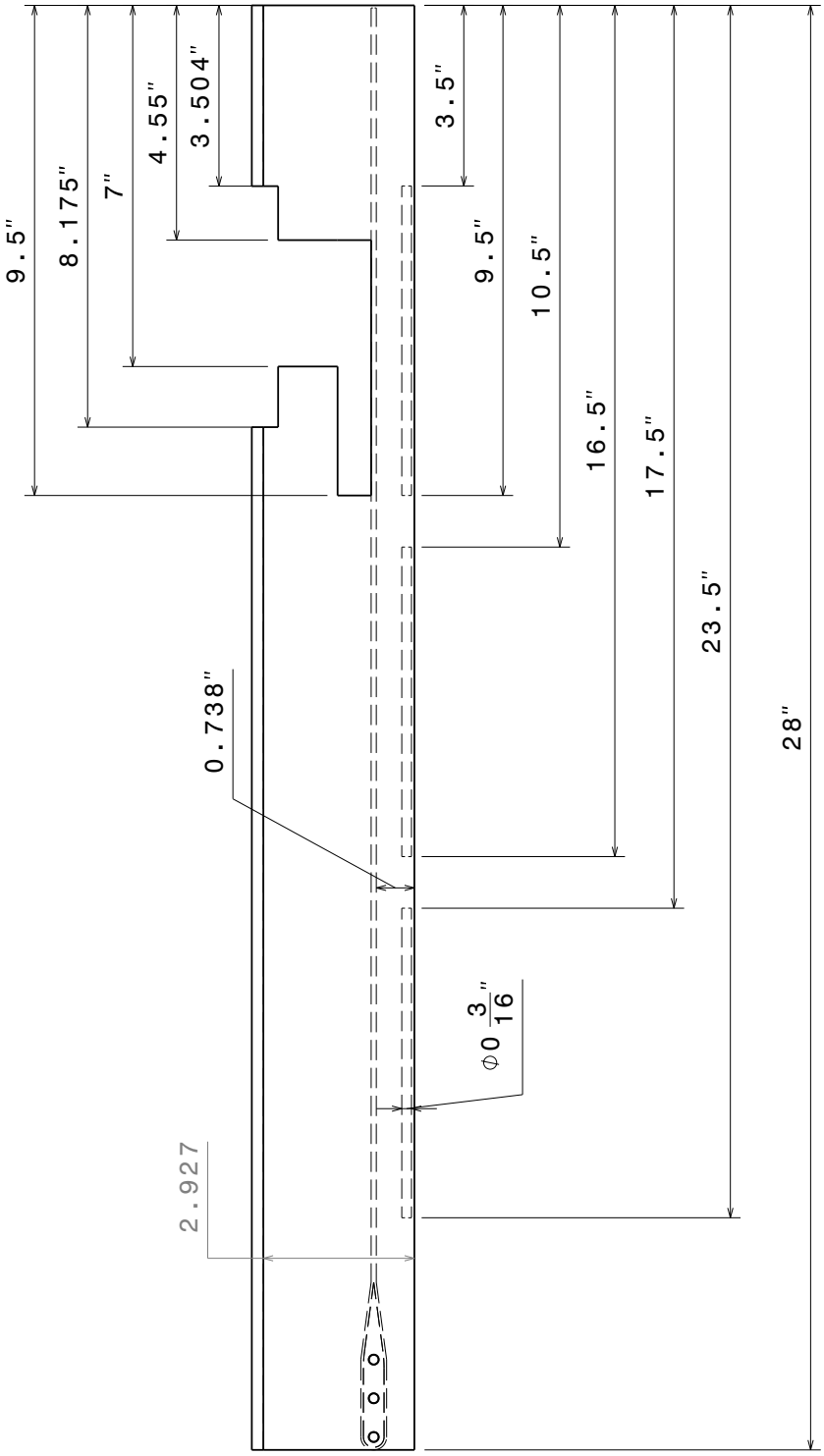

A.8 Spar Assembly

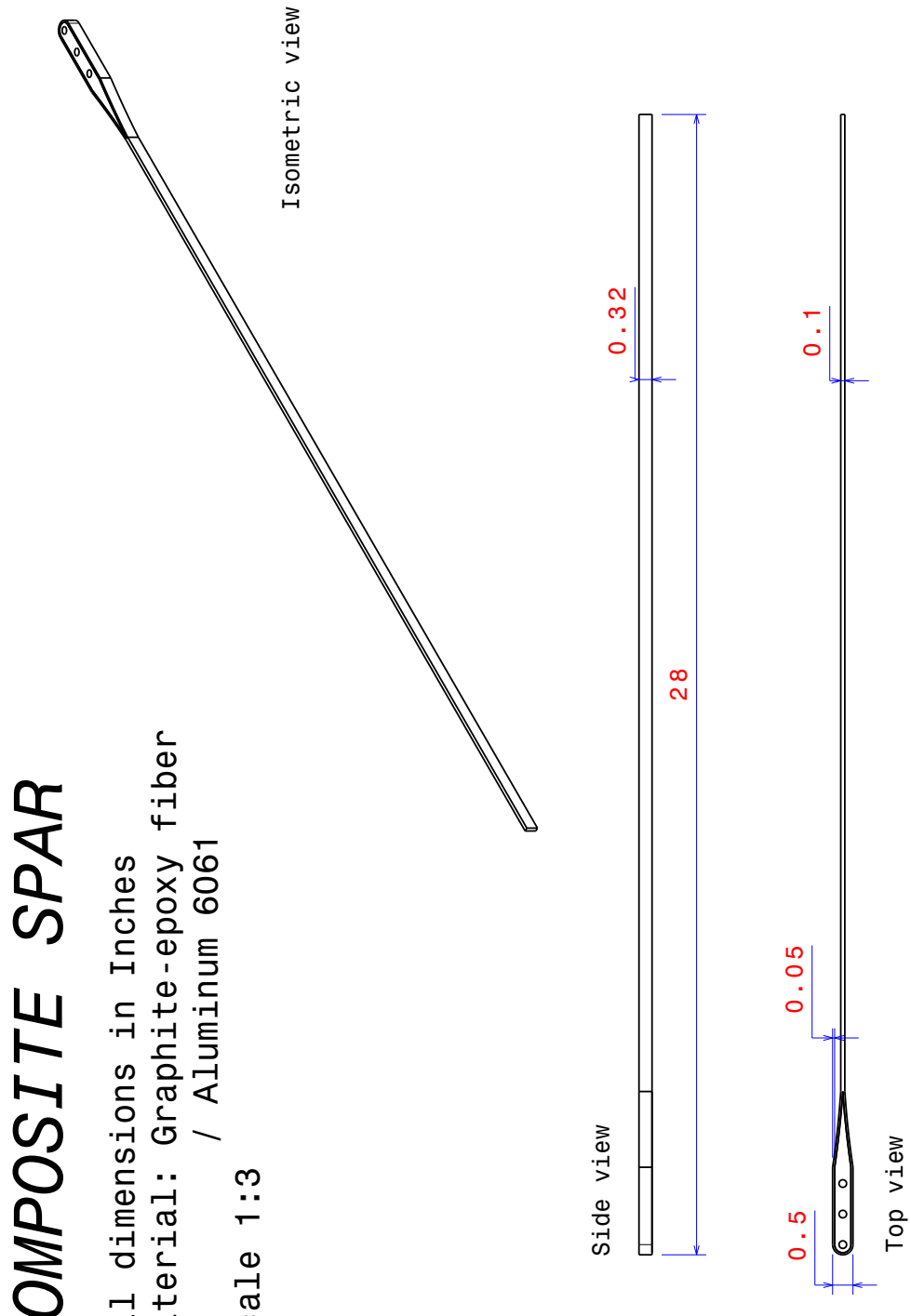

A.9 Root Insert for Composite Spar

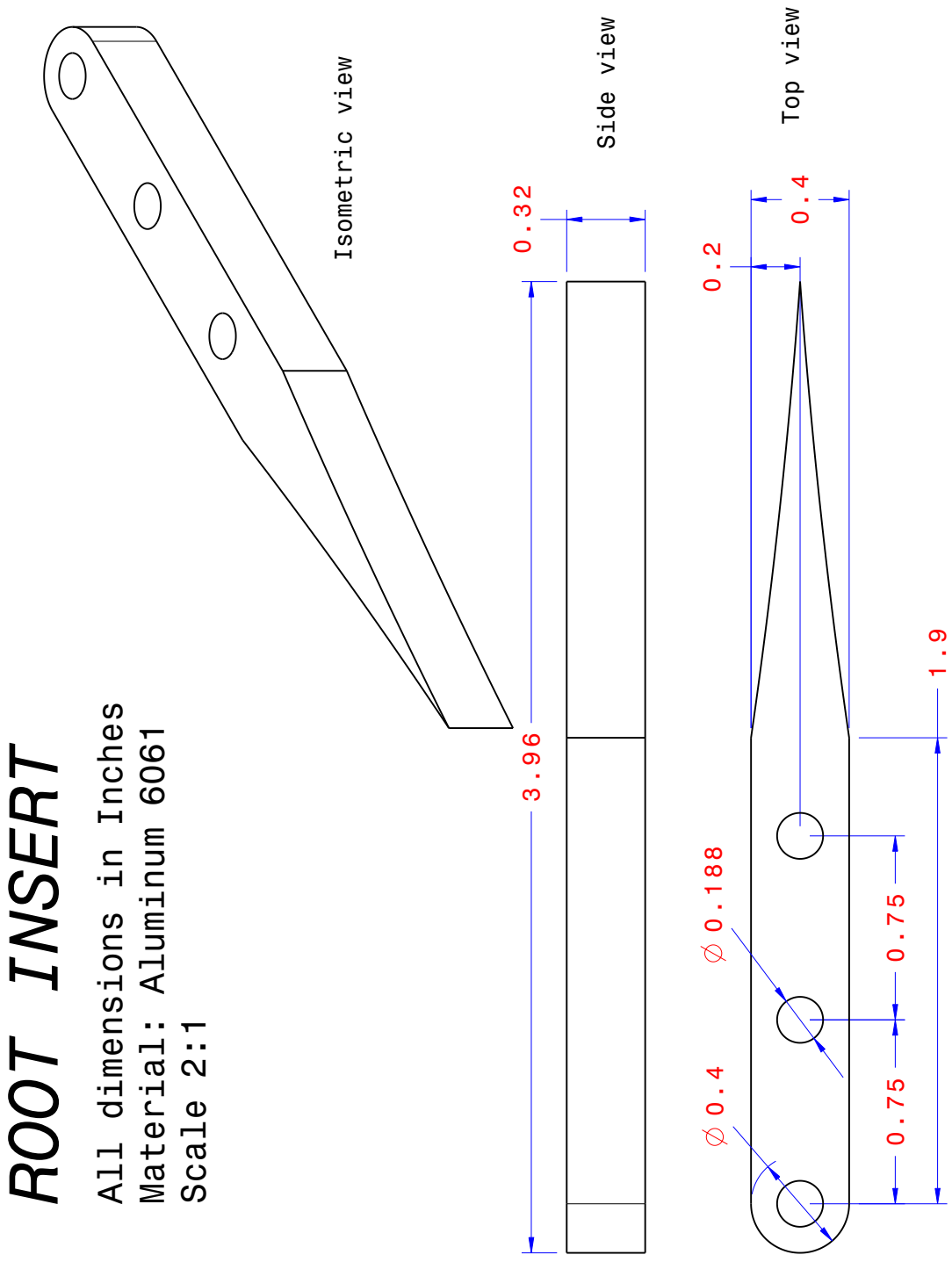

A.10 Flap Anchor

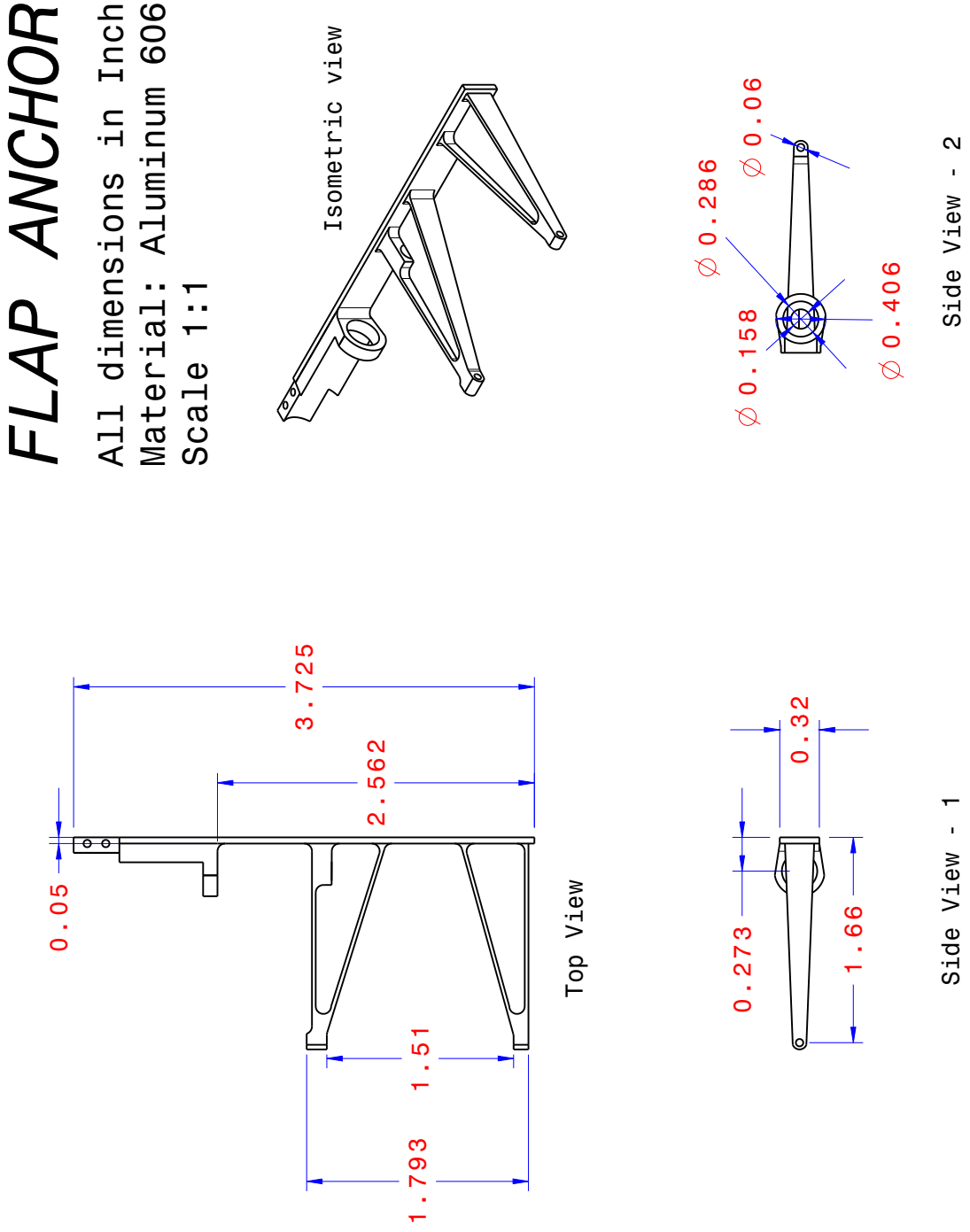

A.11 Flap Mount

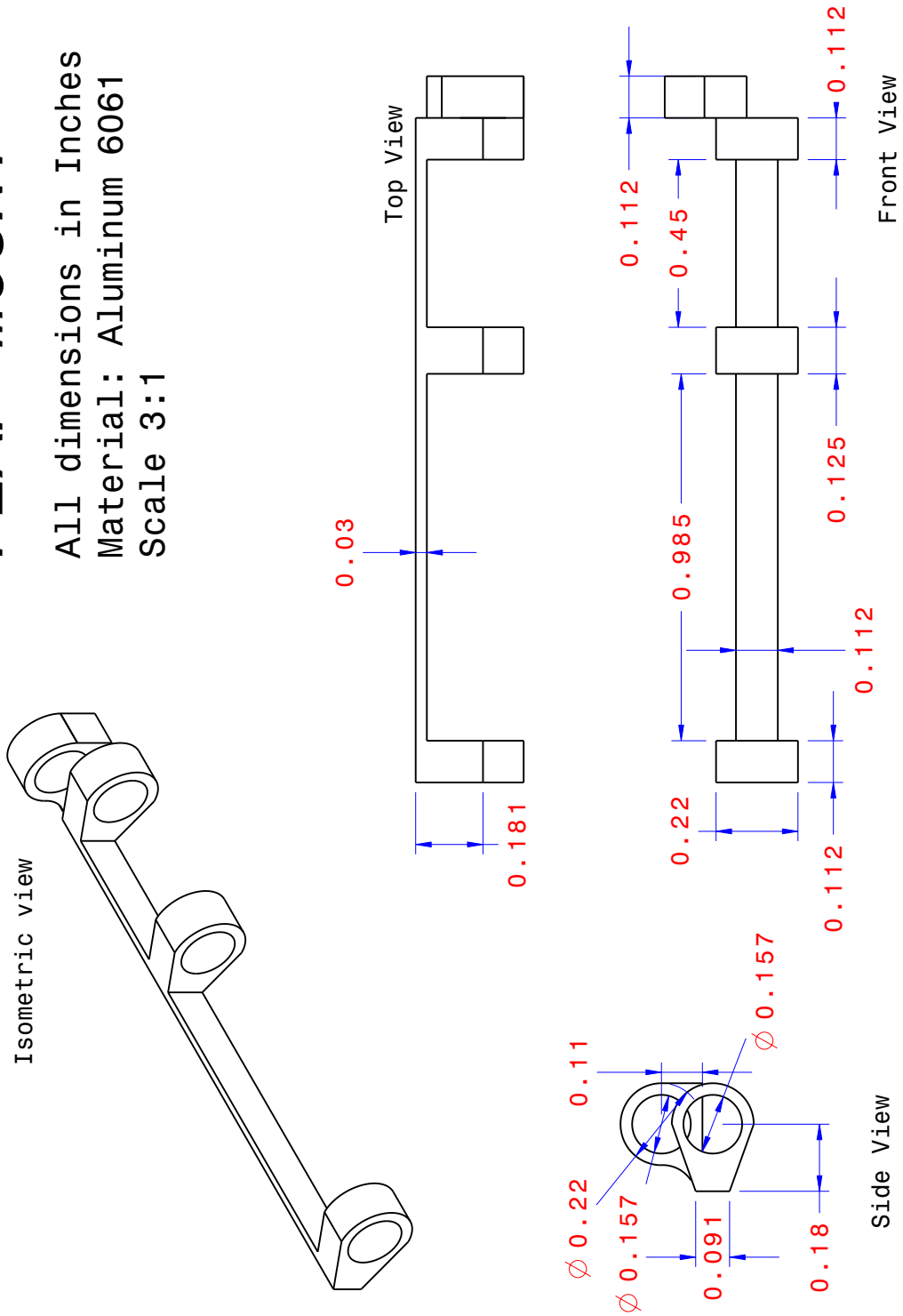

A.12 Flap Rod

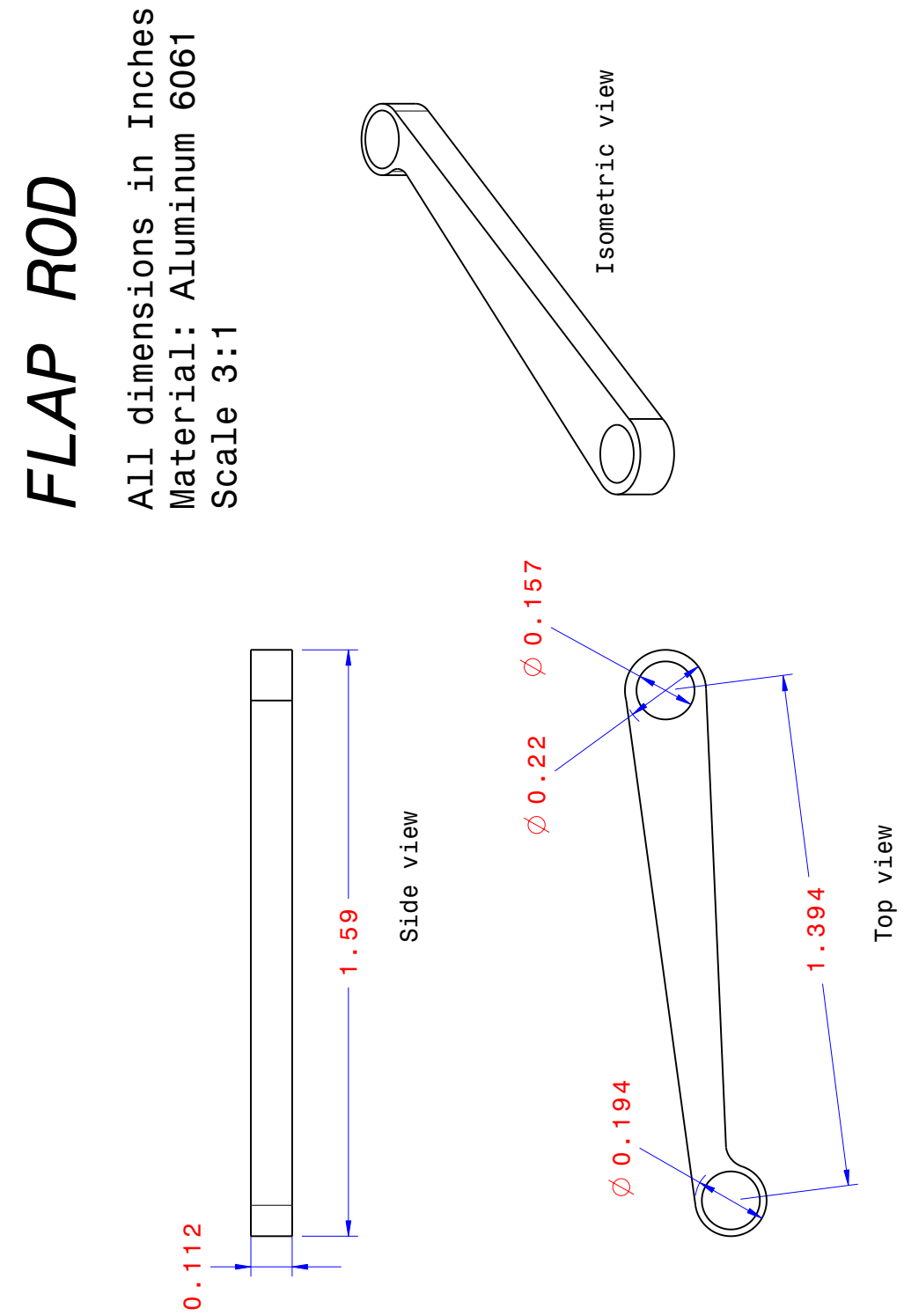
FLAP ROD
All dimensions in Inches
Material: Aluminum 6061
Scale 3:1
Isometric view
Side view
Top view
0.112
1.59
∅ 0.22
∅ 0.157
∅ 0.194
1.394

SHAFT ATTACHMENT 'A'

All dimensions in Inches
Material: Aluminum 6061
Scale 4:1

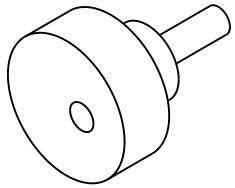

Isometric view

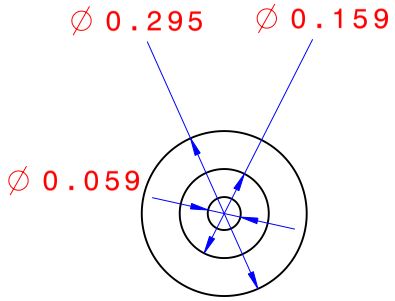

Left view

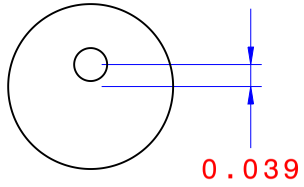

Right view

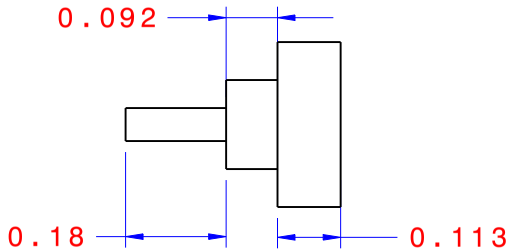

Front view

A.14 Shaft Attachments *B*

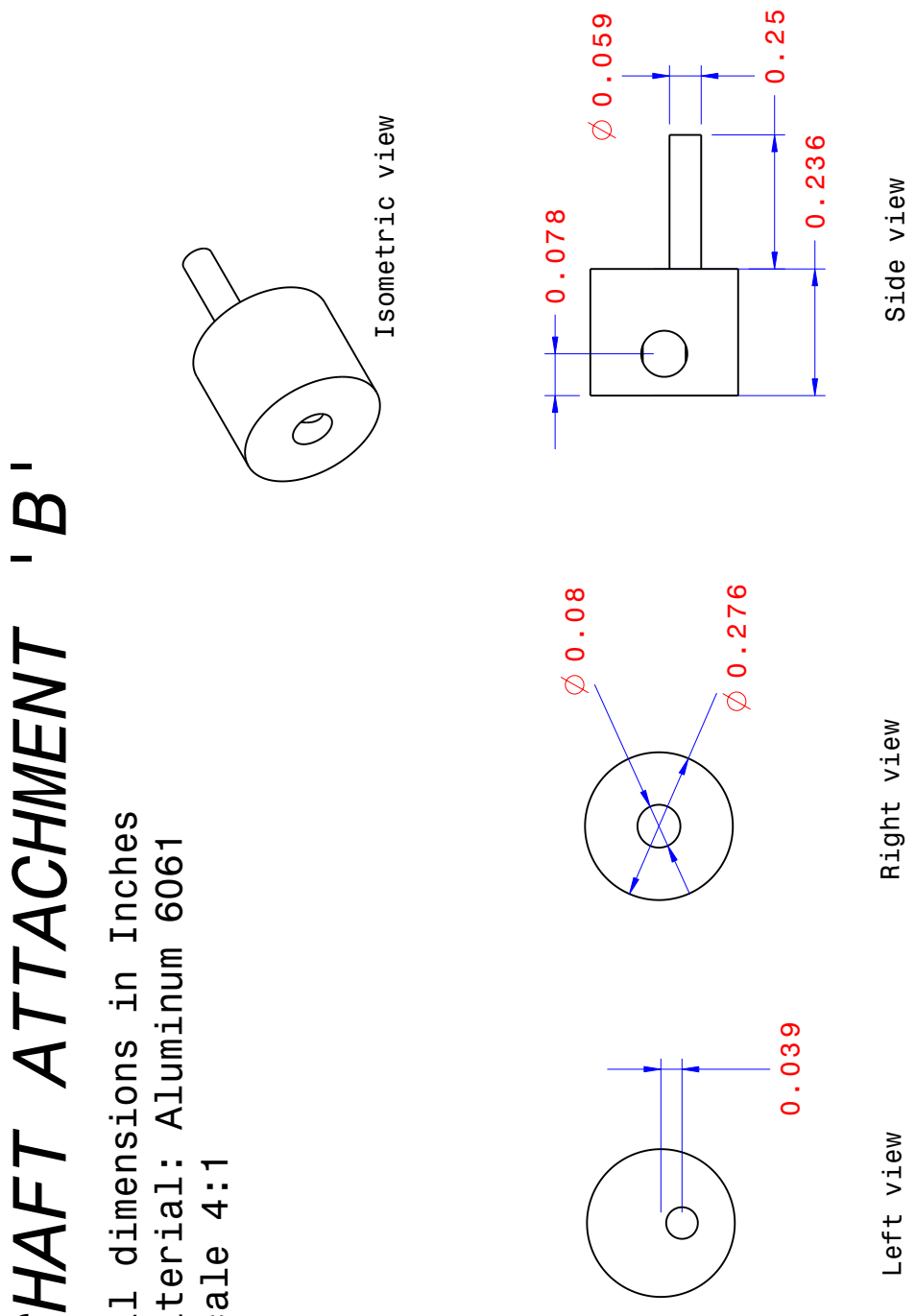

A.15 Soft Pitch Link

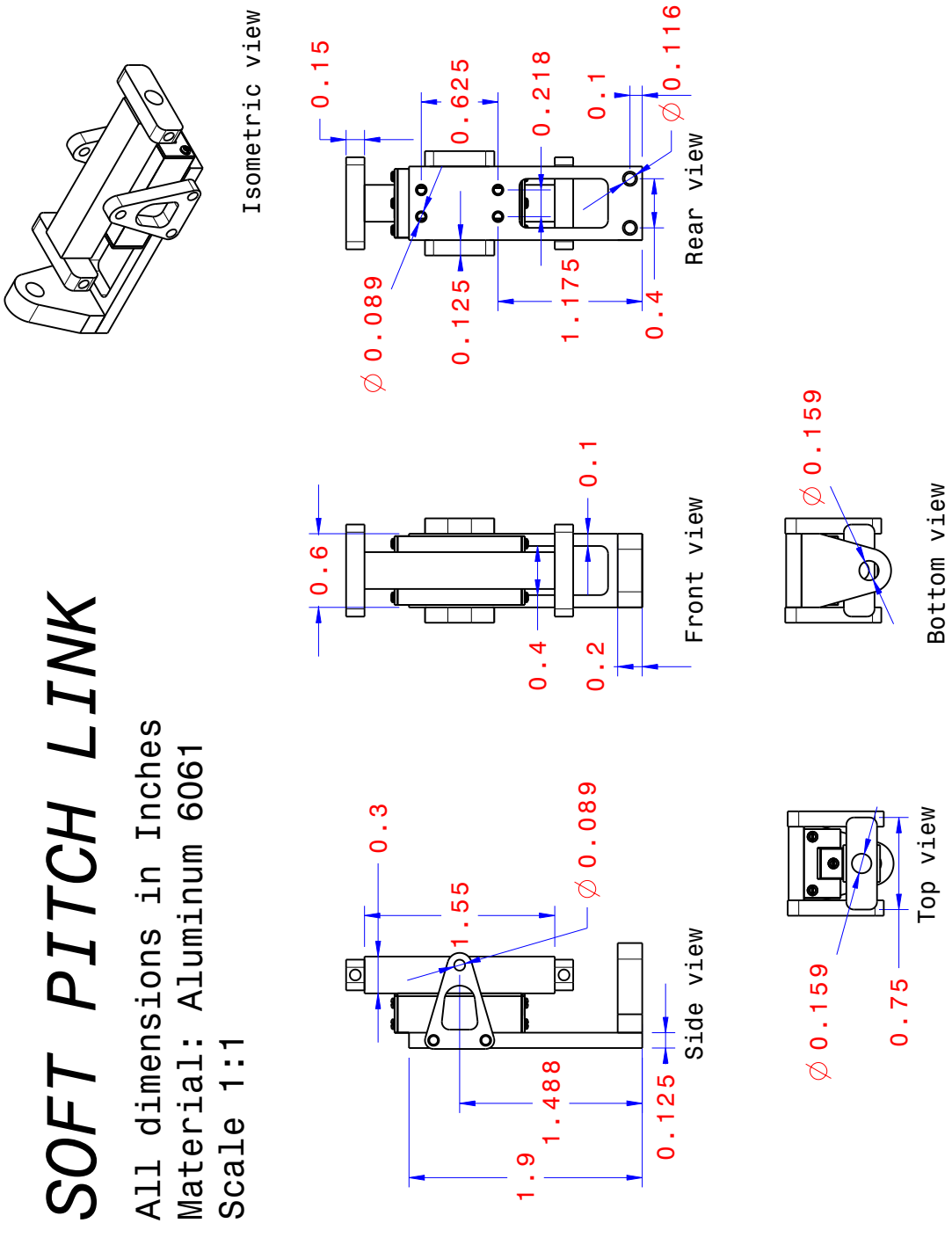

Bibliography

[1] J. De la Cierva. The development of the autogiro. *Journal of the Royal Aeronautical Society*, 30(181), 1926.

[2] J. G. Leishman. Development of the autogiro: A technical perspective. *Journal of Aircraft*, 41(4):765–781, 2004.

[3] Wikipedia: Bell 412. `http://upload.wikimedia.org/wikipedia/commons/e/e2/N301FD.jpg`. Accessed: Apr 14, 2015.

[4] W. Johnson. *Helicopter theory*. Dover Publications, 2 edition, 1994.

[5] J. G. Leishman. *Principles of Helicopter Aerodynamics*. Cambridge university press, 2 edition, 2006.

[6] J Hobbs. *Bristol Helicopters: A Tribute to Raoul Hafner*. Frenchay Publications, Bristol, UK, 1 edition, 1984.

[7] R. P. Pescara. Screw propeller of helicopter flying machines. *US Patent 1,449,129*, Mar 1923.

[8] How Helicopters Work. `http://science.howstuffworks.com/transport/flight/modern/helicopter5.htm`. Accessed: Apr 14, 2015.

[9] Aviation Images - Rotorhead Close-up Gallery - Agusta A109. `http://www.b-domke.de/AviationImages/Rotorhead/14332.html`. Accessed: Apr 14, 2015.

[10] R. Carlson. Helicopter performance transportation's latest chromosome: the 31st annual alexander a. nikolsky lecture. *Journal of the American Helicopter Society*, 47(1):3–17, 2002.

[11] Aviation Images - Rotorhead Close-up Gallery - Sikorsky CH-53G. `http://www.b-domke.de/AviationImages/Rotorhead/15875.html`. Accessed: Apr 14, 2015.

[12] Aviation Images - Rotorhead Close-up Gallery - MBB Bo105M PAH-1. `http://www.b-domke.de/AviationImages/Rotorhead/0416.html`. Accessed: Apr 14, 2015.

[13] K. H. Hohenemser. Hingeless rotorcraft flight dynamics. Technical Report AGARDograph No. 197, 1974.

[14] W. G. Bousman, R. A. Ormiston, and P. H. Mirick. Design considerations for bearingless rotor hubs. In *Proceedings of the 39th Annual Forum of the American Helicopter Society*, St. Louis, MO, 5 1983.

[15] R. Schindler and E. Pfisterer. Impacts of rotor hub design criteria of the operational capabilities of rotorcraft systems. In *Proceedings of the AGARD Symposium on Rotorcraft Design for Operations*, Amsterdam, The Netherlands, Oct 1986.

[16] T. R. Norman, C. R. Cooper, C. A. Fredrickson, and J. R. Herter. Full-scale wind tunnel evaluation of the sikorsky five-bladed bearingless main rotor. In *Proceedings of the 49th Annual Forum of the American Helicopter Society*, St. Louis, MO, 5 1993.

[17] D. K. Berrington. Design and development of the westland sea lynx. *Journal of the American Helicopter Society*, 19(1):16–25, 1974.

[18] R. Cansdale. An aeroelastic model helicopter rotor. Technical Report CP No. 1288, Farnborough, 1974.

[19] B. H. Lau, A. W. Louie, N. Griffiths, and C. P. Sotiriou. Performance and rotor loads measurements of the lynx xz170 helicopter with rectangular blades. Technical Report NASA Technical Memorandum 104000, 1993.

[20] A. R. S. Bramwell, G. Done, and D. Balmford. *Bramwell's Helicopter Dynamics*. Butterworth-Heinemann, 2 edition, 2001.

[21] Aviation Images - Rotorhead Close-up Gallery - Westland Sea Lynx Mk.88A. `http://www.b-domke.de/AviationImages/Rotorhead/32854.html`. Accessed: Apr 14, 2015.

[22] C. d'Ascanio. Helicopter. *US Patent 1,960,141*, May 1934.

[23] C. H. Kaman. Aircraft of rotary wing type. *US Patent 2,455,866*, May 1948.

[24] A. Z. Lemnios and R. Jones. The servo flap - an advanced rotor control system. In *Proceedings of American Helicopter Society Design Specialists' Meeting on Vertical Lift Aircraft Design Conference*, San Francisco, CA, Jan 1990.

[25] F. S. Wei and A. L. Weisbrich. Multicyclic controllable twist rotor data analysis. Technical Report NASA Contractors Report 152251, 1979.

[26] F. S. Wei and R. Jones. Correlation and analysis for sh-2f 101 rotor. *Journal of Aircraft*, 25(7):647–652, 1988.

[27] F. S. Wei. Advanced servo flap rotor using variable blade index angle control. In *Proceedings of 38th AIAA/ASME/ASCE/AHS/ASC Structures, Structural Dynamics, and Materials Conference and Exhibit, and AIAA/ASME/AHS Adaptive Structures Forum*, Kissimmee, FL, Apr 1997.

[28] F. S. Wei and F. Gallagher. Servo-flap rotor performance flight testing and data identification. In *Proceedings of 57th Annual Forum of the American Helicopter Society*, Washington DC, May 2001.

[29] F. S. Wei. Design of soft torsion rotor systems at kaman aerospace corporation. In *Proceedings of the 58th Annual Forum of the American Helicopter Society*, Montreal, Canada, Jun 2002.

[30] F. S. Wei and C. Gunsallus. A new approach to rotor blade performance design improvement. In *Proceedings of the 48th AIAA/ASME/ASCE/AHS/ASC Structures, Structure Dynamics and Material Conference*, Honolulu, Hawaii, Apr 2007.

[31] T. Ning, F. S. Wei, and A. Suen. Servo-flap rotor design parameters identification via spectral analysis of flight data. In *Proceedings of the 46th AIAA Aerospace Sciences Meeting and Exhibit*, Reno, NV, Jan 2008.

[32] F. S. Wei and A. Gates. Improvement of servo-flap rotor design parameters for helicopter performance. In *Proceedings of the 52nd AIAA/ASME/ASCE/AHS/ASC Structures, Structural Dynamics and Materials Conference*, Denver, Colarado, Apr 2011.

[33] F. S. Wei, T. Vasko, and A. Gates. Servo - flap rotor performance design evaluation. In *Proceedings of the 51st AIAA Aerospace Sciences Meeting*, Grapevine, TX, Jan 2013.

[34] F. S. Wei, E. Moore, and A. Gates. An intermeshing rotor helicopter design and test. In *Proceedings of the 56th AIAA/ASCE/AHS/ASC Structures, Structural Dynamics and Materials Conference*, Kissimmee, FL, Jan 2015.

[35] Kaman K-1200 "K-MAX. `http://oh1ninja.la.coocan.jp/details/KMAX/kmax_e.htm`. Accessed: Apr 14, 2015.

[36] B. Rocconella and F. S. Wei. Wind tunnel model testing of the improved k-max servo-flap blade section. In *Proceedings of the 57th Annual Forum of the American Helicopter Society*, Washington DC, May 2001.

[37] R. W. Prouty and H. C. Curtiss. Helicopter control systems: A history. *Journal of Guidance, Control, and Dynamics*, 26(1):12–18, 2003.

[38] P. P. Friedmann. Rotary-wing aeroelasticity with application to vtol vehicles. In *Proceedings of the 31st Structures, Structural Dynamics and Materials Conference*, Long Beach,CA, 1990.

[39] P. P. Friedmann and D. H. Hodges. Rotary wing aeroelasticity a historical perspective. *Journal of Aircraft*, 40(6):1019–1046, 2003.

[40] G. Reichert. Helicopter vibration control - a survey. *Vertica*, 5:1–20, 1981.

[41] R. G. Loewy. Helicopter vibrations- a technological perspective. *Journal of the American Helicopter Society*, 29:4–30, 1984.

[42] W. G. Bousman and W. R. Mantay. A review of research in rotor loads. *NASA/Army Rotorcraft Technology*, 1(Aerodynamics, and Dynamics and Aeroelasticity):180–311, 1988.

[43] W. G. Bousman. Rotorcraft airloads measurements: Extraordinary costs, extraordinary benefits the 31st alexander nikolsky honorary lecture. *Journal of the American Helicopter Society*, 59(3):1–30, 2014.

[44] R. E. Hansford and J. Vorwald. Dynamics workshop on rotor vibratory loads prediction. *Journal of the American Helicopter Society*, 43(1):76–87, 1998.

[45] G. Bir and I. Chopra. University of maryland advanced rotorcraft code : Theory manual. Technical report, 1994.

[46] W. Johnson. CAMRAD II comprehensive analytical model of rotorcraft aerodynamics and dynamics: Theory manual. Technical report, Johnson Aeronautics, Palo Alto, CA, 1993.

[47] A. Datta, M. Nixon, and I. Chopra. Review of rotor loads prediction with the emergence of rotorcraft CFD. *Journal of the American Helicopter Society*, 52(4):287–317, 2007.

[48] A. Datta and W. Johnson. An assessment of the state-of-the-art in multidisciplinary aeromechanical analyses. In *Proceedings of the AHS Specialist's Conference on Aeromechanics*, San Francisco, CA, 1 2008.

[49] W. G. Bousman and T. Norman. Assessment of predictive capability of aeromechanics methods. *Journal of the American Helicopter Society*, 55(1):012001 – 1–12, 2010.

[50] A. Datta, J. Sitaraman, I. Chopra, and J. D. Baeder. CFD/CSD prediction of rotor vibratory loads in high-speed flight. *Journal of Aircraft*, 43(6):1698–1709, 11 2006.

[51] A. Datta and I. Chopra. Prediction of the UH-60a main rotor structural loads using computational fluid dynamics/comprehensive analysis coupling. *Journal of the American Helicopter Society*, 53(4):351–365, 2008.

[52] J. Sitaraman, M. Potsdam, B. Jayaraman, A. Datta, A. Wissink, D. Mavriplis, and H. Saberi. Rotor loads prediction using helios: a multi-solver framework for rotorcraft CFD/CSD analysis. In *Proceedings of the 49th AIAA Aerospace Science Meeting*, Orlando, FL, Jan 2011.

[53] S. Venkateswaran, S. Jayanarayanan, W. Andrew, D. Anubhav, J. Buvana, P. Mark, M. Dimitri, Y. Zhi, O. Daved, S. Hossein, R. Cheng, N. Harriharan, and R. Strawn. Application of the helios computational platform to rotorcraft flowfields. In *Proceedings of the 48th AIAA Aerospace Meeting*, Orlando, FL, Jan 2010.

[54] A. Wissink, B. Jayaraman, A. Datta, J. Sitaraman, M. Potsdam, S. Kamkar, D. Mavriplis, Z. Yang, R. Jain, J. Lim, and R. Strawn. Capability enhancements in version 3 of the helios high-fidelity rotorcraft simulation code. In *Proceedings of the 50th AIAA Aerospace Science Meeting*, Nashville, TN, Jan 2012.

[55] A. Rosen and R. Ben-Ari. Mathematical modelling of a helicopter rotor track and balance: theory. *Journal of Sound and Vibration*, 200(5):589–603, 1997.

[56] R. Ben-Ari and A. Rosen. Mathematical modelling of a helicopter rotor track and balance: results. *Journal of sound and vibration*, 200(5):605–620, 1997.

[57] N. A. Miller. A comparison of main rotor smoothing adjustments using linear and neural network algorithms. Master's thesis, Air Force Institute of Technology, Wright-Patterson Air Force Base, Ohio, 2006.

[58] N. A. Miller and D. L. Kunz. A comparison of main rotor smoothing adjustments using linear and neural network algorithms. *Journal of Sound and Vibration*, 311(3-5):991–1003, 2008.

[59] E. Bechhoefer, A. Fang, and E. Garcia. Rotor track and balance improvements. In *Annual Conference of Prognostics and Health Management Society*, New Orleans, LA, Oct 2013.

[60] C. G. Matalanis, A. Kuczek, B. E. Wake, N. Soldner, U. Jonsson, and V. Lakamraju. Blade integration of a modular active trim tab system for onboard rotor tracking. In *Proceedings of the 67th Annual Forum of the American Helicopter Society*, Virginia Beach, VA, May 2011.

[61] A. Lengyel and M. Wilson. Innovative systems to reduce one per rev vibrations in helicopters. In *Proceedings of the th Annual Forum of the American Helicopter Society*, Forth Worth, TX, May 2012.

[62] S. P. Viswanathan and A. W. Myers. Reduction of helicopter vibration through control of hub-impedance. *Journal of the American Helicopter Society*, 25(4):3–12, 1980.

[63] Kawasaki / Eurocopter BK117 helicopter's Details. `http://oh1ninja.la.coocan.jp/details/BK117/021006_akeno_052.jpg`. Accessed: Apr 24, 2015.

[64] Aviation Images - Rotorhead Close-up Gallery - Sikorsky S-92A. http://www.b-domke.de/AviationImages/Rotorhead/29053.html. Accessed: Apr 24, 2015.

[65] C. Kessler. Active rotor control for helicopters: motivation and survey on higher harmonic control. *CEAS Aeronautical Journal*, 7 2011.

[66] J. Bao. *Development of Mach scale rotors with composite tailored couplings for vibration reduction*. PhD thesis, University of Maryland, College Park MD, 2004.

[67] J. Bao, V. T. Nagaraj, I. Chopra, and A. P. F. Bernhard. Development of mach scale rotors with tailored composite coupling for vibration reduction. *Journal of aircraft*, 43(4):922–931, 2006.

[68] J. Bao, V. T. Nagaraj, I. Chopra, and A. P. F. Bernhard. Wind tunnel test of five sets of mach scale composite tailored rotor with flap-bending / torsion couplings for vibration reduction. *Journal of the American Helicopter Society*, 53(3):215–225, 2008.

[69] D. Braun. Development of antiresonance force isolators for helicopter vibration reduction. *Journal of the American Helicopter Society*, 27(4):37–44, 1982.

[70] A. E. Staple. An evaluation of active control of structural response as a means of reducing helicopter vibration. In *Proceedings of the 15th European Rotorcraft Forum*, Amsterdam, The Netherlands, Sep 1989.

[71] A. E. Staple and D. M. Wells. The development and testing of an active control of structural response system for the EH101 helicopter. In *Proceedings of the 16th European Rotorcraft Forum*, Glasgow, Scotland, Sep 1990.

[72] W. A. Welsh, P. C. Von Hardenberg, P. W. Von Hardenberg, and A. E. Staple. Test and evaluation of fuselage vibration utilizing active control of structural response(ACSR) optimized to ADS-27. In *Proceedings of the 46th Annual Forum of the American Helicopter Society*, Washington, DC, May 1990.

[73] M. Aso and S-I . I. Bandoh. Development of the total vibration reduction (tvr) system. In *Proceedings of the 55th Annual Forum of the American Helicopter Society*, Montreal, Canada, May 1999.

[74] P. Konstanzer, B. Enenkl, P. Aubourg, and P. Cranga. Recent advances in eurocopter's passive and active vibration control. In *Proceedings of the 64th Annual Forum of the American Helicopter Society*, Montreal, Canada, May 2008.

[75] P. R. Payne. Higher harmonic rotor control: the possibilities of third and higher harmonic feathering for delaying the stall limit in helicopters. *Aircraft Engineering and Aerospace Technology*, 30(8):222–226, 1958.

[76] P. J. Arcidiacono. Theoretical performance of helicopters having second and higher harmonic feathering control. *Journal of the American Helicopter Society*, 6(2):8–19, 1961.

[77] J. Shaw and N. Albion. Active control of the helicopter rotor for vibration reduction. *Journal of the American Helicopter Society*, 26(3):32–39, 1981.

[78] K. Nguyen and I. Chopra. Application of higher harmonic control to rotors operating at high speed and thrust. *Journal of the American Helicopter Society*, 35(3):78–89, 1990.

[79] K. Nguyen and I. Chopra. Effects of higher harmonic control on rotor performance and control loads. *Journal of Aircraft*, 29(3):336–342, 1992.

[80] C. E. Hammond. Wind tunnel results showing rotor vibratory loads reduction using higher harmonic blade pitch. *Journal of the American Helicopter Society*, 28(1):10–15, 1983.

[81] E. R. Wood, R. W. Powers, J. H. Cline, and C. E. Hammond. On developing and flight testing a higher harmonic control system. *Journal of the American Helicopter Society*, 30(1):3–20, 1985.

[82] W. Miao, S. B. R. Kottapalli, and H. M. Frye. Flight demonstration of higher harmonic control (HHC) on s-76. In *Proceedings of the 42nd Annual Forum of the American Helicopter Society*, Washington, DC, May 1986.

[83] J. Shaw, N. Albion, E. J. Hanker, and R. S. Teal. Higher harmonic control: Wind tunnel demonstration of fully effective vibratory hub force suppression. *Journal of the American Helicopter Society*, 34(1):14–25, 1989.

[84] W. R. Splettstoesser, R. Kube, W. Wagner, U. Seelhorst, A. Boutier, F. Micheli, E. Mercker, and K. Pengel. Key results from a higher harmonic control aeroacoustic rotor test (HART) in the german-dutch wind tunnel. In *Proceedings of the 21st European Rotorcraft Forum*, St. Petersburg, Russia, 1995.

[85] W. R. Splettstoesser, R. Kube, W. Wagner, U. Seelhorst, A. Boutier, F. Micheli, E. Mercker, and K. Pengel. Key results from a higher harmonic control aeroacoustic rotor test (hart). *Journal of the American Helicopter Society*, 42(1):58–78, 1997.

[86] Y. H. Yu, C. Tung, B. van der Wall, H. J. . J. Pausder, C. Burley, T. Brooks, P. Beaumier, Y. Delrieux, E. Mercker, and K. Pengel. The HART-II test: Rotor wakes and aeroacoustics with higher-harmonic pitch control (HHC) inputs-the joint german/french/dutch/us project. In *Proceedings of the 58th Annual Forum of the American Helicopter Society*, Montreal, Canada, Jun 2002.

[87] B. G. van der Wall, C. L. Burley, Y. Yu, H. Richard, K. Pengel, and P. Beaumier. The HART II test - measurement of helicopter rotor wakes. *Aerospace Science and Technology*, 8(4):273–284, 2004.

[88] P. Kuefmann, R. Bartels, C. Kebler, and B. G. van der Wall. On the design and development of a multiple-swashplate control system for the realization of individual blade control (IBC) for helicopters. In *Proceedings of the 67th Annual Forum of the American Helicopter Society*, Virginia Beach, VA, May 2011.

[89] K. F. Guinn. Individual blade control independent of a swashplate. *Journal of the American Helicopter Society*, 27(3):25–31, 1982.

[90] N. D. Ham. Helicopter individual-blade-control and its applications. In *Proceedings of the 39th Annual Forum of American Helicopter Society*, St. Louis, MO, May 1983.

[91] L. Dadone, J. Cowan, and F. J. McHugh. Variable camber rotor study. Technical Report NASA Contractors Report 166382, 1982.

[92] P. Anusonti-Inthra, R. Sarjeant, M. Frecker, and F. Gandhi. Design of a comformable rotor airfoil using distributed piezoelectric actuators. *AIAA journal*, 43(8):1684–1695, 2005.

[93] P. C. Chen and I. Chopra. Wind tunnel test of a smart rotor model with individual blade twist control. *Journal of Intelligent Material Systems and Structures*, 8(5):414–425, 1997.

[94] J. P. Rodgers and N. W. Hagood. Hover testing of a 1/6th mach-scale ch-47d blade with integral twist actuation. In *Proceedings of the 9th International Conference on Adaptive Structures and Technology*, Cambridge, MA, 1998.

[95] S. J. Shin. *Design, manufacturing and testing of an active twist rotor*. PhD thesis, Massachusetts Institute of Technology, Cambridge, MA, 1999.

[96] W. K. Wilkie, M. L. Wilbur, P. H. Mirick, C. Cesnik, and S. Shin. Aeroelastic analysis of the NASA/army/mit active twist rotor. In *Proceedings of the 55th Annual Forum of the American Helicopter Society*, Montreal, Canada, May 1999.

[97] J. Kim, N. Koratkar, and A. Messac. Optimal design of a swashplateless main rotor featuring active control of blade twist. In *Proceedings of the 43rd AIAA/ASME/ASCE/AHS/ASC Structures, Structural Dynamics, and Materials Conference*, Denver, CO, Apr 2002.

[98] A. P. F. Bernhard and J. Wong. Wind-tunnel evaluation of a sikorsky active rotor controller implemented on the NASA/Army/MIT active twist rotor. *Journal of the American Helicopter Society*, 50(1):65–81, 2005.

[99] S. Shin, C. E. Cesnik, and S. R. Hall. Closed-loop control test of the NASA/Army/MIT active twist rotor for vibration reduction. *Journal of the American Helicopter Society*, 50(2):178–194, 2005.

[100] A. P. F. Bernhard. *Smart helicopter rotor with active blade tips*. PhD thesis, University of Maryland, College Park, MD, 2000.

[101] A. P. F. Bernhard and I. Chopra. Hover test of a mach-scale rotor model with active blade tips. *Journal of the american helicopter society*, 47(4):273–284, 2002.

[102] P. Richter and A. Blaas. Full scale wind tunnel investigation of an individual blade control (IBC) system for the bo 105 hingeless rotor. In *Proceedings of the 19th European Rotorcraft Forum*, Cernobbio, Italy, Sep 1993.

[103] P. Richter and T. Schreiber. Theoretical investigations and wind tunnel tests with HHC-IBC. In *Proceedings of the 20th European Rotorcraft Forum*, Amsterdam, Netherlands, Oct 1994.

[104] U. T. P. Arnold, M. Müller, and P. Richter. Theoretical and experimental prediction of individual blade control benefits. In *Proceedings of the 23rd European Rotorcraft Forum*, Dresden, Germany, 1997.

[105] A. Haber, S. A. Jacklin, and G. DeSimone. Development, manufacturing, and component testing of an individual blade control system for a UH-60 helicopter rotor. In *Proceedings of the American Helicopter Society Aerodynamics, Acoustics, and Test and Evaluation Technical Specialists Meeting*, San Francisco, CA, Jan 2002.

[106] S. A. Jacklin, A. Haber, G. de Simone, T. R. Norman, C. Kitaplioglu, and P. Shinoda. Full-scale wind tunnel test of an individual blade control system for a UH-60 helicopter. In *Proceedings of the 58th Annual Forum of the American Helicopter Society*, Montreal, Canada, Jun 2002.

[107] D. Roth. Advanced vibration reduction by IBC technology. In *Proceedings of the 30th European Rotorcraft Forum*, Munchen, Germany, Sep 2004.

[108] U. T. P. Arnold and D. Furst. Closed loop IBC results from ch-53g flight tests. In *Proceedings of the 31st European Rotorcraft Forum*, Florence, Italy, Sep 2005.

[109] U. T. P. Arnold, D. Fuerst, T. Neuheuser, and R. Bartels. Development of an integrated electrical swashplateless primary and individual blade control system. In *Proceedings of the 63rd Annual Forum of the American Helicopter Society*, Virginia Beach, VA, May 2007.

[110] D. Fuerst, A. Hausberg, and T. Neuheuser. Experimental verification of an electro-mechanical-actuator for a swashplateless primary and individual helicopter blade control system. In *Proceeding of the 64th Annual Forum of the American Helicopter Society*, Montreal, Canada, May 2008.

[111] A. Z. Lemnios and A. F. Smith. An analytical evaluation of the controllable twist rotor performance and dynamic behavior. Technical report, USAAM-RDL, May 1972.

[112] J. L. McCloud. An analytical study of a multicyclic controllable twist rotor. In *Proceedings of the 31st Annual Forum of the American Helicopter Society*, Washington DC, May 1975.

[113] A. Z. Lemnios and F. K. Dunn. Theoretical study of multicyclic control of a controllable twist rotor. Technical Report NASA Contractor Report 151959, 1976.

[114] J. L. Mccloud and A. L. Weisbrich. Wind-tunnel test results of a full-scale multicyclic controllable twist rotor. In *Proceedings of the 34th Annual Forum of the American Helicopter Society*, Washington DC, May 1978.

[115] F. S. Wei, J. P. Basile, and R. Jones. Vibration reduction on servo flap controlled rotor using HHC. In *Proceedings of the American Helicopter Society National Specialists' Meeting on Rotorcraft Dynamics*, Arlington, TX, Nov 1989.

[116] F. S. Wei. Active trailing edge tab control for helicopter rotor vibration reduction. In *Proceedings of the AIAA Dynamics Specialists Conference*, Salt Lake City, UT, Apr 1996.

[117] A. K. Padthe, L. Liu, and P. P. Friedmann. Numerical evaluation of microflaps for on blade control of noise and vibration. In *Proceedings of the 52nd AIAA/ASME/ASCE/AHS/ASC Structures, Structural Dynamics and Materials Conference*, Denver, CO, Apr 2011.

[118] C. Kessler. Active rotor control for helicopters: individual blade control and swashplateless rotor designs. *CEAS Aeronautical Journal*, 1:23–54, 2011.

[119] C. Kessler and P. P. Friedmann. A comprehensive survey of individual blade control emphasizing recent implementations. In *Proceedings of the 15th International Forum on Aeroelasticity and Structural Dynamics*, Frankreich, Paris, 6 2011.

[120] B. Roget and I. Chopra. Individual blade control methodology for a rotor with dissimilar blades. *Journal of the American Helicopter Society*, 48(3):176–185, 2003.

[121] B. Roget. *Individual blade control for vibration reduction of a helicopter with dissimilar blades*. PhD thesis, University of Maryland, College Park, MD, 2004.

[122] H. Yeo. Assessment of active controls for rotor performance enhancement. *Journal of the American Helicopter Society*, 53(2):152–163, 2008.

[123] L. Liu, P. P. Friedmann, I. Kim, and D. S. Bernstein. Rotor performance enhancement and vibration reduction in presence of dynamic stall using actively controlled flaps. *Journal of the American Helicopter Society*, 53(4):338–350, 2008.

[124] K. Nguyen. Active control of helicopter blade stall. *Journal of aircraft*, 35(1):91–98, 1998.

[125] K. Nguyen. Active suppression of stall on helicopter rotors. In *Proceedings of the 25th European Rotorcraft Forum*, Rome, Italy, Sep 1999.

[126] D. Patt, L. Liu, and P. P. Friedmann. Helicopter noise reduction by actively controlled flaps. In *Proceedings of the 11th AIAA/CEAS Aeroacoustics Conference*, Monterey, CA, May 2005.

[127] B. W. Sim, R. D. JanakiRam, N. L. Barbely, and E. Solis. Reduced in-plane, low frequency noise of an active flap rotor. In *Proceedings of the 65th Annual Forum of the American Helicopter Society*, Grapevine, TX, May 2009.

[128] P. P. Friedmann and T. A. Millott. Vibration reduction in rotorcraft using active control-a comparison of various approaches. *Journal of Guidance, Control, and Dynamics*, 18(4):664–673, 1995.

[129] P. P. Friedmann. Vibration reduction in rotorcraft using actively controlled flaps-their evolution and potential for improving rotorcraft technology. In *Proceedings of the 30th European Rotorcraft Forum*, Marseille, France, Sep 2004.

[130] I. Chopra. Status of application of smart structures technology to rotorcraft systems. *Journal of the American Helicopter Society*, 45(4):228–252, 2000.

[131] I. Chopra. Review of state of art of smart structures and integrated systems. *AIAA journal*, 40(11):2145–2187, 2002.

[132] Victor Giurgiutiu. Review of smart-materials actuation solutions for aeroelastic and vibration control. *Journal of Intelligent Material Systems and Structures*, 11(7):525–544, 2000.

[133] J. Sirohi and I. Chopra. Fundamental understanding of piezoelectric strain sensors. *Journal of Intelligent Material Systems and Structures*, 11(4):246–257, 2000.

[134] F. K. Straub, V. Anand, T. S. Birchette, and B. H. Lau. Smart rotor development and wind tunnel test. In *Proceedings of the 35th European Rotorcraft Forum*, Hamburg, Germany, Sep 2009.

[135] T. Lee and I. Chopra. Design issues of a high-stroke, on-blade piezostack actuator for a helicopter rotor with trailing-edge flaps. *Journal of Intelligent Material Systems and Structures*, 11(5):328–342, 2000.

[136] T. Lee and I. Chopra. Design of piezostack-driven trailing-edge flap actuator for helicopter rotors. *Smart Materials and Structures*, 10(1):15–24, 2001.

[137] E. F. Prechtl and S. R. Hall. Design of a high efficiency, large stroke, electromechanical actuator. *Smart Materials and Structures*, 8(1):13–30, 1999.

[138] R. L. Spangler Jr and R. Hall. Piezoelectric actuators for helicopter rotor control. In *Proceedings of the 31st AIAA/ASME/ASCE/AHS/ASC Structures, Structural Dynamics and Material Conference*, Long Beach, CA, 1990.

[139] M. V. Fulton and R. A. Ormiston. Small-scale rotor experiments with on-blade elevons to reduce blade vibratory loads in forward flight. In *Proceedings of the 54th Annual Forum of the American Helicopter Society*, Washington, DC, May 1998.

[140] M. V. Fulton and R. A. Ormiston. Hover testing of a small-scale rotor with on-blade elevons. *Journal of the American Helicopter Society*, 46(2):96–106, 2001.

[141] M. V. Fulton. Aeromechanics of the active elevon rotor. In *Proceedings of the 61st Annual Forum of the American Helicopter Society*, Grapevine, TX, Jun 2005.

[142] M. V. Fulton. Multidisciplinary CFD/CSD analysis of the smart active flap rotor. In *Proceedings of the 66th Annual Forum of the American Helicopter Society*, Phoenix, AZ, May 2010.

[143] N. Koratkar and I. Chopra. Analysis and testing of mach scaled rotor model with piezoelectric bender actuated trailing-edge flaps for helicopter vibration control. In *Proceedings of the 40th AIAA/ASME/ASCE/AHS/ASC Structures, Structural Dynamics and Materials Conference and Adaptive Structures Forum*, St. Louis, MO, 1999.

[144] N. A. Koratkar and I. Chopra. Wind tunnel testing of a mach-scaled rotor model with trailing-edge flaps. *Smart Materials and Structures*, 10(1):1–14, 2001.

[145] N. A. Koratkar and I. Chopra. Open-loop hover testing of a smart rotor model. *AIAA journal*, 40(8):1495–1502, 2002.

[146] N. A. Koratkar and I. Chopra. Wind tunnel testing of a smart rotor model with trailing-edge flaps. *Journal of the American Helicopter Society*, 47(4):263–272, 2002.

[147] B. Roget and I. Chopra. Wind-tunnel testing of rotor with individually controlled trailing-edge flaps for vibration reduction. *Journal of Aircraft*, 45(3):868–879, 2008.

[148] F. K. Straub and A. A. Hassan. Aeromechanic considerations in the design of a rotor with smart material actuated trailing edge flaps. In *Proceedings of the 52nd Annual Forum of the American Helicopter Society*, Washington DC, Jun 1996.

[149] F. K. Straub. A feasibility study of using smart materials for rotor control. *Smart Materials and Structures*, 5(1):1–10, 1996.

[150] F. K. Straub and B. D. Charles. Aeroelastic analysis of rotors with trailing edge flaps using comprehensive codes. *Journal of the American Helicopter Society*, 46(3):192–199, 2001.

[151] F. K. Straub, D. K. Kennedy, D. B. Domzalski, A. A. Hassan, H. Ngo, V. Anand, and T. Birchette. Smart material-actuated rotor technology - smart. *Journal of Intelligent Material Systems and Structures*, 15(4):249–260, 2004.

[152] F. K. Straub and D. K. Kennedy. Design, development, fabrication and testing of an active flap rotor system. In *Proceedings of the 61th Annual Forum of the American Helicopter Society*, Grapevine, TX, Jun 2005.

[153] R. A. Ormiston. Aeroelastic considerations for rotorcraft primary control with on-blade elevons. In *Proceedings of the 57th Annual Forum of the American Helicopter Society*, Washington, DC, May 2001.

[154] J. Shen and I. Chopra. Aeroelastic modeling of trailing-edge flaps with smart material actuators. In *Proceedings of the 41st Structures, Structural Dynamics and Materials Conference and Adaptive Structures Forum*, Atlanta, GA, Apr 2000.

[155] J. Shen. *Comprehensive aeroelastic analysis of helicopter rotor with trailing-edge flap for primary control and vibration control*. PhD thesis, University of Maryland, College Park, MD, 2003.

[156] J. Shen, I. Chopra, and W. Johnson. Performance of swashplateless ultralight helicopter rotor with trailing-edge flaps for primary flight control. In *Proceedings of the 59th Annual Forum of the American Helicopter Society*, Phoenix, AZ, May 2003.

[157] J. Shen and I. Chopra. Swashplateless helicopter rotor with trailing-edge flaps. *Journal of Aircraft*, 41(2):208–214, 2004.

[158] J. Shen and I. Chopra. Aeroelastic modeling of trailing-edge-flap helicopter rotors including actuator dynamics. *The Journal of Aircraft*, 41(6):1465–1472, 2004.

[159] J. Shen and I. Chopra. A parametric design study for a swashplateless helicopter rotor with trailing-edge flaps. *Journal of the American Helicopter Society*, 49(1):43–53, 2004.

[160] J. Shen, M. Yang, and I. Chopra. Swashplateless helicopter rotor with trailing-edge flaps for flight and vibration control. *The Journal of Aircraft*, 43(2):346–352, 2006.

[161] J. Falls and I. Chopra. Recent progress towards development of swashplateless rotor systems. In *Proceedings of the 2nd International Basic Research Conference on Rotorcraft Technology*, Nanjing, China, Nov 2005.

[162] J. Falls and I. Chopra. Piezobimorph actuated servotab for controlling a trailing edge flap. In *Proceedings of the 46th AIAA/ASME/ASCE/AHS/ASC Structures, Structural Dynamics and Materials Conference*, Austin, TX, Apr 2005.

[163] J. Falls, A. Datta, and I. Chopra. Integrated trailing-edge flaps and servotabs for helicopter primary control. In *Proceedings of the 62nd Annual Forum of the American Helicopter Society*, Phoneix, AZ, May 2006.

[164] J. Falls. *Design and performance prediction of swashplateless helicopter rotors with trailing edge flaps and tabs*. PhD thesis, University of Maryland, College Park, MD, 2010.

[165] J. Falls, A. Datta, and I. Chopra. Integrated trailing-edge flaps and servotabs for helicopter primary control. *Journal of the American Helicopter Society*, 55(3):1–15, 2010.

[166] A. Datta and I. Chopra. Validation and understanding of UH-60a vibratory loads in steady level flight. *Journal of the American Helicopter Society*, 49(3):271–287, 2004.

[167] A. Datta and I. Chopra. Validation of structural and aerodynamic modeling using UH-60a airloads program data. *Journal of the American Helicopter Society*, 51(1):43–58, 2006.

[168] A. Jose and J. Baeder. An investigation into the aerodynamics of trailing edge flaps using CFD and analytical methods. In *Proceedings of the 61st Annual Forum of the American Helicopter Society*, Grapevine, TX, Jun 2005.

[169] A. Jose, A. Mishra, and J. Baeder. An investigation into the aerodynamics of trailing edge flaps with overhang and gap. In *Proceedings of the American Helicopter Society Specialists Conference on Aeromechanics*, San Francisco, CA, Jan 2008.

[170] A. Jose and J. D. Baeder. Steady and unsteady aerodynamic modeling of trailing edge flaps with overhang and gap using CFD and lower order models. In *Proceedings of 47th AIAA Aerospace Sciences Meeting*, Orlando, FL, 2009.

[171] A. Jose. *Investigation into the aerodynamics of swashplateless rotors using CFD-CSD analysis*. PhD thesis, University of Maryland, College Park, MD, 2012.

[172] R. Ganguli, B. Jehnert, J. Wolfram, and P. Voersmann. Survivability of helicopter with individual blade primary control failure. *Aeronautical Journal*, 111(1124):645–657, 2007.

[173] R. Ganguli, B. Jehnert, J. Wolfram, and P. Voersmann. Optimal location of centre of gravity for swashplateless helicopter uav and mav. *Aircraft Engineering and Aerospace Technology*, 79(4):335–345, 2007.

[174] Z. A. Chaudhry, B. E. Wake, A. Bagai, P. F. Lorber, and A. J. Collons. Active rotor development for primary and secondary flight control. In *Proceedings of the 65th Annual Forum of the American Helicopter Society*, Grapevine, TX, 2009.

[175] Z. A. Chaudhry, A. J. Collins, U. J. Jonsson, F. Sun, B. E. Wake, M. G. O'callaghan, and J. L-M Yeh. Self-lubricated actuator for on-blade rotor control. *US Patent 7,677,868*, 2010.

[176] P. Lorber, J. J. O'Neill, B. Hein, B. Isabella, J. Andrews, M. Brigley, J. Wong, P. Lemasurier, and B. Wake. Whirl and wind tunnel testing of the sikorsky active flap demonstration rotor. In *Proceedings of the 67th Annual Forum of the American Helicopter Society*, Virginia Beach, VA, May 2011.

[177] H. Saberi, M. Khoshlahjeh, R. A. Ormiston, and M. J. Rutkowski. Overview of rcas and application to advanced rotorcraft problems. In *Proceedings of the 4th Decennial Specialists Conference of the American Helicopter Society on Aeromechanics*, San Francisco, CA, 2004.

[178] P. F. Lorber, B. Hein, J. Wong, and B. Wake. Rotor aeromechanics results from the sikorsky active flap demonstration rotor. In *Proceedings of the 68th Annual Forum of the American Helicopter Society*, Forth Worth, TX, May 2012.

[179] P. F. Lorber, J. J. O'Neill, B. Isabella, J. Andrews, J. Wong, B. Hein, D. Geiger, B. E. Wake, U. Jonsson, and F. Sun. Whirl test of a large scale high authority active flap rotor. In *Proceedings of the 66th Annual Forum of the American Helicopter Society*, Phoenix, AZ, 2010.

[180] B. K. S. Woods, C. S. Kothera, and N. M. Wereley. Wind tunnel testing of a helicopter rotor trailing edge flap actuated via pneumatic artificial muscles. *Journal of Intelligent Material Systems and Structures*, 22(13):1513–1528, 2011.

[181] B. K. S. Woods. *Pneumatic Artificial Muscle Driven Trailing Edge Flaps for Active Rotors*. PhD thesis, University of Maryland, College Park, MD, 2012.

[182] B. K. S. Woods, Y. T. Choi, C. S. Kothera, and N. M. Wereley. Control system development for pneumatic artificial muscle-driven active rotor systems. *Journal of Guidance, Control, and Dynamics*, 36(4):1177–1185, 2013.

[183] B. K. Woods, Y. T. . T. Choi, C. S. Kothera, and N. M. Wereley. Control system development for pneumatic artificial muscle-driven active rotor systems. In *Proceedings of the 67th Annual Forum of the American Helicopter Society*, Virginia Beach, VA, May 2013.

[184] P. Copp and I. Chopra. Continued development of a mach scale swashplateless rotor with integrated trailing edge flaps. In *Proceedings of the 64th Annual Forum of the American Helicopter Society*, Montreal, Canada, 2008.

[185] P. Copp and I. Chopra. Mach scale swashplateless rotor using piezobender-actuated trailing edge flaps for primary control. In *Proceedings of the 21st International Conference on Adaptive Structures and Technologies (ICAST)*, University Park, PA, Oct 2010.

[186] P. Copp. *Swashplateless helicopter experimental investigation: primary control with trailing edge flaps actuated with piezobenders*. PhD thesis, University of Maryland, College Park, MD, 2013.

[187] G. K. Hunt. Similarity requirements for aeroelastic models of helicopter rotors. Technical report, 1973.

[188] C. H. Wolowicz, J. S. Brown Jr, and W. P. Gilbert. Similitude requirements and scaling relationships as applied to model testing. Technical report, 1979.

[189] J. D. Singleton and W. T. Yeager. Important scaling parameters for testing model-scale helicopter rotors. In *Proceedings of the 20th AIAA Advanced Measurement and Ground Testing Technology Conference*, Albuquerque, NM, Jun 1998.

[190] J. D. Singleton and W. T. Yeager. Important scaling parameters for testing model-scale helicopter rotors. *Journal of Aircraft*, 37(3):396–402, 2000.

[191] P. P. Friedmann. Aeroelastic scaling for rotary-wing aircraft with applications. *Journal of Fluids and Structures*, 19(5):635–650, 2004.

[192] Bosch Rexroth. *Data-sheet: Axial piston fixed motor AA2FM*, July 2014.

[193] Bosch Rexroth. *Data-sheet: Axial piston variable pump (A)A10VSO*, July 2009.

[194] Eaton Vickers. *Data-sheet: Remote Electrically Modulated Flow Control Valve FGE-06-30-002-(E)-12*, April 1979.

[195] Exxon Mobil. *Data-sheet: Mobil DTE 20 Series.*

[196] Eaton Vickers. *The systematic approach to contamination control - A complete guide for maximum system performance.*

[197] Eaton Vickers. *Data-sheet: Accessories for Hydraulic Systems.*

[198] Eaton Vickers. *Data-sheet: Solenoid Operated Directional Valves.*

[199] Eaton Vickers. *Data-sheet: Pressure Relief Valves.*

[200] Baldor Reliance. *Data-sheet: AC Induction Motor CM4316T.*

[201] Globe Motors. *Data-sheet: SS-Gearmotors A-1430.*

[202] D. Ceccarini. Optimization study on a composite tension-torsion strap for rotor system. Technical report, 2012.

[203] R. T. Casey. A design and optimization study of a composite rotor system tension-torsion strap. Master's thesis, Rensselaer Polytechnic Institute, Hartford, CT, 2010.

[204] Melexis Microelectronics Integrated Systems. *Data-sheet: MLX90316 Rotary Position Sensor IC.*

[205] Allegro Microsystems. *Data-sheet: Low Noise, Linear Hall Effect Sensor ICs with Analog Output A1324.*

[206] Maurey Instruments. *Data-sheet: Linear Motion Potentiometers.*

[207] M. J. Renzi. An assessment of modern methods for rotor track and balance. Master's thesis, Air Force Institute of Technology, Wright-Patterson Air Force Base, Ohio, 2004.

[208] P. M. Shinoda, H. Yeo, and T. R. Norman. Rotor performance of a UH-60 rotor system in the NASA ames 80-by 120-foot wind tunnel. *Journal of the American Helicopter Society*, 49(4):401–413, 2004.

[209] W. Warmbrodt, C. A. Smith, and W. Johnson. Rotorcraft research testing in the national full-scale aerodynamics complex at NASA ames research center. Technical Report NASA Technical Memorandum 86687, 1985.

[210] R. L. Peterson and J. M. vanAken. Dynamic calibration of the NASA ames rotor test apparatus steady/dynamic rotor balance. Technical Report NASA Technical Memorandum 110393, 1996.

[211] T. R. Norman, P. M. Shinoda, C. Kitaplioglu, S. A. Jacklin, and A. Sheikman. Low-speed wind tunnel investigation of a full-scale UH-60 rotor system. In *Proceedings of the 58th Annual Forum of the American Helicopter Society*, Montreal, Canada, Jun 2002.

[212] W. T. Yeager Jr, M. L. Wilbur, and M. W. Nixon. A review of recent rotorcraft investigations in the langley transonic dynamics tunnel. 2000.

[213] W. T. Yeager Jr and R. G. Kvaternik. A historical overview of aeroelasticity branch and transonic dynamics tunnel contributions to rotorcraft technology and development. Technical report, Aug 2001.

[214] W. T. Yeager, P. H. Mirick, M. Hamouda, H. Nabil, M. L. Wilbur, J. D. Singleton, and W. K. Wilkie. Rotorcraft aeroelastic testing in the langley transonic dynamics tunnel. *Journal of the American Helicopter Society*, 38(3):73–82, 1993.

[215] Jr Yeager, W. T and R. G. Kvaternik. Contributions of the langley transonic dynamics tunnel to rotorcraft technology and development. In *Proceedings of the AIAA Dynamics Specialists Conference*, Atlanta, GA, Apr 2000.

[216] C. Cameron, A. Karpatne, and J. Sirohi. Performance and vibratory hub loads of a mach-scale coaxial rotor in hover. In *Proceedings of the 70th Annual Forum of the American Helicopter Society*, Montreal, Canada, May 2014.

[217] C. G. Cameron, D. Uehara, and J. Sirohi. Transient hub loads and blade deformation of a mach-scale coaxial rotor in hover. In *Proceedings of the 56th AIAA/ASCE/AHS/ASC Structures, Structural Dynamics, and Materials Conference*, Kissimmee, FL, Jan 2015.

[218] Rotorversuchstnde ROTOS und ROTEST. `http://www.dlr.de/ft/en/desktopdefault.aspx/tabid-1387/1915_read-3372/`. Accessed: Apr 24, 2015.

[219] S. Saito, Y. Tanabe, and N. Kobiki. Overview of the jaxa helicopter research activity. Technical Report JAXA Research and Development Memorandum JAXA-RM_13-012E, 2013.

[220] P. Yedamale. Brushless dc (bldc) motor fundamentals. Technical report, 2003.

[221] Maxon Motors. *Data-sheet: EC-10 brushless DC motor.*

[222] Maxon Motors. *Data-sheet: GP-10 planetary nose gearhead.*

[223] Maxon Motors. *1-Q-EC Amplifier AECS-35/3 motor controller - Operating principles.*

[224] A. M. Harrington and C. Kroninger. Characterization of small dc brushed and brushless motors. Technical report, 2013.

[225] P. Pillay and R. Krishnan. Modeling of permanent magnet motor drives. *IEEE Transactions on Industrial Electronics*, 35(4):537–541, 1988.

[226] S. Ogasawara and H. Akagi. An approach to position sensorless drive for brushless dc motors. *Conference Record of the IEEE Industry Applications Society Annual Meeting*, pages 443–447, 1990.

[227] S. Baldursson. Bldc motor modelling and control-a matlab/simulink implementation. Master's thesis, Chalmers University of Technology, Gothenburg, Sweden, 2005.

[228] A. Kurdoglu. Brushless dc motor speed control circuit design. Master's thesis, Istanbul University, Istanbul, Turkey, 2007.

[229] V. Hubik, M. Sveda, and V. Singule. Mathematical model of a sensorless bldc motor for aerospace actuators. In *Proceedings of the 19th IASTED International Conference on Modeling and Simulation*, 2008.

[230] Z. Meng, R. Chen, C. Sun, and Y. An. The mathematical simulation model of brushless dc motor system. In *Proceedings of the 2010 International Conference on Computer Application and System Modeling*, 2010.

[231] N. Hashemnia and B. Asaei. Comparative study of using different electric motors in the electric vehicles. In *Proceedings of the 2008 International Conference on Electrical Machines*, 2008.

[232] Maxon Motors. *Maxon EC Motor Ironless Winding Technology - Short and to the Point.*

[233] D. Montane, Pitmann Motors. *Temperature effects on motor performance.*

[234] Frekote. *Data-sheet: Frekote 700-NC.*

[235] Cytec. *Data-sheet: FM 300 High-Shear Strength Modified Epoxy Film Adhesive.*

[236] Rohacell. *Technical Information: Rohacell IG/IG-F.*

[237] Hexcel Composites. *Data-sheet: 8552 Epoxy Matrix product data.*

[238] S. N. Jung and B. H. Lau. Determination of hart i blade structural properties by laboratory testing. Technical Report NASA Contractor Report - 216039, 2012.

[239] B. Luz. Calculation of the stiffness of an element using vicon. Technical report, 2014.

[240] M. Stora. Stiffness calculation methods. Technical report, 2014.